UNIVERSITÀ DEGLI STUDI DI PAVIA

FACOLTÀ DI INGEGNERIA

DIPARTIMENTO DI INGEGNERIA CIVILE E ARCHITETTURA

DOCTOR OF PHILOSOPHY

Advanced isogeometric methods with a focus on composite laminated structures

Metodi isogeometrici avanzati con applicazioni a strutture composite laminate

---

Author:
Alessia PATTON

Supervisor:
Professor Alessandro REALI

Co-Supervisor:
Doctor Guillermo LORENZO

A thesis submitted in fulfillment of the requirements
for the degree of *Doctor of Philosophy*

in

Design, Modeling, and Simulation in Engineering

""Curiouser and curiouser!" cried Alice (she was so much surprised, that for the moment she quite forgot how to speak good English)."

Lewis Carroll, Alice's Adventures in Wonderland

Abstract

The design and optimization of engineering products demand faster development and better results at lower costs. These challenging objectives can be achieved by readily evaluating multiple design options at the very early stages of the engineering design process. To this end, accurate and cost-efficient computational modeling techniques for solids and fluids offer a reliable support and enable a better understanding of the underlying complex physical phenomena. Additionally, computer simulations can ultimately reduce the necessity for experimental tests, which often turn out to be time-consuming, expensive, and very difficult to carry out. The present work focuses on the development of advanced computational tools in the context of Isogeometric Analysis (IgA), trying to exploit its higher-order continuity properties and typically excellent accuracy-to-computational-effort ratio. More specifically, we also investigate isogeometric collocation (IgC), which can be regarded as a fast strong-form method and an alternative to standard isogeometric Galerkin (IgG) approaches. IgC can achieve high-order convergence rates coupled with a significantly reduced computational cost. However, IgG methods are usually more accurate than IgC with respect to the number of degrees of freedom. Therefore, new IgC approaches are usually benchmarked against an IgG formulation for the same problem.

Here, we first focus on constructing an accurate computational strategy to model laminated composite structures in an attempt to address the unmet demand of cost-efficient simulation techniques for laminates, especially when they are made of a significant number of plies. Our modeling strategy relies on the aforementioned computational advantages of IgA and an equilibrium-based interlaminar stress recovery. In brief, we first calculate an efficient and accurate approximation of the displacement fields (and their derivatives) using a single-element through the thickness of the laminate in combination with either a layer-by-layer integration rule or a homogenized approach. While this relatively inexpensive calculation renders an excellent approximation of the in-plane stresses in the laminate, the resulting out-of-plane stress components are poorly approximated and violate equilibrium constraints. Thus, to recover these interlaminar stresses, we propose a cost-effective pointwise post-processing technique that is based on the direct integration of the equilibrium equations in strong form, involving the straightforward computation of high-order derivatives of the displacement field. This procedure fundamentally requires high regularity in the approximation of the displacement fields, which is fully granted by the properties of IgA shape functions. To test our computational strategy, we first study solid laminated composite plates exclusively resolved *via* a homogenized IgC scheme. Then, we extend our modeling technique to bivariate

laminated Kirchhoff plates, considering both homogenized IgC and IgG formulations. To model this type of structure we use the classical laminate plate theory (CLPT), which provides the lowest computational cost among known strategies in the literature and features a high-order partial differential equation that can be easily handled by the high smoothness of IgA functions. According to CLPT, interlaminar stresses are identically zero when computed using the constitutive equations. Therefore, our stress recovery technique produces a unique, primal approximation of the out-of-plane stress within the CLPT framework. Additionally, we extend our computational strategy for laminate composites to solid shells. The first challenge for this type of structures is that stresses cannot longer be associated to in-plane and out-of-plane components in the global reference system. Thus, we introduce a local description at every point of the structure for which the out-of-plane through-the-thickness stress is going to be recovered. This grants that no additional coupled terms appear in the equilibrium, allowing for a direct reconstruction of the interlaminar stresses without the need to solve the full balance of linear momentum equation. In this work, we resolve solid shells using homogenized IgC and IgG formulations, with the latter further featuring a layer-specific quadrature rule. Moreover, we explore alternative stress recovery techniques that grant lower continuity requirements by exploiting the stress-strain relation within the out-of-plane balance of linear momentum. The proposed stress recovery method proves to be particularly effective to capture the out-of-plane behavior of slender structures with a high number of plies. The IgC formulations achieve comparable accuracy with respect to a renown validation benchmark in the field of composites or an overkill IgG layerwise approach, even when considering a very coarse mesh in some cases. The proposed modeling techniques enable to calculate the full stress state in every location within the plate, including the boundaries, where edge effects usually cause inaccuracy of the solution with other modeling frameworks, and at the interfaces between the layers, where it is crucial to determine an accurate out-of-plane stress field to avoid failure modes like delamination. Additionally, a preliminary study shows that the alternative low-continuity formulations exhibit remarkable accuracy compared to the general stress recovery strategy proposed in this thesis.

In an attempt to possibly include delamination effects into composite structure simulations, we further develop a novel solution technique for phase-field modeling of crack propagation using IgA. This modeling paradigm can naturally handle fracture phenomena with arbitrarily complex crack topologies and has attracted high attention both in the physics and the engineering communities. One of the key features of a crack evolution process is that a fracture cannot heal and, therefore, it is a non-reversible process. Thus, we propose a novel approach for a rigorous enforcement of the irreversibility constraint, which grants non-negative damage increments under prescribed displacements and may be efficiently resolved further providing a reduction of the computational time with respect to standard methods to solve phase-field brittle fracture. Our solution strategy proves to significantly reduce the elapsed time of the execution of the phase-field subroutine for two well-known fracture benchmarks with respect to a state-of-the-art penalty approach, directly imposing the irreversibility constraint and without introducing new variables or modifying the original problem, which is required in penalization methods. Preliminary results using C^1 quadratic B-spline shape functions confirm that the proposed solution scheme can also be used for higher-order discretizations. However, independently of the adopted order, the problem-dependent internal length of the damage phase field is the primary feature that needs to be precisely resolved with the chosen

computational method to obtain accurate results.

Finally, we explore new IgC formulations in the context of fluid-structure interaction (FSI). Computational fluid dynamics (CFD) problems usually require the parametrization of complex 3D domains, which can be extremely challenging using closed volume splines within a standard IgG approach. To overcome this issue, boundary-conforming finite elements can be a viable alternative and lead to a geometrically compatible coupling fluid-structure interface for FSI problems. Thus, we propose to adopt a common spline description of the interface, combining IgC on the structural side and boundary-conforming finite elements (like the so-called NURBS-enhanced finite elements) on the fluid side. Hence, the computational advantages of IgC are available to solve FSI problems. Additionally, IgC provides a unique coupling capability to transfer stresses across interfaces, as it has been proven in contact mechanics problems. In particular, the coupling of the structural and the fluid solution is granted by means of a partitioned approach. Preliminary results for a known FSI benchmark confirm that the spatiotemporal coupling of the fluid and structural problems is achieved and that the necessary projection methods to exchange information from one problem to the other simplify due to the matching geometry at the fluid-structure interface.

Acknowledgements

Firstly, I would like to express my sincere gratitude to my advisor Prof. Alessandro Reali for the continuous support of my Ph.D study and related research, for the patience, motivation, and profound knowledge he shared with me over these three years.

I would also like to thank my co-advisor Dr. Guillermo Lorenzo for his patient support and insightful feedback that pushed me to sharpen my thinking and improve my final work.

My sincere thanks also goes to Prof. Thomas J.R. Hughes, who provided me the great opportunity to join his team at the Oden Institute for Computational Engineering and Sciences of the University of Texas at Austin.

I also wish to thank Dr. Pablo Antolín, Prof. Josef Kiendl, Prof. Umberto Perego, Prof. Matteo Negri, Dr. John-Eric Dufour, and Dr. Norbert Hosters for the stimulating discussions that allowed me to complete this work.

I dedicate this work to my mum and dad for supporting me in all senses and always believing in me. To my little nieces Elin, Lisa, and my nephew Luca, to my brother Ema and to Ane. I've missed you all so much and I hope to hug you soon after Covid-19 pandemic will be over. Thank you Serena for being always by my side in every situation, Valentina, your courage inspires me, Francesca, your energy is compelling for everyone, and Valeria, thank you for always believing in me.

Guille, thanks again for being such a true friend to me. Thanks to Ale Marengo for all the laughs and the good time we have working together. I thank my fellow labmates, especially Lau, Anna, Frá, John, Alex, Lore, Cri, Ali, Max, Sai and Miche, for all the fun we have had in the last three years. Many thanks to the wonderful people I had the chance to meet in Austin: my US labmates Deepesh, Michael, Sasa, and René and my flatmates Schrou, Kaisa, Moch, Severin, and Alessio. Finally, I would like to thank my childhood friends Emilio, Andre, and Ele. I bring you with me everywhere I go.

Contents

Appendices

List of Figures

List of Tables

xxviii

List of Abbreviations

CAD	Computer Aided Design
CCS	Compressed Column Storage
CFD	Computational Fluid Dynamics
CLPT	Classical Laminate Plate Theory
CUF	Carrera Unified Formulation
DOF	Degree Of Freedom
EC	Enhanced Collocation
ESL	Equivalent Single-Layer
FEA	Finite Element Analysis
FG	Functionally Graded
FSDT	First-order Shear Deformation Theory
FSI	Fluid Structure Interaction
IgA	Isogeometric Analysis
IgC	Isogeometric Collocation
IgG	Isogeometric Galerkin
LW	Layerwise
NEFEM	NURBS Enhanced Finite Element Method
NURBS	Non-Uniform Rational B-Splines
PDE	Partial Differential Equation
PSOR	Projected Successive Over-Relaxation
SEN	Single-Edge Notched
SLCP	Symmetric Linear Complementarity Problem

xxx

List of Symbols

Functional analysis

$\mathbb{R}^n$	n-dimensional space of real numbers
C^m	space of functions with a continuous m-th derivative

Continuum mechanics

$\hat{\Omega}$	parameter space
Ω	physical space
Ω_X	physical space in the initial configuration
Ω_x	physical space in the deformed configuration
$\partial\Omega, \Gamma$	boundary of the physical space
Γ_X	boundary of the physical space in the initial configuration
Γ_X	boundary of the physical space in the deformed configuration
Γ_N	boundary portion subjected to Neumann conditions
Γ_M	boundary portion subjected to the prescribed bending moment M_Γ
Γ_Q	boundary portion subjected to the prescribed effective shear Q_Γ
Γ_D	boundary portion subjected to Dirichlet conditions
Γ_φ	boundary portion subjected to the prescribed rotation φ_Γ
Γ_w	boundary portion subjected to the prescribed displacement w_Γ

F	mapping between the parameter space and the physical space
$\{X_1, X_2, X_3\}$	global reference cartesian system
$\{E_1, E_2, E_3\}$	orthonormal basis associated to the global reference cartesian system
$\{x_1, x_2, x_3\}$	local reference cartesian system
$\{a_1, a_2, a_3\}$	orthonormal basis associated to the local reference cartesian system
$\{e_1, e_2, e_3\}$	static snapshot of the moving basis $\{a_1, a_2, a_3\}$
$\{g_1, g_2, g_3\}$	covariant basis
$C_{i\alpha}$	basis change operator between the static snapshot of the local moving basis and the global basis
$D_{i\alpha}$	basis change operator between the local moving basis and the global basis
$\mathbf{F}$	deformation gradient
u	displacement field
v	velocity field
d	phase-field variable
δu	virtual displacement field
δv	virtual velocity field
δd	virtual phase-field variable
$\mathbf{S}$	second Piola-Kirchhoff stress tensor
$\mathbf{T}$	total stress tensor
σ	Cauchy stress tensor
$\mathbf{M}$	bending moment vector
$\mathbf{E}$	Green-Lagrange strain tensor
ε	strain tensor
$\delta\varepsilon$	virtual strain tensor
κ	curvature vector
$\mathbb{C}$	linear elasticity fourth-order tensor
$\tilde{\mathbb{C}}$	homogenized fourth-order linear elasticity tensor of material properties in the global reference system
$\overline{\mathbb{C}}$	homogenized fourth-order linear elasticity tensor of material properties in the local reference system
$\mathbb{D}$	bending material stiffness in the local reference system

$\overline{\mathbb{D}}$	homogenized bending material stiffness in the local reference system
B	body force per unit of volume of the structure in the initial configuration
b	body forces per unit of volume of the structure
f	body forces per unit of mass of the fluid
t	traction forces
N	outward normal in the reference configuration
n	outward normal
δW_{int}	internal virtual work of the system
δW_{ext}	external virtual work of the system
Π	total energy functional
$\mathcal{E}$	elastic energy functional
$\mathcal{D}$	phase-field energy functional

Geometric and mechanical parameters

λ, μ	Lamé's parameters
κ	bulk modulus
E	Young's modulus for an isotropic case
E_1, E_2, E_3	Young's moduli for an orthotropic case
G_{23}, G_{13}, G_{12}	shear moduli for an orthotropic case
ν	Poisson's coefficient for an isotropic case
$\nu_{23}, \nu_{13}, \nu_{12}$	Poisson's coefficients for an orthotropic case
ρ^f	fluid density
μ^f	dynamic viscosity of the fluid
ρ^s	density of the structure
q, p	loading pressure
σ_0	reference pressure
t	total thickness of the laminate
N	number of layers
D	cylinder diameter
R	radius
$\bar{R}$	mean radius
r_i, r_o	inner and outer radius
L	total length of the laminate

S	slenderness parameter (e.g., length-to-thickness ratio or radius-to-thickness ratio)
l_0	internal length
G_c	critical fracture energy
U	inflow velocity

IgA discretization

Basic IgA notation

n, m, l	number of control points in ξ, η, and ζ parametric directions
p, q, r	order of approximation in ξ, η, and ζ parametric directions
$\Xi, \mathcal{H}, \mathcal{Z}$	knot-vector in ξ, η, and ζ parametric directions
ξ_i, η_j, ζ_k	i-th, j-th, and k-th knot
$N_{i,p}(\xi), M_{j,q}(\eta), L_{k,r}(\zeta)$	i-th, j-th, and k-th B-spline basis function of order p, q, and r
$\mathbf{B}_i, \mathbf{B}_{i,j}, \mathbf{B}_{i,j,k}$	control polygon, control net, and control lattice
$\mathbf{C}(\xi)$	B-spline curve
$\mathbf{S}(\xi, \eta), \mathbf{S}(\xi, \eta, \zeta)$	B-spline surface and solid
w_i	weight of i-th NURBS basis function
$R_i^p(\xi), R_{i,j}^{p,q}(\xi, \eta), R_{i,j,k}^{p,q,r}(\xi, \eta, \zeta)$	univariate, bivariate, and trivariate NURBS basis functions

Generalization of the IgA notation for the research in this thesis

d_s	dimension of the physical space
d_p	dimension of the parameter space
Ξ^d	univariate knot vectors in the d-th parameter space
$\boldsymbol{\xi} = \{\xi^1, ..., \xi^{d_p}\}$	parametric coordinates of a point in $\hat{\Omega}$
$\mathbf{m} = \{m_1, ..., m_{d_p}\}$	vector of number of basis functions in each parametric direction
$\mathbf{p} = \{p_1, ..., p_{d_p}\}$	vector of polynomial degrees in each parametric direction
$\mathbf{i} = \{i_1, ..., i_{d_p}\}$	vector of position indices in the tensor product structure

$N_{i_d,p_d}^d(\xi^d)$	univariate B-spline basis function in the d-th parametric direction
$B_{\mathbf{i},\mathbf{p}}(\boldsymbol{\xi})$	multivariate B-spline basis functions
$\mathbf{S}(\boldsymbol{\xi})$	multidimensional B-spline geometries
$\mathbf{P_i}$	control points
$R_{\mathbf{i},\mathbf{p}}(\boldsymbol{\xi})$	multivariate NURBS basis functions
$w_{\mathbf{i}}$	NURBS weights
$\mathbf{S}(\boldsymbol{\xi})$	multidimensional NURBS geometries
$\mathbf{R}_{\mathbf{i},\mathbf{p}}^{(e)}$	$\mathbf{i}$-th contribution of the matrix of multivariate shape functions supported by element e
$\mathbb{B}_{\mathbf{i},\mathbf{p}}^{(e)}$	$\mathbf{i}$-th contribution of the matrix of the derivatives of the multivariate shape functions supported by element e

IgC notation

τ_i^d	i-th Greville abscissa in the d-th parametric direction
$\boldsymbol{\tau}$	multidimensional array of collocation points
$\tilde{\mathbf{R}}_{\mathbf{i},\mathbf{p}}(\boldsymbol{\tau})$	$\mathbf{i}$-th contribution of the matrix of multivariate shape function values at collocation points
$\mathbf{K}(\boldsymbol{\tau})$	matrix of the collocated equilibrium equations
$\tilde{\mathbf{K}}(\boldsymbol{\tau})$	matrix of the collocated Neumann boundary conditions equations

Further useful symbols at the discrete level

$\boldsymbol{u}_h$	approximate displacement field
$\boldsymbol{w}_h$	approximate out-of-plane displacement field
$\boldsymbol{v}_h$	approximate velocity field
d_h	approximate phase-field variable
$\boldsymbol{u}_h^{(e)}$	approximate element displacement field
$\boldsymbol{w}_h^{(e)}$	approximate element out-of-plane displacement field
$\delta\boldsymbol{u}_h^{(e)}$	approximate element virtual displacement field
$\delta\boldsymbol{w}_h^{(e)}$	approximate element virtual out-of-plane displacement field
$\hat{\mathbf{u}}_{\mathbf{i}}$	vector of control variables for the displacement field

$\hat{\mathbf{d}}$	vector of control variables for the phase field
$\hat{\mathbf{u}}_{\mathbf{i}}^{(e)}$,	element vector of control variables for the displacement field
$\delta\hat{\mathbf{u}}_{\mathbf{i}}^{(e)}$	element vector of control variables for the virtual displacement field
$\hat{\mathbf{u}}_{\mathbf{i}}$, $\hat{\mathbf{v}}_{\mathbf{i}}$, $\hat{\mathbf{w}}_{\mathbf{i}}$	vectors of control variables for the displacement field in ξ, η, ζ parametric directions

Error control

e	maximum relative error
ẽ	L^2-norm relative error
Δ	relative difference

Chapter 1

Introduction

1.1 Motivation and Objectives

The development of accurate and efficient modeling techniques for solids and fluids offers a reliable support for the design and optimization of engineering products and allows for a better understanding of complex physical phenomena. Additionally, the derivation of increasingly sophisticated numerical simulation tools helps to reduce the necessity for experimental tests, which often result to be expensive and time-consuming, or very difficult to carry out.

A clear example of the need for more efficient modeling techniques resides in the field of composite materials. This kind of materials can be defined as combinations of two or more constituents that present enhanced properties that could not be acquired using any of the original units alone (see, e.g., [80, 102, 159, 187] and references therein). Composite materials exhibit many appealing mechanical properties, such as superior strength and stiffness while being lightweight, as well as improved corrosion and wear resistance. Thus, the interest for composite structures in the engineering community has continuously been growing in recent years, especially in the aerospace and automotive industries. As a result, the global market size of composites is projected to grow from USD 74.0 billion in 2020 to USD 112.8 billion by 2025 [48]. Recent examples of the extensive usage of composite materials comprise a new generation of commercial aircrafts such as Boeing B787 Dreamliner (see Figure 1.1(a)). Also, over 70% of Airbus A350XWB (see Figure 1.1(b)) is made with advanced materials, including 53% composites. As a result, these aircrafts are lighter, as well as corrosion- and fatigue-free, thereby optimizing maintenance costs and helping to reduce fuel consumption and emissions by 25% [1].

In particular, laminated composite structures are generally formed by a collection of laminae stacked and subsequently glued together (see Figure 1.2) to achieve improved mechanical properties (see, e.g., [86, 159]). Each lamina is commonly composed of a matrix that surrounds and holds a set of fibers in place. The matrix material acts as a load-transfer medium between fibers (a process that takes place through shear stresses) and protects those elements from being exposed to the environment, while the resistance properties of laminated composites are given by the
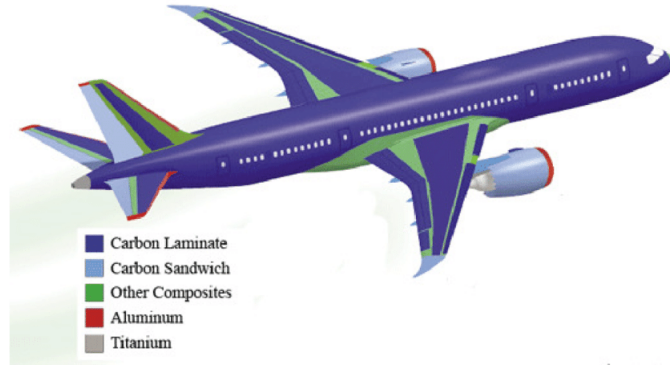
(a) Composite usage in Boeing B787 Dreamliner airplane [47].
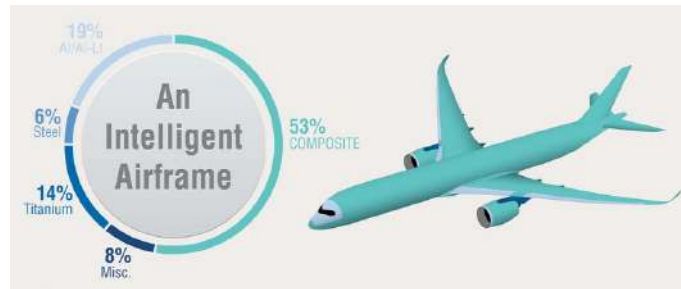
(b) Composite usage in Airbus A350XWB airplane [1].

FIGURE 1.1: Examples of composite usage in the aerospace industry.
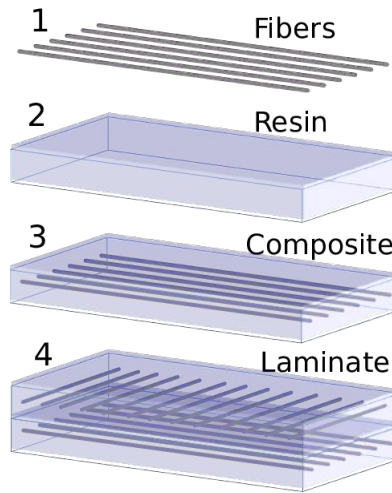
FIGURE 1.2: Composite laminate scheme [99].

fibers, which are stiffer and create a high-strength direction according to their orientation. These fibers can be oriented in multiple directions in each layer, hence giving designers the flexibility to tailor laminate stiffness and strength while still maintaining a reduced weight and matching even demanding structural requirements. Nevertheless, it is a well-known fact that laminated composites are prone to damage (even under simple loading conditions) due to comparatively poorer strength in the out-of-plane direction. As a result, an interface crack might grow between two adjacent plies leading to a failure mode referred to as *delamination* [169] (see Figure 1.3).

The most common sources of delamination are material and structural discontinuities that give rise to relevant interlaminar stresses [136]. In general, the interlaminar stress level is strongly dependent on the composite stacking sequence [146, 147] and the mismatch of engineering properties between adjacent plies [102].

Despite the accelerated diffusion of laminated composites in a wide variety of markets, the design of those materials is often restrained by the lack of cost-efficient modeling techniques. The standard approaches are two-dimensional theories and layerwise (LW) theories [119, 120, 159]. In particular, LW theories typically show a comparatively higher computational cost, especially for a high number of plies. More importantly, the existing strategies allowing for cheap simulations usually fail to directly capture out-of-plane through-the-thickness stresses, which prove to be typically responsible of failure modes such as delamination. Therefore, to properly design or assess the structural response of laminated structures, an accurate evaluation of the stresses through the thickness is of paramount importance [136, 169].

To address the unmet demand for accurate and cost-efficient modeling techniques for laminated composite structures, in this thesis we propose a new numerical strategy that exploits the high continuity properties and excellent accuracy-to-efficiency ratio of isogeometric analysis (IgA) [51, 64, 91, 109, 156, 185] to construct displacement-based methods coupled with a post-processing stress recovery technique (see, e.g., [65, 154, 183]), which allows to restore the out-of-plane through-the-thickness stress state by directly imposing the equilibrium equations. The considered stress recovery approach generally involves higher-order derivatives, which can be computed relying on IgA shape function properties. To this end, we depart from the preliminary work in [62] and develop these new methods for three key types of composite laminated structures: solid plates, bivariate Kirchhoff plates, and solid shells. We will focus on isogeometric collocation (IgC) formulations (see, e.g., [16]) for our displacement-based methods because these approaches are usually more cost-efficient than standard isogeometric Galerkin (IgG) schemes, in particular when higher-order approximation degrees are adopted [162]. However, for a fixed number of degrees of freedom (DOFs), this advantage of IgC may come at the cost of losing accuracy with respect to IgG. Thus, we will also compare the performance of IgC methods against an analytical benchmark case and IgG approaches to precisely determine the level of accuracy of our IgC formulations for the three structural types listed above.

Towards the possible inclusion of delamination effects into composite structure simulations, this thesis also investigates the phase-field modeling of brittle fracture in an IgA context. In this modeling paradigm, the damage process developing in the crack tip region is described by means of a phase field, i.e., an additional continuous variable depending on a material characteristic length that properly accounts for the effect of the strain localization occurring in the process zone in the material response. One of the key features of a crack evolution process is that a fracture cannot heal and, therefore, it is a non-reversible process. To account for this feature, several different approaches have been proposed in the literature for the solution of the phase-field problem under fixed displacements. In [134], the constraint is enforced by defining a further variable, the so-called *history variable*, which can be interpreted as the monotonically growing driving force of the phase field. Instead, in [79] a penalty functional is introduced into the formulation to replace the irreversibility
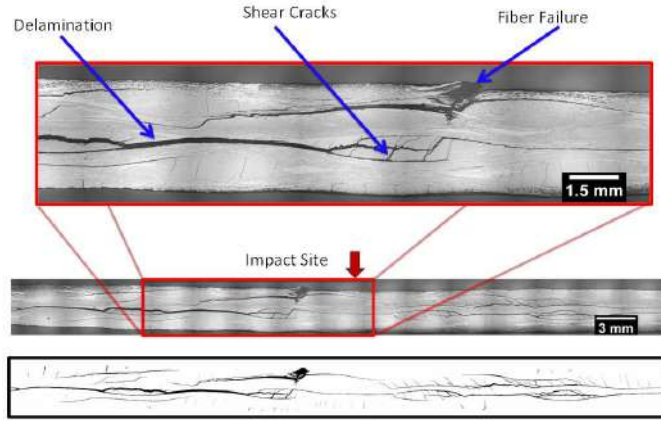
FIGURE 1.3: Cross-sectional images from impacted 2D and 3D woven composites [2].

constraint. Although this penalization is conceived as problem-independent, it alters the structure of the original problem and the penalty parameter strongly needs to be tuned depending on the nature of the considered problem. Therefore, inspired by the work of [45], we propose a novel approach for a rigorous enforcement of the irreversibility constraint, which grants non-negative damage increments under prescribed displacements and may be efficiently resolved further granting a reduction of the computational time with respect to standard methods to solve phase-field brittle fracture.

Finally, to further illustrate the promising potential of IgC approaches to meet the challenging demands of complex engineering applications accurately and efficiently, this thesis also investigates a novel combination of boundary-fitted finite elements and IgC formulations to resolve fluid-structure interaction (FSI) problems. In general, computational fluid dynamics (CFD) problems usually require the parametrization of complex 3D domains, which can be extremely challenging using closed volume splines within a standard IgA approach. Boundary-conforming finite elements can be a viable alternative and lead to a geometrically compatible coupling interface for FSI problems, thereby enabling to use IgA formulations in the structural domain. For instance, using a partitioned method, the work in [89] exploited this idea and demonstrated that the necessary projection methods between the fluid and the structural problems simplify due to the matching geometry, while the accuracy of the flow solution increases at the same time. Therefore, we propose to capitalize on this idea and further develop it by combining boundary-conforming finite elements on the fluid side with IgC on the structural side using a common spline description of the interface. While IgG formulations have been integrated into FSI analysis almost from the beginning of IgA, IgC has been used only for immersed FSI and there has been no application yet to boundary-fitted FSI to the best of our knowledge. Here, we aim to exploit the advantages of IgC and, in particular, its coupling capability in terms of transferring stresses across interfaces, as it has been proven in contact mechanics problems [55]. The coupling of the structural and the fluid solution is greatly facilitated by the common spline interface and granted by means of a partitioned approach, whereby the fluid and the structure are treated as individual fields and solved separately. In particular, the necessary information

is exchanged between structure and fluid using a Neumann/Dirichlet load transfer approach, namely forces resulting from the fluid boundary stresses are projected onto the structure as a Neumann boundary condition, while the structural deformations are transferred to the fluid as a Dirichlet boundary condition. In the future, we believe that this hybrid method to address FSI problems could be seamlessly integrated with our post-processing stress recovery technique for 3D curved laminated composite structures, thereby facilitating an accurate and cost-efficient design of complex geometries to serve fluid dynamics requirements in engineering applications.

1.2   Organization of the thesis

The rest of this thesis is organized as follows. In **Chapter 2**, we present the scientific background for this thesis. We begin by introducing the fundamentals of IgA, IgG approaches, and IgC methods. Then, we provide an overview of several applications of IgG and IgC methods with a focus on structural problems. Additionally, we describe the main techniques to model composite 3D solid plates, bivariate plates, 3D curved geometries, and shells. Then, we present an overview of the existing literature on equilibrium-based stress recovery theories and outline standard solution schemes for the phase-field modeling of brittle fracture. We conclude Chapter 2 by introducing FSI problems and focusing on the spatial coupling of non-matching interface discretizations on the fluid and structural sides. In **Chapter 3**, we propose an accurate equilibium-based interlaminar stress recovery for solid laminated composite plates, which are modeled *via* a homogenized single-element IgC method. This grants an accurate and cost-efficient in-plane solution, while the out-of-plane stress state is recovered by directly imposing the equilibrium equations. In **Chapter 4**, this procedure is successfully extended from 3D solid plates to bivariate laminated Kirchhoff plates, considering both homogenized IgC and IgG formulations. In **Chapter 5**, we proceed to further extend our modeling technique to solid shells. Due to the increasing geometry complexity, stresses referred to the global reference system cannot longer be associated to in-plane and out-of-plane components. Therefore, we introduce a local description at every point of the structure for which the out-of-plane stress is going to be recovered, thereby enabling to locally apply the equilibrium-based stress recovery technique. This grants that no additional coupled terms appear in the equilibrium, allowing for a direct reconstruction without the need to further iterate to resolve the balance of linear momentum equation. Additionally, we present very promising preliminary results obtained *via* an alternative post-processing step that enables to lower the recovery high-order continuity requirements. Then, in **Chapter 6**, we focus on the phase-field modeling of brittle fracture and present a novel approach for the rigorous enforcement of the irreversibility constraint during crack propagation along with an efficient computational approach to implement this modeling strategy. Additionally, in **Chapter 7**, we investigate the use of the advantageous computational properties of IgC approaches to address FSI problems and propose a novel IgA modeling strategy that combines boundary-conforming finite elements on the fluid side with IgC on the structural side. Finally, in **Chapter 8**, we draw our conclusions and discuss future perspectives of the work presented in this thesis.

Furthermore, to acknowledge all main sources of help, I hereby state that:

- **Chapter 3** is based on the article "A. Patton, J.-E. Dufour, P. Antolín, A. Reali. Fast and accurate elastic analysis of laminated composite plates *via* isogeometric collocation and an equilibrium-based stress recovery approach. *Composite Structures*, 225: 111026, 2019."

- **Chapter 4** is based on the article "A. Patton, P. Antolín, J.-E. Dufour, J. Kiendl, A. Reali. Accurate equilibrium-based interlaminar stress recovery for isogeometric laminated composite Kirchhoff plates. *Composite Structures*, 256: 112976, 2021."

- **Chapter 5** is based on the article "A. Patton, P. Antolín, J. Kiendl, A. Reali. Efficient equilibrium-based stress recovery for isogeometric laminated curved structures" (status: under review - submitted for publication to *Composite Structures*).

- **Chapter 6** is based on the manuscript in preparation "A. Marengo, A. Patton, M. Negri, U. Perego, A. Reali. An explicit algorithm for irreversibility enforcement in phase-field modeling of crack propagation".

- **Chapter 7** is based on the manuscript in preparation "N. Hosters, A. Patton, N. Kubicki, A. Reali, S. Elgeti, M. Behr. Combining boundary-conforming finite elements and isogeometric collocation in the context of fluid-structure interaction".

Chapter 2

Scientific background

In this chapter, we introduce IgA, with a focus on the fundamentals of the standard basis functions as well as their geometry and derivatives and we discuss IgA refinement operations. Additionally, we provide details on the approximation of a standard 3D linear elasticity problem for an isotropic homogeneous material with an IgG formulation and we introduce the IgG multipatch approach. Then, we describe IgC and present an overview of existing literature on several applications of IgC with a focus on structural problems. Starting from the linear elasticity problem introduced to illustrate the IgG approach, we build the corresponding strong form IgC approximation, interpreting IgC in a variational sense and we provide a brief description of the IgC multipatch technique. Additionally, we outline a standard Newton-Raphson algorithm to solve nonlinear problems in IgA. Then, we describe modeling techniques for composite plates and shells as well as equilibrium-based stress recovery theories. Finally, we briefly outline the main computational approaches to resolve phase-field models of brittle fracture and introduce FSI problems, with a focus on the spatial coupling of non-matching interface discretizations.

2.1 Isogeometric analysis

2.1.1 Introduction

IgA aims at bridging the gap between Finite Elements Analysis (FEA) and Computer Aided Design (CAD) and, thus, it aspires to tightly connect design and analysis [50]. Adopting an historical perspective, CAD designers generated files that needed to be translated into analysis-suitable geometries, meshed, and input to large-scale FEA codes. Any mesh refinement operation required interaction with CAD geometry. From a quantitative point of view, this modeling task is estimated to take over the 80% of the overall analysis time, and engineering designs are becoming increasingly more complex (see Figure 2.1).

In order to accomplish a full analysis, there are many preparatory steps involved, which do not only require modeling but other phases as well (see Figure 2.2). For example, at Sandia National Laboratories mesh generation operations are estimated
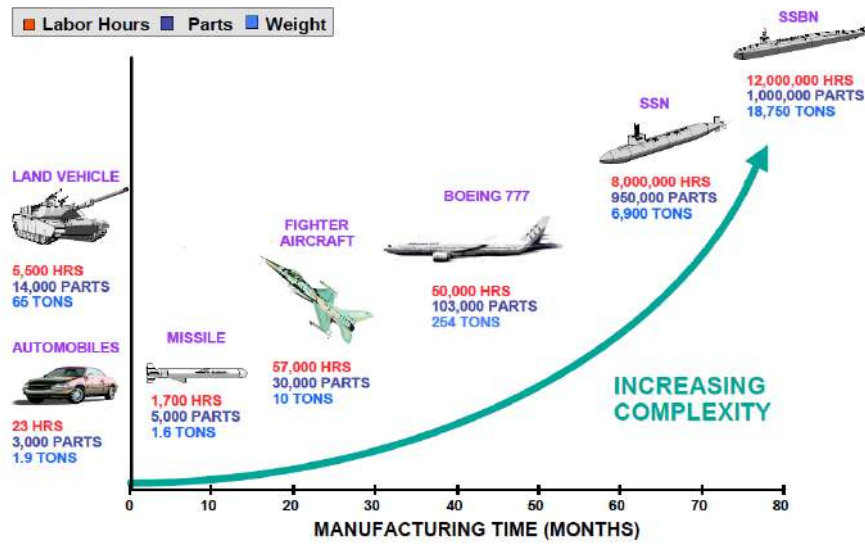
FIGURE 2.1: Increasing complexity in engineering design in terms of manufacturing time (Courtesy of General Dynamics/Electric Boat Corporation) [50].
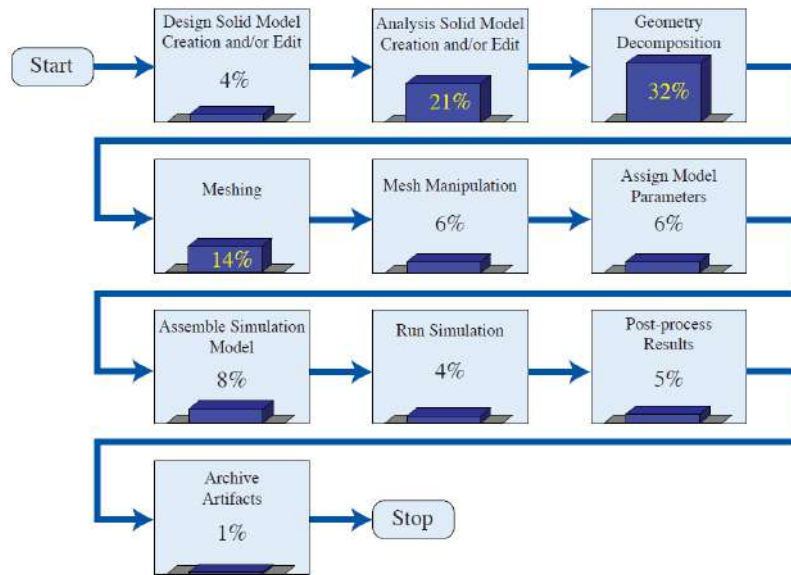
FIGURE 2.2: Estimation of the relative time costs of each component of the model generation and analysis process at Sandia National Laboratories. Note that the process of building the model completely dominates over the time spent performing analysis (Courtesy of Michael Hardwick and Robert Clay, Sandia National Laboratories) [50].

to take about 20% of overall analysis time, whereas creation of the analysis-suitable geometry requires about 60%, and only 20% of overall time is actually devoted to analysis itself. Indeed the 80/20 modeling/analysis ratio seems to be a very common industrial experience. The concept of IgA, introduced by Hughes *et al.* in 2005 [91], may be viewed as a logical extension of the FEA. IgA adopts the isoparametric paradigm and, hence, exploits the same basis functions both for the representation of the geometric computational domains and the problem solution variables. This is accomplished by employing typical smooth CAD functions, such as B-splines and

Non-Uniform Rational B-splines (NURBS). These functions present higher continuity properties than classical FEA shape functions, allowing for an exact representation of complex, curved geometries, while typically leading to improved convergence and a cost-saving simplification of the usually expensive mesh generation and refinement processes required by standard FEA.

Relying on the high-regularity properties of its basis functions, IgA has shown a better accuracy per DOF and an enhanced robustness with respect to standard FEA in a wide variety of solid and structural problems including – as pioneer works in the field – structural vibrations [52, 156], structural dynamics and wave propagation [95], eigenvalue problems [92], nearly incompressible linear and non-linear elasticity as well as plasticity [18, 64], refinement [51] and mesh distortion [121] studies, and phase-field modeling [33, 59], leading also to the development of optimized codes, e.g., [71]. Specifically, with regard to the modeling of plates, we remark the contributions of [185]. Among the landmark studies in the context of shell structures, we highlight [29, 40, 61, 109], while recent works comprise formulations allowing for large-strain plastic deformation [9], the analysis of geometrically nonlinear elastic shells [118], novel approaches for alleviating shear and membrane locking phenomena in solid shells [13], and new strategies to resolve the computational challenges arising when trimmed surfaces are directly employed for isogeometric Kirchhoff–Love shells [49].

Additionally, we remark other notable applications of IgA to other fields of science and engineering, such as fluids (see, e.g., [4, 23, 24, 35, 82, 123]), FSI (see, e.g., [21, 22, 90]), and biomedical applications [125, 140]. IgA also opens the door to geometrically flexible discretizations of higher-order partial differential equations (PDEs) in primal form (see, e.g., [19, 81, 109])

2.1.2   Fundamentals of Isogeometric analysis

In this section, we aim at introducing the basic mathematical concepts of standard IgA employing B-splines and NURBS as basis functions. For further details, readers may refer to [51, 91, 153], and references therein.

2.1.2.1   B-splines

B-splines are piecewise polynomial curves whose components are defined as the linear combination of B-spline basis functions and the coordinates of certain points in the physical space Ω, referred to as *control points*. The collection of control points that define a B-spline curve is called the *control mesh*. Once we fix the order of the B-spline (i.e., the polynomial degree), to construct the basis functions we have to define the so-called *knot vector*.

2.1.2.1.1   Knot vector   A knot vector, in one dimension, is a non-decreasing set of coordinates in the parameter space $\hat{\Omega}$

$$\Xi = \left\{ \xi_1, \xi_2, ..., \xi_{n+p+1} \right\} , \tag{2.1}$$

where $\xi_i \in \mathbb{R}$ is the *i*-th *knot*, i is the knot index ($i = 1, 2, ..., n + p + 1$), p is the polynomial order, and n is the number of basis functions used to construct the B-spline curve, which is equal to the number of control points that define the control mesh. Knots are defined in the parameter space, which they partition into *knot spans*. They can also be repeated, that is, more that one knot may take on the same value. The *multiplicities* of the knot values have important implications for the properties of the basis, as we will discuss further on. As knots can be repeated, some knot spans may have zero length in one dimension. Thus, for an analogy with classical FEA, the isogeometric *elements* are usually defined as the knot spans with non-zero length (see Figures 2.3, 2.4, and 2.5). A knot vector is called *uniform* if its knots are equally spaced and *non-uniform* otherwise. In all numerical examples of this thesis, we will use *open knot vectors*, i.e., knot vectors whose first and last control points are repeated $p + 1$ times. As a consequence, basis functions formed from open knot vectors are interpolatory at the ends of the parameter space interval $[\xi_1, \xi_{n+p+1}]$ in one dimension.

2.1.2.1.2   Basis functions   B-spline basis functions are defined recursively *via* the Cox-de Boor formula [31], starting from piecewise constants ($p = 0$):

$$N_{i,0}(\xi) = \begin{cases} 1 & \textit{if } \xi_i \leq \xi < \xi_{i+1} \\ 0 & \text{otherwise} \end{cases} , \tag{2.2}$$

while for $p = 1, 2, 3, ...$, they read

$$N_{i,p}(\xi) = \frac{\xi - \xi_i}{\xi_{i+p} - \xi_i} N_{i,p-1}(\xi) + \frac{\xi_{i+p+1} - \xi}{\xi_{i+p+1} - \xi_{i+1}} N_{i+1,p-1}(\xi), \tag{2.3}$$

where the convention $0/0 = 0$ is assumed. In Figure 2.3, we display constant, linear, and quadratic B-spline functions obtained with a uniform knot vector $\Xi = \{0, 1, 2, 3, 4, ...\}$.

Among the properties of B-spline shape functions, we remark that:

- the basis constitutes a partition of unity, that is $\sum_{i=1}^{n} N_{i,p}(\xi) = 1$, $\forall \xi \in \hat{\Omega}$;

- each basis function is pointwise non-negative $N_{i,p}(\xi) \geq 0, \forall \xi \in \hat{\Omega}$;

- basis functions of order p are C^{p-1}-continuous across knot spans if the internal knots are not repeated;

- the support of the basis functions of order p is always $p + 1$ knot spans;

- if a knot ξ_i has multiplicity k_i, the basis functions are C^{p-k_i}-continuous at that knot (in particular, when a knot has multiplicity p, the basis functions are C^0 and interpolatory at that location).

Figure 2.4 shows quartic shape functions with differing levels of continuity at every element boundary. At the first internal element boundary, $\xi = 1$, the knot value appears only once in the knot vector, and so we have the maximum level of continuity possible: $C^{p-1} = C^3$. At each subsequent internal knot value, the multiplicity is increased by one, and so the number of continuous derivatives is decreased by one.
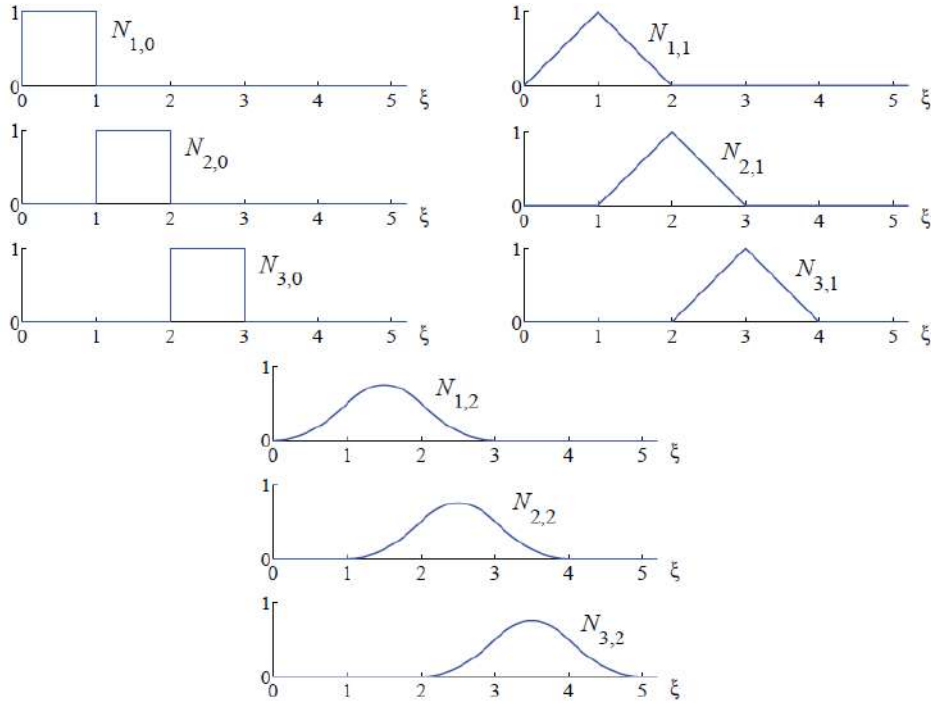
FIGURE 2.3: Basis functions of order 0, 1, and 2 for a uniform knot vector $\Xi = \{0, 1, 2, 3, 4, ...\}$ [50].
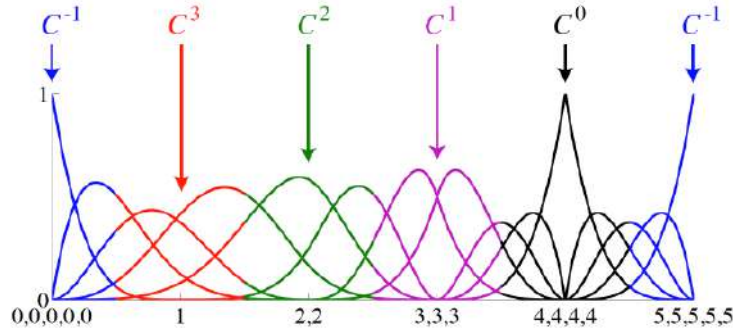
FIGURE 2.4: Quartic ($p = 4$) basis functions for an open, non-uniform knot vector $\Xi = \{0, 0, 0, 0, 0, 1, 2, 2, 3, 3, 3, 4, 4, 4, 4, 5, 5, 5, 5, 5\}$. The continuity across an interior element boundary is a direct result of the polynomial order and the multiplicity of the corresponding knot value [50].

In this case at $\xi = 4$, the C^0 basis is interpolatory. The basis is also interpolatory at the boundary of the domain, where the open knot vector demands the first and last knot value to be repeated $p + 1$ times. The result is C^{-1}-continuity, that is, the basis is fully discontinuous, naturally terminating the domain.

2.1.2.1.3 Derivatives of B-spline basis functions The derivatives of B-spline basis functions are efficiently represented in terms of B-spline lower-order bases. For a given polynomial order and knot vector, the derivative of the i-th basis function is
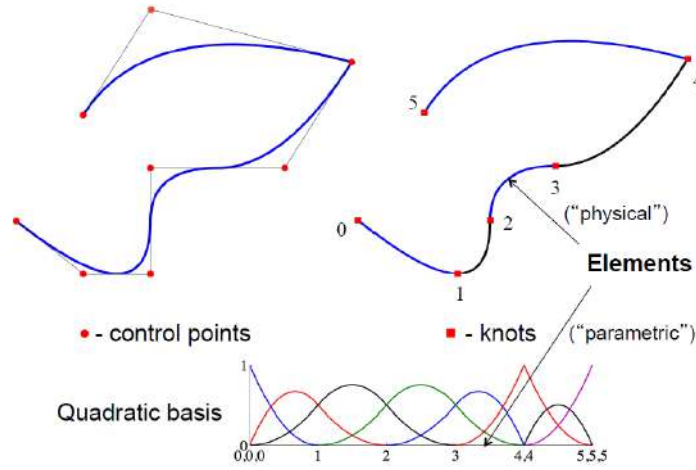
FIGURE 2.5: B-spline quadratic curve defined in the physical space $\Omega \subset \mathbb{R}^2$. Control point locations are denoted by $\bullet$. The knots, which define a mesh by partitioning the curve into elements, are denoted by $\blacksquare$. Basis functions and knot vector are reported on the parametric space $\hat{\Omega}$ at the bottom [51].

given by

$$\frac{d}{d\xi}N_{i,p}(\xi) = \frac{p}{\xi_{i+p} - \xi_i}N_{i,p-1}(\xi) - \frac{p}{\xi_{i+p+1} - \xi_{i+1}}N_{i+1,p-1}(\xi). \tag{2.4}$$

The previous result can be generalized as follows

$$\frac{d^k}{d^k\xi}N_{i,p}(\xi) = \frac{p}{\xi_{i+p} - \xi_i}\left(\frac{d^{k-1}}{d^{k-1}\xi}N_{i,p-1}(\xi)\right) - \frac{p}{\xi_{i+p+1} - \xi_{i+1}}\left(\frac{d^{k-1}}{d^{k-1}\xi}N_{i+1,p-1}(\xi)\right), \tag{2.5}$$

and after expanding we obtain

$$\frac{d^k}{d^k\xi}N_{i,p}(\xi) = \frac{p!}{(p-k)!}\sum_{j=0}^{k}\alpha_{k,j}N_{i+j,p-k}(\xi), \tag{2.6}$$

with

$$\alpha_{0,0} = 1,$$
$$\alpha_{k,0} = \frac{\alpha_{k-1,0}}{\xi_{i+p-k+1} - \xi_i},$$
$$\alpha_{k,j} = \frac{\alpha_{k-1,j} - \alpha_{k-1,j-1}}{\xi_{i+p+j-k+1} - \xi_{i+j}} \qquad j = 1, ..., k-1,$$
$$\alpha_{k,k} = \frac{-\alpha_{k-1,k-1}}{\xi_{i+p+1} - \xi_{i+k}}.$$

The denominator of several of these coefficients can be zero in the presence of repeated knots. Whenever this happens, the coefficient is defined to be zero. Efficient algorithms for these calculations can be found in [153].

2.1.2.2 B-spline curves

Given a knot vector $\Xi = [\xi_1, ..., \xi_{n+p+1}]$, we can build n B-spline basis functions $N_{i,p}$ of polynomial degree p. If we further define a set of n control points in $\mathbb{R}^d$, we can construct a piecewise polynomial B-spline curve $\mathbf{C}(\xi)$ of order p by taking the linear combination of the basis functions weighted by the components of control points, as follows

$$\mathbf{C}(\xi) = \sum_{i=1}^{n} N_{i,p}(\xi)\mathbf{B}_i, \tag{2.7}$$

where $\mathbf{B}_i$ is the i-th control point. The piecewise linear interpolation of the control points is called *control polygon*. In Figure 2.5, we show an example of a quadratic B-spline curve in $\mathbb{R}^2$.

2.1.2.3 B-spline surfaces

Performing a tensor product operation, B-spline surfaces can be constructed starting from a set of $n \times m$ control points $\mathbf{B}_{i,j}$ ($i = 1, 2, ..., n$; $j = 1, 2, ...m$), which form the so-called *control net*. If we define two knot vectors $\Xi = [\xi_1, ..., \xi_{n+p+1}]$ and $\mathcal{H} = [\eta_1, ..., \eta_{m+q+1}]$, where p and q are the polynomial orders, we can construct the 1D basis functions $N_{i,p}$ and $M_{j,q}$, such that we can define the B-spline surface as

$$\mathbf{S}(\xi, \eta) = \sum_{i=1}^{n} \sum_{j=1}^{m} N_{i,p}(\xi) M_{j,q}(\eta)\mathbf{B}_{i,j}. \tag{2.8}$$

2.1.2.4 B-spline solids

B-spline solids are defined in an analogous fashion to B-spline surfaces. Given now a *control lattice* $\mathbf{B}_{i,j,k}$ ($i = 1, 2, ..., n$; $j = 1, 2, ..., m$; $k = 1, 2, ..., l$), the polynomial orders p, q, and r, and the knot vectors $\Xi = [\xi_1, ..., \xi_{n+p+1}]$, $\mathcal{H} = [\eta_1, ..., \eta_{m+q+1}]$ and $\mathcal{Z} = [\zeta_1, ..., \zeta_{l+r+1}]$, the B-spline solid can be defined as:

$$\mathbf{S}(\xi, \eta, \zeta) = \sum_{i=1}^{n} \sum_{j=1}^{m} \sum_{k=1}^{l} N_{i,p}(\xi) M_{j,q}(\eta) L_{k,r}(\zeta)\mathbf{B}_{i,j,k}, \tag{2.9}$$

where $N_{i,p}$, $M_{j,q}$, and $L_{k,r}$ are the corresponding 1D B-spline basis functions along each parametric direction.

2.1.2.5 Refinement

In contrast to FEA, which essentially features h-refinement and p-refinement to enrich the approximation properties of the basis, IgA possesses three different refinement approaches: *knot insertion*, *order elevation*, and *k-refinement*.
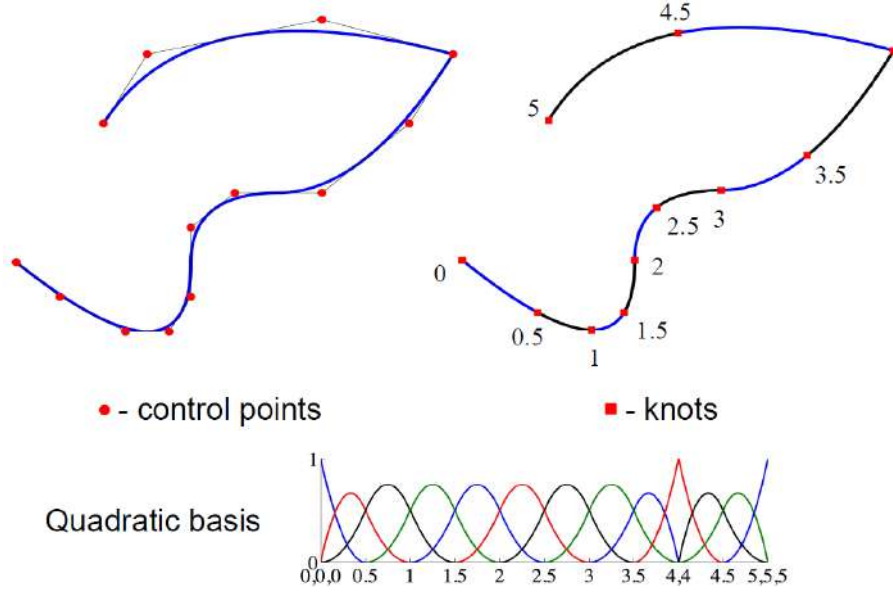
FIGURE 2.6: Example of knot insertion refinement using the curve introduced in Figure 2.5 [51].

2.1.2.5.1 Knot insertion The basis can be enriched using *knot insertion*, which is the IgA counterpart of FEA *h-refinement* because, as new knots are inserted, the number of knot spans is increased. Indeed, knots may be inserted without changing a curve geometrically or parametrically. Given a knot vector $\Xi = [\xi_1, ..., \xi_{n+p+1}]$ we can "extend it" to $\overline{\Xi} = [\overline{\xi}_1 = \xi_1, \overline{\xi}_2 ..., \overline{\xi}_{n+p+1} = \xi_{n+p+1}]$ such that the old knot vector is contained in the new one. The new $n + m$ basis functions can be derived from Cox-de Boor recursion formula in Equations (2.2) and (2.3), which also apply to the enriched knot vector. Additionally, $n + m$ new control points $\overline{\mathcal{B}}$ are formed from linear combination of the old ones $\mathcal{B}$ by

$$\overline{\mathcal{B}} = \mathbf{T}^p \mathcal{B}, \tag{2.10}$$

where

$$T_{ij}^0 = \begin{cases} 1 & \overline{\xi}_i \in [\xi_j, \xi_{j+1}) \\ 0 & \text{otherwise} \end{cases} \tag{2.11}$$

and

$$T_{ij}^{q+1} = \frac{\overline{\xi}_{i+q} - \xi_j}{\xi_{j+q} - \xi_j} T_{ij}^q + \frac{\xi_{j+q+1} - \overline{\xi}_{i+q}}{\xi_{j+q+1} - \xi_{j+1}} T_{ij+1}^q \text{ for } q = 0, 1, 2, ..., p - 1. \tag{2.12}$$

A knot insertion example is presented in Figure 2.6.

2.1.2.5.2 Order elevation *Order elevation* involves raising the polynomial order of the basis functions. Recalling that the basis has $p - k_i$ continuous derivatives across element boundaries, it is clear that when p is increased, k_i must also be increased if we want to preserve the original continuity of the basis functions. Therefore, during order elevation, the multiplicity of each knot value is increased by one, but no new knot values are added. As with knot insertion, neither the geometry nor the parametrization are changed. The process for order elevation begins by replicating
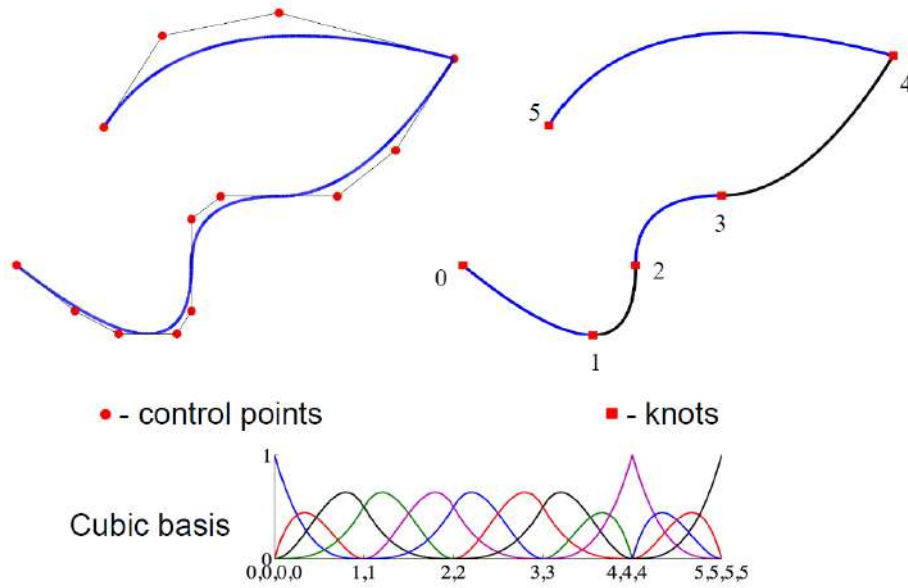
FIGURE 2.7: Example of order elevation using the curve introduced in Figure 2.5 [51].

existing knots until their multiplicity is equal to the polynomial order. This results in each element of the parametric space supporting a local basis that is interpolatory at the boundaries of each element, as in standard FEA. The next step is to elevate the polynomial order on each element. Lastly, excess knots are removed to recover the original continuity across element boundaries. Notice that as we increase the knot vector, we also need to define new control points for the newly added basis functions. Several efficient algorithms combine the mentioned steps to minimize the computational cost of the process [153]. In Figure 2.7, we show an example of order elevation.

2.1.2.5.3 *k*-**refinement**   If a new, unique knot value is inserted between two distinct knot values in a curve of order p, the number of continuous derivatives of the basis functions at the original and inserted knot values is $p - 1$. If we subsequently elevate the order to q, the multiplicity of every distinct knot value (including the knot just inserted) is increased, so that discontinuities in the p-th derivative of the basis are preserved. That is, the basis still has $p - 1$ continuous derivatives at the original and inserted knot values, although the polynomial order is now q. If, instead, we elevate the order of the original, coarsest curve to q and only then insert the unique knot value, the basis will have $q - 1$ continuous derivatives at the original and newly added knot values. This last strategy is called *k-refinement*. Thus, knot insertion and order elevation are not commutative. In Figure 2.8, we compare classical *p*-refinement and *k*-refinement to highlight differences between these two refinement strategies.

2.1.2.6   Non-uniform rational B-splines

A NURBS in $\mathbb{R}^d$ is the projection into a d-dimensional physical space of a non-rational (polynomial) B-spline defined in a $(d + 1)$-dimensional homogeneous coordinate space. NURBS enable to construct a great variety of geometric entities and,

(a) $\Xi = \{0, 0, 1, 1\}$, $p = 1$.

(b) $\Xi = \{0, 0, 0, 1/3, 1/3, 2/3, 2/3, 1, 1, 1\}$, $p = 2$.

(c) $\Xi = \{0, 0, 0, 1/3, 2/3, 1, 1, 1\}$, $p = 2$.
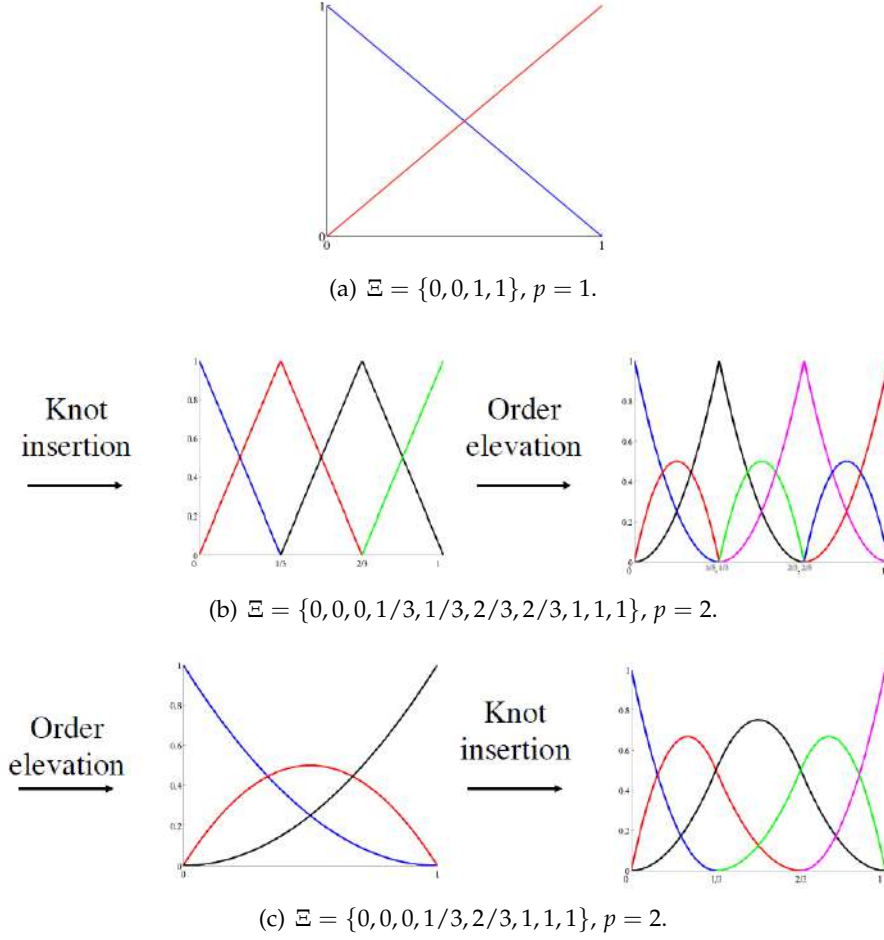
FIGURE 2.8: Classical *p*-refinement *versus* *k*-refinment. (a) Initial case of one linear element. (b) Classical *p*-refinement approach: knot insertion is performed first to create many low order elements. Subsequent order elevation will preserve the C^0-continuity across element boundaries. (c) New *k*-refinement approach: order elevation is performed on the coarsest discretization and then new knots are inserted [51].

in particular, conic sections can be exactly represented. To define a NURBS curve in $\mathbb{R}^d$, we have to start from a knot vector $\Xi = [\xi_1, ..., \xi_{n+p+1}]$ and a set $\mathbf{B}_i^w$ ($i = 1, ..., n$) of control points (*projective points*) for a B-spline curve in $\mathbb{R}^{d+1}$. Then, the control points for the NURBS curve are:

$$(\mathbf{B}_i)_j = (\mathbf{B}_i^w)_j / w_i \qquad j = 1, ..., d, \tag{2.13}$$

with

$$w_i = (\mathbf{B}_i^w)_{d+1}, \tag{2.14}$$

where $(\mathbf{B}_i)_j$ is the *j*-th component of the control point $\mathbf{B}_i$ and w_i is referred to as the *i*-th *weight*. Hence, notice that dividing the projective control points by the weights is equivalent to applying the projective transformation to them. Likewise, NURBS basis functions of order *p* are defined as:

$$R_i^p(\xi) = \frac{N_{i,p}(\xi) w_i}{W(\xi)} = \frac{N_{i,p}(\xi) w_i}{\sum_{\hat{i}=1}^{n} N_{\hat{i},p}(\xi) w_{\hat{i}}}, \tag{2.15}$$

where $W(\xi)$ is the so-called *weighting function*.

The first and second derivatives of univariate NURBS basis functions of order p are calculated as

$$\frac{d}{d\xi}R_i^p(\xi) = w_i \frac{W(\xi)N'_{i,p}(\xi) - W'(\xi)N_{i,p}(\xi)}{(W(\xi))^2}, \qquad (2.16)$$

$$\frac{d^2}{d\xi^2}R_i^p(\xi) = \frac{N''_{i,p}(\xi)w_i}{W(\xi)} + \frac{2N_{i,p}(\xi)w_i(W'(\xi))^2}{(W(\xi))^3} + $$
$$- \frac{2N'_{i,p}(\xi)w_iW'(\xi) + N_{i,p}(\xi)w_iW''(\xi)}{(W(\xi))^2}, \qquad (2.17)$$

where $N'_{i,p}(\xi) = \frac{d}{d\xi}N_{i,p}(\xi)$, $W'(\xi) = \sum_{\hat{i}=1}^n N'_{\hat{i},p}(\xi)w_{\hat{i}}$, and $W''(\xi) = \sum_{\hat{i}=1}^n N''_{\hat{i},p}(\xi)w_{\hat{i}}$.

A NURBS curve $\mathbf{C}(\xi)$ can be constructed as the linear combination of the basis functions weighted by the components of control points and reads

$$\mathbf{C}(\xi) = \sum_{i=1}^n R_i^p(\xi)\mathbf{B}_i. \qquad (2.18)$$

Rational surfaces and solids are defined in an analogous way based on a tensor-product structure in terms of bivariate and trivariate NURBS basis functions, which are respectively defined as

$$R_{i,j}^{p,q}(\xi,\eta) = \frac{N_{i,p}(\xi)M_{j,q}(\eta)w_{i,j}}{\sum_{\hat{i}=1}^n \sum_{\hat{j}=1}^m N_{\hat{i},p}(\xi)M_{\hat{j},q}(\eta)w_{\hat{i},\hat{j}}} \qquad (2.19)$$

and

$$R_{i,j,k}^{p,q,r}(\xi,\eta,\zeta) = \frac{N_{i,p}(\xi)M_{j,q}(\eta)L_{k,r}(\zeta)w_{i,j,k}}{\sum_{\hat{i}=1}^n \sum_{\hat{j}=1}^m \sum_{\hat{k}=1}^l N_{\hat{i},p}(\xi)M_{\hat{j},q}(\eta)L_{\hat{k},r}(\zeta)w_{\hat{i},\hat{j},\hat{k}}}, \qquad (2.20)$$

where $N_{i,p}$, $M_{j,q}$, and $L_{k,r}$ are univariate B-spline functions defined from the corresponding knot vectors $\Xi = [\xi_1,...,\xi_{n+p+1}]$, $\mathcal{H} = [\eta_1,...,\eta_{m+q+1}]$, $\mathcal{Z} = [\zeta_1,...,\zeta_{l+r+1}]$ along each direction of the parametric space. We remark that if the weights are all equal, the NURBS basis functions simplify to B-spline basis functions due to the application of the property of partition of unity to the weighting function. Thus, B-splines are a particular case of NURBS.

2.1.2.7 Generalized notation for multivariate B-splines and NURBS

We introduce a more general and compact notation for the definition of multivariate B-splines and NURBS, which will be used to approximate the numerical formulations in this thesis. Multivariate B-splines are generated through the tensor product of univariate B-splines. We denote with d_p the dimension of the parameter space. Then, the d_p univariate knot vectors can be written as

$$\Xi^d = \{\xi_1^d,...,\xi_{m_d+p_d+1}^d\} \qquad d = 1,...,d_p, \qquad (2.21)$$

where p_d represents the polynomial degree in the parametric direction d, while m_d is the associated number of basis functions. In the numerical examples for solid shells shown in this thesis, we will also denote the in-plane polynomial orders by

$p_1 = p$ and $p_2 = q$, while we will refer to the out-of-plane degree of approximation by $p_3 = r$. A univariate B-spline basis function $N_{i_d, p_d}^d(\xi^d)$ associated to each parametric coordinate ξ^d can be then constructed for each i_d position in the tensor product structure, using the Cox-de Boor recursion formula (see Section 2.1.2.1.2).

Given the univariate basis functions N_{i_d, p_d}^d associated to each parametric direction ξ^d, the multivariate basis functions $B_{\mathbf{i}, \mathbf{p}}(\boldsymbol{\xi})$ are redefined as:

$$B_{\mathbf{i}, \mathbf{p}}(\boldsymbol{\xi}) = \prod_{d=1}^{d_p} N_{i_d, p_d}(\xi^d), \tag{2.22}$$

where $\mathbf{i} = \{i_1, ..., i_{d_p}\}$ is a multi-index describing the position of the multivariate basis function in the tensor-product structure, $\mathbf{p} = \{p_1, ..., p_d\}$ is the vector of polynomial degrees, and $\boldsymbol{\xi} = \{\xi^1, ..., \xi^{d_p}\}$ is the vector of the parametric coordinates in each parametric direction d. B-spline multidimensional geometries are built from a linear combination of multivariate B-spline basis functions as

$$\mathbf{S}(\boldsymbol{\xi}) = \sum_{\mathbf{i}} B_{\mathbf{i}, \mathbf{p}}(\boldsymbol{\xi}) \mathbf{P}_{\mathbf{i}}, \tag{2.23}$$

where $\mathbf{P}_{\mathbf{i}} \in \mathbb{R}^{d_s}$ are the control points, d_s is the dimension of the physical space, and the summation is extended to all combinations of the multi-index $\mathbf{i}$.

As NURBS geometries in $\mathbb{R}^{d_s}$ are instead obtained from a projective transformation of their B-spline counterparts in $\mathbb{R}^{d_s+1}$, using the generalized notation in this section, we can redefine multivariate NURBS basis functions as

$$R_{\mathbf{i}, \mathbf{p}}(\boldsymbol{\xi}) = \frac{B_{\mathbf{i}, \mathbf{p}}(\boldsymbol{\xi}) w_{\mathbf{i}}}{\sum_{\mathbf{j}} B_{\mathbf{j}, \mathbf{p}}(\boldsymbol{\xi}) w_{\mathbf{j}}}, \tag{2.24}$$

where $w_{\mathbf{i}}$ represents the NURBS weight associated to each control point according to the multi-index $\mathbf{i}$. NURBS multidimensional geometries are then built combining multivariate NURBS basis functions and control points:

$$\mathbf{S}(\boldsymbol{\xi}) = \sum_{\mathbf{i}} R_{\mathbf{i}, \mathbf{p}}(\boldsymbol{\xi}) \mathbf{P}_{\mathbf{i}}. \tag{2.25}$$

2.1.2.8   An Isogeometric Galerkin approach for linear isotropic elastostatics

Let $\Omega \subset \mathbb{R}^{d_s}$ represent an isotropic, homogeneous, linear elastic body subjected to body forces $\boldsymbol{b}$, to prescribed displacements $\boldsymbol{g}$ on a portion of the boundary Γ_D, and to prescribed tractions $\boldsymbol{t}$ on the remaining portion Γ_N, such that $\Gamma_N \cup \Gamma_D = \Gamma$ and $\Gamma_N \cap \Gamma_D = \varnothing$. We set $d_s = 3$ and consider the simplest possible case, assuming small strains and displacements, such that

$$\boldsymbol{\sigma} = \mathbb{C} : \boldsymbol{\nabla}^s \boldsymbol{u}, \tag{2.26}$$

where $\boldsymbol{\sigma}$ is the stress tensor, $\mathbb{C}$ is the fourth-order linear elasticity material tensor [63], $\boldsymbol{\nabla}^s$ is the symmetric gradient operator, and $\boldsymbol{u}$ is the displacement field that solves the

elastostatic problem given by

$$\nabla \cdot (\mathbb{C} : \nabla^s u) + b = 0 \qquad \text{in} \quad \Omega, \tag{2.27a}$$

$$(\mathbb{C} : \nabla u^s) \cdot n = t \qquad \text{on} \quad \Gamma_N, \tag{2.27b}$$

$$u = g \qquad \text{on} \quad \Gamma_D. \tag{2.27c}$$

Using the principle of virtual work [63], we can obtain the variational form of the problem by multiplying Equation (2.27) by test functions $\delta u \in [H^1(\Omega)]^3$ satisfying homogeneous Dirichlet boundary condition on Γ_D and, then, integrating by parts. These operations lead to

$$\int_\Omega (\mathbb{C} : \nabla^s u) : \nabla^s \delta u \, \mathrm{d}\Omega = \int_\Omega b \cdot \delta u \, \mathrm{d}\Omega + \int_{\Gamma_N} t \cdot \delta u \, \mathrm{d}\Gamma. \tag{2.28}$$

In the context of the principle of virtual work, the test functions δu are usually called *virtual displacements*. Adopting the isoparametric approach, we can approximate the displacements and the virtual displacements as

$$u \approx u_h = \sum_i R_{\mathbf{i},\mathbf{p}}(\boldsymbol{\xi}) \, \hat{\mathbf{u}}_\mathbf{i}, \tag{2.29}$$

$$\delta u \approx \delta u_h = \sum_i R_{\mathbf{i},\mathbf{p}}(\boldsymbol{\xi}) \, \delta \hat{\mathbf{u}}_\mathbf{i}, \tag{2.30}$$

where h denotes a discretized variable. In Equations (2.29) and (2.30), $\hat{\mathbf{u}}_\mathbf{i}$ and $\delta \hat{\mathbf{u}}_\mathbf{i}$ are the so-called *control variables*, which enable the spline approximation of the displacements and the virtual displacements in this elastostatic problem, respectively. Substituting Equations (2.29) and (2.30) into (2.28), we proceed to discretize the problem and obtain

$$\int_\Omega (\mathbb{C} : \nabla^s u_h) : \nabla^s \delta u_h \, \mathrm{d}\Omega = \int_\Omega b \cdot \delta u_h \, \mathrm{d}\Omega + \int_{\Gamma_N} t \cdot \delta u_h \, \mathrm{d}\Gamma. \tag{2.31}$$

We notice that, after the substitution of Equations (2.29) and (2.30) into (2.28), the resulting equation must be satisfied by any arbitrary choice of $\delta \hat{\mathbf{u}}_\mathbf{i}$, leading to the linear system that is usually written as

$$\mathbf{K} \, \hat{\mathbf{u}} = \mathbf{F}, \tag{2.32}$$

where $\hat{\mathbf{u}}$ is the vector of the unknown displacements, $\mathbf{K}$ is the global stiffness matrix, and $\mathbf{F}$ is the global force vector, whose components are straightforwardly derived from Equations (2.31) and (2.32). To obtain the components of $\mathbf{K}$ and $\mathbf{F}$, the standard approach consists of an element-wise calculation leveraging Gauss quadrature. The result of the element-wise calculations lead to the definition of an element (local) stiffness matrix and an element (local) force vector, which are then *assembled* into their global counterparts in Equation (2.32) using connectivity matrices that relate the local DOFs to the global DOFs. For a more detailed derivation of the IgG formulation of this and other problems, the reader is referred to [50].
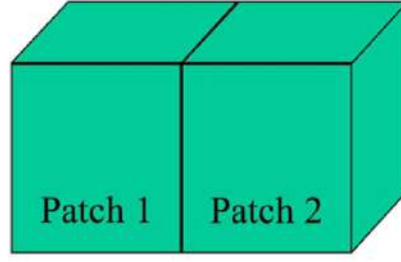
FIGURE 2.9: Example of a two-patch geometry. On the coarsest mesh, the control points on the common interface are in one-to-one correspondence, trivially enforcing C^0 continuity [51].

2.1.2.9   Multiple patches

To model more complex geometrical features it is often required to adopt a multi-patch approach (see [51]), which allows for local refinement operations. The usual situation is the case where the geometric domain of the problem topologically differs from a cube, such that the tensor product structure of the parameter space of a single patch allows for a poor representation of complex, multiply connected domains. Moreover, if the considered problem presents parts of the geometry comprising different materials it may also be convenient to describe these subdomains by different patches. For the sake of simplicity and without loss of generality, we consider the case of two patches that meet on a common interface, as in Figure 2.9. We further assume that the control points and knot vectors in the plane of the face are identical on both patches, thus ensuring that the patches match geometrically and parametrically on that shared face. Superscripts 1 and 2 identify the patch numbers, while with subscripts f and n we denote control points belonging to the common face and control points not on the shared face, respectively. Thus, we can partition the control points for patches 1 and 2 as

$$\mathbf{B}^1 = \begin{bmatrix} \mathbf{B}_n^1 \\ \mathbf{B}_f^1 \end{bmatrix} \text{ and } \mathbf{B}^2 = \begin{bmatrix} \mathbf{B}_n^2 \\ \mathbf{B}_f^2 \end{bmatrix}, \qquad (2.33)$$

such that $\mathbf{B}_f^2 = \mathbf{B}_f^1$. To take into account for the possibility to locally refine patch 2 by knot insertion (see 2.1.2.5.1), we rewrite $\mathbf{B}^2$ as

$$\tilde{\mathbf{B}}^2 = \tilde{\mathbf{T}}_f \mathbf{B}^2 = \begin{bmatrix} \tilde{\mathbf{T}}_f & \mathbf{0} \\ \mathbf{0} & \tilde{\mathbf{T}}_f \end{bmatrix} \begin{bmatrix} \mathbf{B}_n^2 \\ \mathbf{B}_f^2 \end{bmatrix}, \qquad (2.34)$$

where $\tilde{\mathbf{B}}^2$ are the new set of control points for patch 2 and $\tilde{\mathbf{T}}_f$ is the multi-dimensional generalization of the extension operator defined in Equation (2.12). Combining $\mathbf{B}_f^2 = \mathbf{B}_f^1$ and Equation (2.34), we note that C^0-continuity of the geometry is preserved by

$$\tilde{\mathbf{B}}_f^2 = \tilde{\mathbf{T}}_f \mathbf{B}_f^1. \qquad (2.35)$$

We enforce the same continuity constraints for the control variables as

$$\hat{\mathbf{u}}_{\mathbf{i}}^1 = \begin{bmatrix} (\hat{\mathbf{u}}_{\mathbf{i}}^1)_n \\ (\hat{\mathbf{u}}_{\mathbf{i}}^1)_f \end{bmatrix} \text{ and } \hat{\mathbf{u}}_{\mathbf{i}}^2 = \begin{bmatrix} (\hat{\mathbf{u}}_{\mathbf{i}}^2)_n \\ (\tilde{\mathbf{u}}_{\mathbf{i}}^2)_f \end{bmatrix}, \tag{2.36}$$

where $(\tilde{\mathbf{u}}_{\mathbf{i}}^2)_f = \tilde{\mathbf{T}}_f(\hat{\mathbf{u}}_{\mathbf{i}}^1)_f$. Adopting an implementational point of view, we rewrite Equation (2.32) for a two-patch case, obtaining two subproblems

$$\mathbf{K}^1\,\hat{\mathbf{u}}_{\mathbf{i}}^1 = \mathbf{F}^1\,, \tag{2.37a}$$

$$\mathbf{K}^2\,\hat{\mathbf{u}}_{\mathbf{i}}^2 = \mathbf{F}^2\,, \tag{2.37b}$$

where the stiffness matrices for each patch are partitioned as

$$\mathbf{K}^1 = \begin{bmatrix} \mathbf{K}_{nn}^1 & \mathbf{K}_{nf}^1 \\ \mathbf{K}_{fn}^1 & \mathbf{K}_{ff}^1 \end{bmatrix} \text{ and } \mathbf{K}^2 = \begin{bmatrix} \mathbf{K}_{nn}^2 & \mathbf{K}_{nf}^2 \\ \mathbf{K}_{fn}^2 & \mathbf{K}_{ff}^2 \end{bmatrix}. \tag{2.38}$$

Thus, we expand Equation (2.37a) and substitute the partitioning of $\mathbf{K}^1$, obtaining

$$\mathbf{K}_{nn}^1(\hat{\mathbf{u}}_{\mathbf{i}}^1)_n + \mathbf{K}_{nf}^1(\hat{\mathbf{u}}_{\mathbf{i}}^1)_f = \mathbf{F}_n^1 \tag{2.39}$$

and

$$\mathbf{K}_{fn}^1(\hat{\mathbf{u}}_{\mathbf{i}}^1)_n + \mathbf{K}_{ff}^1(\hat{\mathbf{u}}_{\mathbf{i}}^1)_f = \mathbf{F}_f^1\,. \tag{2.40}$$

Enforcing that $(\tilde{\mathbf{u}}_{\mathbf{i}}^2)_f = \tilde{\mathbf{T}}_f(\hat{\mathbf{u}}_{\mathbf{i}}^1)_f$, we repeat the same operations for patch 2

$$\mathbf{K}_{nn}^2(\hat{\mathbf{u}}_{\mathbf{i}}^2)_n + \mathbf{K}_{nf}^2\tilde{\mathbf{T}}_f(\hat{\mathbf{u}}_{\mathbf{i}}^1)_f = \mathbf{F}_n^2 \tag{2.41}$$

and

$$\mathbf{K}_{fn}^2(\hat{\mathbf{u}}_{\mathbf{i}}^2)_n + \mathbf{K}_{ff}^2\tilde{\mathbf{T}}_f(\hat{\mathbf{u}}_{\mathbf{i}}^1)_f = \mathbf{F}_f^2\,. \tag{2.42}$$

Then, we premultiply (2.42) by $\tilde{\mathbf{T}}_f^{\mathsf{T}}$ to constraint the weighting functions and reduce the number of equations to match that of (2.40) as

$$\tilde{\mathbf{T}}_f^{\mathsf{T}}\mathbf{K}_{fn}^2(\hat{\mathbf{u}}_{\mathbf{i}}^2)_n + \tilde{\mathbf{T}}_f^{\mathsf{T}}\mathbf{K}_{ff}^2\tilde{\mathbf{T}}_f(\hat{\mathbf{u}}_{\mathbf{i}}^1)_f = \tilde{\mathbf{T}}_f^{\mathsf{T}}\mathbf{F}_f^2\,. \tag{2.43}$$

Finally, adding Equation (2.40) and (2.43) together and considering Equations (2.39) and (2.41), we can rewrite the global complete problem (i.e., the union of the 2 local subproblems in Equation (2.37)) for the 2 patches as

$$\mathbb{K}\,\hat{\mathbf{U}}_{\mathbf{i}} = \mathbb{F}\,, \tag{2.44}$$

where

$$\mathbb{K} = \begin{bmatrix} \mathbf{K}_{nn}^1 & \mathbf{K}_{nf}^1 & \mathbf{0} \\ \mathbf{K}_{fn}^1 & (\mathbf{K}_{ff}^1 + \tilde{\mathbf{T}}_f^{\mathsf{T}}\mathbf{K}_{ff}^2\tilde{\mathbf{T}}_f) & \tilde{\mathbf{T}}_f^{\mathsf{T}}\mathbf{K}_{fn}^2 \\ \mathbf{0} & \mathbf{K}_{nf}^2\tilde{\mathbf{T}}_f & \mathbf{K}_{nn}^2 \end{bmatrix}, \tag{2.45a}$$

$$\hat{\mathbf{U}}_{\mathbf{i}} = \begin{bmatrix} (\hat{\mathbf{u}}_{\mathbf{i}}^1)_n \\ (\hat{\mathbf{u}}_{\mathbf{i}}^1)_f \\ (\hat{\mathbf{u}}_{\mathbf{i}}^2)_n \end{bmatrix}, \text{ and} \tag{2.45b}$$

$$\mathbb{F} = \begin{bmatrix} \mathbf{F}_n^1 \\ \mathbf{F}_f^1 + \tilde{\mathbf{T}}_f^{\mathrm{T}} \mathbf{F}_f^2 \\ \mathbf{F}_n^2 \end{bmatrix} . \tag{2.45c}$$

2.1.3   Isogeometric collocation

2.1.3.1   Introduction

Collocation methods have been introduced within IgA as an attempt to address a well-known important issue of early IgG formulations, related to the development of efficient integration rules for higher-order approximations (see, e.g., [14, 69, 96, 161]). In fact, element-wise Gauss quadrature, typically used in FEA and originally adopted for IgG approaches, does not properly take into account the inter-element higher continuity of IgA basis functions. This limitation leads to sub-optimal array formation and assembly costs, significantly affecting the performance of IgG methods. Several *ad hoc* quadrature rules have been introduced, but the development of a general and effective solution for IgG methods is still an open problem [161].

IgC overcomes this problem by taking full advantage of the geometrical flexibility and analytical accuracy of IgA while minimizing computational costs. IgC was originally proposed in [16] and can be seen as a Petrov-Galerkin method where the test functions are smoothed Dirac delta functions defined at the so-called *collocation points* (converging to the Dirac delta distributions as the smoothing parameter tends to zero). Therefore, IgC can also be regarded as a sort of stable one-point quadrature Galerkin method that ultimately gives raise to a strong-form method. In fact, the main idea in IgC, in contrast to IgG formulations, consists of the discretization of the governing PDEs in strong form, which is then evaluated at suitable collocation points. The isoparametric paradigm is adopted, such that the same basis functions are used to describe both the geometry and the problem solution, as in a typical IgG context, by means of linear combinations of IgA basis functions and control points and variables, respectively.

As reported in [16], a delicate issue for IgC is the determination of suitable collocation points, since this choice affects optimal convergence for IgC (i.e., of order $p - 1$) in the $W^{2,\infty}$-norm (or, equivalently, in the H^2-norm). Such a proof is valid only in 1D and has not been extended to higher dimensions. However, extensive numerical testing has shown that the convergence rates obtained in 1D are attained also in higher dimensions. Moreover, optimal convergence rates are not recovered in the L^∞- and $W^{1,\infty}$-norms (or, equivalently, in the L^2- and H^1-norms), where it has been numerically shown that orders of convergence p and $p - 1$ for even and odd degrees, respectively, are attained for IgC methods. It is important to note that, despite not being optimal in the L^2- and H^1-norms, the obtained orders of convergence for IgC are increasing with p, whereas the cost of collocation is much lower than that of IgG approaches of the same order, especially as p increases. This makes IgC very competitive with respect to IgG in terms of accuracy-to-computational-cost ratio, especially when higher-order approximation degrees are adopted (see, e.g., [162]). In

(a) Greville abscissae points.

(b) Gauss integration points.
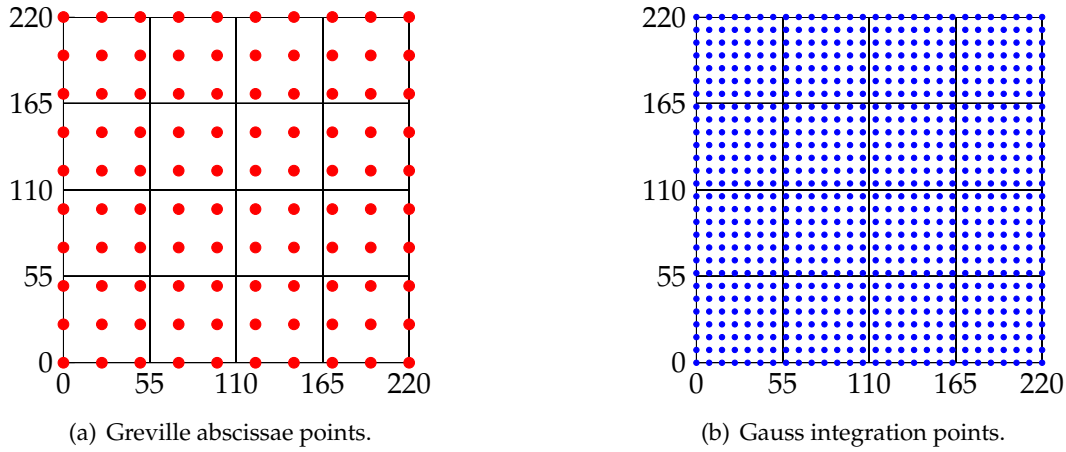
FIGURE 2.10: Comparison of collocation and Gauss integration points required respectively for standard IgC and IgG methods. This 2D case considers 4 elements and a degree of approximation equal to 6 for each parametric direction.

particular, IgC has gained increasing popularity in those situations where evaluation and assembly costs are dominant [15, 67].

The simplest and most widespread approach in the engineering literature is to collocate the governing strong-form equations at the images of Greville abscissae (see, e.g., [101]) and this is the strategy also adopted in this thesis. For alternative choices of collocation points, the reader is referred to [30, 57]. Along each parametric direction d, the Greville abscissae consist of a set of m_d points, obtained from the knot vector components, ξ_i^d, as

$$\tau_i^d = \frac{\xi_{i+1}^d + \xi_{i+2}^d + ... + \xi_{i+p_d}^d}{p_d} \qquad i = 1, ..., m_d , \qquad (2.46)$$

where p_d is the polynomial order for the d-th parametric direction.

Since the discretization is performed through direct collocation of the differential equations, no integrals need to be computed and, consequently, IgC results in a very fast method with respect to IgG. Figure 2.10 shows a comparison between the number of collocation and Gauss quadrature points required respectively by IgC and IgG standard methods for a 2D example featuring 4 elements and basis functions with polynomial order 6 in each parametric direction.

IgC has been particularly successful in the context of structural elements and has proven to be especially stable with regard to mixed methods. In particular, Bernoulli-Euler beam and Kirchhoff plate elements have been proposed within an IgC framework in [157]. Mixed formulations for Timoshenko initially-straight planar beams [186], non-prismatic beams [20], and for curved spatial rods [17] have also been introduced, studied, and then effectively extended to the geometrically nonlinear case [107, 129, 130, 131, 190, 191]. Moreover, IgC has been successfully applied to the solution of Reissner-Mindlin plate problems [108]. New formulations for shear-deformable beams [106, 107], as well as shells [110, 133] have also been solved *via* IgC. Since its introduction, many promising works on IgC methods have also been

published in other fields, including nearly incompressible elasticity and elastoplasticity [70], phase-field modeling [83], contact [55, 115, 189], and poromechanics [139]. In the context of multifield problems, IgC has been used to study the evolution in ferroelectric materials [74]. Additionally, combinations with different spline spaces (e.g., hierarchical splines, generalized B-splines, and T-splines) have been successfully tested in [41, 128, 162], while alternative effective selection strategies for IgC points have been proposed in [11, 83, 138].

2.1.3.2   Isogeometric collocation for elastostatics

Following [15, 55, 162], we can interpret the collocation method in a variational sense. Thus, we recall the elasticity problem in variational form, based on the principle of virtual work and stated in Equation (2.28), and we integrate by parts, obtaining

$$\int_{\Omega} [\,\boldsymbol{\nabla} \cdot (\mathbb{C} : \boldsymbol{\nabla}^{\mathrm{s}} \boldsymbol{u}) + \boldsymbol{b}\,] \cdot \delta \boldsymbol{u} \mathrm{d}\Omega - \int_{\Gamma_N} [\,(\mathbb{C} : \boldsymbol{\nabla}^{\mathrm{s}} \boldsymbol{u}) \cdot \boldsymbol{n} - \boldsymbol{t}\,] \cdot \delta \boldsymbol{u} \, \mathrm{d}\Gamma = 0\,, \qquad (2.47)$$

where $\boldsymbol{\nabla}\cdot$ is the divergence operator. Adopting the isoparametric approach, we approximate again the displacements and virtual displacements *via* Equations (2.29) and (2.30), obtaining

$$\int_{\Omega} [\,\boldsymbol{\nabla} \cdot (\mathbb{C} : \boldsymbol{\nabla}^{\mathrm{s}} \boldsymbol{u}_h) + \boldsymbol{b}\,] \cdot \delta \boldsymbol{u}_h \mathrm{d}\Omega - \int_{\Gamma_N} [\,(\mathbb{C} : \boldsymbol{\nabla}^{\mathrm{s}} \boldsymbol{u}_h) \cdot \boldsymbol{n} - \boldsymbol{t}\,] \cdot \delta \boldsymbol{u}_h \, \mathrm{d}\Gamma = 0\,. \qquad (2.48)$$

The approximated virtual displacements $\delta \boldsymbol{u}_h$ are then set as the Dirac delta function δ (see [15]), which fulfills, for every function $f_{\Omega}(\boldsymbol{x})$, $f_{\Gamma}(\boldsymbol{x})$ continuous about the point $\boldsymbol{x}_i \in \Omega$, $\boldsymbol{x}_i \in \Gamma$, respectively, the so-called *sifting property*

$$\int_{\Omega} f_{\Omega}(\boldsymbol{x})\delta(\boldsymbol{x} - \boldsymbol{x}_i)\,\mathrm{d}\Omega = f_{\Omega}(\boldsymbol{x}_i)\,, \qquad \int_{\Gamma} f_{\Gamma}(\boldsymbol{x})\delta(\boldsymbol{x} - \boldsymbol{x}_i)\,\mathrm{d}\Gamma = f_{\Gamma}(\boldsymbol{x}_i)\,. \qquad (2.49)$$

We consider $d_s = 2$ and $n_{n_p} = m_1 m_2$ control points. Thus, we need $2n_{n_p}$ scalar equations to determine the unknown control variables for the displacements in each direction of the physical space. In the considered collocation scheme, we choose n_{n_p} Greville points, which we denote here by τ_i^d (see Equation (2.46)). In the interior of the problem domain Ω, we write $2(m_1 - 2)(m_2 - 2)$ scalar equations by choosing as test functions the Dirac delta functions centered at the interior collocation points. With reference to Neumann boundary conditions, we distinguish between the collocation points located at the edges, and those located at the corners of the domain. The resulting equations read

$$[\,\boldsymbol{\nabla} \cdot (\mathbb{C} : \boldsymbol{\nabla}^{\mathrm{s}} \boldsymbol{u}_h) + \boldsymbol{b}\,](\tau_i^d) = \boldsymbol{0} \qquad\qquad\qquad \forall \tau_i^d \in \Omega\,, \qquad (2.50a)$$

$$[\,(\mathbb{C} : \boldsymbol{\nabla}^{\mathrm{s}} \boldsymbol{u}_h) \cdot \boldsymbol{n} - \boldsymbol{t}\,](\tau_i^d) = \boldsymbol{0} \qquad\qquad\qquad \forall \tau_i^d \in \mathrm{edge} \subset \Gamma_N\,, \qquad (2.50b)$$

$$[\,(\mathbb{C} : \boldsymbol{\nabla}^{\mathrm{s}} \boldsymbol{u}_h) \cdot \boldsymbol{n}' - \boldsymbol{t}'\,](\tau_i^d) + [\,(\mathbb{C} : \boldsymbol{\nabla}^{\mathrm{s}} \boldsymbol{u}_h) \cdot \boldsymbol{n}'' - \boldsymbol{t}''\,](\tau_i^d) = \boldsymbol{0} \qquad \forall \tau_i^d \equiv \mathrm{corner} \subset \Gamma_N\,, \qquad (2.50c)$$

$$\boldsymbol{u}_h(\tau_i^d) = \boldsymbol{g}(\tau_i^d) \qquad\qquad\qquad\qquad \forall \tau_i^d \in \Gamma_D\,, \qquad (2.50d)$$

where $\boldsymbol{n}'$ and $\boldsymbol{n}''$ are the outward unit normals of the edges meeting at the corner, and $\boldsymbol{t}'$ and $\boldsymbol{t}''$ are the respective imposed tractions.

2.1.3.3 Enhanced collocation

The use of the IgC approach may lead to unsatisfactory accuracy of the results in the presence of Neumann boundary conditions. In those cases, the enhanced collocation (EC) approach is usually introduced to mimic the superior results of the hybrid collocation strategy (see [55, 67]) while maintaining the same computational cost as IgC. In the case of EC, Neumann boundary conditions for $d_s = 2$ are written considering a combination of internal and edge terms, as follows

$$\left[\, \boldsymbol{\nabla} \cdot (\mathbb{C} : \boldsymbol{\nabla}^{\mathrm{s}} \boldsymbol{u}_h) + \boldsymbol{b} \,\right] (\tau_i^d) - \frac{C^*}{h} \left[\, (\mathbb{C} : \boldsymbol{\nabla}^{\mathrm{s}} \boldsymbol{u}_h) \cdot \boldsymbol{n} - \boldsymbol{t} \,\right] (\tau_i^d) = \boldsymbol{0} \qquad \forall \tau_i^d \in \text{edge} \subset \Gamma_N \,, \tag{2.51}$$

where h is the collocation mesh size in the direction perpendicular to the edge, computed as the distance between the first two collocation points encountered starting from the edge and considering the parametric direction perpendicular to the edge. The determination of C^* is not trivial and we refer readers to [55] for a complete discussion on this matter. In this thesis, we assume $C^* = 4$, which can be considered an appropriate choice for all interpolation degrees.

2.1.3.4 Multipatch collocation

Let us consider the case with two bidimensional patches that share a common edge. We assume identical control points and knot vectors on the shared edge for each patch, thereby ensuring that the patches form a geometrically conforming multipatch structure. Therefore, the whole body $\bar{\Omega} \subset \mathbb{R}^2$ is given by the union of the two patches as

$$\bar{\Omega} = \bigcup_{k=1,2} \bar{\Omega}_k \,, \tag{2.52}$$

where $\bar{\Omega}_k$ is the k-th patch. We indicate with Ω the interior part of the multipatch structure and assume that Γ_D and Γ_N are made of a finite union of connected and regular components. Furthermore, we assume that the traction $\boldsymbol{t}$ is piecewise continuous. For the sake of simplicity, we extend the function $\boldsymbol{t}$ by zero on $\bigcup_{k=1,2} \bar{\Omega}_k$. Thus, $\boldsymbol{t}$ represents a vector function living on $\bigcup_{k=1,2} \bar{\Omega}_k$ whose support is contained in Γ_N. Regarding the boundary conditions on Γ_D, we consider a function $\boldsymbol{g} \in [C^0(\Gamma_D)]^2$. The internal part of the whole body Ω is also subjected to a volume loading $\boldsymbol{b} \in [L^\infty(\Omega)]^2$ such that $\boldsymbol{b}|_{\Omega_k} \in [C^0(\Omega_k)]^2$ for $k = 1, 2$. We denote again with $\mathbb{C}$ the fourth-order material elasticity tensor and define $\mathbb{C}_k := \mathbb{C}|_{\Omega_k}$ with all their components being in $C^1(\Omega_k)$, while we allow $\mathbb{C}$ to have jumps from one patch $\bar{\Omega}_k$ to another. Using Equation (2.46), we compute a set of Greville abscissae for each k-th patch $\tau_{i,k}^d$ ($d = 1, 2$ and $k = 1, 2$). Now, we focus on the rules to collocate equations on the boundary of the patch:

- if $\tau_{i,k}^d \in \Gamma_D$, we impose $\boldsymbol{u}_h(\tau_{i,k}^d) = \boldsymbol{g}(\tau_{i,k}^d)$;

- if $\tau_{i,k}^d \in \Gamma_N$, we adapt Equations (2.50b) and (2.50c) accordingly;

- the remaining $\tau_{i,k}^d \in \partial\Omega_k$ belong to the inter-patch boundary.

The final system of equations for the considered case reads

$$[\, \boldsymbol{\nabla} \cdot (\mathbb{C}_k : \boldsymbol{\nabla}^s \boldsymbol{u}_h) + \boldsymbol{b}\,](\tau_{i,k}^d) = \boldsymbol{0} \qquad \forall \tau_{i,k}^d \in \Omega_k\,, \tag{2.53a}$$

$$[\, (\mathbb{C}_k : \boldsymbol{\nabla}^s \boldsymbol{u}_h) \cdot \boldsymbol{n} - \boldsymbol{t}\,](\tau_{i,k}^d) = \boldsymbol{0} \qquad \forall \tau_{i,k}^d \in \text{edge} \subset \Gamma_N\,, \tag{2.53b}$$

$$\begin{aligned} &[\, (\mathbb{C}_k : \boldsymbol{\nabla}^s \boldsymbol{u}_h) \cdot \boldsymbol{n}_k' - \boldsymbol{t}_k'\,](\tau_{i,k}^d) \\ &+ [\, (\mathbb{C}_k : \boldsymbol{\nabla}^s \boldsymbol{u}_h) \cdot \boldsymbol{n}_k'' - \boldsymbol{t}_k''\,](\tau_{i,k}^d) = \boldsymbol{0} \end{aligned} \qquad \forall \tau_{i,k}^d \equiv \text{corner} \subset \Gamma_N\,, \tag{2.53c}$$

$$\sum_{k=1}^{2} [\, (\mathbb{C}_k : \boldsymbol{\nabla}^s \boldsymbol{u}_h) \cdot \boldsymbol{n}_k\,](\tau_{i,k}^d) = \boldsymbol{0} \qquad \forall \tau_{i,k}^d \in \partial\Omega_k,\, \tau_{i,k}^d \notin \Gamma_D,\, \tau_{i,k}^d \notin \Gamma_N\,, \tag{2.53d}$$

$$\boldsymbol{u}_h(\tau_{i,k}^d) = \boldsymbol{g}(\tau_{i,k}^d) \qquad \forall \tau_{i,k}^d \in \Gamma_D\,, \tag{2.53e}$$

where, for the k-th patch, $\boldsymbol{n}_k'$ and $\boldsymbol{n}_k''$ are the outward unit normals of the edges meeting at the corner, and $\boldsymbol{t}_k'$ and $\boldsymbol{t}_k''$ are the respective imposed tractions. While for the IgG formulation discussed in Section 2.1.2.9 we imposed a C^0 displacement continuity condition, for the IgC multipatch method we need to enforce a stress continuity condition at the inter-patch boundary *via* Equation (2.53d), for which $\boldsymbol{n}_k$ is the outward normal of the k-th patch. Finally, we recall that $\boldsymbol{t} = \boldsymbol{0}$ in $\bar{\Omega} \setminus \Gamma_N$.

2.1.4   Standard resolution of nonlinear problems in IgA

The Newton-Raphson method is an established algorithm in computational mechanics to solve nonlinear problems of the form

$$\mathbf{R}(\mathbf{u}) = \mathbf{0}\,, \tag{2.54}$$

where $\mathbf{R}$ is the so-called *residual* of the nonlinear problem and it is constituted by the variational equations of the weak form of the problem, while $\mathbf{u}$ is the vector of solutions. These type of nonlinear equations are solved for $\mathbf{u}$ by applying an iterative process, whereby given a solution estimate $\mathbf{u}_k$ at iteration step k, a new value $\mathbf{u}_{k+1} = \mathbf{u}_k + \Delta\mathbf{u}$ is obtained in terms of an increment $\Delta\mathbf{u}$ establishing the linear approximation [77]

$$\mathbf{R}(\mathbf{u}_{k+1}) \approx \mathbf{R}(\mathbf{u}_k) + D\mathbf{R}(\mathbf{u}_k)\Delta\mathbf{u} = \mathbf{0}\,, \tag{2.55}$$

where the linearization step can be accomplished using the so-called *Gateaux derivative* as follows

$$D\mathbf{R}(\mathbf{u}_k)\Delta\mathbf{u} = \left.\frac{d}{d\epsilon}\right|_{\epsilon=0} \mathbf{R}(\mathbf{u}_k + \epsilon\Delta\mathbf{u}) \tag{2.56}$$

$$= \mathbf{K}(\mathbf{u}_k)\Delta\mathbf{u}\,. \tag{2.57}$$

In Equation (2.56), $\mathbf{K}(\mathbf{u}_k)$ denotes the consistent tangent stiffness matrix with entries defined by

$$\mathrm{K}_{ij}(\mathbf{u}_k) = \left.\frac{\partial \mathbf{R}_i}{\partial \mathbf{u}_j}\right|_{\mathbf{u}_k}. \tag{2.58}$$

We obtain a linear set of equations for $\Delta\mathbf{u}$ to be solved at each Newton-Raphson iteration step

$$\mathbf{K}(\mathbf{u}_k)\Delta\mathbf{u} = -\mathbf{R}(\mathbf{u}_k), \qquad \mathbf{u}_{k+1} = \mathbf{u}_k + \Delta\mathbf{u}. \tag{2.59}$$

Finally, the iteration process stops if the current solution $\mathbf{u}_{k+1}$ does not differ significantly from the solution $\mathbf{u}_k$ of the previous iteration step, i.e., $|\mathbf{u}_{k+1} - \mathbf{u}_k| < \epsilon$, with ϵ corresponding to a user-defined tolerance [77].

2.2 Main modeling strategies for composite structures

Over the past decades, various theories have been proposed to model laminated composite plates and shells. These can be classified into three major categories: three-dimensional elasticity, equivalent single-layer (ESL), and LW theories [38, 119, 120, 159]. Three-dimensional elasticity theories consider the laminated composite structure as a solid without any special treatment of the stacking sequence. This approach is highly accurate, but it requires very heavy simulations. In an attempt to reduce the computational effort, ESL theories treat the 3D laminate as an equivalent single ply adopting suitable kinematic assumptions, such that the number of unknowns is independent of the number of layers. The major drawback of the ESL approach is the assumption that displacements are continuous functions of the thickness coordinate. This assumption leads to continuous transverse strains, which, together with ply-wise different material properties, necessarily leads to discontinuous through-the-thickness out-of-plane stresses, which violate equilibrium constraints. Nevertheless, in addition to inherent simplicity and low computational cost, ESL theories can provide a sufficiently accurate description of the global response in terms of the distribution of interlaminar stresses for thin plates and shells, at least in regions sufficiently far from edges and cut-out boundaries. Numerous theories based on the ESL concept have been proposed [105, 114, 159]. In particular, ESL-based methods include the *classical laminate plate theory* (CLPT), which may be viewed as the extension of the Kirchhoff plate theory to laminated composite plates and assumes that it is possible to neglect the strains acting through the laminate thickness. Instead, the *first-order shear deformation theory* (FSDT) considers the transverse shear strain to be constant with respect to the thickness coordinate and therefore requires shear correction factors, which are difficult to determine for arbitrarily laminated composite plate structures. In an attempt to address this issue, second- and higher-order ESL theories have been proposed [124, 158], which rely on higher-order polynomials in the expansion of the displacement components through the thickness of the laminate. Nevertheless, despite the fact that they do not need correction factors, higher-order theories introduce additional unknowns that do not often have a clear physical meaning and increase the overall computational demand [159].

To overcome the limitations of ESL and 3D elasticity methods, LW theories can be considered as a viable option. LW approaches further distinguish between

displacement-based strategies, for which the displacement field is the primal variable, and mixed theories, which leverage both displacements and transverse stresses as unknowns. Displacement-based LW theories consider an independent displacement field in every single ply (i.e., ply-wise expansions for all three primal variable components) and impose C^0-continuity at the layer interfaces, thereby decreasing the number of unknowns [122, 159]. Hence, LW theories naturally fulfill the requirements that grant a good approximation of the out-of-plane response through the thickness directly from the constitutive equations. On the other hand, mixed LW methods satisfy the interlaminar continuity of transverse stresses *a priori*. The main limitation of the LW theories is that the number of DOFs is directly proportional to the number of layers, unavoidably leading to high computational costs, especially in the case of laminates made of a significant amount of plies. For further theories to model laminated composite structures, such as the *Carrera Unified Formulation* (CUF), the reader is referred to, e.g., [37] and references therein.

IgA has already been used to solve composite and sandwich plates and, in particular, has been shown to provide good results when combined with the LW concept (see, e.g., [62, 84, 85, 176]), benefiting from IgA numerical advantages while keeping a significantly low computational cost. In the context of composite modeling, 2D IgG approaches have also been proposed in the literature [103, 142], with some of them employing enhanced shell and plate theories [3, 155, 160]. In [5], a combination of IgA and CUF has been considered too. Moreover, IgA formulations for higher-order shear deformation theories have been proposed for composite beams [166], plates [177, 178], and shells [39, 72, 180], as well as for several examples of functionally graded (FG) plates (see, e.g., [73, 152, 179] and references therein). With regard to FG shell analysis using IgA, investigations are limited to a few studies including first- [141] and higher-order shear deformation theories [60]. Finally, there is limited literature on the use of IgC for composite structures and we could only identify a recent numerical formulation to study Reissner-Mindlin laminated plates [151].

2.3   Stress recovery theory

The stress recovery theory consists of the direct integration of the equilibrium equations to compute the out-of-plane stress components from the in-plane stresses directly derived from a displacement solution. This idea was first applied in the context of laminated solid plates solved within an IgA formulation in [62]. Stress recovery theory examples in the context of plates solved *via* FEA can be found in original works such as [154], which proposes high-order elements and advocates for a generalization of the process that would include a separate angle of rotation for each layer in the laminate. However, this approach assumes an average rotation of the mid-plane through the entire thickness of the plate, which requires shear coefficients depending on the section shape, and the recovery of the out-of-plane normal stress component is not discussed. Alternatively, the element formulation proposed in [65] comprises different interpolation schemes for different unknowns, which complicates the implementation of the stress recovery procedure. Furthermore, this work emphasizes that a reduced numerical integration is strongly recommended, especially in the case of thin geometries. However, in practice, only the transverse shear components were integrated with reduced order, which may affect the physical behavior of the element by introducing spurious zero energy modes. Instead, another

approach [56, 183] recovers stresses by minimizing the complementary energy functional associated to a separate patch system, on which finite element displacements are prescribed along the boundaries, over a set of stress fields that satisfy *a priori* interior equilibrium within the patch. This hybrid stress approach has been tested for one- and two-dimensional isotropic elasticity problems and has been further analyzed in the context of FSDT laminated plates in [53]. Recently, the equilibrium-based stress recovery has been successfully applied by leveraging radial basis functions as well [44].

2.4 Computational methods to solve phase-field models of brittle fracture

The phase-field modeling of brittle fracture in elastic solids has been the subject of extensive theoretical and computational investigations since the late 1990s [8]. In order to model problems characterized by sharp interfaces, the phase-field approach incorporates a continuous field variable, which may be regarded as a smooth regularization of multiple physical phases characterizing the system. Thus, in brittle fracture problems, the phase field usually identifies non-damaged and damaged material, such that the phase field enables to adapt the material response in the vicinity of the crack. The phase field features a smooth transition between damaged and non-damaged regions of the material and it is characterized by a problem-dependent internal length parameter. One of the major limitation of the phase-field technique resides in its expensive computational cost, especially for engineering-size applications [126], due to the necessity for very fine meshes around crack paths to resolve the internal length parameter. Thus, the development of novel and efficient solution algorithms is of paramount importance to investigate large-size problems for industrial applications.

From an algorithmic point of view, phase-field approaches may be implemented either with monolithic or with staggered schemes. Monolithic approaches, compute the displacement and the phase-field variables simultaneously, while staggered schemes alternatively minimize the two fields. Monolithic techniques are more efficient since they solve the coupled system in terms of displacements and phase-field in one loop of iterations (i.e., as in a Newton-Raphson loop). However, due to the loss of convexity of the problem, convergence is difficult to obtain, although it may be improved *via* further numerical treatments (see e.g., [193]). Conversely, staggered implementations have proven to be more robust [137].

Another delicate issue in the phase-field modeling of brittle fracture consist of how to enforce the irreversibility condition, which requires the damage to be a non-decreasing function during any transformation in a consistent thermodynamic formulation. As a result, the irreversibility turns the phase-field approach into a constrained minimization problem in the form of a variational inequality. Different methods to impose the irreversibility can significantly affect the computational cost of the phase-field solution. Miehe *et al.* [134], introduced a monotonically increasing history field energy function in the phase-field equation to replace the original loading-induced reference energy. Nevertheless, the introduction of the history field makes the phase-field solution differ from the original variational framework and its equivalence to the original minimization problem cannot be proven [79]. On the

other hand, penalty methods such as [79] rely on equality-based formulations and allow to keep the variational nature of the original problem. Nevertheless, penalty methods depend upon the so-called *penalty coefficient*, which needs to be tuned according to the problem under exam. This represents a non-trivial task, since excessively small values of the penalty parameter lead to an inaccurate enforcement of the constraint, while overly large values of this parameter may cause ill-conditioning of the problem.

2.5   Introduction to FSI problems

A fluid exerts forces on any body it flows around. This may lead to significant deformations, changing the flow field around the body again. This builds to an FSI problem, a surface coupled problem formed by the unique interface separating the fluid and the solid domain. Typical examples are aeroelastic effects in aerospace engineering, the movement of artificial heart valves in biomedical engineering, and the behavior of storage tanks in civil engineering. Even if FSI solvers are widely used, the need for accurate but fast numerical methods is still crucial in industrial practice.

2.5.1   Standard strategies to solve FSI problems

The main solution strategies can be divided into two approaches [76]. Assembling and solving the discretized problem relations into one system of equations results in a monolithic approach, which gives the most robust solver. But monolithic systems need a high computational effort in terms of implementation and maintenance. Hence, the partitioned solution strategy – emerging by combining two existing solvers that sequentially solve the fluid and the structure sub-problems – is the most common way to address FSI problems. The effort needed for implementation is limited to the temporal coupling of the staggered solvers, which can be divided into strong and weak. While in the case of a weak coupling interface information is exchanged only up to a limited number of iterations, a strong coupling requires information exchange at all iterations until convergence.

To increase the efficiency of an FSI solver, a problem-dependent discretization is crucial to reduce the number of DOFs, regardless of the applied solution strategy. However, due to the different physical properties of the participating fluids and solids, a problem-oriented discretization of each single field usually leads to a non-matching interface discretization in FSI problems. As a consequence, the need for numerical methods to treat non-matching interfaces arises.

2.5.2   On the need for boundary-conforming methods

Three-dimensional fluid problems usually require a volumetric discretization, which may become extremely complex in FSI problems due to the joint evolution of the fluid-solid interface. The solution of volumetric problems with boundary-conforming IgA methods is currently limited to rather simple geometries. The solution of volume problems is currently possible for simple geometries only, where

(a) SFEM-SFEM coupling.

(b) SFEM-IgG coupling.

(c) NEFEM-IgG coupling.
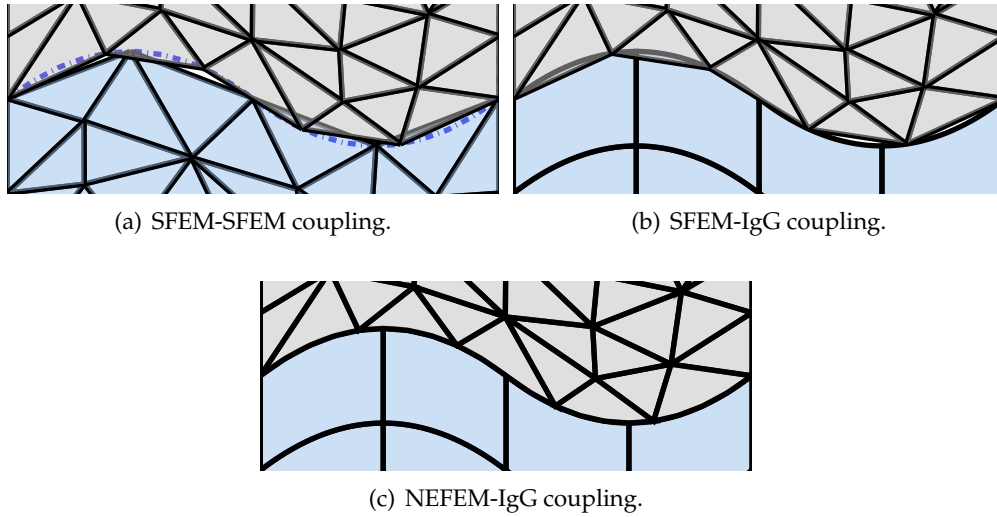
FIGURE 2.11: Spatial coupling strategies for non-matching interface discretizations.

the generation of the spline volume can be realized either manually or with simple effort. Despite the progress in relation to generation of volumetric splines, e.g., [132], the application to complex fluid problems is still limited. Instead, boundary-conforming finite elements can be used to integrate the exact initial geometry of the boundary, which is represented by a spline. One example are elements using blending functions to integrate a curved boundary into a mapping [172]. Another method is the NURBS-enhanced Finite Element method (NEFEM) [36, 164], whereby at least parts of the spline-based geometry can be utilized to include the spline only in the discretization of the elements touching the spline-based boundary. The NE-FEM strategy is possible even in complex cases. Numerical advantages of this methods were demonstrated, e.g., for electromagnetic scattering problems [165], incompressible Navier-Stokes with free-surfaces [170], and linear elasticity [163]. Inspired by NEFEM, a boundary-conforming mapping including the spline-based description of the boundary was derived to be combined with IgA for FSI in [89].

2.5.3 Spatial coupling of non-matching interface discretizations

The standard FEA for FSI usually rely on linear polynomial basis functions, that, used on both sides of the FSI problem, lead to the setup presented in Figure 2.11(a): elements can cut each other, causing gaps and overlaps generation, and the approximated interfaces are matching only at few points. For the spatial coupling of standard finite element methods (SFEM), there are several strategies, e.g., finite interpolation elements [25], weighted residual methods [42] or dual mortar formulations [111]. A method for similar situations with high-order finite elements is discussed in [113]. If a spline-based method is used just on one side of the problem, the situation does not change much [21]: even if the interface is discretized in a geometrically exact manner, e.g., an IgG approach, cuts and gaps at the interface still exist due to the linear approximation on the other side, as sketched in Fig. 2.11(b). Modified versions of the methods mentioned before are capable to allow for a spatial coupling [21]. If IgA methods are used on both sides of the problem, the situation changes only if the interface discretization is represented by the same approximation space.

However, by combining boundary-conforming finite elements (e.g., NEFEM) with an IgG approach, the situation is different. Since the spline-based interface is included in the integration on the fluid elements, a matching interface representation is guaranteed, although the discretization at the interface is still not matching (see Figure 2.11(c)). Using the same interfaces, the spatial coupling is simplified, as discussed in [89]. For example, within a Dirichlet-Neumann scheme consistent nodal forces can be integrated on the fluid side to the right-hand side of the solid problem, while the deformation of the interface can be directly transferred to the fluid mesh, in particular, to the elements on the boundary.

Chapter 3

Fast and accurate elastic analysis of laminated composite plates *via* isogeometric collocation and an equilibrium-based stress recovery approach

In this chapter we present a fast and accurate approach that combines single-patch 3D IgC and an equilibrium-based stress recovery technique to analyze laminated composite solid plates, which are herein conveniently modeled considering only one element through the thickness with homogenized material properties (see Figure 3.1(b)). This guarantees accurate results in terms of displacements and in-plane stress components. To recover an accurate out-of-plane stress state, equilibrium is imposed in strong form as a post-processing correction step, which requires the shape functions to be highly continuous. This continuity demand is fully granted by IgA properties. Several numerical results, obtained using a minimal number of collocation points per direction, assess the good performance of this approach, particularly for increasing values of length-to-thickness plate ratio and number of layers. We remark that the LW concept can also be combined with IgC adopting a multipatch approach (see Section 2.1.3.4), which models each layer as a patch (see Figure 3.1(a)) and enforces normal stress continuity at the inter-patch boundaries [15]. In any case, the proposed IgC method coupled with the equilibrium-based technique is significantly less expensive compared to a LW approach since it employs a considerably lower number of DOFs.

The structure of this chapter is organized as follows. In Section 3.1, we define our 3D IgC strategy to study composite laminated plates. In Section 3.2, we present our reference test case and provide results for the single-element approach. Several numerical benchmarks are displayed, which show a significant improvement between non-treated and post-processed out-of-plane stress components. Then, we provide some mesh sensitivity tests considering an increasing length-to-thickness ratio and numbers of layers to show the effectiveness of the method. Finally, we draw our conclusions in Section 3.3.

(a) Multipatch approach.   (b) Homogenized single-element approach.
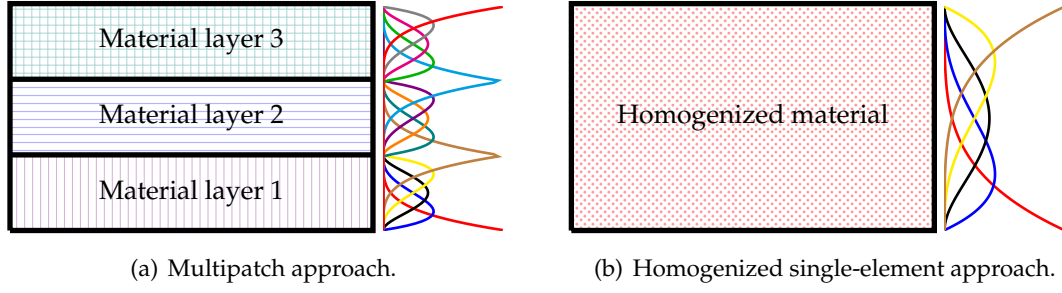
FIGURE 3.1: LW approach and homogenized single-element example of IgA shape functions for a degree of approximation equal to 4.

3.1   An IgC approach to model solid composite plates

3.1.1   IgC formulation for orthotropic elasticity

First, let us recall the classical elasticity problem in strong form considering a small strain regime and detail equilibrium equations using Einstein's summation convention. The following notations are used: $\Omega \subset \mathbb{R}^3$ is an open bounded domain, representing an elastic three-dimensional body, while Γ_N and Γ_D are defined as boundary portions respectively subjected to Neumann and Dirichlet conditions such that $\Gamma_N \cup \Gamma_D = \partial\Omega$ and $\Gamma_N \cap \Gamma_D = \varnothing$. Accordingly, the equilibrium equations and the corresponding boundary conditions are:

$$\sigma_{ij,j} + b_i = 0 \qquad \text{in } \Omega, \tag{3.1a}$$

$$\sigma_{ij} n_j = t_i \qquad \text{on } \Gamma_N, \tag{3.1b}$$

$$u_i = g_i \qquad \text{on } \Gamma_D, \tag{3.1c}$$

where σ_{ij} and u_i represent, respectively, the Cauchy stress tensor and displacement field, b_i and t_i the volume and traction forces, n_j the outward normal unit vector, and g_i the prescribed displacements. The elasticity problem is finally completed by the kinematic relations in small strains

$$\varepsilon_{ij} = \frac{u_{i,j} + u_{j,i}}{2}, \tag{3.2}$$

as well as by the constitutive equations

$$\sigma_{ij} = \mathbb{C}_{ijkl}\varepsilon_{kl}, \tag{3.3}$$

where $\mathbb{C}_{ijkl}$ are the components of the fourth-order linear elasticity tensor of material properties.

As we described in Chapter 1, the basic building block of a laminate is a lamina, i.e., a flat arrangement of unidirectional fibers (considering the simplest case) embedded in a matrix. In order to increase the composite resistance properties, cross-ply laminates can be employed, i.e., all the plies used to form the composite stacking sequence are piled alternating different fiber layers orientations. In this case, all unidirectional layers are individually orthotropic. Since the proposed collocation approach uses one element through the thickness to model the composite plate as

a homogenized single building block, we focus on the collocation formulation for a plate formed by only one orthotropic elastic lamina in this section. Considering three mutually orthogonal planes of material symmetry for each ply, the number of elastic coefficients of the fourth-order elasticity tensor $\mathbb{C}_{ijkl}$ is reduced to 9 in Voigt's notation, which can be expressed in terms of engineering constants as

$$
\mathbb{C} =
\begin{bmatrix}
\mathbb{C}_{11} & \mathbb{C}_{12} & \mathbb{C}_{13} & 0 & 0 & 0 \\
 & \mathbb{C}_{22} & \mathbb{C}_{23} & 0 & 0 & 0 \\
 & & \mathbb{C}_{33} & 0 & 0 & 0 \\
 & \text{symm.} & & \mathbb{C}_{44} & 0 & 0 \\
 & & & & \mathbb{C}_{55} & 0 \\
 & & & & & \mathbb{C}_{66}
\end{bmatrix}
=
\begin{bmatrix}
\dfrac{1}{E_1} & -\dfrac{\nu_{12}}{E_1} & -\dfrac{\nu_{13}}{E_1} & 0 & 0 & 0 \\
 & \dfrac{1}{E_2} & -\dfrac{\nu_{23}}{E_2} & 0 & 0 & 0 \\
 & & \dfrac{1}{E_3} & 0 & 0 & 0 \\
 & \text{symm.} & & \dfrac{1}{G_{23}} & 0 & 0 \\
 & & & & \dfrac{1}{G_{13}} & 0 \\
 & & & & & \dfrac{1}{G_{12}}
\end{bmatrix}^{-1}.
\tag{3.4}
$$

The displacement field components $u = u_1$, $v = u_2$, and $w = u_3$ are then approximated as a linear combination of NURBS multivariate shape functions $R_{\mathbf{i},\mathbf{p}}(\boldsymbol{\xi})$ (defined in Equation (2.24)) and control variables $\hat{\mathbf{u}}_{\mathbf{i}}$, $\hat{\mathbf{v}}_{\mathbf{i}}$, and $\hat{\mathbf{w}}_{\mathbf{i}}$ as follows

$$
u_h = \sum_{\mathbf{i}} R_{\mathbf{i},\mathbf{p}}(\boldsymbol{\xi})\hat{\mathbf{u}}_{\mathbf{i}},
\tag{3.5a}
$$

$$
v_h = \sum_{\mathbf{i}} R_{\mathbf{i},\mathbf{p}}(\boldsymbol{\xi})\hat{\mathbf{v}}_{\mathbf{i}},
\tag{3.5b}
$$

$$
w_h = \sum_{\mathbf{i}} R_{\mathbf{i},\mathbf{p}}(\boldsymbol{\xi})\hat{\mathbf{w}}_{\mathbf{i}}.
\tag{3.5c}
$$

Having defined $\boldsymbol{\tau}$ as the multidimensional array of collocation points (see Equation (2.46)), such that for each i-th point and d-th parametric dimension

$$
\tau_i^d = \frac{\sum_{l=1}^{p_d} \xi_{i+l}}{p_d},
\tag{3.6}
$$

with $i = 1, ..., m_d$, we insert the approximations (3.5) into the kinematics Equations (3.2) and we combine the obtained expressions with the constitutive relations (3.3). Finally, we substitute this result into the equilibrium Equations (3.1a) obtaining

$$
\begin{bmatrix}
\mathbf{K}_{11}(\boldsymbol{\tau}) & \mathbf{K}_{12}(\boldsymbol{\tau}) & \mathbf{K}_{13}(\boldsymbol{\tau}) \\
 & \mathbf{K}_{22}(\boldsymbol{\tau}) & \mathbf{K}_{23}(\boldsymbol{\tau}) \\
\text{symm.} & & \mathbf{K}_{33}(\boldsymbol{\tau})
\end{bmatrix}
\cdot
\begin{pmatrix}
\hat{\mathbf{u}}_{\mathbf{i}} \\
\hat{\mathbf{v}}_{\mathbf{i}} \\
\hat{\mathbf{w}}_{\mathbf{i}}
\end{pmatrix}
= -\boldsymbol{b}(\boldsymbol{\tau}) \qquad \forall \tau_i^d \in \Omega,
\tag{3.7}
$$

where $\mathbf{K}_{ij}(\boldsymbol{\tau})$ cofficients can be expressed as

$$
\mathbf{K}_{11}(\boldsymbol{\tau}) = \mathbb{C}_{11}\frac{\partial^2 R_{\mathbf{i},\mathbf{p}}(\boldsymbol{\tau})}{\partial x_1{}^2} + \mathbb{C}_{66}\frac{\partial^2 R_{\mathbf{i},\mathbf{p}}(\boldsymbol{\tau})}{\partial x_2{}^2} + \mathbb{C}_{55}\frac{\partial^2 R_{\mathbf{i},\mathbf{p}}(\boldsymbol{\tau})}{\partial x_3{}^2},
\tag{3.7a}
$$

$$
\mathbf{K}_{22}(\boldsymbol{\tau}) = \mathbb{C}_{66}\frac{\partial^2 R_{\mathbf{i},\mathbf{p}}(\boldsymbol{\tau})}{\partial x_1{}^2} + \mathbb{C}_{22}\frac{\partial^2 R_{\mathbf{i},\mathbf{p}}(\boldsymbol{\tau})}{\partial x_2{}^2} + \mathbb{C}_{44}\frac{\partial^2 R_{\mathbf{i},\mathbf{p}}(\boldsymbol{\tau})}{\partial x_3{}^2},
\tag{3.7b}
$$

$$\mathbf{K}_{33}(\boldsymbol{\tau}) = \mathbb{C}_{55}\frac{\partial^2 R_{\mathbf{i},\mathbf{p}}(\boldsymbol{\tau})}{\partial x_1{}^2} + \mathbb{C}_{44}\frac{\partial^2 R_{\mathbf{i},\mathbf{p}}(\boldsymbol{\tau})}{\partial x_2{}^2} + \mathbb{C}_{33}\frac{\partial^2 R_{\mathbf{i},\mathbf{p}}(\boldsymbol{\tau})}{\partial x_3{}^2}, \tag{3.7c}$$

$$\mathbf{K}_{23}(\boldsymbol{\tau}) = (\mathbb{C}_{23} + \mathbb{C}_{44})\frac{\partial^2 R_{\mathbf{i},\mathbf{p}}(\boldsymbol{\tau})}{\partial x_2\partial x_3}, \tag{3.7d}$$

$$\mathbf{K}_{13}(\boldsymbol{\tau}) = (\mathbb{C}_{13} + \mathbb{C}_{55})\frac{\partial^2 R_{\mathbf{i},\mathbf{p}}(\boldsymbol{\tau})}{\partial x_1\partial x_3}, \tag{3.7e}$$

$$\mathbf{K}_{12}(\boldsymbol{\tau}) = (\mathbb{C}_{12} + \mathbb{C}_{66})\frac{\partial^2 R_{\mathbf{i},\mathbf{p}}(\boldsymbol{\tau})}{\partial x_1\partial x_2}, \tag{3.7f}$$

and substituting in (3.1b) we obtain:

$$\begin{bmatrix} \tilde{\mathbf{K}}_{11}(\boldsymbol{\tau}) & \tilde{\mathbf{K}}_{12}(\boldsymbol{\tau}) & \tilde{\mathbf{K}}_{13}(\boldsymbol{\tau}) \\ & \tilde{\mathbf{K}}_{22}(\boldsymbol{\tau}) & \tilde{\mathbf{K}}_{23}(\boldsymbol{\tau}) \\ \text{symm.} & & \tilde{\mathbf{K}}_{33}(\boldsymbol{\tau}) \end{bmatrix} \cdot \begin{pmatrix} \hat{\mathbf{u}}_{\mathbf{i}} \\ \hat{\mathbf{v}}_{\mathbf{i}} \\ \hat{\mathbf{w}}_{\mathbf{i}} \end{pmatrix} = \boldsymbol{t}(\boldsymbol{\tau}) \qquad \forall \tau_i^d \in \Gamma_N, \tag{3.8}$$

with $\tilde{\mathbf{K}}_{ij}(\boldsymbol{\tau})$ components having the following form

$$\tilde{\mathbf{K}}_{11}(\boldsymbol{\tau}) = \mathbb{C}_{11}\frac{\partial R_{\mathbf{i},\mathbf{p}}(\boldsymbol{\tau})}{\partial x_1}n_1 + \mathbb{C}_{66}\frac{\partial R_{\mathbf{i},\mathbf{p}}(\boldsymbol{\tau})}{\partial x_2}n_2 + \mathbb{C}_{55}\frac{\partial R_{\mathbf{i},\mathbf{p}}(\boldsymbol{\tau})}{\partial x_3}n_3, \tag{3.8a}$$

$$\tilde{\mathbf{K}}_{22}(\boldsymbol{\tau}) = \mathbb{C}_{66}\frac{\partial R_{\mathbf{i},\mathbf{p}}(\boldsymbol{\tau})}{\partial x_1}n_1 + \mathbb{C}_{22}\frac{\partial R_{\mathbf{i},\mathbf{p}}(\boldsymbol{\tau})}{\partial x_2}n_2 + \mathbb{C}_{44}\frac{\partial R_{\mathbf{i},\mathbf{p}}(\boldsymbol{\tau})}{\partial x_3}n_3, \tag{3.8b}$$

$$\tilde{\mathbf{K}}_{33}(\boldsymbol{\tau}) = \mathbb{C}_{55}\frac{\partial R_{\mathbf{i},\mathbf{p}}(\boldsymbol{\tau})}{\partial x_1}n_1 + \mathbb{C}_{44}\frac{\partial R_{\mathbf{i},\mathbf{p}}(\boldsymbol{\tau})}{\partial x_2}n_2 + \mathbb{C}_{33}\frac{\partial R_{\mathbf{i},\mathbf{p}}(\boldsymbol{\tau})}{\partial x_3}n_3, \tag{3.8c}$$

$$\tilde{\mathbf{K}}_{23}(\boldsymbol{\tau}) = \mathbb{C}_{23}\frac{\partial R_{\mathbf{i},\mathbf{p}}(\boldsymbol{\tau})}{\partial x_3}n_2 + \mathbb{C}_{44}\frac{\partial R_{\mathbf{i},\mathbf{p}}(\boldsymbol{\tau})}{\partial x_2}n_3, \tag{3.8d}$$

$$\tilde{\mathbf{K}}_{13}(\boldsymbol{\tau}) = \mathbb{C}_{13}\frac{\partial R_{\mathbf{i},\mathbf{p}}(\boldsymbol{\tau})}{\partial x_3}n_1 + \mathbb{C}_{55}\frac{\partial R_{\mathbf{i},\mathbf{p}}(\boldsymbol{\tau})}{\partial x_1}n_3, \tag{3.8e}$$

$$\tilde{\mathbf{K}}_{12}(\boldsymbol{\tau}) = \mathbb{C}_{12}\frac{\partial R_{\mathbf{i},\mathbf{p}}(\boldsymbol{\tau})}{\partial x_2}n_1 + \mathbb{C}_{66}\frac{\partial R_{\mathbf{i},\mathbf{p}}(\boldsymbol{\tau})}{\partial x_1}n_2. \tag{3.8f}$$

As we can see from Equations (3.8), Neumann boundary conditions are directly imposed as strong-form equations at the collocation points belonging to the boundary surface Γ_N (see Section 2.1.3.2 and references [15, 55]), with the usual physical meaning of prescribed boundary tractions.

3.1.2   Single-element approach

The single-element approach considers the plate discretized by a single element through the thickness, which strongly reduces the number of DOFs with respect to LW methods [84, 85, 119, 120]. The material matrix is therefore homogenized to account for the presence of the layers as described in Figure 3.1(b).

Remark 3.1. *Considering a single-element homogenized approach is effective only for through-the-thickness symmetric layer distributions, as for non-symmetric ply stacking sequences the plate mid-plane is not balanced. In the case of non-symmetric layer distributions this technique is still applicable when the stacking sequence can be split into two symmetric piles, using one element per homogenized stack with a C^0 interface.*

This method provides accurate results only in terms of displacements and in-plane stress components. In order to recover a proper out-of-plane stress state, we propose to couple the single-element method with a post-processing technique following the approach in [62]. To characterize the variation of the material properties from layer to layer, we homogenize the constitutive behavior to create an equivalent single-layer laminate. Following [171], the explicit expressions for the effective elastic constants of the equivalent laminate (originally made of N plies) are given as

$$\overline{\mathbb{C}}_{11} = \sum_{k=1}^{N} \bar{t}_k \mathbb{C}_{11}^{(k)} + \sum_{k=2}^{N} (\mathbb{C}_{13}^{(k)} - \overline{\mathbb{C}}_{13}) \bar{t}_k \frac{(\mathbb{C}_{13}^{(1)} - \mathbb{C}_{13}^{(k)})}{\mathbb{C}_{33}^{(k)}} \, , \tag{3.9a}$$

$$\overline{\mathbb{C}}_{12} = \sum_{k=1}^{N} \bar{t}_k \mathbb{C}_{12}^{(k)} + \sum_{k=2}^{N} (\mathbb{C}_{13}^{(k)} - \overline{\mathbb{C}}_{13}) \bar{t}_k \frac{(\mathbb{C}_{23}^{(1)} - \mathbb{C}_{23}^{(k)})}{\mathbb{C}_{33}^{(k)}} \, , \tag{3.9b}$$

$$\overline{\mathbb{C}}_{13} = \sum_{k=1}^{N} \bar{t}_k \mathbb{C}_{13}^{(k)} + \sum_{k=2}^{N} (\mathbb{C}_{33}^{(k)} - \overline{\mathbb{C}}_{33}) \bar{t}_k \frac{(\mathbb{C}_{13}^{(1)} - \mathbb{C}_{13}^{(k)})}{\mathbb{C}_{33}^{(k)}} \, , \tag{3.9c}$$

$$\overline{\mathbb{C}}_{22} = \sum_{k=1}^{N} \bar{t}_k \mathbb{C}_{22}^{(k)} + \sum_{k=2}^{N} (\mathbb{C}_{23}^{(k)} - \overline{\mathbb{C}}_{23}) \bar{t}_k \frac{(\mathbb{C}_{23}^{(1)} - \mathbb{C}_{23}^{(k)})}{\mathbb{C}_{33}^{(k)}} \, , \tag{3.9d}$$

$$\overline{\mathbb{C}}_{23} = \sum_{k=1}^{N} \bar{t}_k \mathbb{C}_{23}^{(k)} + \sum_{k=2}^{N} (\mathbb{C}_{33}^{(k)} - \overline{\mathbb{C}}_{33}) \bar{t}_k \frac{(\mathbb{C}_{23}^{(1)} - \mathbb{C}_{23}^{(k)})}{\mathbb{C}_{33}^{(k)}} \, , \tag{3.9e}$$

$$\overline{\mathbb{C}}_{33} = \frac{1}{\left(\sum_{k=1}^{N} \frac{\bar{t}_k}{\mathbb{C}_{33}^{(k)}} \right)} \, , \tag{3.9f}$$

$$\overline{\mathbb{C}}_{44} = \frac{\left(\sum_{k=1}^{N} \frac{\bar{t}_k}{\mathbb{C}_{44}^{(k)}} \Delta_k \right)}{\Delta} \qquad \Delta = \left(\sum_{k=1}^{N} \frac{\bar{t}_k \mathbb{C}_{44}^{(k)}}{\Delta_k} \right) \left(\sum_{k=1}^{N} \frac{\bar{t}_k \mathbb{C}_{55}^{(k)}}{\Delta_k} \right) , \tag{3.9g}$$

$$\overline{\mathbb{C}}_{55} = \frac{\left(\sum_{k=1}^{N} \frac{\bar{t}_k}{\mathbb{C}_{55}^{(k)}} \Delta_k \right)}{\Delta} \qquad \Delta_k = \mathbb{C}_{44}^{k} \mathbb{C}_{55}^{k} \, , \tag{3.9h}$$

$$\overline{\mathbb{C}}_{66} = \sum_{k=1}^{N} \bar{t}_k \mathbb{C}_{66}^{(k)} \, , \tag{3.9i}$$

where $\mathbb{C}_{ij}^{(k)}$ represents the *ij*-th component of the fourth-order elasticity tensor in Voigt's notation (3.4) for the k-th layer and $\bar{t}_k = \dfrac{t_k}{t}$ stands for the volume fraction of the k-th lamina, t being the total thickness of the laminate and t_k the thickness of the k-th ply.

3.1.3 Post-processing step: reconstruction from equilibrium

As interlaminar delamination and other fracture processes rely mostly on out-of-plane components, a proper through-the-thickness stress description is required. In order to recover a more accurate stress state, we perform a post-processing step based on the equilibrium equations, relying on the higher regularity granted by IgA

shape functions. This procedure, which takes its roots in [56, 65, 154, 183] (see Section 2.3), has already been proven to be successful for IgG [62]. Inside the plate, the stresses should satisfy the equilibrium Equation (3.1a), which can be expanded as

$$\sigma_{11,1} + \sigma_{12,2} + \sigma_{13,3} = -b_1 \,, \tag{3.10a}$$

$$\sigma_{12,1} + \sigma_{22,2} + \sigma_{23,3} = -b_2 \,, \tag{3.10b}$$

$$\sigma_{13,1} + \sigma_{23,2} + \sigma_{33,3} = -b_3 \,. \tag{3.10c}$$

Assuming the in-plane stress components to approximate the laminate behavior well (as it will be shown in Section 3.2), we can integrate Equations 3.10a and 3.10b along the thickness, recovering the out-of-plane shear stresses as

$$\sigma_{13}(x_3) = -\int_{\bar{x}_3}^{x_3} (\sigma_{11,1}(\zeta) + \sigma_{12,2}(\zeta) + b_1(\zeta)) d\zeta + \sigma_{13}(\bar{x}_3) \,, \tag{3.11a}$$

$$\sigma_{23}(x_3) = -\int_{\bar{x}_3}^{x_3} (\sigma_{12,1}(\zeta) + \sigma_{22,2}(\zeta) + b_2(\zeta)) d\zeta + \sigma_{23}(\bar{x}_3) \,, \tag{3.11b}$$

where ζ represents the coordinate along the thickness direction.

Finally, we can insert Equations (3.11a) and (3.11b) into (3.10c), recovering the σ_{33} component as

$$\sigma_{33}(x_3) = -\int_{\bar{x}_3}^{x_3} (\sigma_{13,1}(\zeta) + \sigma_{23,2}(\zeta) + b_3(\zeta)) d\zeta + \sigma_{33}(\bar{x}_3) \,. \tag{3.12}$$

Following [62], the integral constants are chosen to fulfill the boundary conditions at the top or bottom surfaces of the plate.

Recalling that, from Equations (3.2) and (3.3),

$$\sigma_{ij,k} = \overline{\mathbb{C}}_{ijmn} \frac{u_{m,nk} + u_{n,mk}}{2} \,, \tag{3.13}$$

where the homogenized tensor $\overline{\mathbb{C}}$ is constant, the necessity of a highly regular displacement solution in order to recover a proper stress state becomes clear. Such a condition can be easily achieved using IgC with a reduced computational cost. We also remark that the proposed method strongly relies on the possibility to obtain an accurate description (with a relatively coarse mesh) of the in-plane stress state.

Furthermore, we highlight that integrals (3.11) and (3.12) are computed numerically using a composite trapezoidal quadrature rule. Namely, we integrate along the thickness direction starting from the bottom to the top of the laminate and *vice versa*, and then average the obtained numerical approximations.

3.2 Numerical tests

In this section, to assess whether the proposed method can effectively reproduce the behavior of solid composite plates, we consider a classical benchmark problem [145] and we address different aspects such as the effectiveness of the proposed post-processing step, the sensitivity of the method to parameters of interest (i.e., number of layers and length-to-thickness ratio), and its convergence.
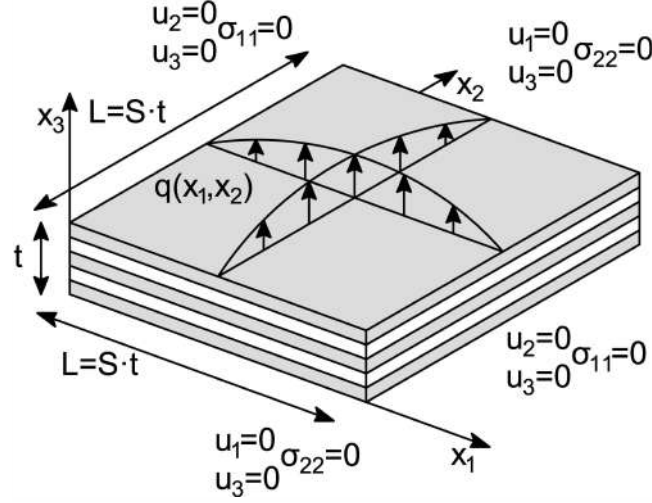
FIGURE 3.2: Pagano test case [145]. Problem geometry and boundary conditions.

3.2.1 Reference solution: the Pagano layered plate

A square laminated composite plate of total thickness t and made of N orthotropic layers is considered. This structure is simply supported and a normal sinusoidal traction is applied on the upper surface, while the lower surface is traction-free, as shown in Figure 3.2[1]. In the proposed numerical tests, we consider different numbers of layers, namely 3, 11, and 33. The thickness of every single layer is set to 1 mm, and the edge length, L, is chosen to be S times larger than the total thickness t of the laminate. Different choices of length-to-thickness ratio are considered (i.e., $S = 20$, 30, 40, and 50), which allow to draw interesting considerations about the laminate behavior in the proposed convergence tests. For all examples we consider the same loading conditions proposed by Pagano, i.e., a double sinus with periodicity equal to twice the length of the plate.

The Neumann boundary conditions on the plate surfaces $x_3 = 0$ and $x_3 = t$ are

$$\sigma_{13}(x_1, x_2, 0) = \sigma_{13}(x_1, x_2, t) = 0,$$
$$\sigma_{23}(x_1, x_2, 0) = \sigma_{23}(x_1, x_2, t) = 0,$$
(3.14a)

$$\sigma_{33}(x_1, x_2, 0) = 0,$$
(3.14b)

$$\sigma_{33}(x_1, x_2, t) = q(x_1, x_2) = \sigma_0 \sin(\frac{\pi x_1}{St}) \sin(\frac{\pi x_2}{St}),$$
(3.14c)

where $\sigma_0 = 1$ MPa.

---

[1]We remark that we modified Pagano's original test case in terms of placement of the reference system $\{x_1, x_2, x_3\}$. In our case, the $x_1 x_2$-plane does not coincide with the geometrical mid-plane of the laminate, but with the bottom surface of the plate (see Figure 3.2). This shift of the reference system allows for a simple and straightforward comparison between the analytical solution and the post-processed IgC solution, since for the latter method the numerical integrals are computed starting either from the bottom plate surface to the top one or *vice versa*.

The simply supported edge conditions are taken as

$$u_1(x_1, 0, x_3) = u_1(x_1, L, x_3) = 0,$$ (3.15a)

$$u_2(0, x_2, x_3) = u_2(L, x_2, x_3) = 0,$$ (3.15b)

$$u_3(0, x_2, x_3) = u_3(L, x_2, x_3) = u_3(x_1, 0, x_3) = u_3(x_1, L, x_3) = 0,$$ (3.15c)

$$\sigma_{11}(0, x_2, x_3) = \sigma_{11}(L, x_2, x_3) = 0,$$ (3.15d)

$$\sigma_{22}(x_1, 0, x_3) = \sigma_{22}(x_1, L, x_3) = 0.$$ (3.15e)

As depicted in Figure 3.2, the laminated plate is composed of layers organized in an alternated distribution of orthotropic plies (i.e., a 90°/0° stacking sequence in our case). Layer material parameters considered in the numerical tests are summarized in Table 3.1 for 0°-oriented plies.

TABLE 3.1: Material properties for 0°-oriented layers employed in the numerical tests.

E_1	E_2	E_3	G_{23}	G_{13}	G_{12}	ν_{23}	ν_{13}	ν_{12}
[GPa]	[GPa]	[GPa]	[GPa]	[GPa]	[GPa]	[-]	[-]	[-]
25000	1000	1000	200	500	500	0.25	0.25	0.25

Additionally, all results are then expressed in terms of the following normalized stress components

$$\bar{\sigma}_{ij} = \frac{\sigma_{ij}}{\sigma_0 S^2} \qquad i, j = 1, 2,$$ (3.16a)

$$\bar{\sigma}_{i3} = \frac{\sigma_{i3}}{\sigma_0 S} \qquad i = 1, 2,$$ (3.16b)

$$\bar{\sigma}_{33} = \frac{\sigma_{33}}{\sigma_0}.$$ (3.16c)

For a detailed derivation on the analytical solution to the Pagano's problem considered here, the interested reader is referred to Appendix 3.A.

3.2.2 Post-processed out-of-plane stresses

In this section, we present and discuss the results obtained using the proposed IgC approach, as compared with Pagano's analytical solution [145]. To give an idea of the improvement granted by the post-processing of out-of-plane stress components, in Figures 3.3 and 3.4 we compare the reference solution with non-treated and post-processed results for the cases of solid laminated plates made of 3 and 11 layers, considering a length-to-thickness ratio $S = 20$. All numerical simulations are carried out using an in-plane degree of approximation $p = q = 6$ and 10x10 collocation points, corresponding to 4 elements for each in-plane parametric direction, while we

(a) Normalized σ_{11}

(b) Normalized σ_{13}

(c) Normalized σ_{22}

(d) Normalized σ_{23}

(e) Normalized σ_{12}

(f) Normalized σ_{33}
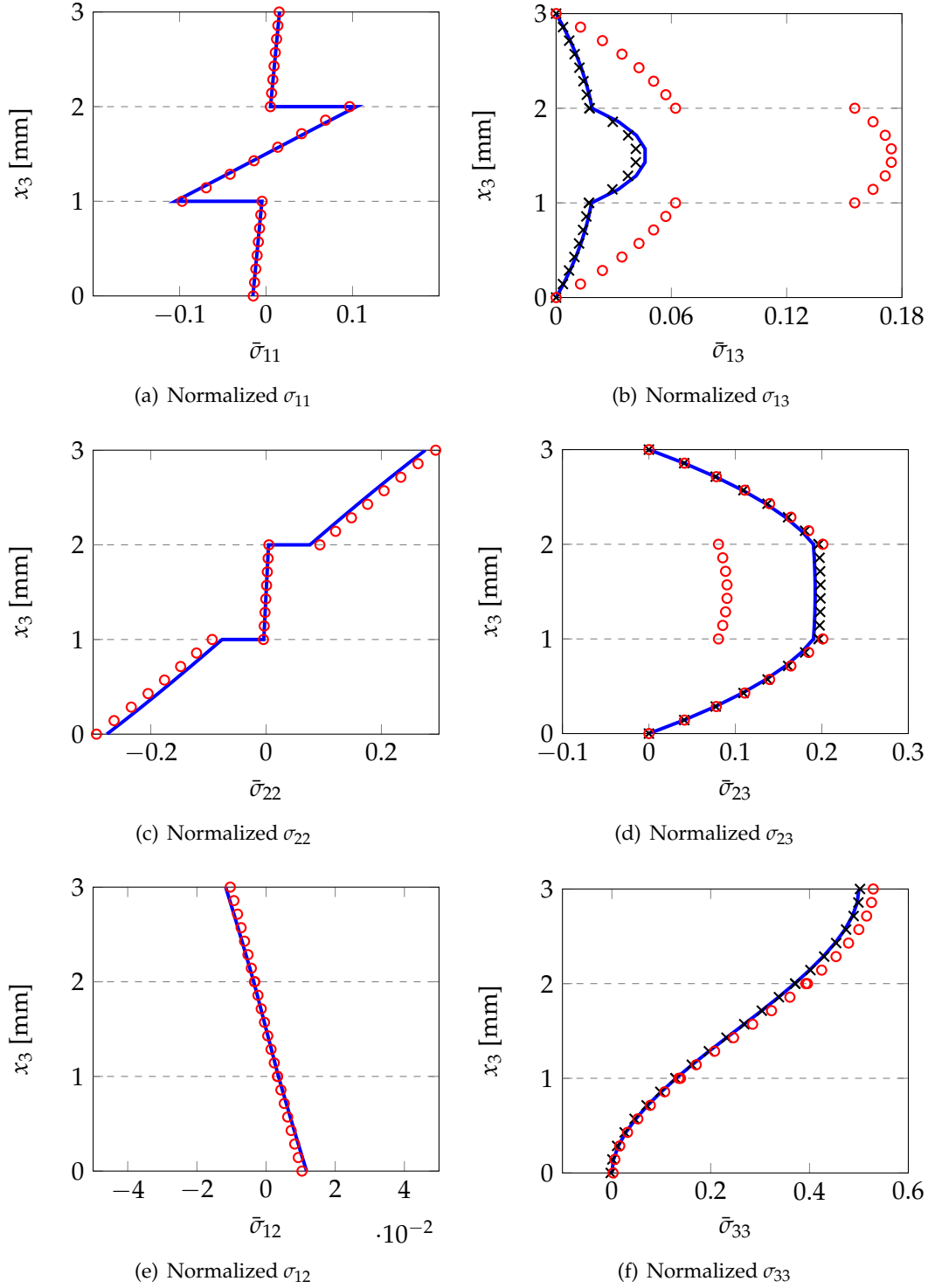
FIGURE 3.3: Through-the-thickness stress solutions for the 3D Pagano's problem [145] evaluated at $x_1 = x_2 = 0.25L$. Case: plate with 3 layers and length-to-thickness ratio $S = 20$, such that $L = St = 60$ mm (—— Pagano's solution, ○ homogenized IgC solution without post-processing obtained with 10x10x5 collocation points corresponding to 4 in-plane elements and one out-of-plane element, and $p = q = 6$ and $r = 4$ degrees of approximation, × post-processed homogenized IgC solution computed with 10x10x5 collocation points corresponding to 4 in-plane elements and one out-of-plane element, and $p = q = 6$ and $r = 4$).

(a) Normalized σ_{11}

(b) Normalized σ_{13}

(c) Normalized σ_{22}

(d) Normalized σ_{23}

(e) Normalized σ_{12}

(f) Normalized σ_{33}
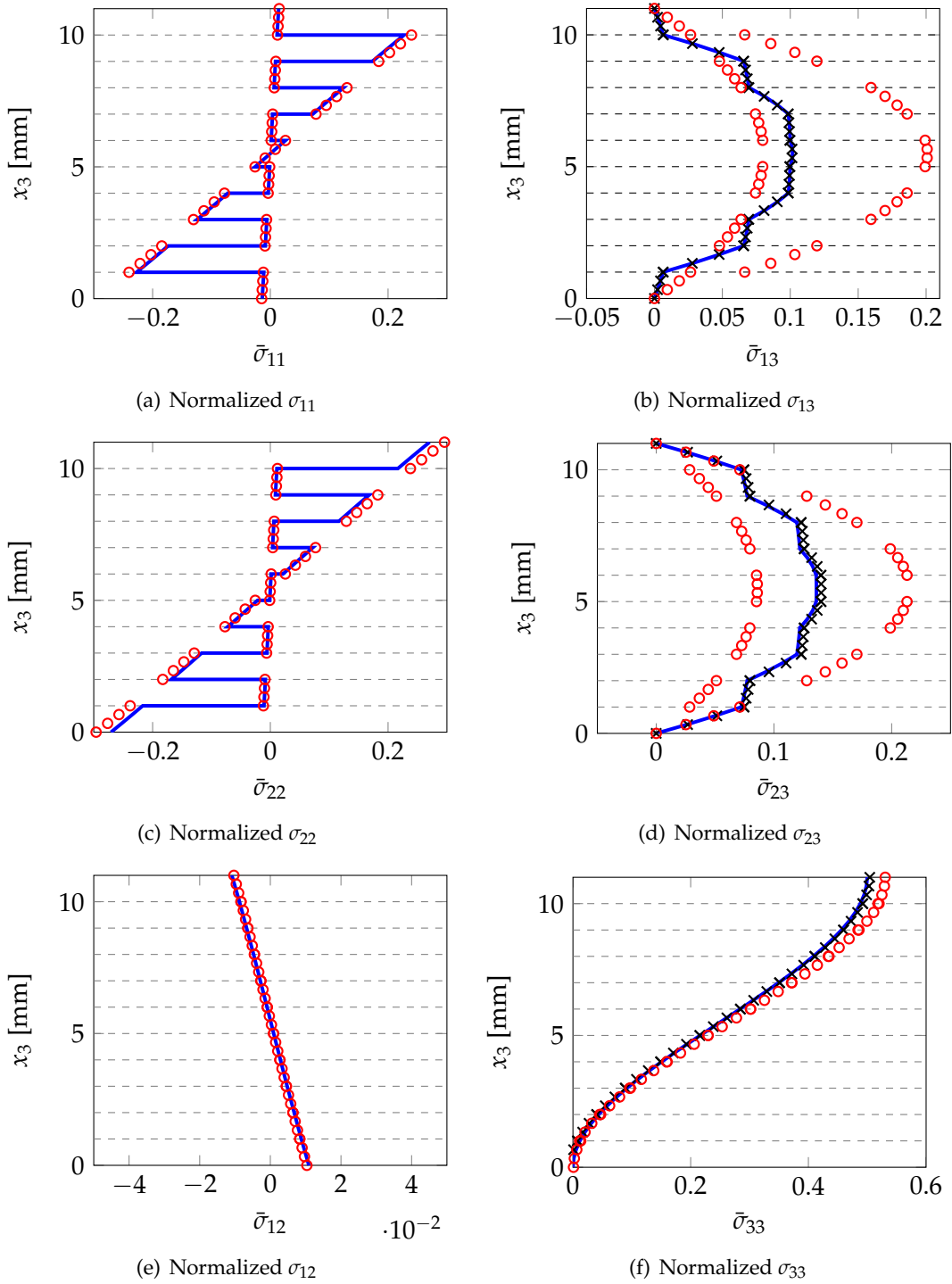
FIGURE 3.4: Through-the-thickness stress solutions for the 3D Pagano's problem [145] evaluated at $x_1 = x_2 = 0.25L$. Case: plate with 11 layers and length-to-thickness ratio $S = 20$, such that $L = St = 220$ mm (—— Pagano's solution, ○ homogenized IgC solution without post-processing obtained with 10x10x5 collocation points corresponding to 4 in-plane elements and one out-of-plane element, and $p = q = 6$ and $r = 4$ degrees of approximation, × post-processed homogenized IgC solution computed with 10x10x5 collocation points corresponding to 4 in-plane elements and one out-of-plane element, and $p = q = 6$ and $r = 4$).

use an approximation degree $r = 4$ and one element through the thickness (i.e., $r + 1$ collocation points). The sampling point where we show results is located at $x_1 = x_2 = 0.25L$. As expected, for both considered cases the in-plane stresses show a good behavior, while the out-of-plane stress components, without a post-processing treatment, are erroneously discontinuous. The proposed results clearly show the improvement granted by the post-processing of out-of-plane components. To show the effect of post-processing at different locations of the plate, in Figures 3.5-3.7 the out-of-plane stress state profile is recovered sampling the laminae every quarter of length in both in-plane directions for the case of a length-to-thickness ratio equal to 20 and 11 layers.

3.2.3 Convergence behavior and parametric study on length-to-thickness ratio

In order to validate the proposed stress recovery approach in a wider variety of cases, computations with a different ratio between the thickness of the plate and its length are performed respectively for 3, 11, and 33 layers, considering an increasing number of in-plane elements (i.e., 1, 2, 4, and 8). Adopting the following error definition

$$\mathrm{e}(\sigma_{i3}) = \frac{\max(|\sigma_{i3}^{\mathrm{analytic}} - \sigma_{i3}^{\mathrm{recovered}}|)}{\max(|\sigma_{i3}^{\mathrm{analytic}}|)}, \ i = 1, 2, 3, \tag{3.17}$$

Figures 3.8 and 3.9 assess the validity of our methodology for varying length-to-thickness ratios. Note that Equation (3.17) is used only to estimate the error inside the domain to avoid indeterminate forms. Different combinations of degree of approximations have also been considered. A poorer out-of-plane stress approximation is obtained using a degree equal to 4 in every direction. In addition, with this choice locking phenomena may occur for increasing values of the length-to-thickness ratio. Based on the results shown in Figures 3.8 and 3.9, we conclude that using an in-plane degree of approximation equal to 6 and equal to 4 through the thickness seems to be a reasonable choice to correctly reproduce the 3D stress state. Using instead uniform approximation degrees $p = q = r = 6$ does not seem to significantly improve the results (see Figures 3.8, 3.9, and Table 3.2). Additionally, we observe that the post-processing method provides better results for increasing values of length-to-thickness ratio; and therefore proves to be particularly convenient for very large and thin plates. The post-processed results are also better for a high number of layers, which is clear since a laminae with a large number of thin layers resembles a plate with average properties. An outstanding result of our mesh sensitivity analysis is that collocation perfectly captures the behavior of the plates not only using one element through the thickness but also employing only one element in the plane of the plate. A single element of degrees $p = q = 6$ and $r = 4$, comprising a total of 7x7x5 collocation points, is able to provide maximum percentage errors of 5% or lower in the 3-layer test for $S \geq 30$ and of $\leq 1\%$ in the cases with 11 and 33 layers.

Quantitative results are presented in Table 3.2 for various plate cases, considering a number of layers equal to 11 and 10 collocation points for each in-plane parametric direction. Different number of layers (i.e., 3 and 33) are instead investigated in Appendix 3.B, where increasing length-to-thickness ratios ($S = 20, 30, 40,$ and 50) are considered and the maximum relative error results are reported for a reference point
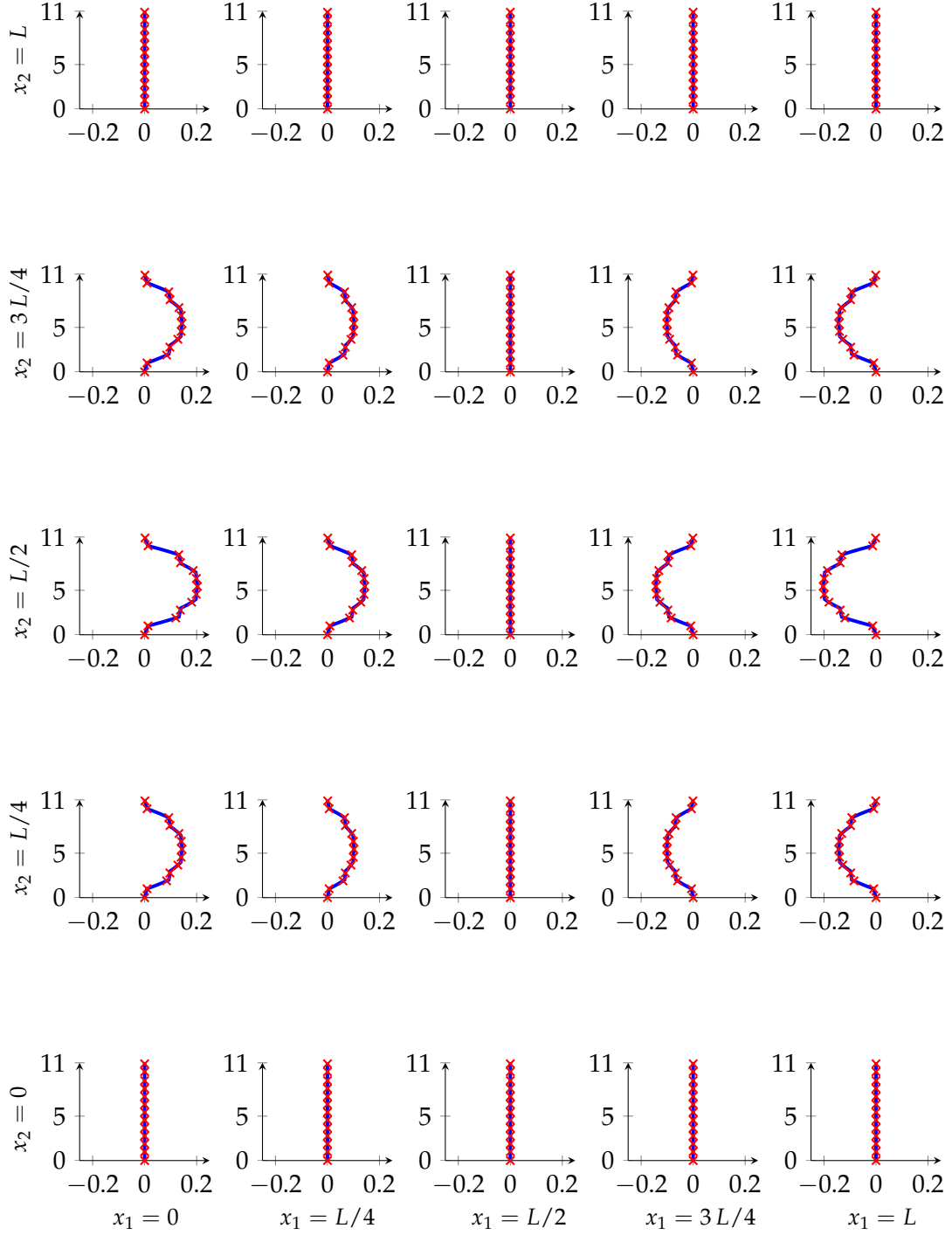
FIGURE 3.5: Through-the-thickness out-of-plane $\bar{\sigma}_{13}$ profiles for the 11-layer case for in-plane sampling points situated at every quarter of length in both in-plane directions x_1 and x_2. For each subplot, the horizontal axis shows the values of $\bar{\sigma}_{13}$ and the vertical axis the through-the-thickness coordinate x_3. L represents the total length of the plate, which for this case is $L = 220\,\text{mm}$ ($L = St$ with $t = 11\,\text{mm}$ and $S = 20$), while the number of layers is 11 (× post-processed solution, —— analytical solution [145]).

located at $x_1 = x_2 = 0.25L$. Different degrees of approximation are also investigated in Appendix 3.B. These additional results further support that using an out-of-plane degree of approximation equal to 4 leads to a sufficiently accurate stress state. Furthermore, the out-of-plane stress profile reconstruction results in Appendix 3.B show
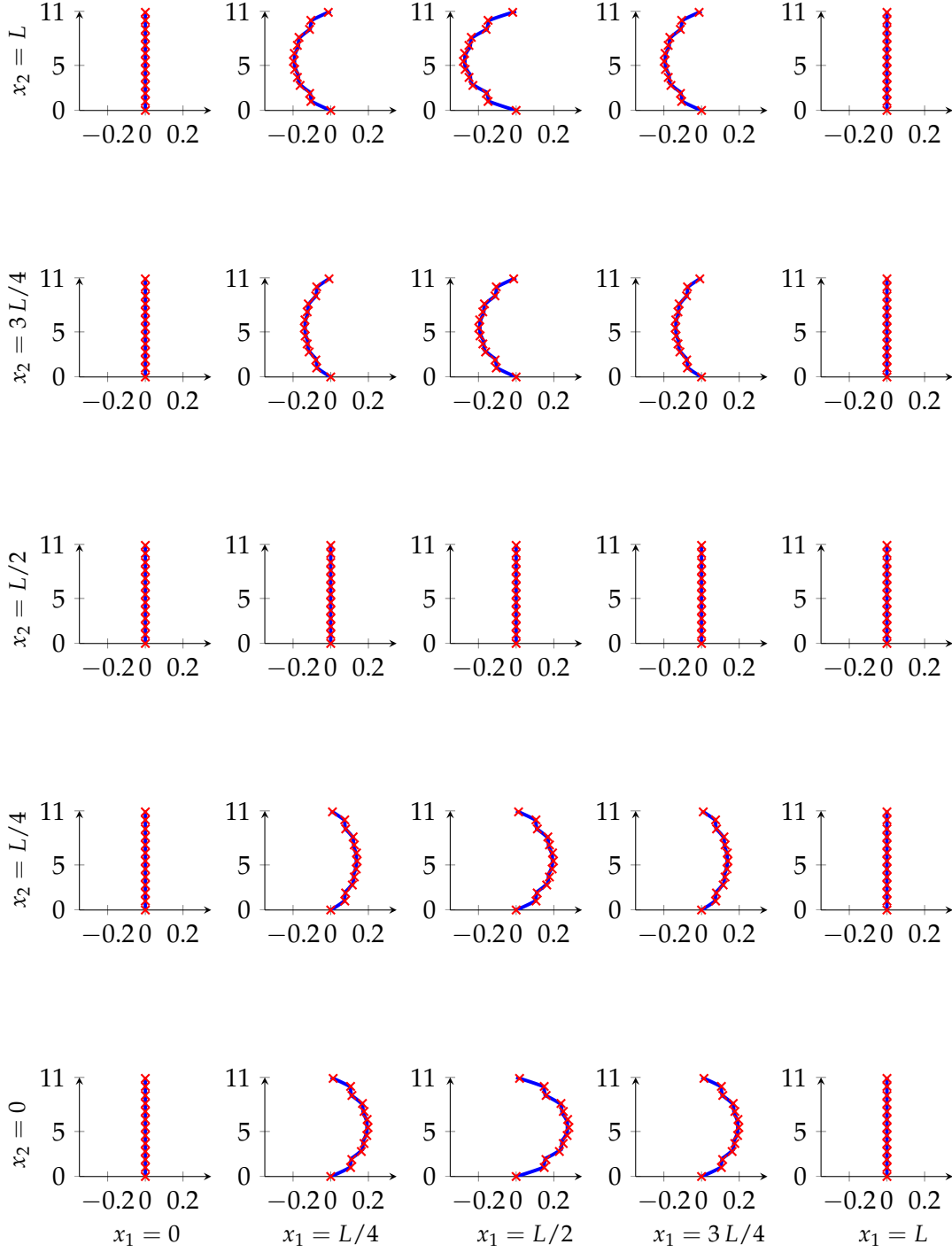
FIGURE 3.6: Through-the-thickness out-of-plane $\bar{\sigma}_{23}$ profiles for the 11-layer case for in-plane sampling points situated at every quarter of length in both in-plane directions x_1 and x_2. For each subplot, the horizontal axis shows the values of $\bar{\sigma}_{23}$ and the vertical axis the through-the-thickness coordinate x_3. L represents the total length of the plate, which for this case is $L = 220$ mm ($L = St$ with $t = 11$ mm and $S = 20$), while the number of layers is 11 (× post-processed solution, — analytical solution [145]).

a remarkable improvement for increasing values of the number of layers and slenderness parameter S.
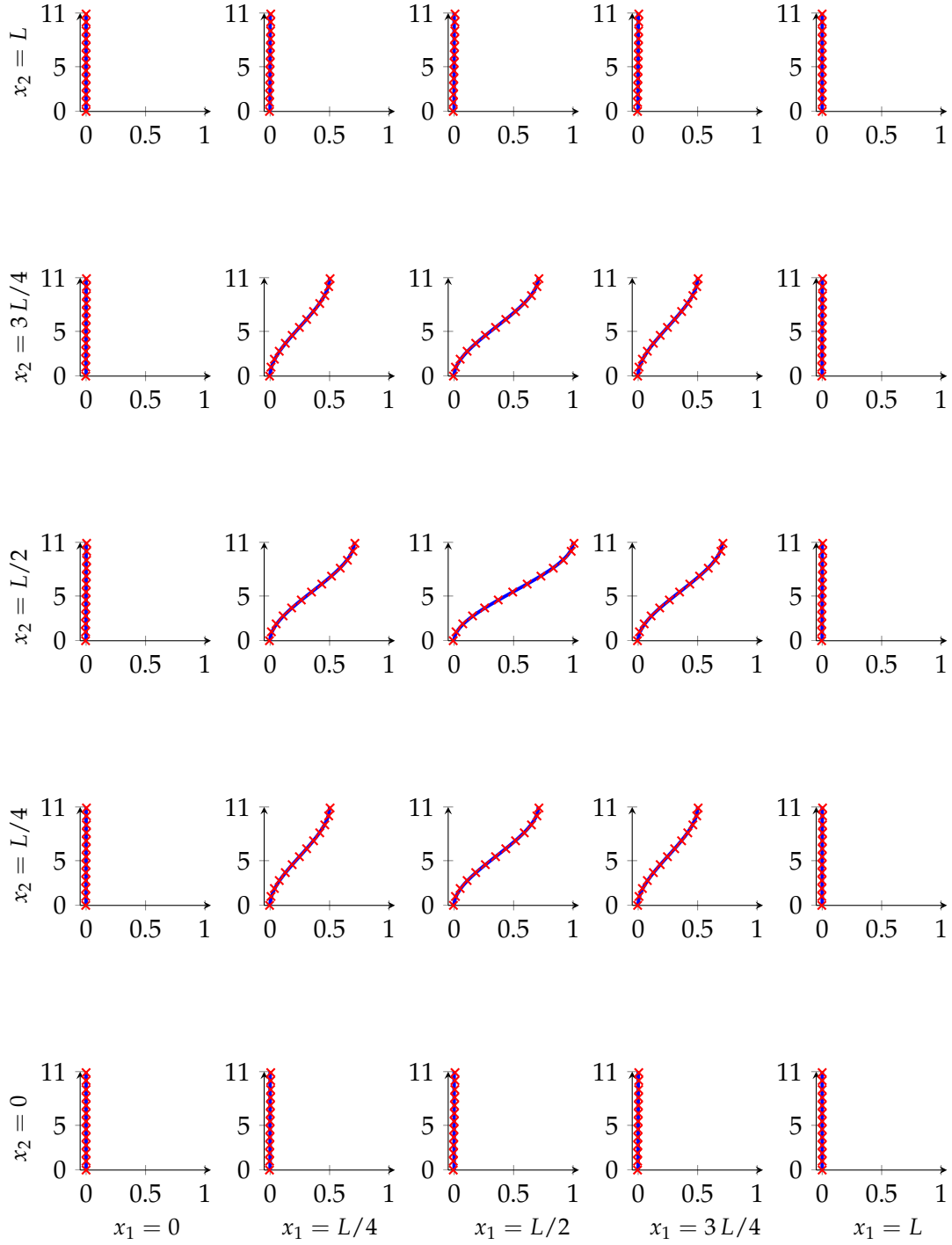
FIGURE 3.7: Through-the-thickness out-of-plane $\bar{\sigma}_{33}$ profiles for the 11-layer case for in-plane sampling points situated at every quarter of length in both in-plane directions x_1 and x_2. For each subplot, the horizontal axis shows the values of $\bar{\sigma}_{33}$ and the vertical axis the through-the-thickness coordinate x_3. L represents the total length of the plate, which for this case is $L = 220$ mm ($L = St$ with $t = 11$ mm and $S = 20$), while the number of layers is 11 (× post-processed solution, —— analytical solution [145]).

Laminated composites often exhibit inter-laminar normal and shear stress concentrations near material and geometric discontinuities leading to the so-called *free*
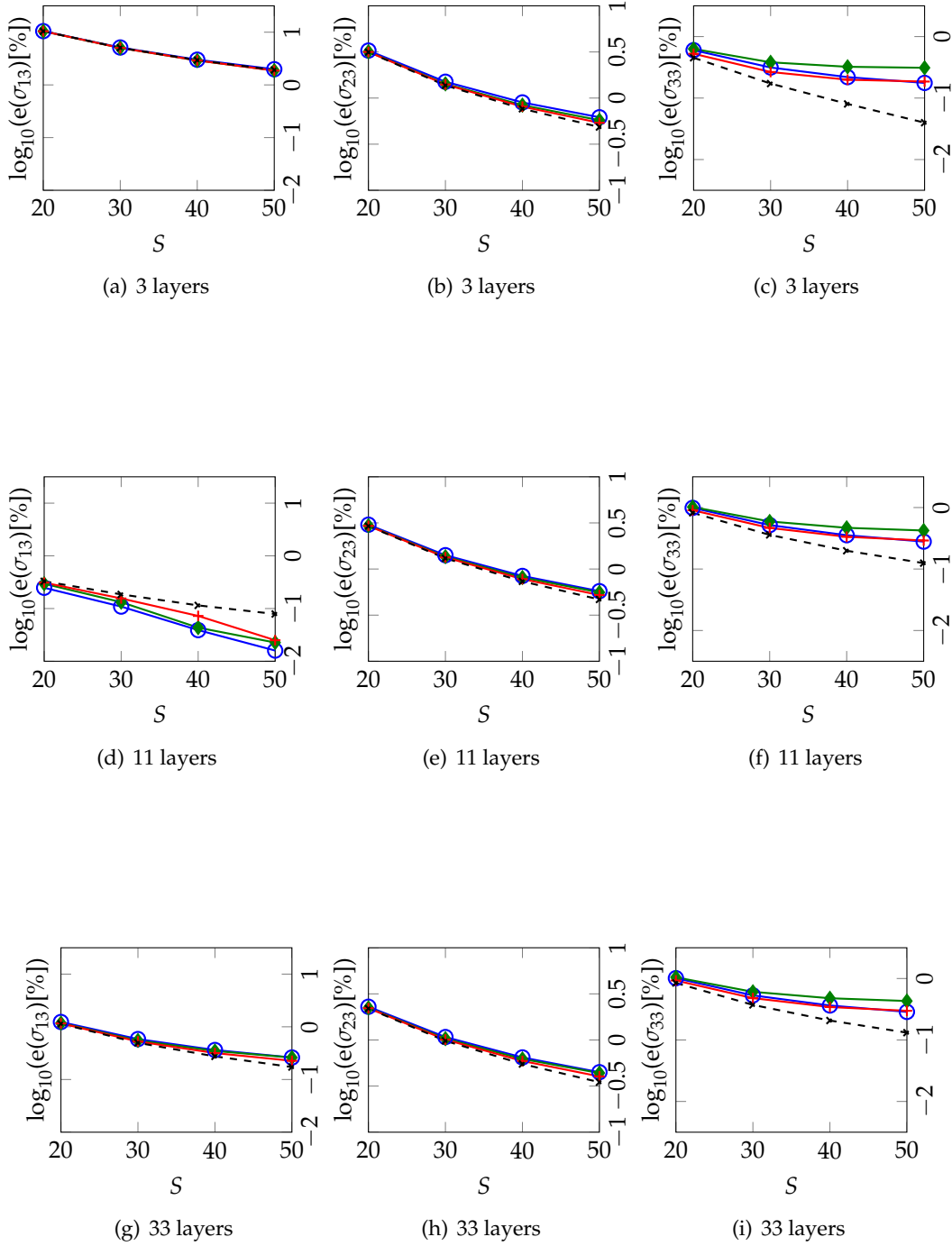
FIGURE 3.8: Maximum relative percentage error evaluation at $x_1 = x_2 = 0.25L$ for in-plane degrees of approximation equal to 6 and out-of-plane degree of approximation equal to 4. Different length-to-thickness ratios S are investigated for a number of layers equal to 3, 11, and 33 (⊸○⊸ 1 element, ⬥ 2 elements, ⊹ 4 elements, - ✳ - 8 elements).

edge effect [169]. To illustrate the ability of the proposed method to describe three-dimensional effects also at plate boundaries, we report in Figure 3.10 color maps of the analytical and the reconstructed stress components, along with the absolute value of their difference, at x_3 locations where such a difference is maximum. It is possible to observe that even in the worst case scenarios, stress errors are relatively small. These results are obtained considering a plate with length-to-thickness ratio
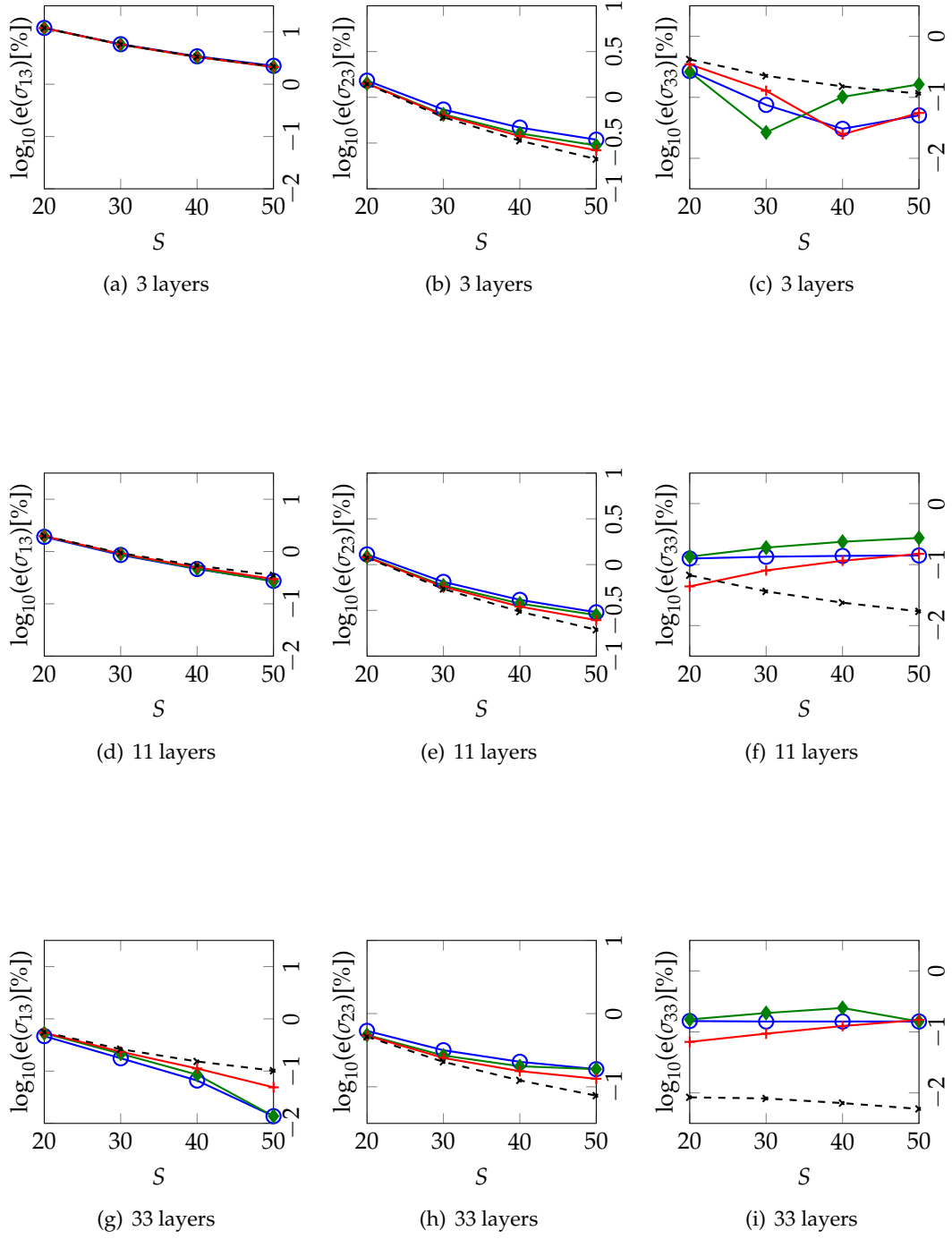
FIGURE 3.9: Maximum relative percentage error evaluation at $x_1 = x_2 = 0.25L$ for degrees of approximation equal to 6 in all directions. Different length-to-thickness ratios S are investigated for a number of layers equal to 3, 11, and 33 (—○— 1 element, —◆— 2 elements, —+— 4 elements, - ⨯ - 8 elements).

equal to 20, 11 layers, and 10 collocation points per in-plane direction.
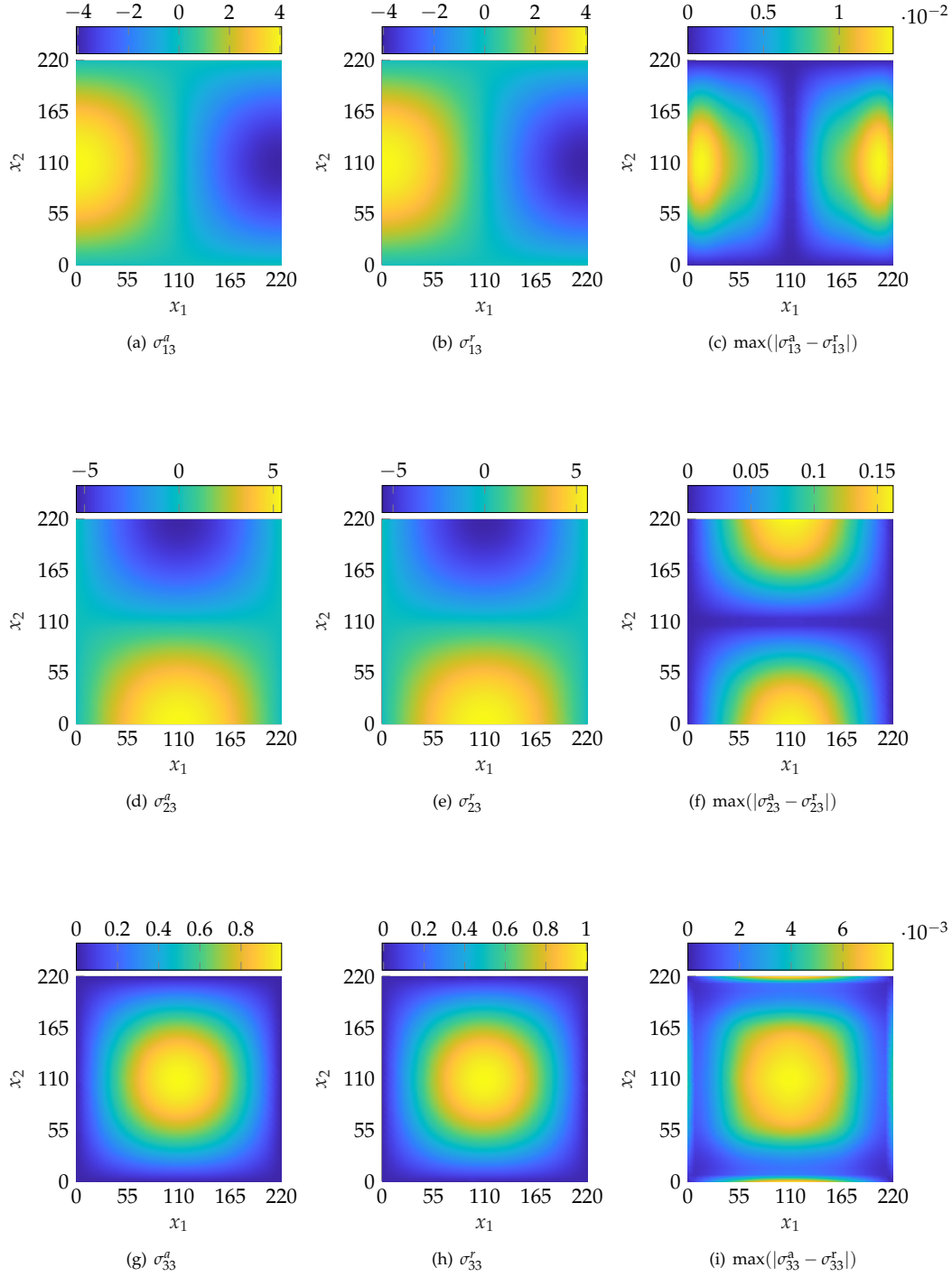
FIGURE 3.10: Analysis of the free-edge effect. Left column: analytical distribution of σ_{i3}^a ($i = 1, 2, 3$). Middle column: reconstructed distribution of σ_{i3}^r ($i = 1, 2, 3$) computed with 10x10x5 collocation points corresponding to 4 in-plane elements and one out-of-plane element, a degree of approximation equal to 6 per in-plane direction, and an out-of-plane degree of approximation equal to 4. Right column: absolute value of the difference $\sigma_{i3}^a - \sigma_{i3}^r$. The plot for each out-of-plane stress σ_{i3} corresponds to the x_3 location where the value of $|\sigma_{i3}^a - \sigma_{i3}^r|$ is maximum. A length-to-thickness ratio S equal to 20 and 11 layers are considered.

TABLE 3.2: Simply supported composite plate under sinusoidal load with a number of layers equal to 11. Maximum relative error of the out-of-plane stress state with respect to Pagano's solution [145] at $x_1 = x_2 = 0.25L$. We compare IgC before and after the application of the post-processing technique (post-processed IgC) for different approximation degrees (p, q, r) and length-to-thickness ratios (S), while we use 4 elements in each in-plane direction (i.e., 10x10 collocation points in the plane of the plate).

Degrees of approximation		$p = q = 6, r = 4$			$p = q = r = 6$		
S	Method	$e(\sigma_{13})$ [%]	$e(\sigma_{23})$ [%]	$e(\sigma_{33})$ [%]	$e(\sigma_{13})$ [%]	$e(\sigma_{23})$ [%]	$e(\sigma_{33})$ [%]
20	IgC	97.6	56.7	6.34	96.6	56.1	6.31
	post-processed IgC	0.31	2.94	0.90	1.97	1.20	0.05
30	IgC	98.7	55.6	6.36	98.3	55.4	6.34
	post-processed IgC	0.16	1.34	0.47	0.91	0.57	0.08
40	IgC	99.2	55.3	6.37	98.9	55.2	6.36
	post-processed IgC	0.07	0.78	0.34	0.50	0.35	0.12
50	IgC	99.4	55.1	6.38	99.2	55.1	6.38
	post-processed IgC	0.03	0.52	0.29	0.30	0.25	0.15

3.3   Conclusions

In this chapter we present a new efficient approach to simulate solid laminated plates characterized by a symmetric distribution of plies. This technique combines a 3D IgC approach with a post-processing step procedure based on equilibrium equations. Since we adopt a single-element approach, to take into account variation of the material properties through the plate thickness, we average the constitutive behavior of each layer considering a homogenized response. Following this simple approach, we showed that acceptable results can be obtained only in terms of displacements and in-plain stresses. Therefore, we propose to perform a post-processing step to recover the out-of-plane stress state, which requires the shape functions to be highly continuous. This continuity demand is fully granted by typical IgA shape functions. After the post-processing correction is applied, good results are recovered also in terms of out-of-plane stresses, even for very coarse meshes. The post-processing stress recovery technique is only based on the integration of equilibrium equations through the thickness, and all the required components can be easily computed by differentiating the displacement solution. Several numerical tests are carried out to assess the sensitivity of the proposed technique to different length-to-thickness ratios and number of layers. Regardless of the number of layers, the method gives better results the more slender the composites are. Multiple numbers of alternated layers and sequences of stacks (both even and odd) have been studied in our applications. Nevertheless, only tests that consider an odd number of layers or an odd disposition of an even number of stacks show good results. This was expected because considering a homogenized response of the material is effective only for symmetric distributions of plies (see Remark 3.1). Further research topics currently under investigation focus on the extension of this approach to more complex problems involving large deformations.

Appendix 3.A: Analytical solution to Pagano's problem

The reference solution to Pagano's layered plate introduced in Section 3.2.1 is derived starting from the Equation (3.3), which is valid for any layer and can be written using (3.4) as

$$
\begin{pmatrix} \sigma_{11} \\ \sigma_{22} \\ \sigma_{33} \end{pmatrix} = \begin{bmatrix} \mathbb{C}_{11} & \mathbb{C}_{12} & \mathbb{C}_{13} \\ \mathbb{C}_{21} & \mathbb{C}_{22} & \mathbb{C}_{23} \\ \mathbb{C}_{31} & \mathbb{C}_{32} & \mathbb{C}_{33} \end{bmatrix} \begin{pmatrix} \varepsilon_{11} \\ \varepsilon_{22} \\ \varepsilon_{33} \end{pmatrix} \tag{3.A.1}
$$

and

$$
\tau_{23} = \mathbb{C}_{44} 2\varepsilon_{23}, \tag{3.A.2}
$$
$$
\tau_{13} = \mathbb{C}_{55} 2\varepsilon_{13}, \tag{3.A.3}
$$
$$
\tau_{12} = \mathbb{C}_{66} 2\varepsilon_{12}, \tag{3.A.4}
$$

while the governing field equations can be written in terms of displacement components u, v, and w as

$$
\mathbb{C}_{11} u_{,11} + \mathbb{C}_{66} u_{,22} + \mathbb{C}_{55} u_{,33} + (\mathbb{C}_{12} + \mathbb{C}_{66}) v_{,12} + (\mathbb{C}_{13} + \mathbb{C}_{55}) w_{,13} = 0, \tag{3.A.5a}
$$
$$
(\mathbb{C}_{12} + \mathbb{C}_{66}) u_{,12} + \mathbb{C}_{66} v_{11} + \mathbb{C}_{22} v_{,22} + \mathbb{C}_{44} v_{,33} + (\mathbb{C}_{23} + \mathbb{C}_{44}) w_{,23} = 0, \tag{3.A.5b}
$$
$$
(\mathbb{C}_{13} + \mathbb{C}_{55}) u_{,13} + (\mathbb{C}_{23} + \mathbb{C}_{44}) v_{,23} + \mathbb{C}_{55} w_{,11} + \mathbb{C}_{44} w_{,22} + \mathbb{C}_{33} w_{,33} = 0. \tag{3.A.5c}
$$

Thus, the laminate response is defined by the solution of the boundary value problem satisfying the balance of linear momentum Equation (3.A.5) within each layer, the boundary conditions expressed by (3.14) and (3.15), and the interface continuity conditions, which impose the equality of displacements (u, v, and w) as well as out-of-plane stresses (τ_{13}, τ_{23}, and σ_{33}) belonging to adjacent layers at each interface.

Starting from these consideration, here we report the analytical solution of the problem for one layer [145]. A trial displacement form is given by

$$
u = U(x_3) \cos(p(n)x_1) \sin(q(m)x_2), \tag{3.A.6a}
$$
$$
v = V(x_3) \sin(p(n)x_1) \cos(q(m)x_2), \tag{3.A.6b}
$$
$$
w = W(x_3) \sin(p(n)x_1) \sin(q(m)x_2), \tag{3.A.6c}
$$

where the dependence upon x_3 coordinate is described only by U, V, and W functions and

$$
p(n) = \frac{n\pi}{a}, \tag{3.A.7a}
$$
$$
q(m) = \frac{m\pi}{b}, \tag{3.A.7b}
$$

with $n, m \in \mathbb{N}$, and where a and b are the lengths of the plate sides. In our case $m = n = 1$, i.e., $p = q = \frac{\pi}{St}$ [2].

---

[2]The notation in this appendix is somewhat independent from the rest of the chapter unless otherwise stated. In particular, we note that p, q, $p(n)$, and $q(m)$ are merely part of the parametrization of the analytical solution to Pagano's problem and are not related to the in-plane degrees of approximation used in the main text of this chapter. The same applies for G_j, R_j, S_j, and m_j in the next pages.

Assuming that

$$(U, V, W) = (U^*, V^*, W^*) \exp(sz) \,, \tag{3.A.8}$$

where U^*, V^*, and W^* are constants, we substitute Equations (3.A.6) and (3.A.8) in the internal equilibrium Equations (3.A.5), which leads to an algebraic system to calculate U^*, V^*, and W^* (see [145] for further details). Non-trivial solutions of this system exist only if the determinant of the coefficient matrix vanishes, which leads to the following equation

$$- As^6 + Bs^4 + Cs^2 + D = 0 \,, \tag{3.A.9}$$

where

$$
\begin{aligned}
A ={}& \mathbb{C}_{33}\mathbb{C}_{44}\mathbb{C}_{55} \,, \\
B ={}& p^2[\mathbb{C}_{44}(\mathbb{C}_{11}\mathbb{C}_{33} - \mathbb{C}_{13}^2) + \mathbb{C}_{55}(\mathbb{C}_{33}\mathbb{C}_{66} - 2\mathbb{C}_{13}\mathbb{C}_{44})] + \\
&+ q^2[\mathbb{C}_{55}(\mathbb{C}_{22}\mathbb{C}_{33} - \mathbb{C}_{23}^2) + \mathbb{C}_{44}(\mathbb{C}_{33}\mathbb{C}_{66} - 2\mathbb{C}_{23}\mathbb{C}_{55})] \,, \\
C ={}& -p^4[\mathbb{C}_{66}(\mathbb{C}_{11}\mathbb{C}_{33} - \mathbb{C}_{13}^2) + \mathbb{C}_{55}(\mathbb{C}_{11}\mathbb{C}_{44} - 2\mathbb{C}_{13}\mathbb{C}_{66})] + \\
&+ p^2 q^2[-\mathbb{C}_{11}(\mathbb{C}_{22}\mathbb{C}_{33} - \mathbb{C}_{23}^2) - 2(\mathbb{C}_{12} + \mathbb{C}_{66})(\mathbb{C}_{13} + \mathbb{C}_{55})(\mathbb{C}_{23} + \mathbb{C}_{44}) - \\
&+ 2\mathbb{C}_{44}\mathbb{C}_{55}\mathbb{C}_{66} + 2\mathbb{C}_{11}\mathbb{C}_{23}\mathbb{C}_{44} + \mathbb{C}_{12}\mathbb{C}_{33}(\mathbb{C}_{12} + 2\mathbb{C}_{66}) + \mathbb{C}_{13}\mathbb{C}_{22}(\mathbb{C}_{13} + 2\mathbb{C}_{55})] + \\
&- q^4[\mathbb{C}_{66}(\mathbb{C}_{22}\mathbb{C}_{33} - \mathbb{C}_{23}^2) + \mathbb{C}_{44}(\mathbb{C}_{22}\mathbb{C}_{55} - 2\mathbb{C}_{23}\mathbb{C}_{66})] \,, \\
D ={}& p^6\mathbb{C}_{11}\mathbb{C}_{55}\mathbb{C}_{66} + p^4 q^2[\mathbb{C}_{55}(\mathbb{C}_{11}\mathbb{C}_{22} - \mathbb{C}_{12}^2) + \mathbb{C}_{66}(\mathbb{C}_{11}\mathbb{C}_{44} - 2\mathbb{C}_{12}\mathbb{C}_{55})] + \\
&+ p^2 q^4[\mathbb{C}_{44}(\mathbb{C}_{11}\mathbb{C}_{22} - \mathbb{C}_{12}^2) + \mathbb{C}_{66}(\mathbb{C}_{22}\mathbb{C}_{55} - 2\mathbb{C}_{12}\mathbb{C}_{44})] + q^6\mathbb{C}_{22}\mathbb{C}_{44}\mathbb{C}_{66} \,.
\end{aligned}
$$

Thus, we rewrite Equation (3.A.9) in terms of γ by making the replacement $\gamma = s^2 - \dfrac{B}{3A}$, obtaining

$$\gamma^3 + d\gamma + f = 0 \,. \tag{3.A.10}$$

In Equation (3.A.10) the terms d and f read

$$
\begin{aligned}
d &= \frac{(3CA + B^2)}{(-3A^2)} \,, \\
f &= \frac{(2B^3 + 9ABC + 27DA^2)}{(-27A^3)} \,.
\end{aligned}
\tag{3.A.11}
$$

Once the roots of Equation (3.A.10) are obtained (in our case *via* MATLAB® com-mand `roots`), a general solution can be written for U, V, W as

$$U(x_3) = \sum_{j=1}^{3} U_j(x_3) \,, \tag{3.A.12a}$$

$$V(x_3) = \sum_{j=1}^{3} L_j U_j(x_3) \,, \tag{3.A.12b}$$

$$W(x_3) = \sum_{j=1}^{3} R_j W_j(x_3) \,, \tag{3.A.12c}$$

where, for $j = 1, 2, 3$,

$$U_j(x_3) = F_j C_j(x_3) + G_j S_j(x_3) \tag{3.A.13a}$$

$$W_j(x_3) = G_j C_j(x_3) + \alpha_j F_j S_j(x_3), \tag{3.A.13b}$$

with

$$
\begin{aligned}
L_j =& \frac{pq}{J_j}\{\alpha_j m_j^2[\mathbb{C}_{33}(\mathbb{C}_{12} + \mathbb{C}_{66}) - (\mathbb{C}_{23} + \mathbb{C}_{44})(\mathbb{C}_{13} + \mathbb{C}_{55})] + \\
& - (\mathbb{C}_{12} + \mathbb{C}_{66})(\mathbb{C}_{55}p^2 + \mathbb{C}_{44}q^2)\}, \\
R_j =& \frac{pm_j}{J_j}[\alpha_j m_j^2 \mathbb{C}_{44}(\mathbb{C}_{13} + \mathbb{C}_{55}) - (\mathbb{C}_{13} + \mathbb{C}_{55})(\mathbb{C}_{66}p^2 + \mathbb{C}_{22}q^2) + \\
& + q^2(\mathbb{C}_{23} + \mathbb{C}_{44})(\mathbb{C}_{12} + \mathbb{C}_{66})], \\
J_j =& \mathbb{C}_{33}\mathbb{C}_{44}m_j^4 + \alpha_j m_j^2[-p^2(\mathbb{C}_{44}\mathbb{C}_{55} + \mathbb{C}_{33}\mathbb{C}_{66}) + q^2(\mathbb{C}_{23}^2 - \mathbb{C}_{22}\mathbb{C}_{33} + 2\mathbb{C}_{23}\mathbb{C}_{44})] + \\
& + (\mathbb{C}_{66}p^2 + \mathbb{C}_{22}q^2)(\mathbb{C}_{55}p^2 + \mathbb{C}_{44}q^2).
\end{aligned}
$$

In Equation (3.A.13), F_j and G_j are constants to be determined imposing the boundary conditions in Equation (3.14) for a single layer. For multilayered plates instead, the 6 boundary conditions (3.14) are increased by $6(N-1)$ interface continuity conditions of the out-of-plane stresses. Moreover, according to the sign of $\left(\gamma_j + \frac{B}{3A}\right)$, $C_j(x_3)$ and $S_j(x_3)$ terms take the form of

$$C_j(x_3) = \cosh(m_j x_3), \ S_j(x_3) = \sinh(m_j x_3), \ \alpha_j = 1, \ \text{if} \ \left(\gamma_j + \frac{B}{3A}\right) > 0, \tag{3.A.14a}$$

$$C_j(x_3) = \cos(m_j x_3), \ S_j(x_3) = \sin(m_j x_3), \ \alpha_j = -1, \ \text{if} \ \left(\gamma_j + \frac{B}{3A}\right) < 0, \tag{3.A.14b}$$

with

$$m_j = \sqrt{\left|\gamma_j + \frac{B}{3A}\right|}. \tag{3.A.15}$$

Finally, using the strain-displacement relations of linear elasticity (3.A.1)-(3.A.4) in conjunction with Equation (3.A.12), we find that the stress components are given by

$$\sigma_{ii} = \sin(px_1)\sin(qx_2)\sum_{j=1}^{3} M_{ij}U_j(x_3) \qquad i = 1,2,3, \tag{3.A.16a}$$

$$\tau_{23} = \mathbb{C}_{44}\sin(px_1)\cos(qx_2)\sum_{j=1}^{3}(m_j L_j + qR_j)W_j(x_3), \tag{3.A.16b}$$

$$\tau_{13} = \mathbb{C}_{55}\cos(px_1)\sin(qx_2)\sum_{j=1}^{3}(m_j + pR_j)W_j(x_3), \tag{3.A.16c}$$

$$\tau_{12} = \mathbb{C}_{66}\cos(px_1)\cos(qx_2)\sum_{j=1}^{3}(q + pL_j)U_j(x_3), \tag{3.A.16d}$$

where

$$M_{ij} = -p\mathbb{C}_{1i} - q\mathbb{C}_{2i}L_j + \alpha_j m_j R_j \mathbb{C}_{3i} \qquad i,j = 1,2,3. \tag{3.A.17}$$

Appendix 3.B: Additional results

Results in terms of maximum relative error considering a plate with a number of layers equal to 3 and 33 are herein presented in Table 3.B.1 for a reference point located at $x_1 = x_2 = 0.25L$. Increasing length-to-thickness ratios ($S = 20, 30, 40$, and 50) are investigated for different degrees of approximations (i.e., $p = q = 6$ and $r = 4$, and $p = q = r = 6$), using 10x10x5 collocation points corresponding to 4 elements for each in-plane parametric direction and one element through-the-thickness.

TABLE 3.B.1: Simply supported composite plate under sinusoidal load. Maximum relative error of the out-of-plane stress state with respect to Pagano's solution [145] at $x_1 = x_2 = 0.25L$. We compare IgC before and after the application of the post-processing technique (post-processed IgC) for different approximation degrees (p, q, r) and length-to-thickness ratios (S), while we use 4 elements in each in-plane direction (i.e., 10x10 collocation points in the plane of the plate).

(a) Plate case with a number of layers equal to 3.

Degrees of approximation		$p = q = 6, r = 4$			$p = q = r = 6$		
S	Method	$e(\sigma_{13})$ [%]	$e(\sigma_{23})$ [%]	$e(\sigma_{33})$ [%]	$e(\sigma_{13})$ [%]	$e(\sigma_{23})$ [%]	$e(\sigma_{33})$ [%]
20	IgC	292	57.2	5.80	291	57.2	5.79
	post-processed IgC	10.4	3.16	0.54	11.9	1.41	0.33
30	IgC	311	57.5	5.77	311	57.5	5.77
	post-processed IgC	5.05	1.40	0.28	5.75	0.63	0.11
40	IgC	319	57.6	5.76	319	57.6	5.76
	post-processed IgC	2.91	0.81	0.21	3.32	0.38	0.02
50	IgC	323	57.6	5.76	322	57.6	5.76
	post-processed IgC	1.87	0.54	0.20	2.14	0.26	0.07

(b) Plate case with a number of layers equal to 33.

Degrees of approximation		$p = q = 6, r = 4$			$p = q = r = 6$		
S	Method	$e(\sigma_{13})$ [%]	$e(\sigma_{23})$ [%]	$e(\sigma_{33})$ [%]	$e(\sigma_{13})$ [%]	$e(\sigma_{23})$ [%]	$e(\sigma_{33})$ [%]
20	IgC	81.6	69.7	6.33	80.7	68.9	6.33
	post-processed IgC	1.16	2.21	0.93	0.54	0.50	0.07
30	IgC	81.5	69.0	6.34	81.2	68.7	6.34
	post-processed IgC	0.53	1.01	0.48	0.23	0.25	0.09
40	IgC	81.5	68.7	6.35	81.3	68.6	6.34
	post-processed IgC	0.32	0.59	0.34	0.11	0.16	0.12
50	IgC	81.6	68.6	6.35	81.4	68.5	6.35
	post-processed IgC	0.23	0.40	0.30	0.05	0.13	0.16

Chapter 4

Accurate equilibrium-based interlaminar stress recovery for isogeometric laminated composite Kirchhoff plates

In this chapter, we extend the stress recovery strategy, introduced in Chapter 3, to model the out-of-plane behavior of Kirchhoff laminated plates and present a displacement-based CLPT approach, which provides the lowest computational cost among known literature strategies, within an IgA framework. According to this plate theory, interlaminar stresses are identically zero when computed using the constitutive equations. However, these stresses do exist in reality, and they can be responsible for failures in composite laminates because of the difference in the material properties between the layers. Therefore, the proposed modeling strategy is coupled with a post-processing technique that directly relies on equilibrium and grants a highly accurate prediction of the out-of-plane stress state even from a very coarse 2D displacement solution (e.g., using one high-order element to model the plate mid-plane for rectangular laminates). More specifically, the obtained displacement solution is used to compute the necessary in-plane derivatives to recover the out-of-plane stresses directly imposing equilibrium in strong form. Since this *a posteriori* step relies on high-order in-plane continuity requirements, IgA represents a natural simulation framework due to its accuracy and higher continuity properties. Both IgG and IgC formulations are herein considered. The effectiveness of the proposed approach is proven by extensive numerical tests. The adopted post-processing technique, as introduced in Section 2.3, takes its origin in [53, 65, 154] and has already been proven to provide good results for 3D solid plates in the context of IgG approaches [62], IgC [149] (see Chapter 3), and methods based on radial basis functions [44]). Therefore, the effectiveness of the proposed approach relies on the capability to obtain accurate in-plane results with only one element through the thickness and on the possibility to compute accurate stresses and stress derivatives from the obtained displacement field, thanks to the higher-order continuity properties of the in-plane IgA shape functions.

The structure of this chapter is as follows. In Section 4.1, we focus on CLPT basics, considering Kirchhoff plates under bending with *multiple specially orthotropic layers*. The proposed numerical IgA formulations for laminated composite plates are presented in Section 4.2. Displacement-based ESL modeling strategies do not allow for an immediate assessment of the out-of-plane stress distributions, which can be recovered using an equilibrium-based post-processing technique, as detailed in Section 4.3. In Section 4.4, several numerical benchmarks are considered, showing the ability of the proposed approach to obtain accurate in-plane and out-of-plane stress states. Furthermore, we test the behavior of different meshes for increasing length-to-thickness ratios and numbers of layers to show the effectiveness of the method. We also investigate the behavior of our approach at the plate boundary, where stress concentrations might occur in laminates due to different material distributions in each ply. Finally, conclusions are drawn in Section 4.5.

4.1   Kirchhoff laminated plates

In this section we focus on plates with multiple specially orthotropic layers, i.e., laminates characterized by multiple plies for which the bending-stretching coupling coefficients and bending-twisting contributions are zero. This leads to a great simplification of the analysis because the bending deformation is uncoupled from the extensional deformation [159]. Therefore, focusing on the bending case, we acknowledge that the proposed approach is rigorous only for plates characterized by symmetric ply stacking sequences, as the coupling phenomenon between bending and stretching is in general not negligible for layer arrangements that are non-symmetric about the mid-plane. Nevertheless, we will numerically prove in Section 4.4 that the presented technique is able to provide reasonable approximations to more complex laminates, such as *antisymmetric cross-ply laminates*, which are composite plates characterized by an even number of layers of equal thickness and the same material properties with alternating 0° and 90° fiber orientations.

Under these premises, we recall that the bending case according to the CLPT is based on the following displacement field

$$u_1(x_1, x_2, x_3) = -x_3 w_{,1}\,, \tag{4.1a}$$

$$u_2(x_1, x_2, x_3) = -x_3 w_{,2}\,, \tag{4.1b}$$

$$u_3(x_1, x_2) = w\,, \tag{4.1c}$$

where (u_1, u_2, u_3) are the displacement components along the cartesian coordinate directions (x_1, x_2, x_3) of a point belonging to the plate mid-plane (for which x_3 is the out-of-plane coordinate) and w is the *transverse deflection*. The displacement field (4.1) implies that straight fibers, normal to the $x_1 x_2$-plane before deformation, remain straight and normal to the mid-surface after deformation. In the Equation (4.1) and hereinafter we adopt the convention that the portion of a subscript prior to a comma indicates components, while the portion after the comma refers to partial derivatives; for example, $\sigma_{12,13} = \dfrac{\partial^2 \sigma_{12}}{\partial x_1 \partial x_3}$. We further assume small deformations and small strains.

4.1.1 Constitutive relations

Assuming the displacement field (4.1), the Kirchhoff plate model neglects both transverse shears and transverse normal effects, while the non-zero corresponding strains ε_{11}, ε_{22}, and ε_{12} cause σ_{11}, σ_{22}, and σ_{12} stresses.

Hereinafter, Einstein's notation on repeated indices is used, as well as the convention for which indices in Latin letters take values {1,2,3} whereas indices in Greek letters take values {1,2}. Accordingly, in-plane strains are defined as

$$\varepsilon_{\gamma\delta} = -x_3 w_{,\gamma\delta} = -x_3 \kappa_{\gamma\delta} \,, \tag{4.2}$$

where $\kappa_{\gamma\delta} = w_{,\gamma\delta}$ are the *curvatures* of the deflected mid-surface and the stress-strain relations for a linear elastic Kirchhoff plate are given by

$$\sigma_{\alpha\beta} = \mathbb{C}_{\alpha\beta\gamma\delta}\varepsilon_{\gamma\delta} \,. \tag{4.3}$$

In Chapter 1, we have introduced laminated composite plates as structures made of variously oriented orthotropic elastic plies. For the sake of simplicity, but without loss of generality, we focus here on specially orthotropic layers, for which the principal material coordinates coincide with those of the plate. Therefore, the number of elastic coefficients of the fourth order elasticity tensor $\mathbb{C}_{ijkl}$ reduces to nine, which, in Voigt's notation, can be expressed in terms of engineering constants as in Equation (3.4). We remark that the orthotropic elasticity tensor $\mathbb{C}$ is not necessarily constant for each ply. Therefore, with $\mathbb{C}(x_3)$ we denote its through-the-thickness dependency, which is a key aspect in the description of quantities referred to the plate mid-plane.

We introduce the bending moments M_{11}, M_{22}, and M_{12} which are stress resultants with the dimension of moments per unit length

$$M_{\alpha\beta} = \int_{-t/2}^{t/2} x_3 \sigma_{\alpha\beta} \mathrm{d}x_3 \,, \tag{4.4}$$

and, substituting Equation (4.2) into (4.3), we combine the obtained expressions with the bending moment relations (4.4) obtaining

$$M_{\alpha\beta} = -\int_{-t/2}^{t/2} x_3^2 \mathbb{C}_{\alpha\beta\gamma\delta}(x_3)\kappa_{\gamma\delta}\mathrm{d}x_3 \,, \tag{4.5}$$

where t is the total plate thickness.

Finally, recalling that $\kappa_{\gamma\delta}$ does not depend on the out-of-plane coordinate, we can rewrite (4.5) as

$$M_{\alpha\beta} = -\mathbb{D}_{\alpha\beta\gamma\delta}\kappa_{\gamma\delta} \,, \tag{4.6}$$

where $\mathbb{D}_{\alpha\beta\gamma\delta}$ is the bending material stiffness, defined as

$$\mathbb{D}_{\alpha\beta\gamma\delta} = \int_{-t/2}^{t/2} x_3^2 \mathbb{C}_{\alpha\beta\gamma\delta}(x_3)\mathrm{d}x_3 \,. \tag{4.7}$$

4.1.2 Boundary-value problem

The boundary-value problem associated with an elastic Kirchhoff plate under bending can be formulated as follows. Let Ω be an open subset of $\mathbb{R}^2$, subjected to a transversal load $q : \Omega \mapsto \mathbb{R}$ (i.e., normal to the plate mid-plane). We assume that Ω has a sufficiently smooth boundary Γ with a well-defined normal $\boldsymbol{n}$. Γ can be decomposed as $\Gamma = \overline{\Gamma_w \cup \Gamma_Q}$ and $\Gamma = \overline{\Gamma_\varphi \cup \Gamma_M}$ with $\Gamma_w \neq \varnothing$ and $\Gamma_w \cap \Gamma_Q = \varnothing$, $\Gamma_\varphi \cap \Gamma_M = \varnothing$. Given the distributed load q, and the boundary condition functions $w_\Gamma : \Gamma_w \mapsto \mathbb{R}$, $\varphi_\Gamma : \Gamma_\varphi \mapsto \mathbb{R}$, $Q_\Gamma : \Gamma_Q \mapsto \mathbb{R}$, $M_\Gamma : \Gamma_M \mapsto \mathbb{R}$, we look for the transverse deflection $w : \Omega \mapsto \mathbb{R}$ such that

$$
\begin{aligned}
M_{\alpha\beta,\alpha\beta} &= q & &\text{in} \quad \Omega, & (4.8\text{a})\\
M_{\alpha\beta} &= -\mathbb{D}_{\alpha\beta\gamma\delta}(x_3)\kappa_{\gamma\delta} = -\mathbb{D}_{\alpha\beta\gamma\delta}(x_3)w_{,\gamma\delta} & &\text{in} \quad \Omega, & (4.8\text{b})\\
w &= w_\Gamma & &\text{on} \quad \Gamma_w, & (4.8\text{c})\\
w_{,\alpha}n_\alpha &= \varphi_\Gamma & &\text{on} \quad \Gamma_\varphi, & (4.8\text{d})\\
(M_{\alpha\beta,\beta} + M_{\alpha\delta,\delta})n_\alpha &= Q_\Gamma \quad\text{with}\quad \delta \neq \alpha & &\text{on} \quad \Gamma_Q, & (4.8\text{e})\\
n_\alpha M_{\alpha\beta} n_\beta &= M_\Gamma & &\text{on} \quad \Gamma_M, & (4.8\text{f})
\end{aligned}
$$

where w_Γ, φ_Γ, and M_Γ represent, respectively, the prescribed normal out-of-plane displacement, rotation, and moment. Instead, Q_Γ stands for the normal component of the so-called *effective shear* (see [75, 157, 188]), classically defined by the combination of the effect of the transverse shear forces (i.e., $M_{\alpha\beta,\beta}n_\alpha$) and shear forces emanating from the twisting moments (i.e., $M_{\alpha\delta,\delta}n_\alpha$) on the boundary.

4.1.3 Weak form

In a variational approach, the governing equations are obtained with the principle of virtual displacements. A given mechanical system can take many possible configurations in accordance with its geometric constraints. Of all the admissible configurations (i.e., the set of configurations that satisfy the geometric constraints), only one also satisfies equilibrium. These configurations can be regarded as infinitesimal variations, during which the compatibility constraints of the system are not violated. Such variations are called virtual displacements and do not have any relation to the actual displacements that might occur due to a change in the applied loads [159]. Thus, for a plate occupying a region $\Omega \subset \mathbb{R}^2$ and subjected to pure bending, the only contribution to the internal virtual work (in the primal field virtual transverse displacement, δw) is given by the in-plane bending moments, $M_{\alpha\beta}$, and their relative virtual work conjugate curvatures, $\delta\kappa_{\alpha\beta}$, as

$$
\delta W_{int}[\delta w] = \int_\Omega M_{\alpha\beta}\delta\kappa_{\alpha\beta}\mathrm{d}\Omega. \tag{4.9}
$$

The external virtual work is given instead by the sum of three components [75]. These are respectively due to applied transverse loads, $\delta W_{ext,q}$, applied edge moments and transverse shears, $\delta W_{ext,B}$, and to corner loads, $\delta W_{ext,C}$, i.e.,

$$
\delta W_{ext}[\delta w] = \delta W_{ext,q}[\delta w] + \delta W_{ext,B}[\delta w] + \delta W_{ext,C}[\delta w]. \tag{4.10}
$$

The first two terms read

$$\delta W_{ext,q}[\delta w] = \int_{\Omega} q\,\delta w\,\mathrm{d}\Omega\,, \tag{4.11}$$

and

$$\delta W_{ext,B}[\delta w] = \int_{\Gamma} (Q_{\Gamma}\delta w_{\Gamma} + M_{\Gamma}\delta\phi_{\Gamma})\mathrm{d}\Gamma\,. \tag{4.12}$$

Finally, if the plate has n_c corners at which the displacement w_j, with $j = 1, 2, ..., n_c$, is not prescribed, the term $\delta W_{ext,C}$ comes into play considering the so-called *corner forces*, i.e., jumps in the corresponding twisting moments. For the sake of simplicity, in this work we assume that the transverse displacement of a corner is always prescribed, which grants that the contribution of that corner to the external virtual work vanishes because its corresponding displacement variation is zero. This assumption does not constitute any limitation to the purpose of the present work.

4.2 Numerical formulations

In this section we detail the numerical IgA formulations to approximate the problem variables and thus the equations governing the laminated Kirchhoff plate.

4.2.1 Homogenized constitutive relations

To capture the laminated composite through-the-thickness behavior, we need to account for the proper material distribution layer by layer even though the Kirchhoff theory assumes that a mid-surface plane can be used to represent the three-dimensional solid plate in a two-dimensional form. In order to include the complete ply stacking sequence contribution, we consider the required 3D material tensor (3.4) components for each k-th layer and, to create an equivalent single bivariate plate, we homogenize the material properties according to [171] by means of the following relations

$$\overline{\mathbb{C}}_{ab} = \sum_{k=1}^{N} \bar{t}_k \mathbb{C}_{ab}^{(k)} + \sum_{k=2}^{N} (\mathbb{C}_{a3}^{(k)} - \overline{\mathbb{C}}_{a3})\bar{t}_k \frac{(\mathbb{C}_{b3}^{(1)} - \mathbb{C}_{b3}^{(k)})}{\mathbb{C}_{33}^{(k)}} \qquad a, b = 1, 2\,, \tag{4.13a}$$

$$\overline{\mathbb{C}}_{66} = \sum_{k=1}^{N} \bar{t}_k \mathbb{C}_{66}^{(k)}\,, \tag{4.13b}$$

where N is the number of layers, $\bar{t}_k = \dfrac{t_k}{t}$ represents the volume fraction of the k-th lamina, t being the total plate thickness, and t_k the k-th ply thickness.

At this point $\overline{\mathbb{C}}$ [1] is independent of the x_3 coordinate and we can recover the homogenized bending material stiffness [2] from Equation (4.7) as

$$\overline{\mathbb{D}} = \begin{pmatrix} \overline{\mathbb{D}}_{11} & \overline{\mathbb{D}}_{12} & 0 \\ & \overline{\mathbb{D}}_{22} & 0 \\ \text{symm.} & & \overline{\mathbb{D}}_{66} \end{pmatrix} = \frac{t^3}{12} \begin{pmatrix} \overline{\mathbb{C}}_{11} & \overline{\mathbb{C}}_{12} & 0 \\ & \overline{\mathbb{C}}_{22} & 0 \\ \text{symm.} & & \overline{\mathbb{C}}_{66} \end{pmatrix}. \qquad (4.14)$$

4.2.2 Isogeometric collocation method

Having defined $\boldsymbol{\tau}$ as the matrix of collocation points (see Equation (2.46)), such that each i-th entry is $\tau_i^d = \frac{\sum_{l=1}^{p_d} \xi_{i+l}}{p_d}$, with $d = 1, 2$ and $i = 1, ..., m_d$, we approximate the displacement field w as a linear combination of bivariate shape functions $B_{\mathbf{i},\mathbf{p}}(\boldsymbol{\xi})$ and control variables $\hat{\mathbf{w}}_{\mathbf{i}}$ as

$$\mathbf{w}(\boldsymbol{\tau}) = \sum_{\mathbf{i}} B_{\mathbf{i},\mathbf{p}}(\boldsymbol{\tau}) \hat{\mathbf{w}}_{\mathbf{i}}. \qquad (4.15)$$

Following [157], without loss of generality, we describe our collocation strategy for the case of a simply supported plate, that is, $\Gamma_w = \Gamma_M = \Gamma$.

In Voigt's notation, we can rewrite Equation (4.6) as

$$\mathbf{M} = -\overline{\mathbb{D}}\boldsymbol{\kappa}, \qquad (4.16)$$

where the bending moment vector is equal to

$$\mathbf{M} = \begin{bmatrix} M_{11} & M_{22} & M_{12} \end{bmatrix}^{\mathrm{T}} \qquad (4.17)$$

and the curvature vector $\boldsymbol{\kappa}$ is defined as

$$\boldsymbol{\kappa} = \begin{bmatrix} \kappa_{11} & \kappa_{22} & 2\kappa_{12} \end{bmatrix}^{\mathrm{T}} = \begin{bmatrix} w_{,11} & w_{,22} & 2w_{,12} \end{bmatrix}^{\mathrm{T}}. \qquad (4.18)$$

We then insert the approximate displacements (4.15) into the bending moment Equations (4.16) and we further substitute the result into equilibrium Equations (4.8a), obtaining

$$- \mathbf{K}(\boldsymbol{\tau})\hat{\mathbf{w}}_{\mathbf{i}} = \mathbf{q}(\boldsymbol{\tau}) \qquad \forall \tau_i^d \in \Omega, \qquad (4.19)$$

where $\mathbf{K}(\boldsymbol{\tau})$ can be expressed as

$$\mathbf{K}(\boldsymbol{\tau}) = \overline{\mathbb{D}}_{11} \frac{\partial^4 B_{\mathbf{i},\mathbf{p}}(\boldsymbol{\tau})}{\partial x_1{}^4} + 2\left(\overline{\mathbb{D}}_{12} + 2\overline{\mathbb{D}}_{66}\right) \frac{\partial^4 B_{\mathbf{i},\mathbf{p}}(\boldsymbol{\tau})}{\partial x_1{}^2 \partial x_2{}^2} + \overline{\mathbb{D}}_{22} \frac{\partial^4 B_{\mathbf{i},\mathbf{p}}(\boldsymbol{\tau})}{\partial x_2{}^4}, \qquad (4.20)$$

while, substituting in (4.8f), we obtain instead

$$- \tilde{\mathbf{K}}(\boldsymbol{\tau})\hat{\mathbf{w}}_{\mathbf{i}} = \mathbf{M}_\Gamma(\boldsymbol{\tau}) \qquad \forall \tau_i^d \in \Gamma_M, \qquad (4.21)$$

---

[1]We note that in order to obtain $\overline{\mathbb{C}}$ the out-of-plane shear moduli are not considered in accordance with the homogenization rule in [171] adapted for a bivariate case.

[2]We would like to underline that all the presented numerical strategies and results in this chapter refer to the obtained homogenized bending material stiffness $\overline{\mathbb{D}}$.

with $\tilde{\mathbf{K}}(\boldsymbol{\tau})$ having the following form

$$\tilde{\mathbf{K}}(\boldsymbol{\tau}) = \overline{\mathbb{D}}_{11}\frac{\partial^2 B_{\mathbf{i},\mathbf{p}}(\boldsymbol{\tau})}{\partial x_1{}^2}n_1^2 + \overline{\mathbb{D}}_{12}\left(\frac{\partial^2 B_{\mathbf{i},\mathbf{p}}(\boldsymbol{\tau})}{\partial x_2{}^2}n_1^2 + \frac{\partial^2 B_{\mathbf{i},\mathbf{p}}(\boldsymbol{\tau})}{\partial x_1{}^2}n_2^2\right)$$
$$+ \overline{\mathbb{D}}_{22}\frac{\partial^2 B_{\mathbf{i},\mathbf{p}}(\boldsymbol{\tau})}{\partial x_2{}^2}n_2^2 + 4\overline{\mathbb{D}}_{66}\frac{\partial^2 B_{\mathbf{i},\mathbf{p}}(\boldsymbol{\tau})}{\partial x_1\partial x_2}n_1 n_2 .$$

(4.22)

Regarding the imposition of boundary conditions, the strategy is exactly the same as thoroughly discussed by Reali and Gomez for an isotropic plate, and we therefore refer interested readers to [157] for further details.

4.2.3 Isogeometric Galerkin method

For an IgG approach, the variation of the energy functional in a system can be regarded as the sum of all its element-wise variations, thus

$$\delta W_{int} = \sum_e^{N_e} \delta W_{int}^{(e)},$$

(4.23)

$$\delta W_{ext} = \sum_e^{N_e} \delta W_{ext}^{(e)},$$

(4.24)

where N_e denotes the number of elements in the plate domain and the superscript (e) is the element index. Then, approximating the displacement fields as a linear combination of bivariate shape functions and control variables as

$$w^{(e)}(\bar{\boldsymbol{\xi}}) = B_{\mathbf{i},\mathbf{p}}^{(e)}(\bar{\boldsymbol{\xi}})\hat{\mathbf{w}}_{\mathbf{i}}^{(e)},$$

(4.25a)

$$\delta w^{(e)}(\bar{\boldsymbol{\xi}}) = B_{\mathbf{i},\mathbf{p}}^{(e)}(\bar{\boldsymbol{\xi}})\delta\hat{\mathbf{w}}_{\mathbf{i}}^{(e)},$$

(4.25b)

we substitute (4.25) into (4.23) obtaining the approximate element internal energy variation

$$\delta W_{int}^{(e)} = (\delta\hat{\mathbf{w}}_{\mathbf{i}}^{(e)})^{\mathrm{T}}\int_{\Omega_e}(\mathbb{B}_{\mathbf{i},\mathbf{p}}^{(e)})^{\mathrm{T}}\,\overline{\mathbb{D}}\,\mathbb{B}_{\mathbf{j},\mathbf{p}}^{(e)}\,\mathrm{d}\Omega_e\,\hat{\mathbf{w}}_{\mathbf{j}}^{(e)} \approx (\delta\hat{\mathbf{w}}_{\mathbf{i}}^{(e)})^{\mathrm{T}}\mathbb{K}_{\mathbf{ij}}^{(e)}\hat{\mathbf{w}}_{\mathbf{j}}^{(e)},$$

(4.26)

where $\mathbb{K}_{\mathbf{ij}}^{(e)}$ is the **ij**-th contribution of the element stiffness matrix computed by approximating the integral with a quadrature rule. In this work, we consider standard Gauss integration. In Equation (4.26), $\mathbb{B}_{\mathbf{i},\mathbf{p}}^{(e)}$ is defined as

$$\mathbb{B}_{\mathbf{i},\mathbf{p}}^{(e)} = \begin{bmatrix} \dfrac{\partial^2 B_{\mathbf{i},\mathbf{p}}^{(e)}(\bar{\boldsymbol{\xi}})}{\partial x_1{}^2} \\[2mm] \dfrac{\partial^2 B_{\mathbf{i},\mathbf{p}}^{(e)}(\bar{\boldsymbol{\xi}})}{\partial x_2{}^2} \\[2mm] 2\dfrac{\partial^2 B_{\mathbf{i},\mathbf{p}}^{(e)}(\bar{\boldsymbol{\xi}})}{\partial x_1\partial x_2} \end{bmatrix},$$

(4.27)

where $\bar{\boldsymbol{\xi}}$ is the matrix of the quadrature point positions.

4.3 Stress recovery procedure

Since Kirchhoff theory is intrinsically two-dimensional, assessments of out-of-plane stress distributions are not immediately possible. Thus, the strategies proposed in Sections 4.2.2 and 4.2.3 are not suitable by themselves for the calculation of interlaminar stresses. However, these strategies can be easily coupled with an *a posteriori* step based on equilibrium to recover the out-of-plane stresses, following the approach in Chapter 3 and references [62, 149]. We remark that this stress recovery already proved to allow a rigorous layer-by-layer reconstruction of out-of-plane stresses for laminated solid plates in the context of both IgG [62] and IgC (see Chapter 3 and reference [149]).

As in Chapter 3, the starting point is the fact that stresses must satisfy the equilibrium equations

$$\nabla \cdot \sigma + b = 0 \tag{4.28}$$

at every point, where $\nabla \cdot$ represents the divergence operator. Equilibrium equations (4.28) can be expressed componentwise as in Equation (3.10). Integrating Equations (3.10a) and (3.10b) along the thickness, we can recover the out-of-plane shear stresses as Equations (3.11a) and (3.11b). In this chapter, all integrals along the plate thickness direction ζ are computed using a composite trapezoidal quadrature rule.

Once we substitute the appropriate derivatives of the out-of-plane shear stresses (3.11) into Equation (3.10c), integrating along the thickness, we can recover also σ_{33} as:

$$\sigma_{33}(x_3) = \int_{\bar{x}_3}^{x_3} \left[\int_{\bar{x}_3}^{\zeta} (\sigma_{11,11}(\xi) + \sigma_{22,22}(\xi) + 2\sigma_{12,12}(\xi) + b_{1,1}(\xi) + b_{2,2}(\xi)) d\xi \right] d\zeta$$
$$- \int_{\bar{x}_3}^{x_3} b_3(\zeta) d\zeta - (x_3 - \bar{x}_3)(\sigma_{13,1}(\bar{x}_3) + \sigma_{23,2}(\bar{x}_3)) + \sigma_{33}(\bar{x}_3),$$

$$\tag{4.29}$$

where the integral constants should be chosen to fulfill the boundary conditions at the top or bottom surfaces $\bar{x}_3$ [62].

The derivatives of the in-plane stress components that are necessary for the proposed post-processing step are computed as

$$\sigma_{\alpha\beta,\gamma} = \mathbb{C}_{\alpha\beta\zeta\eta}(x_3)(-x_3\kappa_{\zeta\eta,\gamma}) = \mathbb{C}_{\alpha\beta\zeta\eta}(x_3)(-x_3 w_{,\zeta\eta\gamma}), \tag{4.30a}$$

$$\sigma_{\alpha\beta,\gamma\delta} = \mathbb{C}_{\alpha\beta\zeta\eta}(x_3)(-x_3\kappa_{\zeta\eta,\gamma\delta}) = \mathbb{C}_{\alpha\beta\zeta\eta}(x_3)(-x_3 w_{,\zeta\eta\gamma\delta}). \tag{4.30b}$$

From Equations (4.30a) and (4.30b) it is clear that the proposed post-processing step requires the shape functions to be highly continuous (i.e., C^3-continuous), which can be easily achieved by means of IgA. In the following section, we show convincing numerical experiments proving that such a post-processing technique works nicely in the context of both IgG and IgC. We remark that these derivatives can be obtained even from a very coarse displacement solution.

In Figure 4.1, we present a flowchart that summarizes the proposed modeling approach for laminated composite Kirchhoff plates, from the computation of the displacement field (either obtained using the introduced IgG or IgC method) to the *a posteriori* out-of-plane stress recovery.
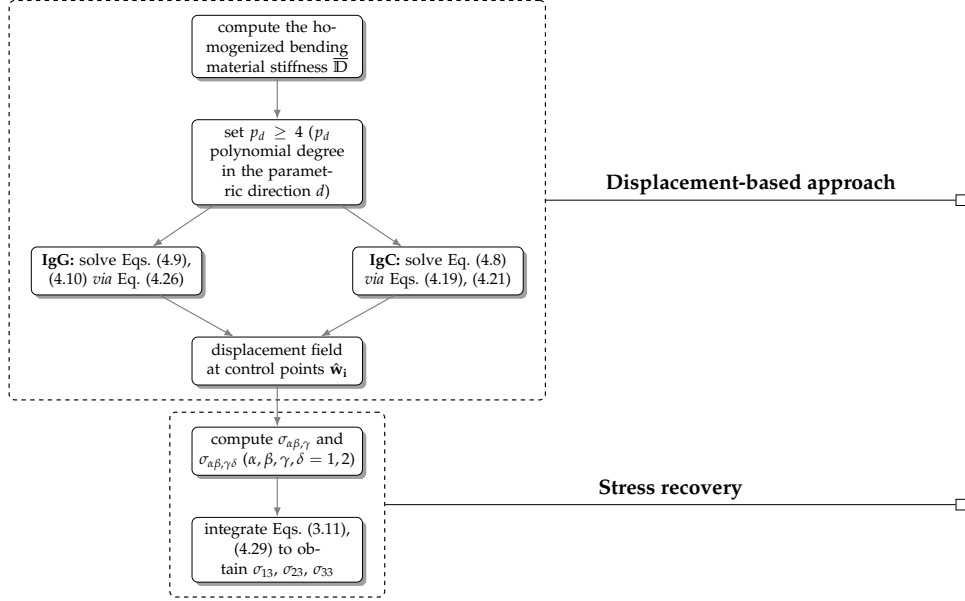
FIGURE 4.1: Two-step modeling approach for laminated composite Kirchhoff plates: from the computation of the displacement field (either obtained using the introduced IgG or IgC method) to the *a posteriori* out-of-plane stress recovery.

4.4 Numerical results

In this section, we present several examples for the static analysis of composite laminated Kirchhoff plates under bending. To this end, we first present a set of tests featuring rectangular laminate plates to validate our stress recovery method against Pagano's analytical solution [145], and hence showcase the accuracy of the proposed post-processing technique in reconstructing the out-of-plane stress field. We also assess the sensitivity of the method with respect to parameters of interest, namely the number of layers and the length-to-thickness ratio. Furthermore, we consider a more complex benchmark to showcase the effectiveness of the proposed technique in the case of non-trivial geometries.

4.4.1 The Pagano test case: benchmark adaptation to bivariate plates

The Pagano test case considers a solid cross-ply plate of total thickness t, made of N orthotropic layers (see Section 3.2.1 for further details). The structure is simply supported on all edges and subjected to a transverse sinusoidal loading $q(x_1, x_2)$, on the top surface, while the bottom one is traction-free. The thickness of every single layer is set to 1 mm, and the edge length, L, is chosen to be S times larger than the total thickness of the laminate. We approximate Pagano's solid benchmark with a bivariate plate as in Figure 4.2. The material parameters taken into account for all numerical tests are summarized in Table 4.1 for 0°-oriented plies, while we consider the same loading pressure $q(x_1, x_2)$ as in Equation 3.14c, now applied at the plate mid-plane.
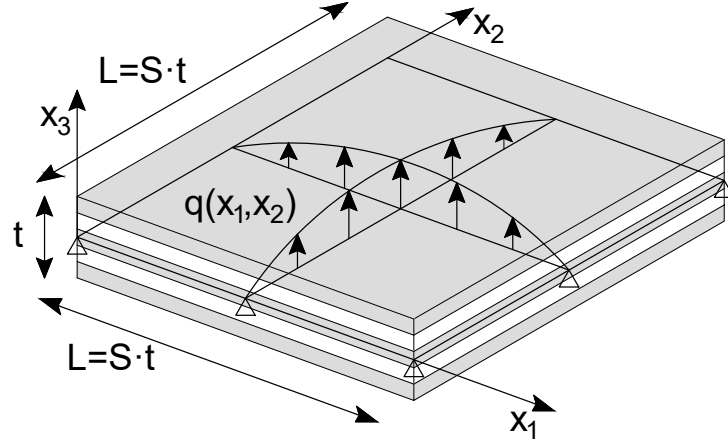
FIGURE 4.2: The Pagano test case [145]. Problem geometry.

TABLE 4.1: Adopted material properties for 0°-oriented layers.

E_1	E_2	E_3	G_{23}	G_{13}	G_{12}	ν_{23}	ν_{13}	ν_{12}
[GPa]	[GPa]	[GPa]	[GPa]	[GPa]	[GPa]	[-]	[-]	[-]
25000	1000	1000	200	500	500	0.25	0.25	0.25

With reference to Equations (4.8f) and (4.8c), the simply-supported edge conditions are taken as

$$M_\Gamma = 0 \quad \text{and} \quad w_\Gamma = 0 \quad \text{on} \quad \Gamma_w = \Gamma_M = \Gamma. \tag{4.31}$$

We remark that the boundary condition $M_\Gamma = 0$ is strongly imposed for IgC, while it is naturally satisfied in IgG.

Finally, all results reported in this chapter are expressed in terms of normalized stress components as

$$\bar{\sigma}_{ij} = \frac{\sigma_{ij}}{\sigma_0 S^2} \qquad i, j = 1, 2, \tag{4.32a}$$

$$\bar{\sigma}_{i3} = \frac{\sigma_{i3}}{\sigma_0 S} \qquad i = 1, 2, \tag{4.32b}$$

$$\bar{\sigma}_{33} = \frac{\sigma_{33}}{\sigma_0}. \tag{4.32c}$$

The interested reader is referred to Appendix 3.A for further details in the derivation of the analytical solution of the Pagano's problem considered herein.

4.4.1.1 Validation of the stress recovery method

We present and comment several numerical examples considering a cross-ply distribution of layers, namely a 90°/0° stacking sequence from the bottom to the top of the plate. All numerical simulations are carried out using an in-plane degree of approximation $p = q = 6$, which fulfills the continuity requirements described in Section 4.3, and a very coarse grid comprising of 7x7 control points, or equivalently DOFs, which corresponds to only one element (which has been verified to grant good results for this problem, see Section 3.2.3).

As an example, in Figure 4.3 we present the solution profiles of the in-plane stresses for a sampling point located at $x_1 = x_2 = L/4$ and computed with both approaches described in Section 4.2.2 and 4.2.3. We observe that the recovered stresses prove to be accurate even for a rather small length-to-thickness plate ratio ($S = 20$).

For the same sampling point and plate geometry, in Figure 4.4 we readily reconstruct an accurate out-of-plane stress state by applying the post-processing steps based on equilibrium presented in Section 4.3. We highlight that this procedure can be regarded as inexpensive in comparison to a full 3D analysis and can be performed pointwise only at locations of interest. We remark that using the CLPT to rigorously model non-symmetric cross-ply laminates, we would need to account for bending-stretching contributions. However, for these type of laminates the bending-stretching coefficient matrix is not full and, in addition, the coupling effect decreases as the number of layers is increased [159, 192]. Also, the presented numerical results are compared to Pagano's analytical solution, which is sufficiently general to describe the exact elastic response of rectangular, simply-supported laminates consisting of any number of orthotropic layers [145]. Therefore, we can regard these bending-stretching coupling effects to be negligible and assume the proposed modeling approach to be an effective tool in understanding the behavior of non-symmetric cross-ply laminates.

Remark 4.1. *In Chapter 3 and reference [149], we combined IgC and the presented equilibrium-based stress recovery procedure with a homogenized through-the-thickness single-element approach to describe the structural response of solid laminates. However, this strategy is only applicable for symmetric cross-ply distributions, as in non-symmetric cases the plate mid-plane would not be balanced. Conversely, homogenizing the material properties and using the CLPT together with IgC and the proposed post-processing technique, we are able to accurately capture the behavior of both symmetric and non-symmetric cross-ply laminated plates (despite neglecting bending-stretching coupling effects), and hence directly reconstruct the out-of-plane stresses from 2D displacement-based computations.*

In Figures 4.5-4.10, the out-of-plane stress state profile is recovered sampling the composite plate every quarter of length in both in-plane directions, to show the post-processing effect at different locations of the plate for both a symmetric and a non-symmetric ply distribution of 11 and 34 layers, respectively (see Remark 4.1). Across all sampled points, the proposed approach accurately captures the 3D stresses in every single layer when compared to Pagano's solution. Also, the model remains accurate at the boundaries, where solution inaccuracy is typically expected [136], and satisfies the traction-free conditions for transverse shear stresses at the top and bottom surfaces of the laminate.
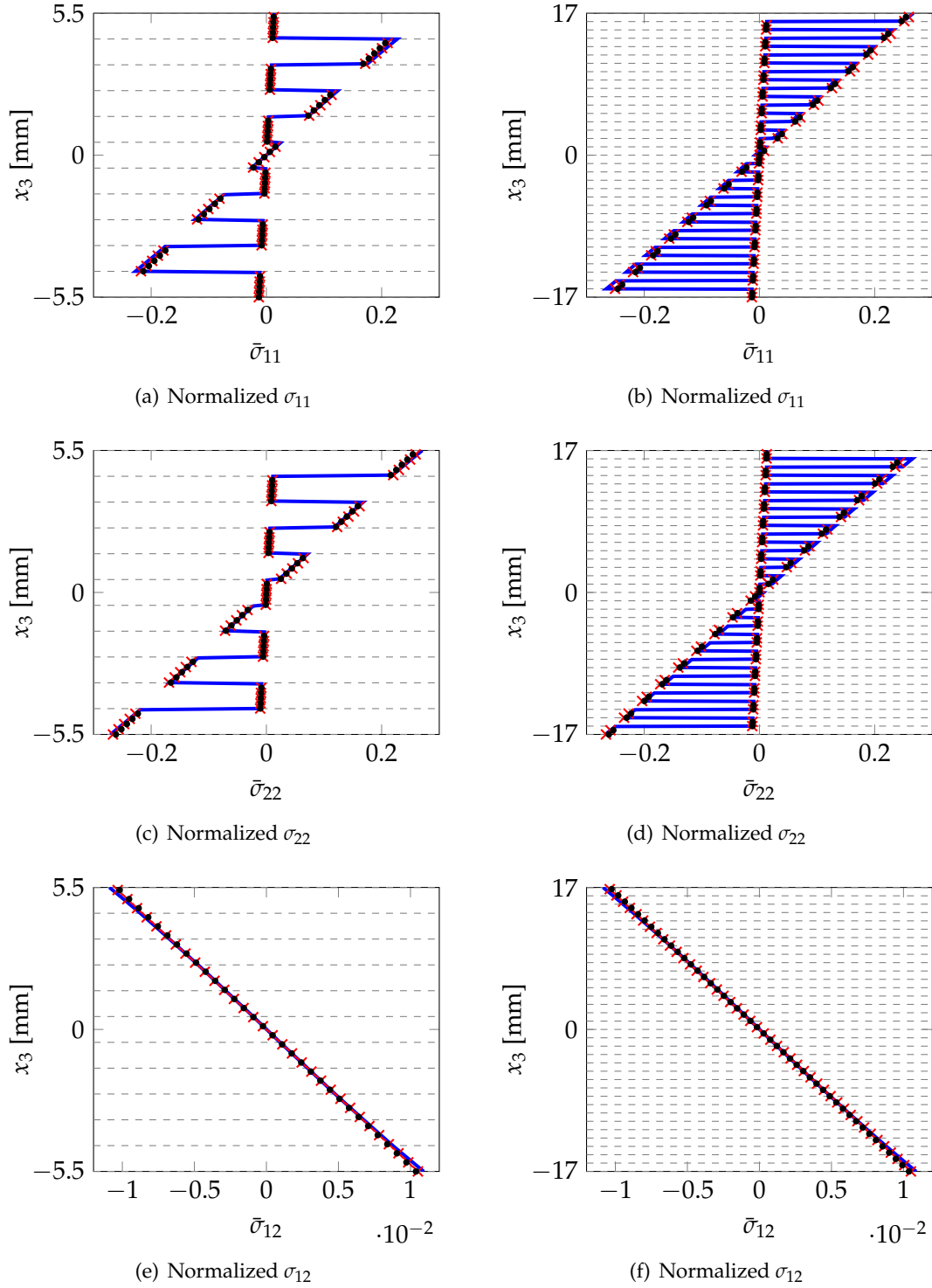
FIGURE 4.3: Through-the-thickness in-plane stress solution for the Pagano's problem [145] evaluated at $x_1 = x_2 = L/4$. Plate cases with length-to-thickness ratio $S = 20$: Left column - 11 layers, i.e., $L = St = 220$ mm; Right column - 34 layers, i.e., $L = St = 680$ mm (——— Pagano's analytical solution *versus* post-processed numerical solutions obtained with degree of approximation $p = q = 6$ and 7x7 control points corresponding to 1 in-plane element: × IgG, • IgC).
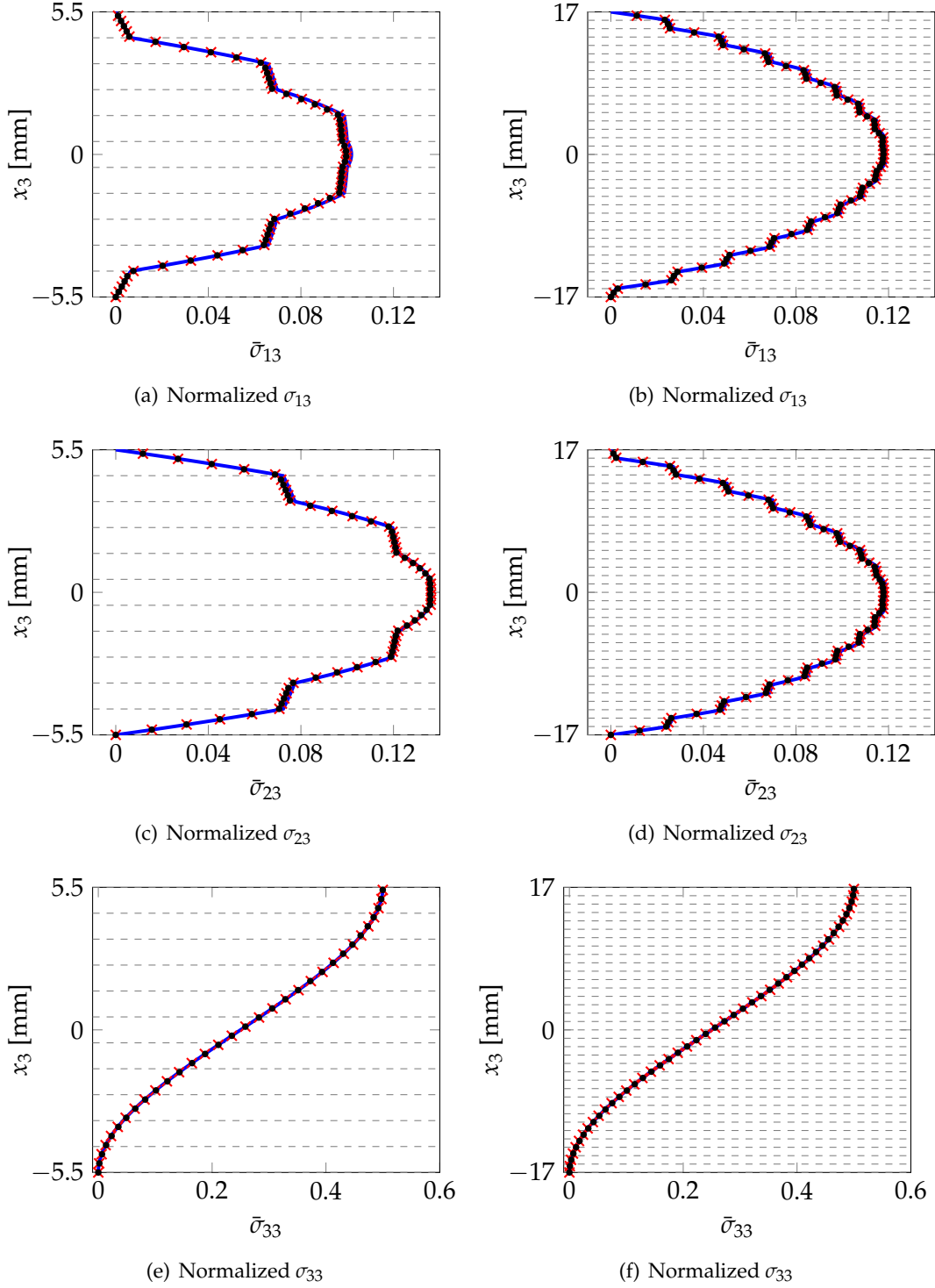
FIGURE 4.4: Through-the-thickness recovered out-of-plane stress solution for the Pagano's problem [145] evaluated at $x_1 = x_2 = L/4$. Plate cases with length-to-thickness ratio $S = 20$: Left column - 11 layers, i.e., $L = St = 220$ mm; Right column - 34 layers, i.e., $L = St = 680$ mm (—— Pagano's analytical solution *versus* post-processed numerical solutions obtained with degree of approximation $p = q = 6$ and 7x7 control points corresponding to 1 in-plane element: ×IgG, •IgC).
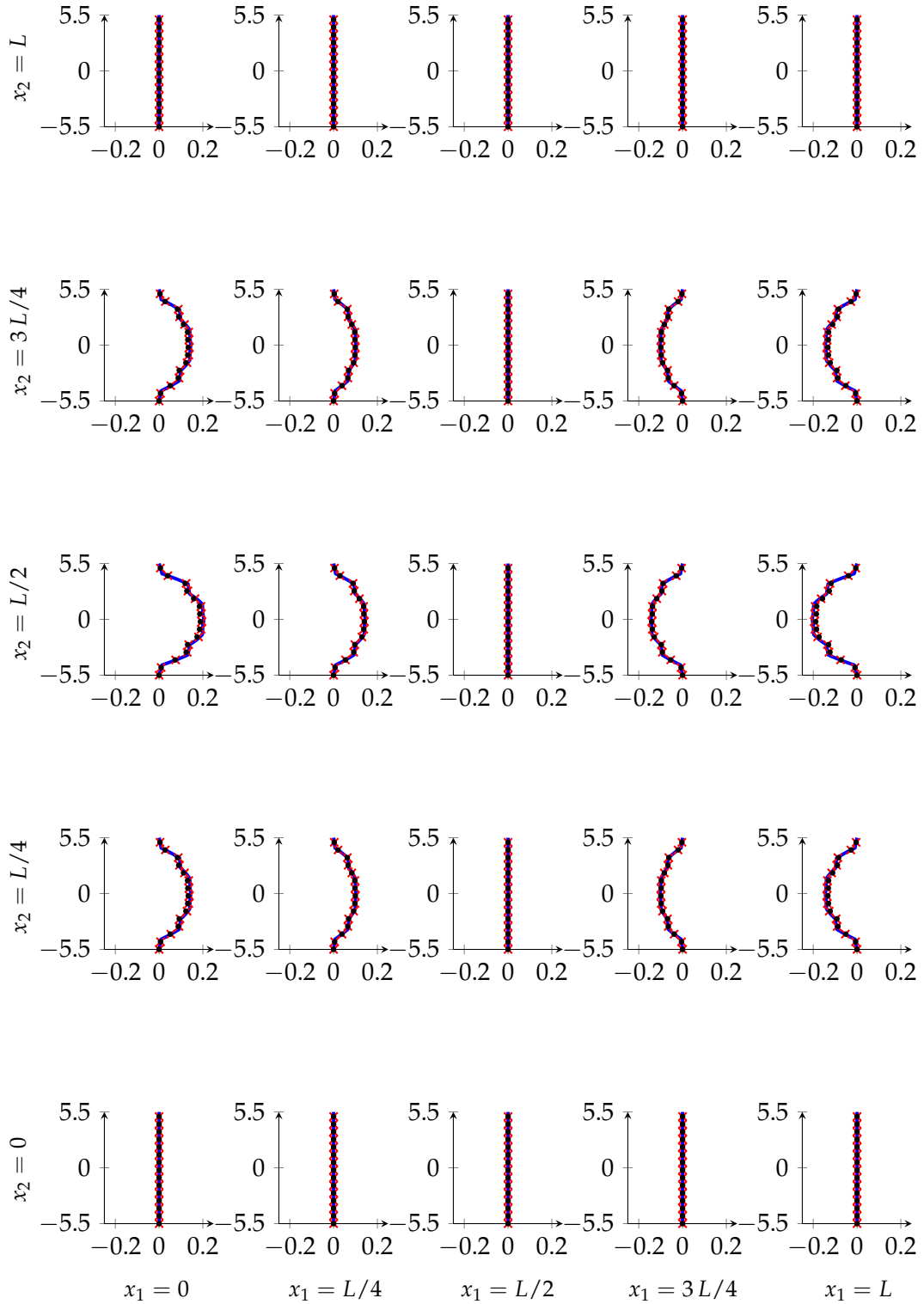
FIGURE 4.5: Through-the-thickness out-of-plane $\bar{\sigma}_{13}$ profiles for the 11-layer case for in-plane sampling points situated at every quarter of length in both in-plane directions x_1 and x_2. For each subplot, the horizontal axis shows the values of $\bar{\sigma}_{13}$ and the vertical axis the through-the-thickness coordinate x_3. L represents the total length of the plate, which for this case is $L = 220$ mm ($L = St$ with $t = 11$ mm and $S = 20$), while the number of layers is 11 (⸺ Pagano's analytical solution [145] *versus* recovered numerical solutions obtained with degree of approximation $p = q = 6$ and 7x7 control points corresponding to 1 in-plane element: × IgG, • IgC).

FIGURE 4.6: Through-the-thickness out-of-plane $\bar{\sigma}_{23}$ profiles for the 11-layer case for in-plane sampling points situated at every quarter of length in both in-plane directions x_1 and x_2. For each subplot, the horizontal axis shows the values of $\bar{\sigma}_{23}$ and the vertical axis the through-the-thickness coordinate x_3. L represents the total length of the plate, which for this case is $L = 220\,\text{mm}$ ($L = St$ with $t = 11\,\text{mm}$ and $S = 20$), while the number of layers is 11 (——— Pagano's analytical solution [145] *versus* recovered numerical solutions obtained with degree of approximation $p = q = 6$ and 7x7 control points corresponding to 1 in-plane element: × IgG, • IgC).

FIGURE 4.7: Through-the-thickness out-of-plane $\bar{\sigma}_{33}$ profiles for the 11-layer case for in-plane sampling points situated at every quarter of length in both in-plane directions x_1 and x_2. For each subplot, the horizontal axis shows the values of $\bar{\sigma}_{33}$ and the vertical axis the through-the-thickness coordinate x_3. L represents the total length of the plate, which for this case is $L = 220$ mm ($L = St$ with $t = 11$ mm and $S = 20$), while the number of layers is 11 (——— Pagano's analytical solution [145] *versus* recovered numerical solutions obtained with degree of approximation $p = q = 6$ and 7x7 control points corresponding to 1 in-plane element: × IgG, • IgC).

FIGURE 4.8: Through-the-thickness out-of-plane $\bar{\sigma}_{13}$ profiles for the 34-layer case for in-plane sampling points situated at every quarter of length in both in-plane directions x_1 and x_2. For each subplot, the horizontal axis shows the values of $\bar{\sigma}_{13}$ and the vertical axis the through-the-thickness coordinate x_3. L represents the total length of the plate, which for this case is $L = 680\,\text{mm}$ ($L = St$ with $t = 34\,\text{mm}$ and $S = 20$), while the number of layers is 34 (—— Pagano's analytical solution [145] *versus* recovered numerical solutions obtained with degree of approximation $p = q = 6$ and 7x7 control points corresponding to 1 in-plane element: × IgG, • IgC).

FIGURE 4.9: Through-the-thickness out-of-plane $\bar{\sigma}_{23}$ profiles for the 34-layer case for in-plane sampling points situated at every quarter of length in both in-plane directions x_1 and x_2. For each subplot, the horizontal axis shows the values of $\bar{\sigma}_{23}$ and the vertical axis the through-the-thickness coordinate x_3. L represents the total length of the plate, which for this case is $L = 680\,\text{mm}$ ($L = St$ with $t = 34\,\text{mm}$ and $S = 20$), while the number of layers is 34 (—— Pagano's analytical solution [145] *versus* recovered numerical solutions obtained with degree of approximation $p = q = 6$ and 7x7 control points corresponding to 1 in-plane element: × IgG, • IgC).

FIGURE 4.10: Through-the-thickness out-of-plane $\bar{\sigma}_{33}$ profiles for the 34-layer case for in-plane sampling points situated at every quarter of length in both in-plane directions x_1 and x_2. For each subplot, the horizontal axis shows the values of $\bar{\sigma}_{33}$ and the vertical axis the through-the-thickness coordinate x_3. L represents the total length of the plate, which for this case is $L = 680$ mm ($L = St$ with $t = 34$ mm and $S = 20$), while the number of layers is 34 (—— Pagano's analytical solution [145] *versus* recovered numerical solutions obtained with degree of approximation $p = q = 6$ and 7x7 control points corresponding to 1 in-plane element: ×IgG, •IgC).

4.4.1.2 Parametric study on length-to-thickness ratio

In order to further investigate the proposed stress recovery approach, we perform a series of tests considering multiple length-to-thickness ratios (S = 20, 30, 40, and 50) for the plates with 11 and 34 layers and examining an increasing number of DOFs (namely 7, 14, and 21 per in-plane direction).

In Figure 4.11, we assess the performance of both IgG and IgC approaches coupled with the presented post-processing technique at $x_1 = x_2 = L/4$, adopting the following L^2 error definition

$$
\tilde{e}(\sigma_{i3}) = \sqrt{\frac{\int_{x_3} (\sigma_{i3}^{\text{analytic}}(\bar{x}_1, \bar{x}_2, x_3) - \sigma_{i3}^{\text{recovered}}(\bar{x}_1, \bar{x}_2, x_3))^2 \, dx_3}{\int_{x_3} (\sigma_{i3}^{\text{analytic}}(\bar{x}_1, \bar{x}_2, x_3))^2 \, dx_3}} \qquad i = 1, 2, 3 \, . \quad (4.33)
$$

Figure 4.11 shows that the post-processing approach seems to be particularly suitable for plates characterized by a significant number of layers. Moreover, we observe that the modeling error, given by the *a posteriori* step, dominates over the approximation error. Thus, further mesh refinement operations do not seem to provide a significant benefit for the considered numerical tests. We want to highlight, however, that errors are typically in the 1.5% range or lower in the simulation results shown in Figure 4.11.

We would like to remark that further tests have been carried out for a lower-degree displacement field approximation (i.e., $4 \leq p = q < 6$), which led to a less accurate out-of-plane stress reconstruction in particular for IgC. In our experience, adopting a degree of approximation equal to 6 seems to be a reasonable choice to correctly reproduce the complete 3D stress state for CLPT approximated either *via* IgG or IgC and combined with the equilibrium-based stress recovery. Also, using only one element of degree 6 to approximate the plate mid-plane (i.e., 7x7 control points) is sufficient to provide good results in the considered example, which is characterized by a simple geometry.

4.4.1.3 Behavior at the plate boundary

Interlaminar stresses in laminates subjected to transverse loadings may become important near the structure edges. For example, in the case of cross-ply laminates, out-of-plane stresses usually face weaker material strength properties according to the stacking sequence. This leads to stress concentrations in the proximity of material discontinuities, which may result, in premature failure of the structure due to delamination [136].

Thus, we further test the proposed post-processing technique at the plate boundary, studying both symmetric and non-symmetric cross-ply plate cases (i.e., stacking sequences made of 11 and 34 layers). To this end, we consider an increasing length-to-thickness ratio (i.e., S = 20, 30, 40, and 50) for fixed degrees of approximation $p = q = 6$ using 7x7 control points. We report in Tables 4.2-4.13 the pointwise out-of-plane stress relative difference at a fixed point ($\bar{x}_1, \bar{x}_2, \bar{x}_3$) in the plate domain, which
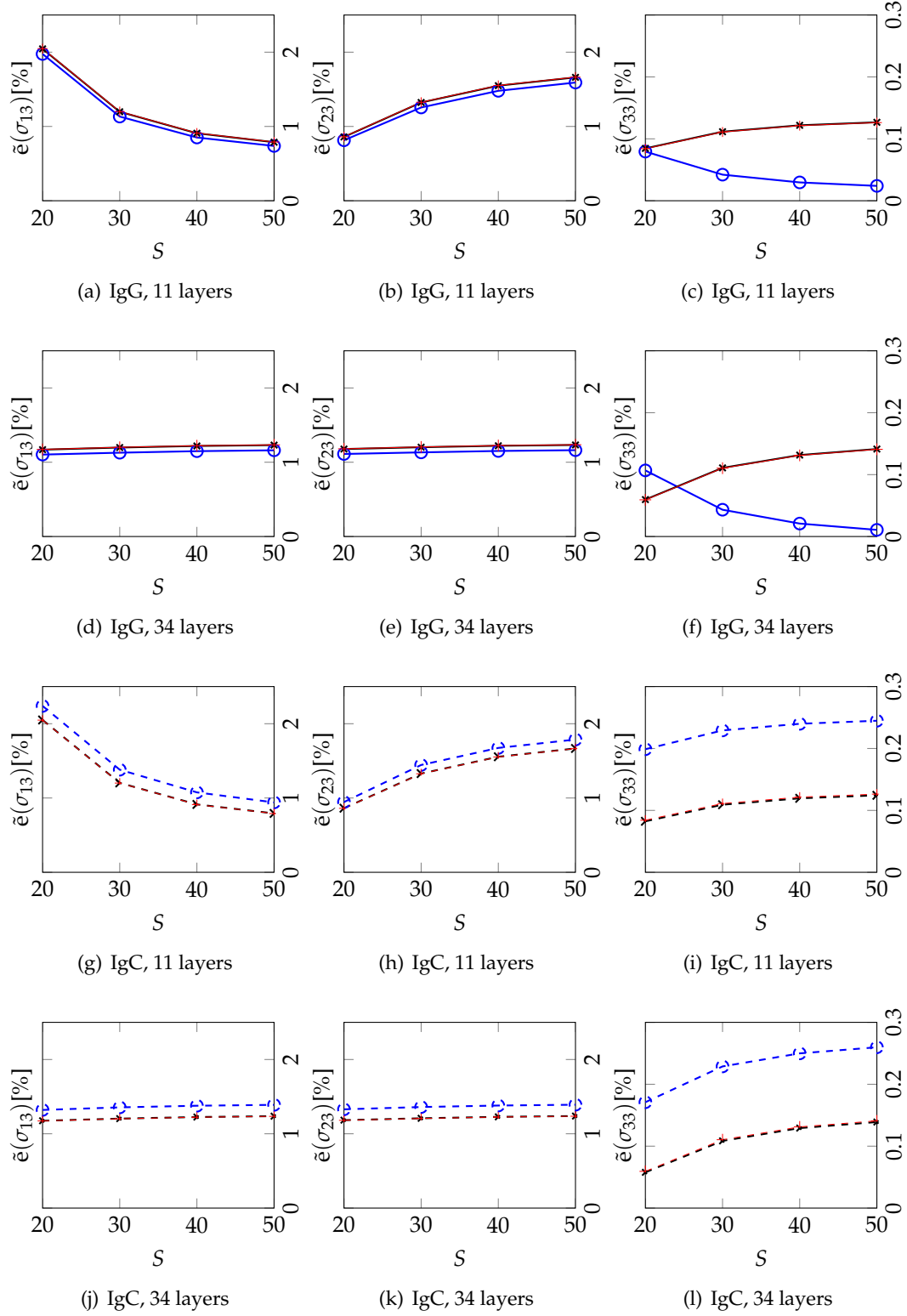
FIGURE 4.11: L^2 relative percentage error evaluation at $x_1 = x_2 = L/4$ using an in-plane degree of approximation equal to 6. Different length-to-thickness ratios S are investigated for a number of layers equal to 11 and 34 (IgG - number of control points per in-plane direction: 7 —○—, 14 —✳—, 21 —+—. IgC - number of control points per in-plane direction: 7 - ○- , 14 - ✦ -, 21 - + -). Solutions obtained using 14 and 21 control points are virtually indistinguishable for both IgG and IgC cases.

is defined as

$$\Delta(\sigma_{i3}) = \frac{|\sigma_{i3}^{\text{analytic}}(\bar{x}_1, \bar{x}_2, \bar{x}_3) - \sigma_{i3}^{\text{recovered}}(\bar{x}_1, \bar{x}_2, \bar{x}_3)|}{|\sigma_{i3}^{\text{analytic}}(\bar{x}_1, \bar{x}_2, \bar{x}_3)|} \qquad i = 1, 2, 3. \qquad (4.34)$$

In Tables 4.2-4.13, we consider a set of points of interest on the plate border and in the interior of the plate to provide a comprehensive assessment of our numerical methods across the whole plate geometry. Because $\sigma_{i3}^{\text{analytic}} = 0$ in some of those points, in those locations we focus on the absolute difference between analytic and recovered stresses instead, computed as

$$\Delta(\sigma_{i3}) = |\sigma_{i3}^{\text{analytic}}(\bar{x}_1, \bar{x}_2, \bar{x}_3) - \sigma_{i3}^{\text{recovered}}(\bar{x}_1, \bar{x}_2, \bar{x}_3)| \qquad i = 1, 2, 3. \qquad (4.35)$$

In Tables 4.2-4.13, we have noted if this latter definition has been employed by using the asterisk (*) next to the reported values.

The results in Tables 4.2-4.13 show that, for a plate made of 11 layers, a single in-plane element with 7x7 DOFs is able to provide maximum differences of 4% or lower (3% or lower for a 34-layer plate) on the boundary and of 2.5% or lower (less than 1% for a 34-layer case) inside the domain for the considered IgG method coupled with the proposed post-processing stress recovery. Under the same modeling conditions, IgC combined with the equilibrium-based stress recovery strategy allows to obtain maximum differences of 8% or lower (6.5% or lower for a 34-layer plate) on the border and of 3% or lower (1.5% or lower for a 34-layer case) inside the plate. Finally, relative differences for normal out-of-plane σ_{33} are, on average, one order magnitude less than those that correspond to the shear stress (i.e., σ_{13} and σ_{23}).

TABLE 4.2: Simply-supported composite plate under a sinusoidal load with 11 layers. Out-of-plane stress state difference with respect to Pagano's solution [145] at $x = (0, L/2, 0)$. We compare post-processed IgG and post-processed IgC for a degree of approximation $p = q = 6$ and 7x7 control points. Values marked with the asterisk (*) are computed *via* Equation (4.35).

S	Method	$\sigma_{13}(0, L/2, 0)$ [MPa]	$\sigma_{23}(0, L/2, 0)$ [MPa]	$\sigma_{33}(0, L/2, 0)$ [MPa]	$\Delta(\sigma_{13})$ [%]	$\Delta(\sigma_{23})$ [%]	$\Delta(\sigma_{33})$ [%]
20	analytical	4.0728	0.0000	0.0000	-	-	-
	post-processed IgG	3.9290	0.0000	0.0001	3.5295	0.0000*	0.0055*
	post-processed IgC	3.7848	0.0000	0.0001	7.0706	0.0000*	0.0100*
30	analytical	6.0598	0.0000	0.0000	-	-	-
	post-processed IgG	5.8935	0.0000	0.0001	2.7445	0.0000*	0.0055*
	post-processed IgC	5.6772	0.0000	0.0001	6.3145	0.0000*	0.0100*
40	analytical	8.0545	0.0000	0.0000	-	-	-
	post-processed IgG	7.8580	0.0000	0.0001	2.4395	0.0000*	0.0055*
	post-processed IgC	7.5696	0.0000	0.0001	6.0206	0.0000*	0.0100*
50	analytical	10.0530	0.0000	0.0000	-	-	-
	post-processed IgG	9.8225	0.0000	-0.0001	2.2923	0.0000*	0.0055*
	post-processed IgC	9.4620	0.0000	0.0001	5.8789	0.0000*	0.0100*

TABLE 4.3: Simply-supported composite plate under a sinusoidal load with 11 layers. Out-of-plane stress state difference with respect to Pagano's solution [145] at $x = (0, L/2, h/4)$. We compare post-processed IgG and post-processed IgC for a degree of approximation $p = q = 6$ and 7x7 control points. Values marked with the asterisk (*) are computed *via* Equation (4.35).

S	Method	$\sigma_{13}(0,L/2,h/4)$ [MPa]	$\sigma_{23}(0,L/2,h/4)$ [MPa]	$\sigma_{33}(0,L/2,h/4)$ [MPa]	$\Delta(\sigma_{13})$ [%]	$\Delta(\sigma_{23})$ [%]	$\Delta(\sigma_{33})$ [%]
	analytical	2.7527	0.0000	0.0000	-	-	-
20	post-processed IgG	2.6394	0.0000	-0.0045	4.1167	0.0000*	0.4464*
	post-processed IgC	2.5433	0.0000	-0.0082	7.6056	0.0000*	0.8161*
	analytical	4.0817	0.0000	0.0000	-	-	-
30	post-processed IgG	3.9590	0.0000	-0.0045	3.0059	0.0000*	0.4464*
	post-processed IgC	3.8150	0.0000	-0.0082	6.5352	0.0000*	0.8161*
	analytical	5.4188	0.0000	0.0000	-	-	-
40	post-processed IgG	5.2787	0.0000	-0.0045	2.5849	0.0000*	0.4464*
	post-processed IgC	5.0866	0.0000	-0.0082	6.1295	0.0000*	0.8161*
	analytical	6.7595	0.0000	0.0000	-	-	-
50	post-processed IgG	6.5984	0.0000	-0.0045	2.3838	0.0000*	0.4464*
	post-processed IgC	6.3583	0.0000	-0.0082	5.9357	0.0000*	0.8161*

TABLE 4.4: Simply-supported composite plate under a sinusoidal load with 11 layers. Out-of-plane stress state difference with respect to Pagano's solution [145] at $x = (L/4, L/4, 0)$. We compare post-processed IgG and post-processed IgC for a degree of approximation $p = q = 6$ and 7x7 control points. Values marked with the asterisk (*) are computed *via* Equation (4.35).

S	Method	$\sigma_{13}(L/4,L/4,0)$ [MPa]	$\sigma_{23}(L/4,L/4,0)$ [MPa]	$\sigma_{33}(L/4,L/4,0)$ [MPa]	$\Delta(\sigma_{13})$ [%]	$\Delta(\sigma_{23})$ [%]	$\Delta(\sigma_{33})$ [%]
	analytical	2.0364	2.7220	0.2483	-	-	-
20	post-processed IgG	1.9974	2.7240	0.2483	1.9166	0.0751	0.0026
	post-processed IgC	1.9919	2.7183	0.2483	2.1852	0.1340	0.0080
	analytical	3.0299	4.1212	0.2483	-	-	-
30	post-processed IgG	2.9960	4.0860	0.2483	1.1185	0.8526	0.0000
	post-processed IgC	2.9878	4.0775	0.2483	1.3893	1.0598	0.0054
	analytical	4.0273	5.5138	0.2483	-	-	-
40	post-processed IgG	3.9947	5.4481	0.2483	0.8083	1.1926	0.0003
	post-processed IgC	3.9838	5.4367	0.2483	1.0800	1.3991	0.0051
	analytical	5.0265	6.9035	0.2483	-	-	-
50	post-processed IgG	4.9934	6.8101	0.2483	0.6588	1.3529	0.0004
	post-processed IgC	4.9797	6.7958	0.2483	0.9308	1.5591	0.0051

TABLE 4.5: Simply-supported composite plate under a sinusoidal load with 11 layers. Out-of-plane stress state difference with respect to Pagano's solution [145] at $x = (L/4, L/4, h/4)$. We compare post-processed IgG and post-processed IgC for a degree of approximation $p = q = 6$ and 7x7 control points. Values marked with the asterisk (*) are computed *via* Equation (4.35).

S	Method	$\sigma_{13} (L/4, L/4, h/4)$ [MPa]	$\sigma_{23} (L/4, L/4, h/4)$ [MPa]	$\sigma_{33} (L/4, L/4, h/4)$ [MPa]	$\Delta(\sigma_{13})$ [%]	$\Delta(\sigma_{23})$ [%]	$\Delta(\sigma_{33})$ [%]
20	analytical	1.3763	2.2187	0.4209	-	-	-
	post-processed IgG	1.3415	2.2104	0.4213	2.5348	0.3720	0.0931
	post-processed IgC	1.3375	2.2060	0.4202	2.8209	0.5713	0.1711
30	analytical	2.0409	3.3489	0.4211	-	-	-
	post-processed IgG	2.0122	3.3156	0.4213	1.4056	0.9939	0.0485
	post-processed IgC	2.0063	3.3090	0.4202	1.6951	1.1921	0.2156
40	analytical	2.7094	4.4758	0.4212	-	-	-
	post-processed IgG	2.6829	4.4208	0.4213	0.9777	1.2278	0.0334
	post-processed IgC	2.6750	4.4120	0.4202	1.2684	1.4255	0.2306
50	analytical	3.3798	5.6010	0.4212	-	-	-
	post-processed IgG	3.3536	5.5260	0.4213	0.7733	1.3392	0.0265
	post-processed IgC	3.3438	5.5150	0.4202	1.0646	1.5366	0.2375

TABLE 4.6: Simply-supported composite plate under a sinusoidal load with 11 layers. Out-of-plane stress state difference with respect to Pagano's solution [145] at $x = (L/2, 0, 0)$. We compare post-processed IgG and post-processed IgC for a degree of approximation $p = q = 6$ and 7x7 control points. Values marked with the asterisk (*) are computed *via* Equation (4.35).

S	Method	$\sigma_{13}(L/2,0,0)$ [MPa]	$\sigma_{23}(L/2,0,0)$ [MPa]	$\sigma_{33}(L/2,0,0)$ [MPa]	$\Delta(\sigma_{13})$ [%]	$\Delta(\sigma_{23})$ [%]	$\Delta(\sigma_{33})$ [%]
20	analytical	0.0000	5.4440	0.0000	-	-	-
	post-processed IgG	0.0000	5.3558	0.0001	0.0000*	1.6191	0.0057*
	post-processed IgC	0.0000	5.1533	0.0001	0.0000*	5.3394	0.0106*
30	analytical	0.0000	8.2424	0.0000	-	-	-
	post-processed IgG	0.0000	8.0337	0.0001	0.0000*	2.5310	0.0057*
	post-processed IgC	0.0000	7.7299	0.0001	0.0000*	6.2169	0.0106*
40	analytical	0.0000	11.0276	0.0000	-	-	-
	post-processed IgG	0.0000	10.7117	0.0001	0.0000*	2.8653	0.0057*
	post-processed IgC	0.0000	10.3066	0.0001	0.0000*	6.5386	0.0106*
50	Analytical	0.0000	13.8069	0.0000	-	-	-
	post-processed IgG	0.0000	13.3896	0.0001	0.0000*	3.0229	0.0057*
	post-processed IgC	0.0000	12.8832	0.0001	0.0000*	6.6902	0.0106*

TABLE 4.7: Simply-supported composite plate under a sinusoidal load with 11 layers. Out-of-plane stress state difference with respect to Pagano's solution [145] at $x = (L/2, 0, h/4)$. We compare post-processed IgG and post-processed IgC for a degree of approximation $p = q = 6$ and 7x7 control points. Values marked with the asterisk (*) are computed *via* Equation (4.35).

S	Method	$\sigma_{13}(L/2,0,h/4)$ [MPa]	$\sigma_{23}(L/2,0,h/4)$ [MPa]	$\sigma_{33}(L/2,0,h/4)$ [MPa]	$\Delta(\sigma_{13})$ [%]	$\Delta(\sigma_{23})$ [%]	$\Delta(\sigma_{33})$ [%]
20	analytical	0.0000	4.4373	0.0000	-	-	-
	post-processed IgG	0.0000	4.3456	-0.0047	0.0000*	2.0680	0.4720*
	post-processed IgC	0.0000	4.1806	-0.0087	0.0000*	5.7856	0.8691*
30	analytical	0.0000	6.6978	0.0000	-	-	-
	post-processed IgG	0.0000	6.5183	-0.0047	0.0000*	2.6794	0.4720*
	post-processed IgC	0.0000	6.2709	-0.0087	0.0000*	6.3738	0.8691*
40	analytical	0.0000	8.9516	0.0000	-	-	-
	post-processed IgG	0.0000	8.6911	-0.0047	0.0000*	2.9094	0.4720*
	post-processed IgC	0.0000	8.3612	-0.0087	0.0000*	6.5950	0.8691*
50	analytical	0.0000	11.2021	0.0000	-	-	-
	post-processed IgG	0.0000	10.8639	-0.0047	0.0000*	3.0188	0.4720*
	post-processed IgC	0.0000	10.4515	-0.0087	0.0000*	6.7003	0.8691*

TABLE 4.8: Simply-supported composite plate under a sinusoidal load with 34 layers. Out-of-plane stress state difference with respect to Pagano's solution [145] at $x = (0, L/2, 0)$. We compare post-processed IgG and post-processed IgC for a degree of approximation $p = q = 6$ and 7x7 control points. Values marked with the asterisk (*) are computed *via* Equation (4.35).

S	Method	$\sigma_{13}(0,L/2,0)$ [MPa]	$\sigma_{23}(0,L/2,0)$ [MPa]	$\sigma_{33}(0,L/2,0)$ [MPa]	$\Delta(\sigma_{13})$ [%]	$\Delta(\sigma_{23})$ [%]	$\Delta(\sigma_{33})$ [%]
20	analytical	4.7476	0.0000	0.0000	-	-	-
	post-processed IgG	4.6422	0.0000	0.0000	2.2199	0.0000*	0.0019*
	post-processed IgC	4.4689	0.0000	0.0000	5.8699	0.0000*	0.0034*
30	analytical	7.1411	0.0000	0.0000	-	-	-
	post-processed IgG	6.9633	0.0000	0.0000	2.4890	0.0000*	0.0019*
	post-processed IgC	6.7034	0.0000	0.0000	6.1289	0.0000*	0.0034*
40	analytical	9.5307	0.0000	0.0000	-	-	-
	post-processed IgG	9.2844	0.0000	0.0000	2.5839	0.0000*	0.0019*
	post-processed IgC	8.9378	0.0000	0.0000	6.2203	0.0000*	0.0034*
50	Analytical	11.9187	0.0000	0.0000	-	-	-
	post-processed IgG	11.6055	0.0000	0.0000	2.6280	0.0000*	0.0019*
	post-processed IgC	11.1723	0.0000	0.0000	6.2627	0.0000*	0.0034*

TABLE 4.9: Simply-supported composite plate under a sinusoidal load with 34 layers. Out-of-plane stress state difference with respect to Pagano's solution [145] at $x = (0, L/2, h/4)$. We compare post-processed IgG and post-processed IgC for a degree of approximation $p = q = 6$ and 7x7 control points. Values marked with the asterisk (*) are computed *via* Equation (4.35).

S	Method	$\sigma_{13}(0, L/2, h/4)$ [MPa]	$\sigma_{23}(0, L/2, h/4)$ [MPa]	$\sigma_{33}(0, L/2, h/4)$ [MPa]	$\Delta(\sigma_{13})$ [%]	$\Delta(\sigma_{23})$ [%]	$\Delta(\sigma_{33})$ [%]
20	analytical	3.7058	0.0000	0.0000	-	-	-
	post-processed IgG	3.5969	0.0000	-0.0046	2.9384	0.0000*	0.4610*
	post-processed IgC	3.4624	0.0000	-0.0085	6.5684	0.0000*	0.8461*
30	analytical	5.5563	0.0000	0.0000	-	-	-
	post-processed IgG	5.3954	0.0000	-0.0046	2.8963	0.0000*	0.4610*
	post-processed IgC	5.1936	0.0000	-0.0085	6.5279	0.0000*	0.8461*
40	analytical	7.4073	0.0000	0.0000	-	-	-
	post-processed IgG	7.1938	0.0000	-0.0046	2.8821	0.0000*	0.4610*
	post-processed IgC	6.9248	0.0000	-0.0085	6.5143	0.0000*	0.8461*
50	analytical	9.2585	0.0000	0.0000	-	-	-
	post-processed IgG	8.9923	0.0000	-0.0046	2.8757	0.0000*	0.4610*
	post-processed IgC	8.6560	0.0000	-0.0085	6.5081	0.0000*	0.8461*

TABLE 4.10: Simply-supported composite plate under a sinusoidal load with 34 layers. Out-of-plane stress state difference with respect to Pagano's solution [145] at $x = (L/4, L/4, 0)$. We compare post-processed IgG and post-processed IgC for a degree of approximation $p = q = 6$ and 7x7 control points. Values marked with the asterisk (*) are computed *via* Equation (4.35).

S	Method	$\sigma_{13}(L/4, L/4, 0)$ [MPa]	$\sigma_{23}(L/4, L/4, 0)$ [MPa]	$\sigma_{33}(L/4, L/4, 0)$ [MPa]	$\Delta(\sigma_{13})$ [%]	$\Delta(\sigma_{23})$ [%]	$\Delta(\sigma_{33})$ [%]
20	analytical	2.3738	2.3746	0.2494	-	-	-
	post-processed IgG	2.3606	2.3609	0.2494	0.5570	0.5767	0.0029
	post-processed IgC	2.3550	2.3553	0.2495	0.7930	0.8127	0.0046
30	analytical	3.5705	3.5713	0.2494	-	-	-
	post-processed IgG	3.5409	3.5413	0.2494	0.8307	0.8404	0.0001
	post-processed IgC	3.5325	3.5329	0.2495	1.0660	1.0757	0.0019
40	analytical	4.7653	4.7663	0.2494	-	-	-
	post-processed IgG	4.7212	4.7218	0.2494	0.9272	0.9332	0.0002
	post-processed IgC	4.7099	4.7106	0.2495	1.1623	1.1683	0.0015
50	analytical	5.9594	5.9604	0.2494	-	-	-
	post-processed IgG	5.9014	5.9022	0.2494	0.9720	0.9763	0.0003
	post-processed IgC	5.8874	5.8882	0.2495	1.2071	1.2113	0.0014

TABLE 4.11: Simply-supported composite plate under a sinusoidal load with 34 layers. Out-of-plane stress state difference with respect to Pagano's solution [145] at $x = (L/4, L/4, h/4)$. We compare post-processed IgG and post-processed IgC for a degree of approximation $p = q = 6$ and 7x7 control points. Values marked with the asterisk (*) are computed *via* Equation (4.35).

S	Method	$\sigma_{13}\,(L/4,L/4,h/4)$ [MPa]	$\sigma_{23}\,(L/4,L/4,h/4)$ [MPa]	$\sigma_{33}\,(L/4,L/4,h/4)$ [MPa]	$\Delta(\sigma_{13})$ [%]	$\Delta(\sigma_{23})$ [%]	$\Delta(\sigma_{33})$ [%]
20	analytical	1.8529	1.7370	0.4212	-	-	-
	post-processed IgG	1.8291	1.7154	0.4217	1.2830	1.2387	0.1167
	post-processed IgC	1.8249	1.7113	0.4206	1.5130	1.4777	0.1476
30	analytical	2.7782	2.6027	0.4215	-	-	-
	post-processed IgG	2.7437	2.5732	0.4217	1.2402	1.1343	0.0481
	post-processed IgC	2.7373	2.5669	0.4206	1.4703	1.3735	0.2160
40	analytical	3.7037	3.4690	0.4216	-	-	-
	post-processed IgG	3.6583	3.4309	0.4217	1.2258	1.0978	0.0241
	post-processed IgC	3.6497	3.4226	0.4206	1.4559	1.3371	0.2399
50	analytical	4.6293	4.3355	0.4217	-	-	-
	post-processed IgG	4.5728	4.2886	0.4217	1.2192	1.0809	0.0130
	post-processed IgC	4.5622	4.2782	0.4206	1.4494	1.3203	0.2510

TABLE 4.12: Simply-supported composite plate under a sinusoidal load with 34 layers. Out-of-plane stress state difference with respect to Pagano's solution [145] at $x = (L/2, 0, 0)$. We compare post-processed IgG and post-processed IgC for a degree of approximation $p = q = 6$ and 7x7 control points. Values marked with the asterisk (*) are computed *via* Equation (4.35).

S	Method	$\sigma_{13}(L/2,0,0)$ [MPa]	$\sigma_{23}(L/2,0,0)$ [MPa]	$\sigma_{33}(L/2,0,0)$ [MPa]	$\Delta(\sigma_{13})$ [%]	$\Delta(\sigma_{23})$ [%]	$\Delta(\sigma_{33})$ [%]
20	analytical	0.0000	4.7492	0.0000	-	-	-
	post-processed IgG	0.0000	4.6428	0.0000	0.0000*	2.2394	0.0018*
	post-processed IgC	0.0000	4.4695	0.0000	0.0000*	5.8886	0.0032*
30	analytical	0.0000	7.1427	0.0000	-	-	-
	post-processed IgG	0.0000	6.9642	0.0000	0.0000*	2.4986	0.0018*
	post-processed IgC	0.0000	6.7043	0.0000	0.0000*	6.1382	0.0032*
40	analytical	0.0000	9.5325	0.0000	-	-	-
	post-processed IgG	0.0000	9.2856	0.0000	0.0000*	2.5899	0.0018*
	post-processed IgC	0.0000	8.9390	0.0000	0.0000*	6.2260	0.0032*
50	analytical	0.0000	11.9208	0.0000	-	-	-
	post-processed IgG	0.0000	11.6070	0.0000	0.0000*	2.6322	0.0018*
	post-processed IgC	0.0000	11.1738	0.0000	0.0000*	6.2668	0.0032*

TABLE 4.13: Simply-supported composite plate under a sinusoidal load with 34 layers. Out-of-plane stress state difference with respect to Pagano's solution [145] at $x = (L/2, 0, h/4)$. We compare post-processed IgG and post-processed IgC for a degree of approximation $p = q = 6$ and 7x7 control points. Values marked with the asterisk (*) are computed *via* Equation (4.35).

S	Method	$\sigma_{13}(L/2, 0, h/4)$ [MPa]	$\sigma_{23}(L/2, 0, h/4)$ [MPa]	$\sigma_{33}(L/2, 0, h/4)$ [MPa]	$\Delta(\sigma_{13})$ [%]	$\Delta(\sigma_{23})$ [%]	$\Delta(\sigma_{33})$ [%]
	analytical	0.0000	3.4739	0.0000	-	-	-
20	post-processed IgG	0.0000	3.3737	-0.0046	0.0000*	2.8853	0.4583*
	post-processed IgC	0.0000	3.2480	-0.0084	0.0000*	6.5031	0.8413*
	analytical	0.0000	5.2054	0.0000	-	-	-
30	post-processed IgG	0.0000	5.0605	-0.0046	0.0000*	2.7826	0.4583*
	post-processed IgC	0.0000	4.8720	-0.0084	0.0000*	6.4042	0.8413*
	analytical	0.0000	6.9380	0.0000	-	-	-
40	post-processed IgG	0.0000	6.7474	-0.0046	0.0000*	2.7468	0.4583*
	post-processed IgC	0.0000	6.4960	-0.0084	0.0000*	6.3697	0.8413*
	analytical	0.0000	8.6710	0.0000	-	-	-
50	post-processed IgG	0.0000	8.4342	-0.0046	0.0000*	2.7302	0.4583*
	post-processed IgC	0.0000	8.1200	-0.0084	0.0000*	6.3537	0.8413*

4.4.2   Simply-supported circular plate

As a last benchmark, we consider a multilayered simply-supported circular plate, defined over a domain of radius $R = St = 220$ mm, where S represents here the radius-to-thickness ratio and t is the total thickness of the laminate. We consider $S = 20$ and a cross-ply distribution of 11 layers, namely a 90°/0° stacking sequence from the bottom to the top of the plate. The plate is subject to a uniformly distributed load $p(x_1, x_2) = 1$ MPa, we use the material properties reported in Table 4.1, and the reference system $x_1 O x_2$ is located at the center of the circular plate.

Following [68], in Figure 4.12 we compare the reconstructed out-of-plane results obtained with IgG and IgC (degrees of approximation $p = q = 6$ and 14x14 control points) with those from an overkill 3D solid Abaqus Unified FEA solution (version Abaqus/CAE 2017) comprising 466,136 C3D20R elements (i.e., 20-node quadratic brick elements with reduced integration). We acknowledge that this commercial software provides other cheaper modeling possibilities in terms of shell approaches. Nevertheless, to the best of our knowledge they do not provide σ_{33} component results. Studying the plate *via* C3D20R finite elements allows to obtain the through-the-thickness profiles for all out-of-plane stresses paying a high computational cost. In fact, this modeling strategy represents a full 3D analysis and requires at last two elements per layer to have a suitable through-the-thickness description [68]. Furthermore, we notice that, according to [68], the quadratic C3D20R element might not produce a highly accurate estimation of the transverse shear components (e.g., for the σ_{23} component in the particular case analyzed in [68]). In Figure 4.12, we also notice some differences between the shear components computed by Abaqus Unified FEA and those predicted by our method. Further reasons for such differences might be related to the fact that our modeling strategy recovers the out-of-plane stresses starting from a displacement field obtained considering a homogenized plate model, while

(a) Normalized σ_{13}

(b) Normalized σ_{23}

(c) Normalized σ_{33}
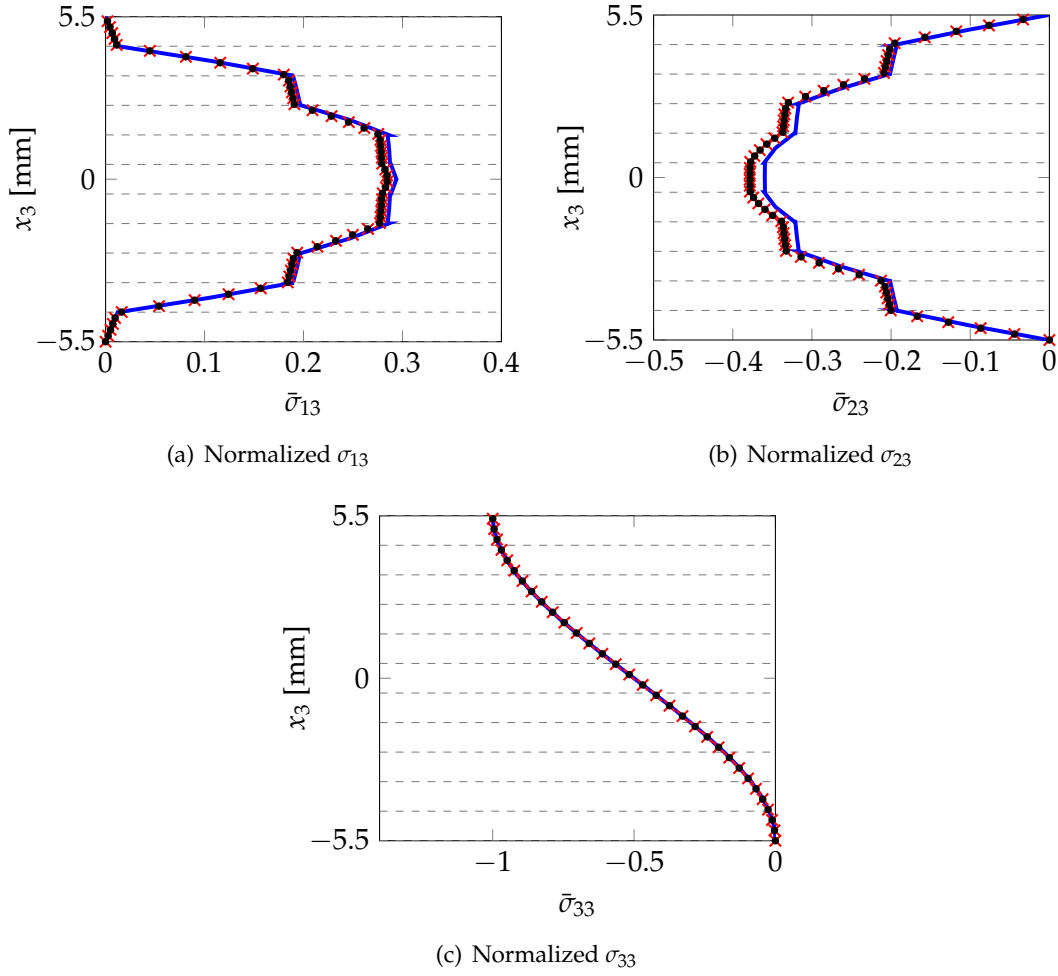
FIGURE 4.12: Through-the-thickness recovered out-of-plane stress solution for the simply-supported multilayered circular plate at $x_1 = -x_2 = 89.3$ mm. Plate case with 11 layers and mean radius-to-thickness ratio $S = 20$ (——— overkill Abaqus Unified FEA solution with 466,136 C3D20R finite elements versus post-processed numerical solutions obtained with degree of approximation $p = q = 6$, and 14x14 control points: × IgG, • IgC).

the reference Abaqus Unified FEA solution is computed for a 3D solid with full representation of each layer. However, we may conclude that the proposed equilibrium-based stress recovery approach successfully approximates the stress state for the circular plate given by Abaqus Unified FEA, even when post-processing an IgC or an IgG solution obtained from a very coarse mesh of 14x14 control points. Finally, we also highlight that the high continuity granted by IgA shape functions may be of key importance for dealing with problems characterized by complex geometrical features, like the one under investigation in this section.

4.5 Conclusions

Moving from the equilibrium-based post-processing technique that we have proposed in Chapter 3 for 3D solid plates approximated by IgG [62] or IgC [149] methods, in this chapter, we have considered the application of such an approach for

the accurate and inexpensive recovery of interlaminar stresses in Kirchhoff plates resolved *via* IgA. The adopted equilibrium-based stress recovery strategy has been shown to be particularly effective in this framework for both IgG and IgC methods. While our post-processing approach to recover out-of-plane stresses in 3D solid plates is only applicable for laminates with an odd number of layers or an oddly distributed even number of layers (see Remark 4.1), the extension of our equilibrium-based stress recovery method to Kirchhoff plates can also handle laminates with an even number of non-symmetric layers, with no limitation in terms of computational accuracy or efficiency. The fundamental ingredients to obtain such good results for Kirchhoff plates in this chapter are again the high accuracy and regularity granted by high-order IgA methods (even with coarse meshes). Our numerical tests for a simple geometry like the rectangular plate involved in Pagano's test case have shown that even a mesh constituted by a single sixth-order element is able to provide very good results in terms of in-plane and out-of-plane stresses, for both IgG and IgC discretizations. Extensive numerical experiments have confirmed the high efficiency of the proposed equilibrium-based stress recovery approach in the context of Kirchhoff plates. Finally, the application of this procedure to nonlinear problems will be the subject of future research.

Chapter 5

Efficient equilibrium-based stress recovery for isogeometric laminated curved structures

In this chapter, we focus on modeling the interlaminar stresses of laminated composite solid shells in the framework of higher-order and higher-continuity NURBS-based IgA by extending the procedure presented in Chapters 3 and 4 for solid and Kirchhoff plates, respectively [62, 148, 149]. The effectiveness of the isogeometric paradigm in the modeling of laminated composite solid shells is demonstrated through several numerical examples that feature a 3D cylindrical shell under bending. The proposed strategy can be regarded as a two-step procedure: first, the structure is modeled using only one element through the thickness and a highly continuous displacement field is obtained *via* (coarse) solid isogeometric computations, which rely either on a layer-by-layer integration rule or a homogenized approach; then, the interlaminar stresses are recovered from the resulting isogeometric displacement solutions by imposing equilibrium in strong form and exploiting the high-continuity properties of IgA to calculate the necessary high-order derivatives in the equilibrium equations. The ability to compute the interlaminar shear stresses also allows to successfully recover the normal out-of-plane stress component. Notice that, while the displacement field is obtained in a global framework, the interlaminar stresses are recovered locally, which grants that no further coupled terms arise in the equilibrium equations. This allows to handle the higher geometric complexity of the solid shell case without the need to iteratively resolve the balance of linear momentum system. In addition, IgA provides superior geometric modeling features for curved geometries, such as the possibility to exactly represent conic sections. Thus, we present several numerical results that confirm the good performance of our stress recovery strategy for laminated solid shells, especially for composite stacks with significant radius-to-thickness ratio and number of plies. In particular, our method is a very appealing technology for the latter case, where a LW approach employing a number of DOFs directly proportional to the number of plies would be much more computationally demanding.

The structure of this chapter is detailed as follows. The governing equations for the 3D orthotropic elastic case are outlined in Section 5.1, after introducing a global
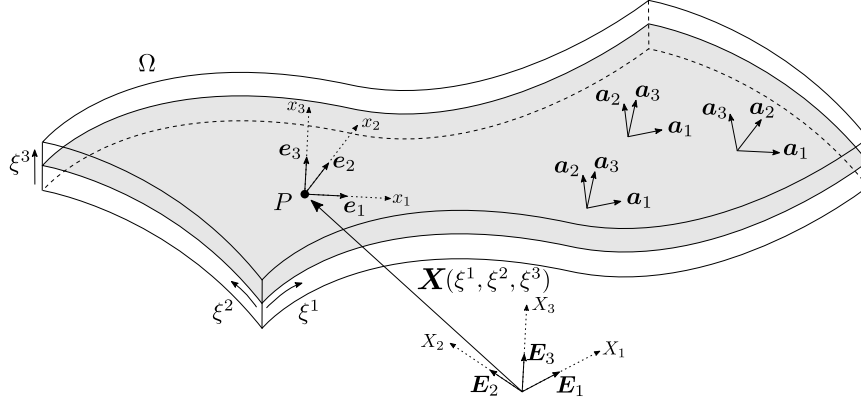
FIGURE 5.1: Global and local reference cartesian systems associated to the curved structure.

and a local description of the needed kinematics and constitutive relations. We refer readers to Appendix 5.A for a possible choice of an appropriate pointwise local basis and further details on the evaluation of the local derivatives of the stress components. In Section 5.2, we present the extension of our equilibrium-based stress recovery strategy for laminated solid shells. To this end, we depart from an approximated global displacement field, which is obtained using a 3D IgA single-element approach based on either a calibrated layer-by-layer integration rule or a homogenized approach that we introduce in Section 5.3. In Section 5.4, we present several benchmarks comprising different mean radius-to-thickness ratios and number of layers to showcase the effectiveness of the method. Additionally, Appendix 5.B includes preliminary results with a novel strategy that aims at lowering the high-order continuity requirements of the stress recovery. We finally draw our conclusions in Section 5.5.

5.1 Governing equations for the orthotropic elastic case

In this section, we study the equations that govern the 3D orthotropic elasticity problem. For this purpose, we introduce a global and a local cartesian reference system, as well as the associated kinematic quantities and constitutive relations needed to address the curved geometry problem. The reason why we underline this global-local dual description of engineering quantities lies in our double-step stress recovery approach: first, we calculate a global displacement solution and, then, we postprocess it locally to recover the out-of-plane stress components from the in-plane stress field calculated from the global displacement solution. Finally, we detail the governing equations for the orthotropic solid case both in strong and weak form.

5.1.1 Kinematics: a global and local perspective

Let us consider an open bounded domain $\Omega \subset \mathbb{R}^3$ representing an elastic three-dimensional body, defined as a spline parametrization, such that Ω is the image of a unit cube $\hat{\Omega} = [0,1]^3$ through the map $\boldsymbol{F} : (\xi^1, \xi^2, \xi^3) \in \hat{\Omega} \to \boldsymbol{X} \in \Omega$, i.e., $\Omega = \boldsymbol{F}(\hat{\Omega})$.

Let us also introduce a global reference cartesian system $\{X_1, X_2, X_3\}$ and its associated orthonormal global basis $\{E_1, E_2, E_3\}$, as well as a local orthornormal basis $\{a_1, a_2, a_3\}$, defined for every point of the body (see Figure 5.1). This local basis is described according to the structure's mid-surface (represented in gray color in Figure 5.1), such that vectors a_1 and a_2 define the in-plane directions of the structure and a_3 is aligned with the out-of-plane direction. Thus, the same local basis $\{a_1, a_2, a_3\}$ is associated to all the points along the thickness that have the same in-plane parametric coordinates (ξ^1, ξ^2). Apart from these requirements, the basis $\{a_1, a_2, a_3\}$ can be chosen freely. In Appendix 5.A, we propose a particular choice based on an orthonormalization of the covariant basis of F.

The out-of-plane stress components will be recovered starting from the in-plane ones at selected points. Once a point is set, and therefore defined by its in-plane coordinates (ξ^1, ξ^2), we post-process a precise stress description along the third coordinate ξ^3. Thus, for a given point of interest P we introduce a fixed local cartesian reference system $\{x_1, x_2, x_3\}$ and its associated orthonormal basis $\{e_1, e_2, e_3\}$ (see Figure 5.1). This fixed local system is an auxiliary reference system that will be used during the calculations involved in the recovery of the stress at P. The basis $\{e_1, e_2, e_3\}$ is just a static snapshot of the moving basis $\{a_1, a_2, a_3\}$ evaluated at P. Thus, due to the fact that $\{e_1, e_2, e_3\}$ is fixed, its derivatives with respect to both reference systems vanish:

$$\frac{\mathrm{d}e_\alpha}{\mathrm{d}X_i} = 0, \quad \frac{\mathrm{d}e_\alpha}{\mathrm{d}x_\beta} = 0 \tag{5.1}$$

and the same applies to its subsequent derivatives. Nevertheless, this is not true, in general, for the moving local basis $\{a_1, a_2, a_3\}$.

In the expression above, and the rest of this section, Latin indices are used for quantities expressed in the basis $\{E_1, E_2, E_3\}$, whereas the Greek indices refer to quantities expressed in the local bases $\{e_1, e_2, e_3\}$ and $\{a_1, a_2, a_3\}$. In addition, all indices span from 1 to 3 and we adopt Einstein's notation, i.e., repeated indices imply the summation of the involved components unless otherwise stated. For the sake of conciseness, henceforward, the global and local reference systems and bases are denoted, respectively, as $\{X_i\}$, $\{x_\alpha\}$, $\{E_i\}$, $\{e_\alpha\}$, and $\{a_\alpha\}$.

The global basis $\{E_i\}$ can be expressed in terms of the basis $\{e_\alpha\}$, and *vice versa*, as:

$$E_i = C_{i\alpha}\, e_\alpha , \tag{5.2a}$$

$$e_\alpha = C_{i\alpha}\, E_i , \tag{5.2b}$$

where the basis change operator $C_{i\alpha}$ is defined as:

$$C_{i\alpha} = \frac{\mathrm{d}X_i}{\mathrm{d}x_\alpha} = \frac{\mathrm{d}x_\alpha}{\mathrm{d}X_i} = E_i \cdot e_\alpha . \tag{5.3}$$

Due to the fact that $\{E_i\}$ and $\{e_\alpha\}$ are orthonormal bases, the change of basis operator is orthogonal. It is worth noting that, as both reference systems $\{X_i\}$ and $\{x_\alpha\}$ are fixed, $C_{i\alpha}$ is constant, i.e.:

$$\frac{\mathrm{d}C_{i\alpha}}{\mathrm{d}X_j} = 0, \quad \frac{\mathrm{d}C_{i\alpha}}{\mathrm{d}x_\beta} = 0, \tag{5.4}$$

and the same applies to subsequent derivatives.

Likewise, the global basis $\{E_i\}$ can be expressed in terms of the local moving basis $\{a_\alpha\}$ as:

$$E_i = D_{i\alpha}\, a_\alpha \,, \tag{5.5}$$

where the basis change operator $D_{i\alpha}$ is defined as:

$$D_{i\alpha} = E_i \cdot a_\alpha \,. \tag{5.6}$$

In general, $D_{i\alpha}$ is not constant, and therefore its derivatives with respect to $\{X_i\}$ or $\{x_\alpha\}$ do not vanish.

5.1.2   Constitutive relations

Considering the global basis $\{E_i\}$ introduced above, we can express the 3D elastic displacement field as $u = \tilde{u}_i\, E_i$, where with $(\tilde{\cdot})$ we refer to quantities expressed in the global basis $\{E_i\}$. We shall now assume small strains and small displacements, such that strains are given by the tensor $\varepsilon = \nabla^s u$, whose components in the global basis are $\varepsilon = \tilde{\varepsilon}_{ij}\, E_i \otimes E_j$, where:

$$\tilde{\varepsilon}_{ij} = \frac{1}{2}\left(\frac{\mathrm{d}\tilde{u}_i}{\mathrm{d}X_j} + \frac{\mathrm{d}\tilde{u}_j}{\mathrm{d}X_i}\right) \,. \tag{5.7}$$

The displacement and strain fields can be expressed as well in the local basis $\{e_\alpha\}$ as $u = u_\alpha e_\alpha$ and $\varepsilon = \varepsilon_{\alpha\beta}e_\alpha \otimes e_\beta$, respectively. Applying the change of basis defined in Equation (5.2), the components u_α and $\varepsilon_{\alpha\beta}$ are computed as:

$$u_\alpha = \tilde{u}_i\, C_{i\alpha} \,, \tag{5.8}$$

$$\varepsilon_{\alpha\beta} = \tilde{\varepsilon}_{ij}\, C_{i\alpha}\, C_{j\beta} \,. \tag{5.9}$$

In the case of linear elasticity, we introduce the stress field as

$$\sigma = \mathbb{C} : \varepsilon \,, \tag{5.10}$$

where $\mathbb{C}$ is the fourth-order material elasticity tensor, that can be expressed at every point using the global $\{E_i\}$ or local $\{a_\alpha\}$ bases as:

$$\mathbb{C} = \tilde{\mathbb{C}}_{ijkl}\, E_i \otimes E_j \otimes E_k \otimes E_l = \mathbb{C}_{\alpha\beta\gamma\delta}\, a_\alpha \otimes a_\beta \otimes a_\gamma \otimes a_\delta \,, \tag{5.11}$$

whose components are related through the change of basis operator (5.6) as:

$$\tilde{\mathbb{C}}_{ijkl} = D_{i\alpha}\, D_{j\beta}\, D_{k\gamma}\, D_{l\delta}\, \mathbb{C}_{\alpha\beta\gamma\delta} \,. \tag{5.12}$$

Focusing on the linear orthotropic elasticity case, $\mathbb{C}$ may be expressed in a more convenient way using the local basis $\{a_i\}$. In fact, in the case that ply fiber directions locally coincide with the basis $\{a_i\}$, the number of elastic coefficients of $\mathbb{C}_{\alpha\beta\gamma\delta}$

reduces to nine. In Voigt's notation, $\mathbb{C}$ can be expressed in terms of engineering constants as in Equation (3.4).

Like the displacement or the strain, also the stress can be expressed either in the global basis as $\boldsymbol{\sigma} = \tilde{\sigma}_{ij}\, \boldsymbol{E}_i \otimes \boldsymbol{E}_j$ or the local one as $\boldsymbol{\sigma} = \sigma_{\alpha\beta}\, \boldsymbol{e}_\alpha \otimes \boldsymbol{e}_\beta$, where:

$$\tilde{\sigma}_{ij} = \tilde{\mathbb{C}}_{ijkl}\, \tilde{\varepsilon}_{kl}\,, \tag{5.13a}$$

$$\sigma_{\alpha\beta} = \tilde{\sigma}_{ij} C_{i\alpha}\, C_{j\beta}\,. \tag{5.13b}$$

5.1.3 Strong form

The considered elastic three-dimensional body is subjected to volume forces $\boldsymbol{b}$, prescribed displacements $\boldsymbol{g}$ on the Dirichlet portion of the boundary Γ_D, and prescribed tractions $\boldsymbol{t}$ acting on the remaining Neumann portion Γ_N, such that $\Gamma_N \cup \Gamma_D = \partial\Omega$ and $\Gamma_N \cap \Gamma_D = \varnothing$.

We recall the balance of linear momentum equation in strong form and the corresponding boundary conditions for the linear elasticity problem:

$$\boldsymbol{\nabla} \cdot \boldsymbol{\sigma} + \boldsymbol{b} = \boldsymbol{0} \qquad \text{in} \quad \Omega\,, \tag{5.14a}$$

$$\boldsymbol{\sigma} \cdot \boldsymbol{n} = \boldsymbol{t} \qquad \text{on} \quad \Gamma_N\,, \tag{5.14b}$$

$$\boldsymbol{u} = \boldsymbol{g} \qquad \text{on} \quad \Gamma_D\,, \tag{5.14c}$$

where $\boldsymbol{\nabla}\cdot$ represents the divergence operator computed with respect to the global cartesian reference system $\{X_i\}$ and $\boldsymbol{n}$ is the outward normal unit vector. The stress tensor $\boldsymbol{\sigma} = \tilde{\sigma}_{ij}\, \boldsymbol{E}_i \otimes \boldsymbol{E}_j$ has its components defined as in Equation (5.13a), while $\boldsymbol{b} = \tilde{b}_i\, \boldsymbol{E}_i$, $\boldsymbol{t} = \tilde{t}_i\, \boldsymbol{E}_i$, and $\boldsymbol{g} = \tilde{g}_i\, \boldsymbol{E}_i$, with $\tilde{b}_i$, $\tilde{t}_i$, and $\tilde{g}_i$ being, respectively, the body force, traction, and imposed displacement components in the basis $\{\boldsymbol{E}_i\}$.

Considering the system of Equations (5.14), the term $\boldsymbol{\nabla} \cdot \boldsymbol{\sigma}$ needs to be further detailed in terms of the global reference system $\{X_i\}$. Therefore, we need to develop Equation (5.14a) expressing the stress tensor in terms of the constitutive relation in Equation (5.10)

$$\boldsymbol{\nabla} \cdot \boldsymbol{\sigma} = (\boldsymbol{\nabla} \cdot \mathbb{C}) : \boldsymbol{\varepsilon} + \mathbb{C} \vdots \boldsymbol{\nabla}\boldsymbol{\varepsilon}\,, \tag{5.15}$$

where $\vdots$ represents the triple contraction operator and

$$\boldsymbol{\nabla} \cdot \boldsymbol{\sigma} = \tilde{\sigma}_{ij,j}\, \boldsymbol{E}_i\,. \tag{5.16}$$

Finally, $\tilde{\sigma}_{ij,j}$ is computed as:

$$\tilde{\sigma}_{ij,j} = \frac{\mathrm{d}\tilde{\sigma}_{ij}}{\mathrm{d}X_j} = \boldsymbol{E}_i \cdot (\boldsymbol{\nabla} \cdot \boldsymbol{\sigma}) = \boldsymbol{E}_i \cdot [(\boldsymbol{\nabla} \cdot \mathbb{C}) : \boldsymbol{\varepsilon}] + \boldsymbol{E}_i \cdot (\mathbb{C} \vdots \boldsymbol{\nabla}\boldsymbol{\varepsilon})\,. \tag{5.17}$$

We refer readers to Appendix 5.A for further details on the evaluation of these components.

5.1.4 Principle of virtual work

The balance of linear momentum Equation (5.14a) can be imposed in a weak sense relying on the principle of virtual work, which states that the sum of the system virtual internal, δW_{int}, and external, δW_{ext}, work is zero in an equilibrium state:

$$\delta W_{int} + \delta W_{ext} = 0. \tag{5.18}$$

Therefore, the linear elasticity problem in variational form, reads

$$\int_\Omega \sigma : \delta \varepsilon \, d\Omega - \int_\Omega b \cdot \delta u \, d\Omega - \int_{\Gamma_N} t \cdot \delta u \, d\Gamma = 0, \tag{5.19}$$

where δu and $\delta \varepsilon$, respectively, are the virtual displacement field and the virtual strain field defined in the global reference system $\{X_i\}$.

5.2 Stress recovery for curved laminated composite structures

In this section we describe the proposed post-processing strategy for curved laminated composite structures, which is general and, provided the sufficient continuity, allows to recover the out-of-plane stresses independently of the designated numerical method to approximate the displacement field.

In an equilibrium state, stresses inside the material should satisfy at every point the equilibrium equation (5.14a), which, using the global reference system $\{X_i\}$, can be further detailed componentwise as:

$$\tilde{\sigma}_{11,1} + \tilde{\sigma}_{12,2} + \tilde{\sigma}_{13,3} + \tilde{b}_1 = 0, \tag{5.20a}$$

$$\tilde{\sigma}_{12,1} + \tilde{\sigma}_{22,2} + \tilde{\sigma}_{23,3} + \tilde{b}_2 = 0, \tag{5.20b}$$

$$\tilde{\sigma}_{13,1} + \tilde{\sigma}_{23,2} + \tilde{\sigma}_{33,3} + \tilde{b}_3 = 0. \tag{5.20c}$$

In an analogous way, the equilibrium equations can be written with respect to the local cartesian reference system $\{x_\alpha\}$, such that x_1, x_2, and x_3 are taken as the fibre, matrix, and normal directions, respectively, as:

$$\sigma_{11,1} + \sigma_{12,2} + \sigma_{13,3} + b_1 = 0, \tag{5.21a}$$

$$\sigma_{12,1} + \sigma_{22,2} + \sigma_{23,3} + b_2 = 0, \tag{5.21b}$$

$$\sigma_{13,1} + \sigma_{23,2} + \sigma_{33,3} + b_3 = 0, \tag{5.21c}$$

where $b_\alpha = \tilde{b}_i \, C_{i\alpha}$ and $\sigma_{\alpha\beta,\mu}$ are the stress derivatives:

$$\sigma_{\alpha\beta,\mu} = \frac{d\sigma_{\alpha\beta}}{dx_\mu}. \tag{5.22}$$

The advantage of using the local system $\{x_\alpha\}$ (see Figure 5.2) lies in the fact that the stress components σ_{11}, σ_{22}, and σ_{12} are now the in-plane components, which are well-known from the global displacement field $\tilde{u}_i$ using Equation (5.13), while σ_{13}, σ_{23}, and σ_{33} represent the out-of-plane stresses, which are instead not correctly
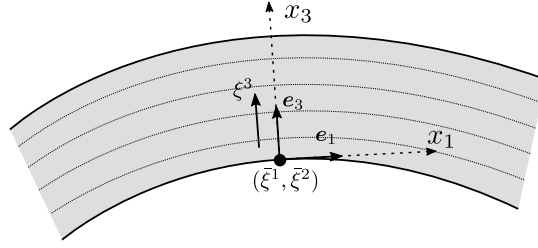
FIGURE 5.2: Local reference cartesian system at a point $(\bar{\xi}^1, \bar{\xi}^2)$ for the stress recovery.

captured (as it has already been investigated in Chapter 3 and references [62, 149] for the 3D plate case and as it will be shown in Figures 5.6 and 5.7 of Section 5.4). Our goal is to obtain a good description of the out-of-plane stress components along the composite thickness direction, extending the procedure detailed in [62] and Chapter 3 for the 3D plate case. It is important to remark that due to the fact that the stress divergence is computed with respect to $\{x_\alpha\}$, which is a fixed cartesian reference system, no additional terms appear in Equation (5.21) as it would be the case for Equation (5.20).

Remark 5.1. *Another possibility would be to express σ in its curvilinear components (either covariant or contravariant) and to develop the equation $\nabla \cdot \sigma + b = 0$ using one of those bases. However, using curvilinear coordinates, new terms would arise in the componentwise equilibrium equations and, most importantly, these new terms would couple together the in-plane and out-of-plane stress components, making impossible to apply the stress recovery procedure proposed in Chapter 3 and reference [62] in a straightforward manner.*

Thus, integrating Equations (5.21a) and (5.21b) along the thickness direction x_3, the shear out-of-plane stress components can be computed as:

$$\sigma_{13}(x_3) = -\int_{\underline{x}_3}^{x_3} \big(\sigma_{11,1}(\zeta) + \sigma_{12,2}(\zeta) + b_1(\zeta)\big)\mathrm{d}\zeta + \sigma_{13}(\underline{x}_3)\,, \tag{5.23a}$$

$$\sigma_{23}(x_3) = -\int_{\underline{x}_3}^{x_3} \big(\sigma_{12,1}(\zeta) + \sigma_{22,2}(\zeta) + b_2(\zeta)\big)\mathrm{d}\zeta + \sigma_{23}(\underline{x}_3)\,, \tag{5.23b}$$

where $\underline{x}_3$ indicates the value of x_3 at the bottom of the solid structure (see Figure 5.2).

To recover the out-of-plane normal stress profile σ_{33}, we focus on each k-th layer and substitute the appropriate derivatives of the out-of-plane shear stresses (5.23) into Equation (5.21c):

$$\begin{aligned}\sigma_{33,3}^{(k)}(x_3^{(k)}) = &\int_{\underline{x}_3^{(k)}}^{x_3^{(k)}} \big(\sigma_{11,11}(\zeta) + \sigma_{22,22}(\zeta) + 2\sigma_{12,12}(\zeta) + b_{1,1}(\zeta) + b_{2,2}(\zeta)\big)\mathrm{d}\zeta \\ &- \big(\sigma_{13,1}(\underline{x}_3^{(k)}) + \sigma_{23,2}(\underline{x}_3^{(k)})\big) - b_3(\underline{x}_3^{(k)})\,,\end{aligned} \tag{5.24}$$

where $\underline{x}_3^{(k)} \leq x_3^{(k)} \leq \bar{x}_3^{(k)}$, with $\underline{x}_3^{(k)}$ and $\bar{x}_3^{(k)}$ being, respectively, the values of the out-of-plane coordinate at the bottom and the top of the k-th layer, while $\sigma_{\alpha\beta,\mu\nu}$ is the stress second derivative:

$$\sigma_{\alpha\beta,\mu\nu} = \frac{\mathrm{d}^2\sigma_{\alpha\beta}}{\mathrm{d}x_\mu \mathrm{d}x_\nu}\,. \tag{5.25}$$

Finally, we further integrate Equation (5.24) along the thickness obtaining

$$\sigma_{33}(x_3) = \int_{\underline{x}_3}^{x_3} \sigma_{33,3}(\xi)\mathrm{d}\xi + \sigma_{33}(\underline{x}_3)\,. \tag{5.26}$$

The stress derivatives $\sigma_{\alpha\beta,\mu}$ and $\sigma_{\alpha\beta,\mu\nu}$ involved in Equations (5.23) and (5.24) are detailed in Appendix 5.A.

Remark 5.2. *It should be noted that integrals* (5.23), (5.24), *and* (5.26) *are computed numerically using a composite trapezoidal quadrature rule. Also, new stress boundary conditions (namely, $\sigma_{13,1}(\underline{x}_3^{(k)})$ and $\sigma_{23,2}(\underline{x}_3^{(k)})$) arise in Equation (5.24) for each k-th layer. The ability to compute those constants is of paramount importance to grant an optimal reconstruction of the normal out-of-plane stress profiles. In fact, while σ_{33} is continuous through the thickness by equilibrium, its derivative with respect to x_3 is not. Thus, neglecting $\sigma_{13,1}(\underline{x}_3^{(k)})$ and $\sigma_{23,2}(\underline{x}_3^{(k)})$ contributions in the evaluation of $\sigma_{33,3}(x_3)$ leads to a continuous layerwise profile of this term and, after integration, to an inaccurate normal out-of-plane stress component distribution.*

With reference to Equations (5.23), (5.24), and (5.26), it is clear that, to apply the proposed post-processing technique, a highly regular displacement solution is needed. More specifically, the required in-plane derivatives $\sigma_{\alpha\beta,\mu}$ and $\sigma_{\alpha\beta,\mu\nu}$ (detailed respectively in the Appendix 5.A in Equations (5.A.9a) and (5.A.9b)) need to be computed from a C^2-continuous in-plane displacement solution, which can be achieved within an IgA framework.

Additionally, in Appendix 5.B we introduce a novel strategy that aims at lowering the high-order continuity requirements of the stress recovery. We present the main ideas and some preliminary results, but further investigations need to be carried out to explore and assess this approach.

5.3   IgA strategies for 3D laminated curved geometries made of multiple orthotropic layers

In Section 5.2, we described our stress recovery technique, which can be applied regardless the numerical approximation method as long as it is able to provide the required continuity. Due to its high-order continuity properties, IgA proves to be a natural choice for the proposed approach, while other techniques, such as FEA, would require a hybrid *a posteriori* interpolation *via*, e.g., splines or radial basis functions. Thus, we hereby detail the proposed displacement-based IgG and IgC strategies to analyze laminated composite solid shells.

The considered modeling strategies can be regarded as three-dimensional ESL approaches, which model the 3D laminate employing only one element through the thickness. Besides the intrinsic difference between IgG and IgC methods in terms of how the balance of linear momentum equation is approximated (either at the weak or strong form level, respectively), the two approaches also differ in the way material properties are considered. For an IgG method, constitutive features can be taken into account through the thickness using either a calibrated layer-by-layer

integration rule or a homogenized approach, whereas the latter represents the most direct ESL strategy for IgC to the authors' knowledge.

5.3.1 Isogeometric Galerkin method

Addressing the element point of view and adopting a standard Gauss quadrature, the global displacement $\boldsymbol{u}$ and virtual displacement field $\delta\boldsymbol{u}$ are approximated as a linear combination of local multivariate shape functions $R_{\mathbf{i,p}}^{(e)}(\bar{\boldsymbol{\xi}})$ (defined in Equation (2.24)) and local control variables $\hat{\mathbf{u}}_{\mathbf{i}}^{(e)}$ and $\delta\hat{\mathbf{u}}_{\mathbf{i}}^{(e)}$ as

$$u_h^{(e)}(\bar{\boldsymbol{\xi}}) = \sum_{\mathbf{i}} \mathbf{R}_{\mathbf{i,p}}^{(e)}(\bar{\boldsymbol{\xi}})\, \hat{\mathbf{u}}_{\mathbf{i}}^{(e)}\,, \tag{5.27a}$$

$$\delta u_h^{(e)}(\bar{\boldsymbol{\xi}}) = \sum_{\mathbf{i}} \mathbf{R}_{\mathbf{i,p}}^{(e)}(\bar{\boldsymbol{\xi}})\, \delta\hat{\mathbf{u}}_{\mathbf{i}}^{(e)}\,, \tag{5.27b}$$

where the superscript (e) is the element index ($e = 1, ..., N_e$, with N_e being the total number of elements), while with h we denote any approximated field. The $\mathbf{i}$-th contribution of the multivariate shape function element matrix $\mathbf{R}_{\mathbf{i,p}}^{(e)}(\bar{\boldsymbol{\xi}})$ is instead defined as

$$\mathbf{R}_{\mathbf{i,p}}^{(e)}(\bar{\boldsymbol{\xi}}) = \begin{bmatrix} R_{\mathbf{i,p}}^{(e)}(\bar{\boldsymbol{\xi}}) & 0 & 0 \\ 0 & R_{\mathbf{i,p}}^{(e)}(\bar{\boldsymbol{\xi}}) & 0 \\ 0 & 0 & R_{\mathbf{i,p}}^{(e)}(\bar{\boldsymbol{\xi}}) \end{bmatrix}, \tag{5.28}$$

where $\bar{\boldsymbol{\xi}}$ is the multidimensional array of the quadrature point positions that are of relevance for the considered element e.

Thus, we discretize the virtual internal work in Equation (5.19) starting from the approximated element internal energy variation as

$$\delta W_{int} = \sum_{e=1}^{N_e} \int_{\Omega_e} (\mathbb{C}^{(k)} : \boldsymbol{\nabla}^s u_h^{(e)}(\bar{\boldsymbol{\xi}})) : \boldsymbol{\nabla}^s \delta u_h^{(e)}(\bar{\boldsymbol{\xi}})\, \mathrm{d}\Omega_e\,. \tag{5.29}$$

Laminated composites often exhibit material properties which may vary layer by layer even when they are pointwisely referred to the principal material coordinates. Using a special plywise integration rule consisting of $r + 1$ Gauss points per layer (as displayed in Figure 5.3), the IgG method provides a natural approach to account for this through-the-thickness dependency. In fact, we remark that $\mathbb{C}^{(k)}$ (i.e., $\mathbb{C}^{(k)} = \tilde{C}_{ijkl}^{(k)} \boldsymbol{E}_i \otimes \boldsymbol{E}_j \otimes \boldsymbol{E}_k \otimes \boldsymbol{E}_l$, with $\tilde{C}_{ijkl}^{(k)}$ defined in Equation (5.12)) represents the global material property tensor for the k-th layer, which can be traced during the elementwise assembly relying on the out-of-plane Gauss point number, allowing to significantly improve the overall post-processing quality in Section 5.4.

Remark 5.3. *Using a layer-by-layer integration rule allows to correctly capture the behavior of composites for any stacking sequence (e.g., both an even and odd number of variously oriented layers can be accounted for), or consider more general constitutive models, such as plasticity. Furthermore, we highlight that, based on our numerical experiments, considering $r + 1$ quadrature points per layer leads to basically the same accuracy as using $r - 1$, in accordance with the solid plate case modeled via IgG (see [62]).*
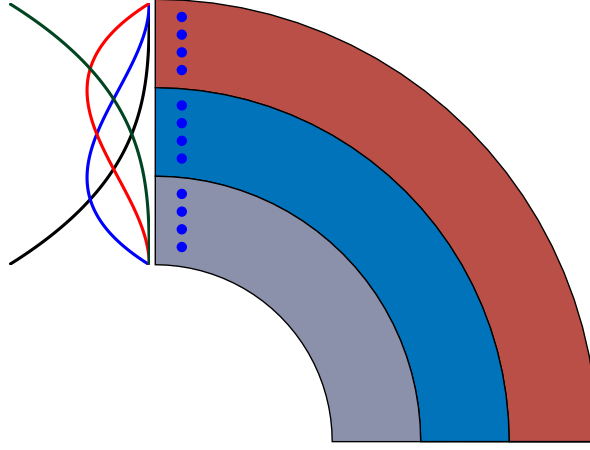
FIGURE 5.3: Single-element approach for the IgG method with special through-the-thickness integration rule (i.e., $r + 1$ Gauss points per layer). Example of shape functions for an out-of-plane degree of approximation $r = 3$. The blue bullets represent the position of the quadrature points along the thickness.

An alternative to the proposed integration method would be to split the assembly of stiffness matrices into their in-plane and out-of-plane contributions as in [12], thereby reducing the assembly cost significantly.

5.3.2 Isogeometric collocation method

In this section we describe our 3D IgC strategy to model laminated composite solid shells. Following Chapter 3 and [149], we propose a homogenized single-element approach, which takes into account layerwise variations of orthotropic material properties, homogenizing the constitutive behavior to form an equivalent single-layer laminate as in Figure 5.4. While this approach represents an obvious choice in the context of IgC, it can be regarded instead as a less accurate but cheaper alternative for the IgG method proposed in Section 5.3.1. In fact, to compute the displacement solution needed for the post-processing, the homogenized approach requires $r + 1$ integration points regardless the number of layers, while, using the previously introduced special integration rule, $r + 1$ Gauss points are employed for each ply.

Under these premises, for IgC, we homogenize the material properties according to [171] and using the relations introduced in Section 3.1.2 (see Equation (3.9)) in a more compact form as

$$\overline{\mathbb{C}}_{\zeta\eta} = \sum_{k=1}^{N} \bar{t}_k \mathbb{C}_{\zeta\eta}^{(k)} + \sum_{k=2}^{N} (\mathbb{C}_{\zeta3}^{(k)} - \overline{\mathbb{C}}_{\zeta3}) \bar{t}_k \frac{(\mathbb{C}_{\eta3}^{(1)} - \mathbb{C}_{\eta3}^{(k)})}{\mathbb{C}_{33}^{(k)}} \qquad \begin{matrix} \zeta = 1,2 \\ \eta = 1,2,3\,, \end{matrix} \tag{5.30a}$$

$$\overline{\mathbb{C}}_{33} = \frac{1}{\left(\sum_{k=1}^{N} \frac{\bar{t}_k}{\mathbb{C}_{33}^{(k)}} \right)}\,, \tag{5.30b}$$

$$\overline{\mathbb{C}}_{\theta\theta} = \frac{\left(\sum_{k=1}^{N} \frac{\bar{t}_k \mathbb{C}_{\theta\theta}^{(k)}}{\Delta_k} \right)}{\Delta} \qquad \theta = 4,5\,, \tag{5.30c}$$

$$\overline{\mathbb{C}}_{66} = \sum_{k=1}^{N} \bar{t}_k \mathbb{C}_{66}^{(k)} , \tag{5.30d}$$

with $\Delta = \prod_{\theta\theta=4}^{5} \left(\sum_{k=1}^{N} \frac{\bar{t}_k \mathbb{C}_{\theta\theta}^{(k)}}{\Delta_k} \right)$ and $\Delta_k = \prod_{\theta\theta=4}^{5} \mathbb{C}_{\theta\theta}^{k}$.

In Equation (5.30), N is the number of layers, $\mathbb{C}_{\zeta\eta}^{(k)}$ represents the $\zeta\eta$-th local com-
ponent of the fourth-order elasticity tensor in Voigt's notation (3.4) for the k-th layer,
and $\bar{t}_k = t_k/t$ stands for the volume fraction of the k-th lamina, t being the total
thickness and t_k the k-th thickness. In order to be used in the global framework
(see Equation (5.17)), the homogenized material tensor $\overline{\mathbb{C}} = \overline{\mathbb{C}}_{\alpha\beta\gamma\delta} \, \boldsymbol{a}_\alpha \otimes \boldsymbol{a}_\beta \otimes \boldsymbol{a}_\gamma \otimes \boldsymbol{a}_\delta$,
mapped from Voigt's to its full representation in indicial notation, is transformed
according to the basis change operator $D_{i\alpha}$, analogously to Equation (5.12), as

$$\tilde{\overline{\mathbb{C}}}_{ijkl} = D_{i\alpha} \, D_{j\beta} \, D_{k\gamma} \, D_{l\delta} \, \overline{\mathbb{C}}_{\alpha\beta\gamma\delta} . \tag{5.31}$$

Remark 5.4. *Considering a local reference system allows to define whether the ply stacking
sequence is symmetric or not with respect to the solid geometrical mid-surface. Adopting this
pointwise perspective, we remark that the homogenized single-element approach is immedi-
ately effective only for symmetric ply distributions as, for non-symmetric ones, the laminate
geometric and material mid-surface do not coincide. In any case, symmetric stacking se-
quences typically cover the most common cases in practice and, in the need for laminates
made of non-symmetric layer distributions, this technique finds still application when the
stacking sequence can be split into two symmetric piles, using one element per homogenized
stack with a C^0 interface (see Chapter 3 and reference [149]).*

Having defined how material properties are tuned for the homogenized single-
element approach, we proceed to detail our IgC strategy. We recall that colloca-
tion methods (see [16] and Section 2.1.3 for further details) directly discretize in
strong form the differential equations governing the problem evaluated at colloca-
tion points. Once again, we adopt the simplest and most widespread approach in
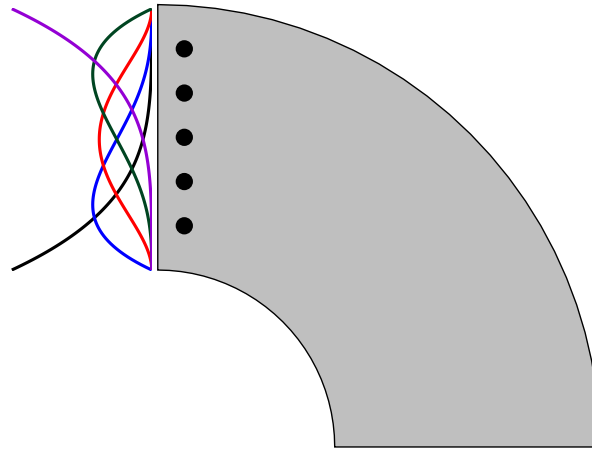
FIGURE 5.4: Homogenized single-element approach for IgC ($r + 1$ evaluation points inde-
pendently on the number of layers). Example of shape functions for an out-of-plane degree
of approximation $r = 4$. The black bullets represent the position of the quadrature points
along the thickness.

the engineering literature (see [30, 57] for alternative choices) and collocate at the images of Greville abscissae (see Equation (2.46)).

Having defined $\boldsymbol{\tau}$ as the multidimensional array of collocation points, the global displacement field $\boldsymbol{u}$ is approximated as a linear combination of NURBS multivariate shape functions $R_{\mathbf{i},\mathbf{p}}(\boldsymbol{\tau})$ and control variables $\hat{\mathbf{u}}_{\mathbf{i}}$ as

$$\boldsymbol{u} \approx \boldsymbol{u}_h(\boldsymbol{\tau}) = \sum_{\mathbf{i}} \tilde{\mathbf{R}}_{\mathbf{i},\mathbf{p}}(\boldsymbol{\tau})\,\hat{\mathbf{u}}_{\mathbf{i}}\,, \tag{5.32}$$

where we recall that $\boldsymbol{\tau}$ has been defined such that, for each i-th point and d-th parametric dimension, $\tau_i^d = \dfrac{\sum_{l=1}^{p_d} \xi_{i+l}}{p_d}$ with $i = 1, ..., m_d$. Then, the $\mathbf{i}$-th contribution of the multivariate shape functions matrix $\tilde{\mathbf{R}}_{\mathbf{i},\mathbf{p}}(\boldsymbol{\tau})$ is characterized as follows

$$\tilde{\mathbf{R}}_{\mathbf{i},\mathbf{p}}(\boldsymbol{\tau}) = \begin{bmatrix} R_{\mathbf{i},\mathbf{p}}(\boldsymbol{\tau}) & 0 & 0 \\ 0 & R_{\mathbf{i},\mathbf{p}}(\boldsymbol{\tau}) & 0 \\ 0 & 0 & R_{\mathbf{i},\mathbf{p}}(\boldsymbol{\tau}) \end{bmatrix}. \tag{5.33}$$

Finally, the approximation of system (5.14) reads as

$$[(\boldsymbol{\nabla} \cdot \overline{\mathbb{C}}) : \boldsymbol{\nabla}^s \boldsymbol{u}_h](\tau_i^d) + [\overline{\mathbb{C}} \vdots \boldsymbol{\nabla}(\boldsymbol{\nabla}^s \boldsymbol{u}_h)](\tau_i^d) + \boldsymbol{b}_h(\tau_i^d) = \mathbf{0} \qquad \forall \tau_i^d \in \Omega\,, \tag{5.34a}$$

$$[(\overline{\mathbb{C}} : \boldsymbol{\nabla}^s \boldsymbol{u}_h) \cdot \boldsymbol{n}](\tau_i^d) = \boldsymbol{t}_h(\tau_i^d) \qquad \forall \tau_i^d \in \Gamma_N\,, \tag{5.34b}$$

$$\boldsymbol{u}_h(\tau_i^d) = \boldsymbol{g}_h(\tau_i^d) \qquad \forall \tau_i^d \in \Gamma_D\,, \tag{5.34c}$$

where all quantities are evaluated in the global reference system as detailed in Section 5.1.

5.4 Numerical tests

In this section, we propose several benchmarks to showcase the effectiveness of the presented equilibrium-based stress recovery. To this extent, we consider a hollow cross-ply cylindrical solid shell under bending and we validate the obtained results against an overkill C^0 LW solution, addressing the main differences with respect to the proposed through-the-thickness integration IgG and homogenized IgC approaches, as well as the sensitivity of the method to two parameters of interest: i.e., number of layers and thickness-to-mean radius ratio.

5.4.1 Composite solid cylinder under bending

A hollow cross-ply cylindrical solid shell of total thickness t and made of N orthotropic layers is considered as in [184]. The structure, as detailed in Figure 5.5, is simply supported at both ends and subjected to a transverse sinusoidal loading, $q(X_1, X_2, X_3)$ on the inner surface, while the outer surface is traction-free. The thickness of every single layer is set to 1 mm and the edge length L is chosen to be equal to the mean radius $\bar{R}$, such that $\bar{R}$ is S times larger than the total thickness of the laminate, $S = \bar{R}/t = L/t$. Thus, S represents the inverse of the slender parameter or thickness-to-mean radius ratio.
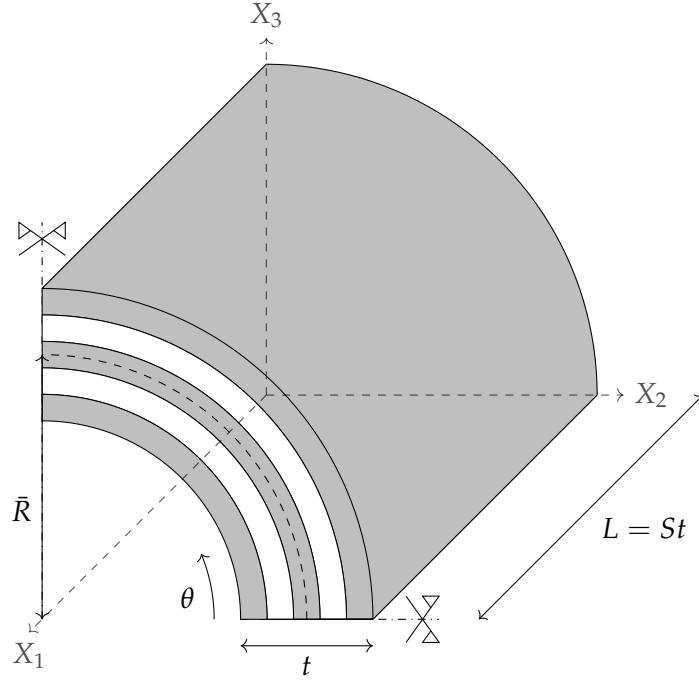
FIGURE 5.5: Quarter of composite cylindrical solid shell: problem geometry.

TABLE 5.1: Numerical tests material properties for 0°-oriented layers.

E_1	E_2	E_3	G_{23}	G_{13}	G_{12}	ν_{23}	ν_{13}	ν_{12}
[MPa]	[MPa]	[MPa]	[MPa]	[MPa]	[MPa]	[-]	[-]	[-]
25	1	1	0.2	0.5	0.5	0.25	0.25	0.25

Layer material parameters taken into account for all the proposed numerical tests are summarized in Table 5.1 for 0°-oriented plies, while the considered loading pressure is equal to

$$q(X_1, X_2, X_3) = \sigma_0 \cos(4\theta) \sin\left(\frac{\pi X_1}{St}\right), \tag{5.35}$$

where $\sigma_0 = $ -1 MPa and $\theta = \theta(X_2, X_3) \in [0, \bar{\theta}] = [0, \pi/2]$ is oriented anticlockwise as depicted in Figure 5.5. The inner and the outer surface radii are, respectively, $r_i = \bar{R} - \dfrac{t}{2}$ and $r_o = \bar{R} + \dfrac{t}{2}$.

The simply supported edge conditions are taken as

$$\tilde{\sigma}_{11} = 0 \text{ and } \tilde{u}_2 = \tilde{u}_3 = 0 \text{ at } X_1 = 0 \text{ and } X_1 = L, \tag{5.36}$$

while Neumann boundary conditions on the tube inner and outer surfaces are

$$\tilde{\sigma}_{13} = \tilde{\sigma}_{23} = 0 \text{ and } \tilde{\sigma}_{33} = q(X_1, X_2, X_3) \qquad \text{at } \sqrt{X_2^2 + X_3^2} = r_i, \tag{5.37a}$$

$$\tilde{\sigma}_{13} = \tilde{\sigma}_{23} = \tilde{\sigma}_{33} = 0 \qquad \text{at } \sqrt{X_2^2 + X_3^2} = r_o. \tag{5.37b}$$

Taking advantage of the problem's symmetry, we model only a quarter of cylinder, adding the following constraints

$$\tilde{\sigma}_{23} = \tilde{\sigma}_{12} = 0 \text{ and } \tilde{u}_2 = 0 \text{ at } X_2 = 0 \,, \tag{5.38a}$$

$$\tilde{\sigma}_{23} = \tilde{\sigma}_{13} = 0 \text{ and } \tilde{u}_3 = 0 \text{ at } X_3 = 0 \,. \tag{5.38b}$$

All results in the local reference system are then normalized[1] as

$$\overline{\sigma}_{ij} = \frac{\sigma_{ij}}{|\sigma_0|} \qquad i,j = 1,2,3 \,. \tag{5.39}$$

5.4.2   Single-element approach results: the post-processing effect

In this section, we present and comment several numerical results that consider a quarter of composite cylinder with $S = 20$ and a cross-ply distribution of 11 layers, namely a $0°/90°$ stacking sequence. LW methods allow to capture the mechanical state inside the laminate more accurately. Therefore, the stress profiles, either obtained *via* the appropriate constitutive law or recovered through the equilibrium imposition, are validated against an overkill IgG LW solution, computed according to [62], which uses degrees of approximation $p = q = 6, r = 4$ and a number of control points equal to 36x36x5xN (where N is the number of layers). More specifically, this LW reference solution is computed by modeling each material layer of the laminate by one patch through the thickness and keeping C^0 continuity at each ply interface. This technique allows to obtain a continuous out-of-plane stress profile through the thickness, but it is also computationally demanding because it requires a number of unknowns directly proportional to the number of layers.

5.4.2.1   IgG method with an *ad hoc* through-the-thickness integration rule

The numerical simulations in this section are post-processed starting from a single-element IgG approximation of the global displacements with an *ad hoc* integration rule that uses $r + 1$ Gauss points per layer. This simulation was performed by employing 22x22x4 control points, an in-plane degree of approximation $p = q = 4$, and an out-of plane degree of approximation $r = 3$.

     As a first example, in Figure 5.6, we present solution profiles for a sampling point located at $(X_1 = L/3, \theta = \bar{\theta}/3)$ in the left column, which prove the ability of the proposed approach to grant accurate in-plane results. Also, the right column in Figure 5.6 compares the out-of-plane stress state for the same sampling point with and without applying the presented post-processing step (see Section 5.2). These results show a remarkable improvement in the solution profiles of the out-of-plane stresses, which, after recovery, are continuous through-the-thickness as required by equilibrium. To provide a better contrast with respect to the untreated out-of-plane stresses in Figure 5.6, we recall that the use of a single element through the thickness with C^∞ shape functions leads to continuous through-the-thickness displacements

---

[1]We note that the results in Chapter 5 account for a different normalization with respect to Chapter 3 and 4, due to the fact that the Young's moduli as well as the shear elastic moduli considered in Section 5.4 are 6 order of magnitude less than the values used in Sections 3.2 and 4.4.

and, hence, strains. Then, if these strains are multiplied by layerwise discontinuous material properties, as in the case of cross-ply laminates, this results in a numerical approximation of the stresses that is discontinuous through the thickness, and therefore contravening equilibrium for out-of-plane stress components.

(a) Normalized σ_{11}

(b) Normalized σ_{13}

(c) Normalized σ_{22}

(d) Normalized σ_{23}

(e) Normalized σ_{12}

(f) Normalized σ_{33}
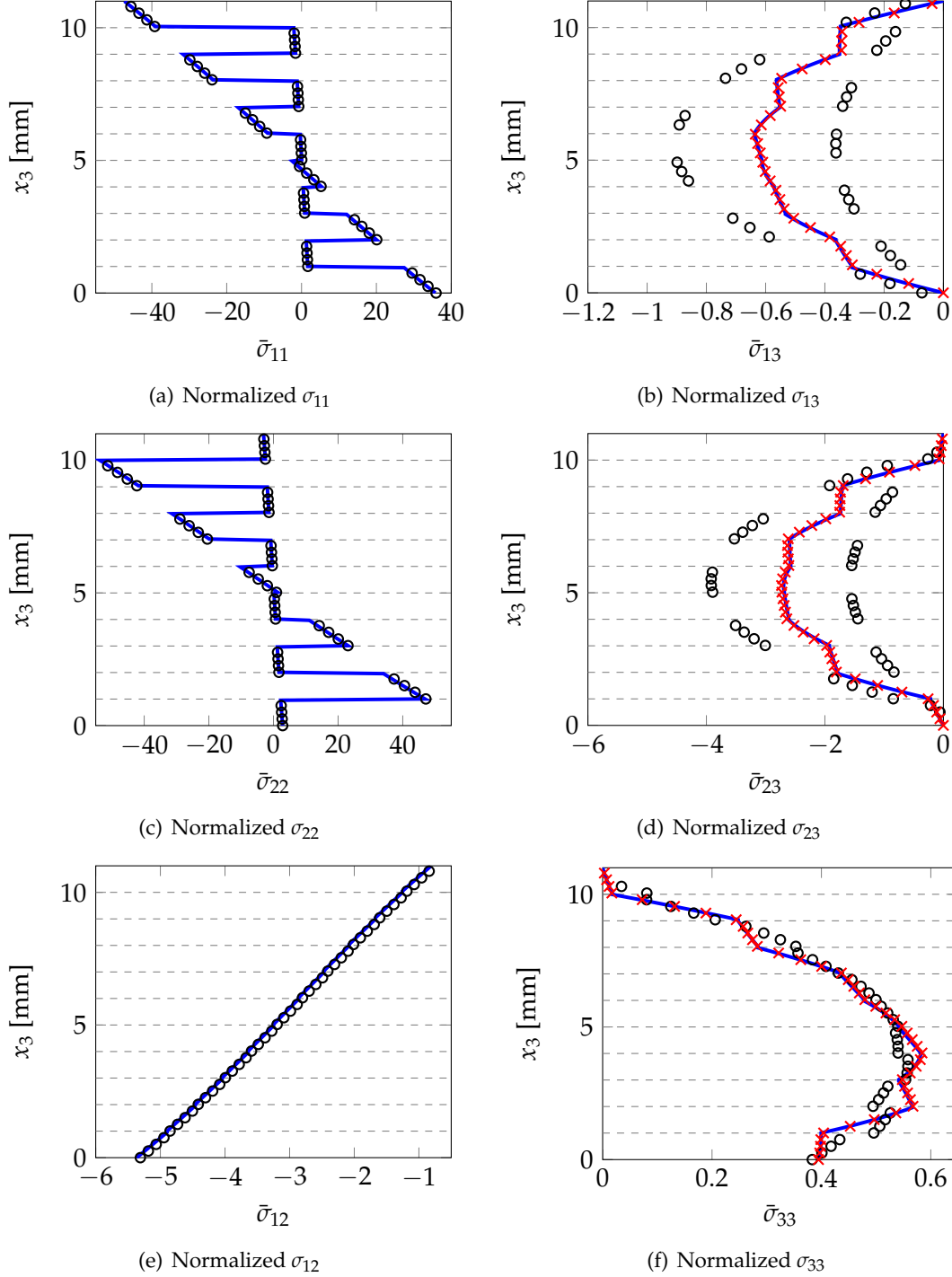
FIGURE 5.6: Through-the-thickness stress profiles evaluated at $(X_1 = L/3, \theta = \bar{\theta}/3)$ for IgG (degrees of approximation $p = q = 4$, $r = 3$, and 22x22x4 control points). Case: hollow cross-ply cylindrical solid shell with mean radius-to-thickness ratio $S = 20$, 11 layers, and $L = \bar{R}$ (——— overkill IgG LW solution, ○ single-element approach solution without post-processing, × post-processed solution).

(a) Normalized σ_{11}

(b) Normalized σ_{13}

(c) Normalized σ_{22}

(d) Normalized σ_{23}

(e) Normalized σ_{12}

(f) Normalized σ_{33}
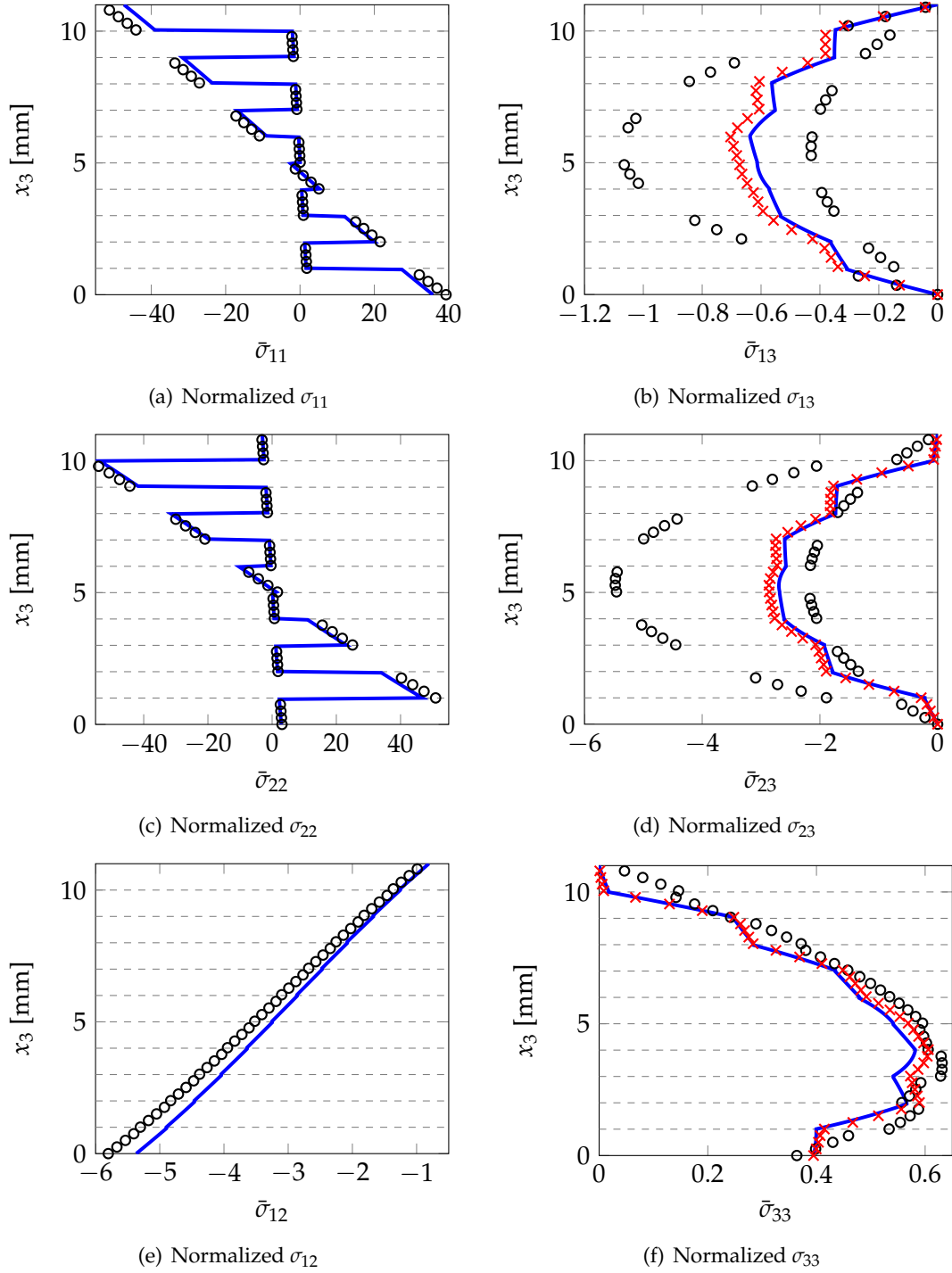
FIGURE 5.7: Through-the-thickness stress profiles evaluated at $(X_1 = L/3, \theta = \bar{\theta}/3)$ for IgC (degrees of approximation $p = q = 6$, $r = 4$, and 22x22x5 control points). Case: hollow cross-ply cylindrical solid shell with mean radius-to-thickness ratio $S = 20$, 11 layers, and $L = \bar{R}$ (—— overkill IgG LW solution, ○ single-element approach solution without post-processing, × post-processed solution).

5.4.2.2 Homogenized IgC approach results

In this section we report and discuss the stress recovery results derived from a global displacement field calculated with IgC and the homogenized single element through the thickness (see Section 5.3.2) at the same sampling point ($X_1 = L/3$, $\theta = \bar{\theta}/3$) as in Figure 5.6. For IgC we consider degrees of approximation $p = q = 6$, $r = 4$ and 22x22x5 control points. In Figure 5.7, we show the in-plane stress results in the left column, which prove to be in good agreement with the reference IgG LW solution. In the right column, we depict out-of-plane stresses either obtained from the appropriate constitutive law or recovered from equilibrium equations. The overall solution, both for in-plane and out-of-plane stresses is comparable to the reference solution, although it is also less precise than the stress fields calculated using IgG with the special integration rule. Further numerical tests using IgG coupled with a homogenized single element through the thickness show the same kind of stress profiles as provided by IgC in Figure 5.7. Thus, we believe that this behavior is most probably due to the material through-the-thickness homogenization. In any case, this approach leads to a less accurate but still very good solution, especially for the σ_{23} component, which represents the prominent out-of-plane stress for this type of benchmark.

In Figures 5.8-5.10, we compare recovered out-of-plane stress profiles, either obtained *via* a displacement-based IgG or IgC solution, against the considered reference results obtained with the overkill IgG LW method. To this end, the composite solid cylinder is sampled every quarter of length in both in-plane directions, showing the effectiveness of the presented post-processing all over the solid shell. In particular, this approach accurately captures the behavior of the cylindrical solid shell at the boundaries, namely satisfies Neumann boundary conditions for transverse shear stresses at the inner and outer surfaces of the laminate as in Equation (5.37) and the symmetry conditions with respect to σ_{13} and σ_{23} as in Equation (5.38).

5.4.2.3 Parametric study on mean radius-to-thickness cylinder ratio

The proposed stress recovery approach is further tested considering different benchmarks with a varying slenderness parameter (i.e., $S = 20$, 30, 40, and 50) for 11 and 33 layers as well as an increasing number of in-plane control points.

As a measure to assess the performance of the proposed stress recovery we introduce the following relative maximum error definition along the thickness

$$\mathrm{e}(\sigma_{i3}) = \frac{\max|\sigma_{i3}^{\mathrm{LW}}(\bar{x}_1, \bar{x}_2, x_3) - \sigma_{i3}^{\mathrm{recovered}}(\bar{x}_1, \bar{x}_2, x_3)|}{\max|\sigma_{i3}^{\mathrm{LW}}(\bar{x}_1, \bar{x}_2, x_3)|} \qquad i = 1,2,3, \qquad (5.40)$$

for which in the case of a zero stress profile we just compute the absolute maximum error to avoid 0/0 division. Additionally, the term $\sigma_{i3}^{\mathrm{LW}}(\bar{x}_1, \bar{x}_2, x_3)$ ($i = 1,2,3$) in Equation (5.40) represents the out-of-plane stress patterns from the reference solution obtained *via* an overkill IgG LW approach that comprises again a degree of approximation $p = q = 6$, $r = 4$ and a number of control points equal to 36x36x5xN N (where N is the number of layers).
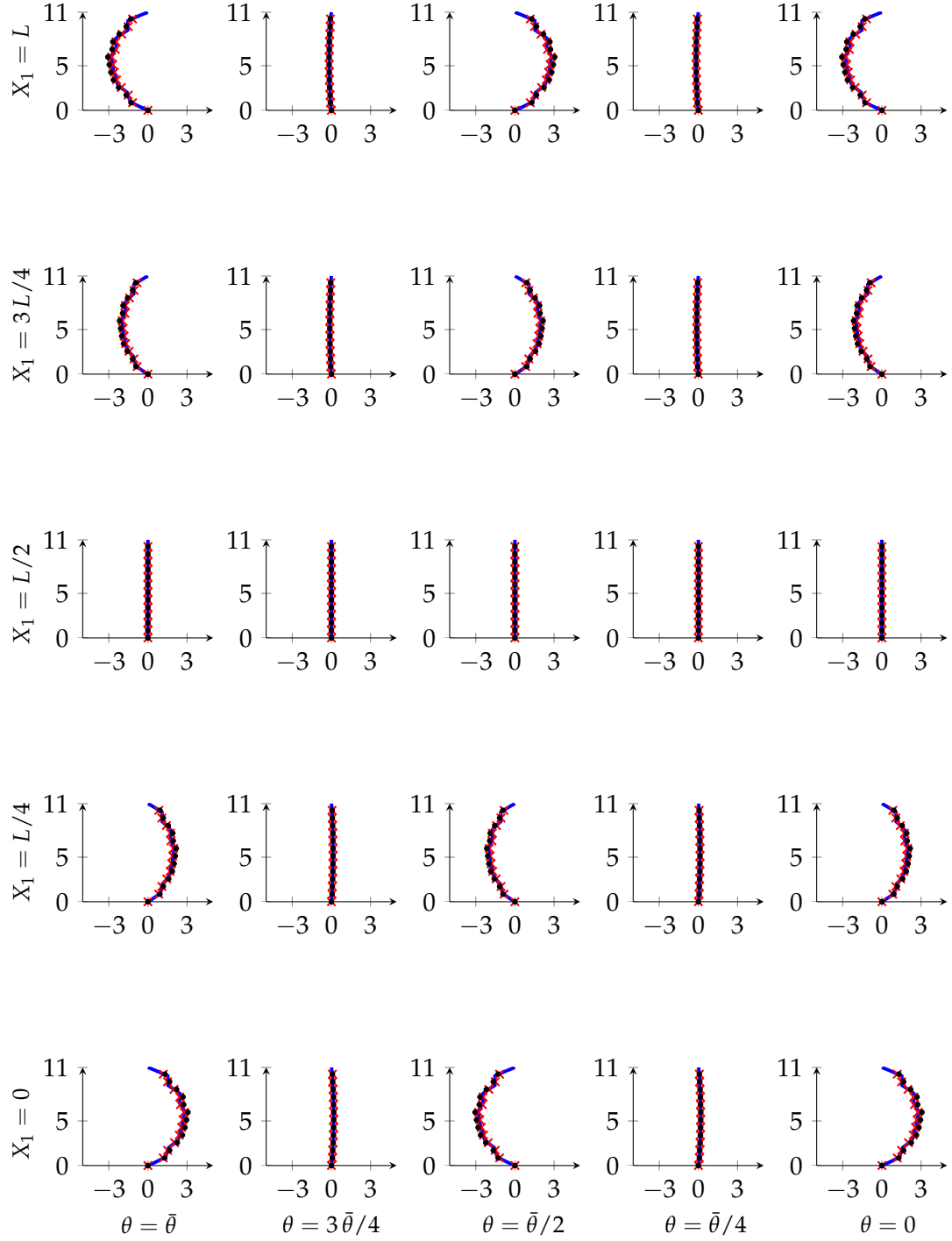
FIGURE 5.8: Through-the-thickness out-of-plane $\bar{\sigma}_{13}$ profiles for the 11-layer case for in-plane sampling points situated at every quarter of length in both in-plane directions θ and X_1. For each subplot, the horizontal axis shows the values of $\bar{\sigma}_{13}$ and the vertical axis the local coordinate x_3. L represents the total length of the plate, which for this case is $L = 220\,\text{mm}$ ($L = St$ with $t = 11\,\text{mm}$ and $S = 20$), while the number of layers is 11. × IgG post-processed solution ($p = q = 4$, $r = 3$, and 22x22x4 control points), • IgC post-processed solution ($p = q = 6$, $r = 4$, and 22x22x5 control points), —— overkill IgG LW solution ($p = q = 6$, $r = 4$, and 36x36x55 control points).

FIGURE 5.9: Through-the-thickness out-of-plane $\bar{\sigma}_{23}$ profiles for the 11-layer case for in-plane sampling points situated at every quarter of length in both in-plane directions θ and X_1. For each subplot, the horizontal axis shows the values of $\bar{\sigma}_{23}$ and the vertical axis the local coordinate x_3. L represents the total length of the plate, which for this case is $L = 220\,\text{mm}$ ($L = St$ with $t = 11\,\text{mm}$ and $S = 20$), while the number of layers is 11. × IgG post-processed solution ($p = q = 4$, $r = 3$, and 22x22x4 control points), • IgC post-processed solution ($p = q = 6$, $r = 4$, and 22x22x5 control points), —— overkill IgG LW solution ($p = q = 6$, $r = 4$, and 36x36x55 control points).

FIGURE 5.10: Through-the-thickness out-of-plane $\bar{\sigma}_{33}$ profiles for the 11-layer case for in-plane sampling points situated at every quarter of length in both in-plane directions θ and X_1. For each subplot, the horizontal axis shows the values of $\bar{\sigma}_{33}$ and the vertical axis the local coordinate x_3. L represents the total length of the plate, which for this case is $L = 220\,\text{mm}$ ($L = St$ with $t = 11\,\text{mm}$ and $S = 20$), while the number of layers is 11. × IgG post-processed solution ($p = q = 4$, $r = 3$, and 22x22x4 control points), • IgC post-processed solution ($p = q = 6$, $r = 4$, and 22x22x5 control points), —— overkill IgG LW solution ($p = q = 6$, $r = 4$, and 36x36x55 control points).

In Figure 5.11, we assess the performance of both the IgG approach and the homogenized IgC method coupled with the presented post-processing technique at $(X_1 = L/3, \theta = \bar{\theta}/3)$.

The stress recovery approach seems to be particularly suitable to describe the behavior of slender laminates characterized by a significant number of layers, leading to errors that are typically in the 10% range or lower at convergence despite the chosen displacement-based approach. More specifically, IgG provides errors in the order of 2% and 1% in average for the analyzed 11- and 33-layer cases, respectively, while IgC allows to obtain errors in the range of 5%-10% or lower, whenever $S \geq 30$. Furthermore, IgC proves to be more sensitive to variations of the slenderness parameter S with respect to the proposed IgG approach. This is due to the fact that a slender laminate made of a significant number of layers is closer to a structure with average material properties. We would like to remark that the degrees of approximation adopted for the considered example are taken accordingly to Chapter 3 and references [62, 149], which proved to be suitable choices to model less complex geometries.

In Figure 5.11, we also observe that considering a mesh comprising 22x22 in-plane control points allows to obtain a sufficiently accurate stress solution and further in-plane refinement operations do not seem to significantly improve the quality of the overall solution. This is due to the fact that the modeling error, given by the equilibrium-based direct integration, dominates over the approximation error.

Finally, to highlight the quantitative gain given by the proposed stress recovery application, we report in Table 5.2 the relative maximum error at $(X_1 = L/3, \theta = \bar{\theta}/3)$ obtained considering out-of-plane stress components either directly computed *via* the appropriate constitutive law or reconstructed.

TABLE 5.2: Simply-supported hollow cross-ply cylindrical solid shell under sinusoidal load with a number of layers equal to 11. Out-of-plane stress maximum relative error along the thickness with respect to an overkill IgG LW solution (degrees of approximation $p = q = 6$, $r = 4$ and number of control points equal to 36x36x55) at $(X_1 = L/3, \theta = \bar{\theta}/3)$. Assessment of IgG and IgC before and after the application of the proposed post-processing technique to recover out-of-plane stresses for different approximation degrees and a fixed mesh comprising 22x22 in-plane control points.

	Method	IgG			IgC		
	Degrees of approximation	$p = q = 4, r = 3$			$p = q = 6, r = 4$		
S	Out-of-plane maximum relative error	e(σ_{13})	e(σ_{23})	e(σ_{33})	e(σ_{13})	e(σ_{23})	e(σ_{33})
	at $(X_1 = L/3, \theta = \bar{\theta}/3)$	[%]	[%]	[%]	[%]	[%]	[%]
20	before post-processing	46.6	47.8	18.7	71.2	105	23.1
	after post-processing	2.25	1.72	1.38	10.4	6.54	5.41
30	before post-processing	46.8	47.6	19.8	67.0	103	27.4
	after post-processing	2.28	1.77	1.18	6.39	4.37	4.63
40	before post-processing	47.0	47.7	22.6	65.4	100	30.5
	after post-processing	2.36	1.83	1.22	4.76	2.79	4.40
50	before post-processing	47.3	47.8	25.2	64.9	97.9	33.1
	after post-processing	2.43	1.88	1.23	3.98	1.76	4.37
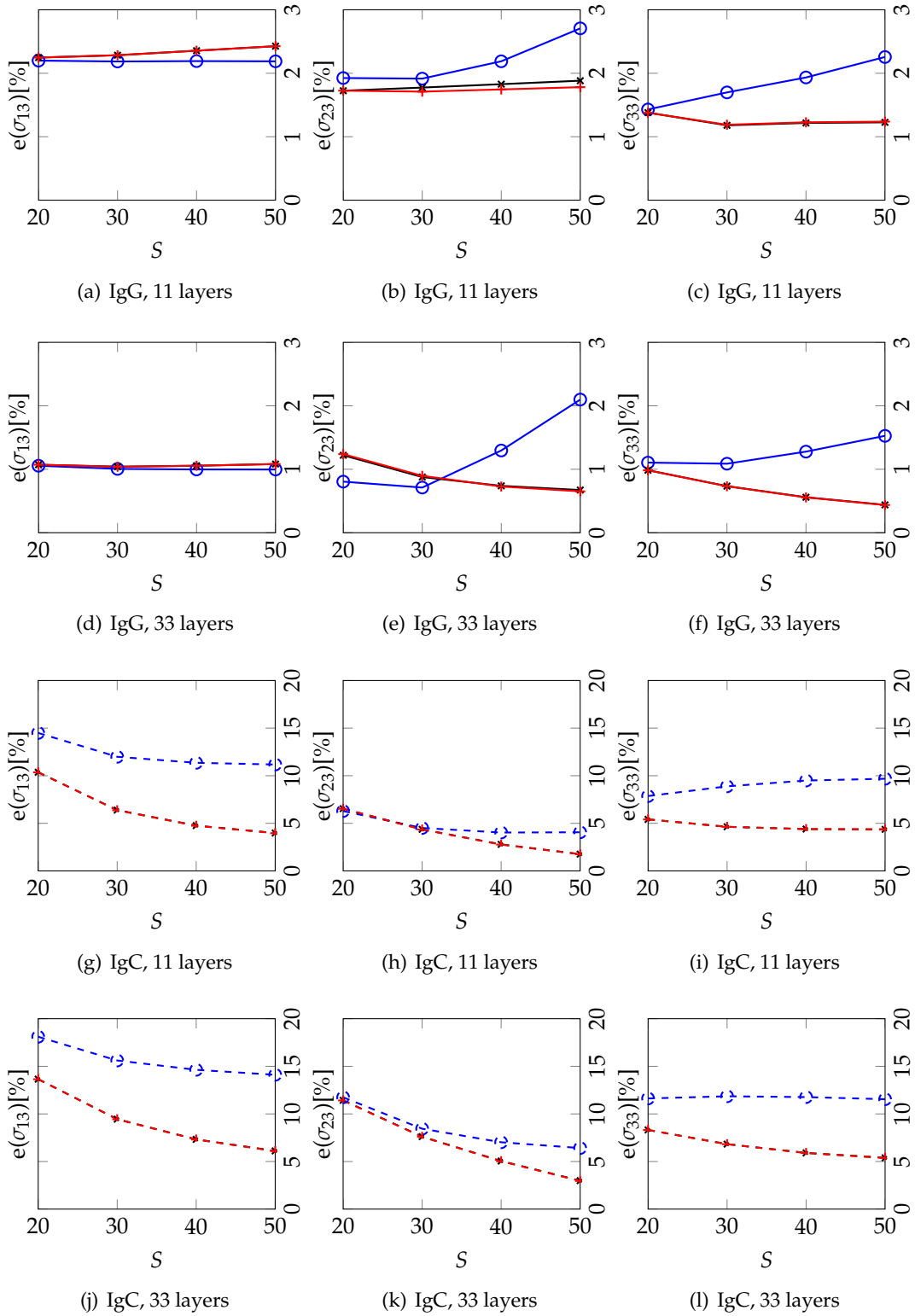
FIGURE 5.11: Simply-supported hollow cross-ply cylindrical solid shell under sinusoidal load: maximum relative percentage error evaluation at ($X_1 = L/3$, $\theta = \bar{\theta}/3$) of the post-processed single-element approach, with respect to an overkill IgG LW solution (degrees of approximation $p = q = 6$, $r = 4$ and number of control points equal to 36x36x55). Different mean radius-to-thickness ratios S are investigated for a number of layers equal to 11 and 33 (IgG - degrees of approximation $p = q = 4$, $r = 3$ and number of in-plane control points per parametric direction: ⊸ 11, ⊸✶⊸ 22, ⊹ 44; IgC - degrees of approximation $p = q = 6$, $r = 4$ and number of control points per in-plane direction: 11 ⌐⊸⌐ , 22 ⌐➤⌐ , 44 ⌐✚⌐). Solutions obtained using 22 and 44 control points are virtually indistinguishable in most cases for both IgG and IgC cases.

5.5 Conclusions

In this chapter we propose an efficient two-step single-element displacement-based approach to model the stress field in laminated solid shells. This technique combines coarse 3D isogeometric computations, either using a calibrated layer-by-layer integration rule or a homogenized approach, with an *a posteriori* step where equilibrium is directly imposed in strong form. Both IgG and IgC methods are successfully investigated. Homogenization is immediately effective only for symmetric ply distributions, which cover most common cases in practice. While this approach represents a natural choice for IgC, it can be regarded as a less accurate but cost-effective alternative for the proposed IgG method, requiring only $r + 1$ quadrature points through the thickness. However, despite being more computationally demanding, the proposed layer-by-layer integration rule (i.e., $r + 1$ Gauss points per ply) for the IgG approach allows to correctly capture the behavior of composites for any stacking sequence and to investigate more complex constitutive models.

Using only one element through the thickness with highly continuous shape functions provides a good in-plane solution, but the out-of-plane stress profiles violate the continuity requirements prescribed by equilibrium. Adopting a local system, which grants that no additional terms appear in the balance of linear momentum equations, an accurate solution is attainable also in terms of out-of-plane stress components after the post-processing step.

The proposed stress recovery method results in a straightforward approach in terms of implementation since it is only based on the numerical integration of equilibrium equations through the thickness and all the required components can be easily computed by differentiating the global displacement fields. The *a posteriori* step requires the shape functions to be highly continuous (as fully granted by IgA), is direct, and can be easily performed at locations of interest, resulting in a very interesting alternative to LW techniques. Several benchmarks confirm the excellent behavior of the proposed approach also on the laminate boundary and have assessed the sensitivity of the stress recovery to different parameters, namely the mean radius-to-thickness ratio and number of layers. Our results show that the proposed post-processing technique is especially accurate in the case of slender composites made of a significant number of layers.

Future research topics consist of the extension of our equilibrium-based stress recovery approach to bivariate shells and the inclusion of large deformations. Also, more efficient through-the-thickness integration strategies will be considered in forthcoming studies. Finally, in Appendix 5.B we have also investigated a strategy to recover the out-of-plane normal stress component using only first-order derivatives of the shear interlaminar stresses with respect to the in-plane coordinates in the context of solid composite structures. This study, even though at a preliminary stage, lowers the high-order continuity requirements of the recovery. Further investigations need to be carried out to explore this approach as well.

Appendix 5.A: Components of the stress derivatives

5.A.1   Stress derivatives with respect to the local reference system

In Section 5.2, the stress recovery procedure proposed in Chapter 3 and reference [62, 149] is extended to the case of curved laminated structures. In this regard, we need to compute the first and second derivatives of the stress tensor in the chosen local reference system $\{x_\alpha\}$. Therefore, starting from the displacement field in the global cartesian system $\{X_i\}$, $d\sigma/dx_\mu$ and $d^2\sigma/dx_\mu dx_\nu$ have to be calculated.

From Equation (5.10), the stress derivatives can be computed as

$$\frac{d\sigma}{dx_\mu} = \frac{d\mathbb{C}}{dx_\mu} : \varepsilon + \mathbb{C} : \frac{d\varepsilon}{dx_\mu}, \tag{5.A.1}$$

$$\frac{d^2\sigma}{dx_\mu dx_\nu} = \frac{d^2\mathbb{C}}{dx_\mu dx_\nu} : \varepsilon + \frac{d\mathbb{C}}{dx_\mu} : \frac{d\varepsilon}{dx_\nu} + \frac{d\mathbb{C}}{dx_\nu} : \frac{d\varepsilon}{dx_\mu} + \mathbb{C} : \frac{d^2\varepsilon}{dx_\mu dx_\nu}, \tag{5.A.2}$$

which need to be further detailed in terms of explicit expressions for the first and second derivatives of $\mathbb{C}$ and ε.

The strain and its derivatives can be easily obtained with respect to the local system $\{x_\alpha\}$ as:

$$\varepsilon = \varepsilon_{\alpha\beta} e_\alpha \otimes e_\beta, \tag{5.A.3a}$$

$$\frac{d\varepsilon}{dx_\mu} = \varepsilon_{\alpha\beta,\mu} e_\alpha \otimes e_\beta, \tag{5.A.3b}$$

$$\frac{d^2\varepsilon}{dx_\mu dx_\nu} = \varepsilon_{\alpha\beta,\mu\nu} e_\alpha \otimes e_\beta. \tag{5.A.3c}$$

From Equation (5.7), and applying the chain rule, the components $\varepsilon_{\alpha\beta}$, $\varepsilon_{\alpha\beta,\mu}$, and $\varepsilon_{\alpha\beta,\mu\nu}$ are computed as:

$$\varepsilon_{\alpha\beta} = \tilde{\varepsilon}_{ij} C_{i\alpha} C_{j\beta} = \frac{1}{2} \left(\tilde{u}_{i,j} + \tilde{u}_{j,i} \right) C_{i\alpha} C_{j\beta}, \tag{5.A.4a}$$

$$\varepsilon_{\alpha\beta,\mu} = \frac{d\varepsilon_{\alpha\beta}}{dx_\mu} = \frac{d\varepsilon_{\alpha\beta}}{dX_k} \frac{dX_k}{dx_\mu} = \frac{1}{2} \left(\tilde{u}_{i,jk} + \tilde{u}_{j,ik} \right) C_{i\alpha} C_{j\beta} C_{k\mu}, \tag{5.A.4b}$$

$$\varepsilon_{\alpha\beta,\mu\nu} = \frac{d^2\varepsilon_{\alpha\beta}}{dx_\mu dx_\nu} = \frac{\varepsilon_{\alpha\beta,\mu}}{dX_l} \frac{dX_l}{dx_\nu} = \frac{1}{2} \left(\tilde{u}_{i,jkl} + \tilde{u}_{j,ikl} \right) C_{i\alpha} C_{j\beta} C_{k\mu} C_{l\nu}, \tag{5.A.4c}$$

where we applied the definition (5.3) and the property (5.4). The displacement derivatives $\tilde{u}_{i,j}$, $\tilde{u}_{i,jk}$, and $\tilde{u}_{i,jkl}$ are simply computed as:

$$\tilde{u}_{i,j} = \frac{d\tilde{u}_i}{dX_j}, \tag{5.A.5a}$$

$$\tilde{u}_{i,jk} = \frac{d^2\tilde{u}_i}{dX_j dX_k}, \tag{5.A.5b}$$

$$\tilde{u}_{i,jkl} = \frac{d^3\tilde{u}_i}{dX_j dX_k dX_l}. \tag{5.A.5c}$$

Furthermore, we would like to remark that the derivatives $\tilde{u}_{i,j}$, $\tilde{u}_{i,jk}$, and $\tilde{u}_{i,jkl}$ are evaluated starting from the global components of the solution $\tilde{u}_i$ in a straightforward manner. In fact, relying on high-order continuity properties, IgA allows to easily perform the necessary computations.

In the same way, the derivatives of $\mathbb{C}$, defined starting from Equation (5.11), are computed as

$$\frac{d\mathbb{C}}{dx_\mu} = \mathbb{C}_{\alpha\beta\gamma\delta,\mu} \boldsymbol{a}_\alpha \otimes \boldsymbol{a}_\beta \otimes \boldsymbol{a}_\gamma \otimes \boldsymbol{a}_\delta + \mathbb{C}_{\alpha\beta\gamma\delta} \frac{d}{dx_\mu} \left(\boldsymbol{a}_\alpha \otimes \boldsymbol{a}_\beta \otimes \boldsymbol{a}_\gamma \otimes \boldsymbol{a}_\delta \right), \quad \text{(5.A.6a)}$$

$$\frac{d^2\mathbb{C}}{dx_\mu dx_\nu} = \mathbb{C}_{\alpha\beta\gamma\delta,\mu\nu} \boldsymbol{a}_\alpha \otimes \boldsymbol{a}_\beta \otimes \boldsymbol{a}_\gamma \otimes \boldsymbol{a}_\delta + \mathbb{C}_{\alpha\beta\gamma\delta,\mu} \frac{d}{dx_\nu} \left(\boldsymbol{a}_\alpha \otimes \boldsymbol{a}_\beta \otimes \boldsymbol{a}_\gamma \otimes \boldsymbol{a}_\delta \right)$$
$$+ \mathbb{C}_{\alpha\beta\gamma\delta,\nu} \frac{d}{dx_\mu} \left(\boldsymbol{a}_\alpha \otimes \boldsymbol{a}_\beta \otimes \boldsymbol{a}_\gamma \otimes \boldsymbol{a}_\delta \right) + \mathbb{C}_{\alpha\beta\gamma\delta} \frac{d^2}{dx_\mu dx_\nu} \left(\boldsymbol{a}_\alpha \otimes \boldsymbol{a}_\beta \otimes \boldsymbol{a}_\gamma \otimes \boldsymbol{a}_\delta \right),$$
$$\text{(5.A.6b)}$$

where

$$\mathbb{C}_{\alpha\beta\gamma\delta,\mu} = \frac{d\mathbb{C}_{\alpha\beta\gamma\delta}}{dx_\mu}, \quad \text{(5.A.7a)}$$

$$\mathbb{C}_{\alpha\beta\gamma\delta,\mu\nu} = \frac{d^2\mathbb{C}_{\alpha\beta\gamma\delta}}{dx_\mu dx_\nu}. \quad \text{(5.A.7b)}$$

In Equation (5.A.6), the derivatives $d\boldsymbol{a}_\alpha/dx_\mu$ and $d^2\boldsymbol{a}_\alpha/dx_\mu dx_\nu$ do not vanish in general, as already discussed in Section 5.1.1. For heterogeneous materials, in which the material coefficients may change from point to point, the terms $\mathbb{C}_{\alpha\beta\gamma\delta,\mu}$ and $\mathbb{C}_{\alpha\beta\gamma\delta,\mu\nu}$ may be also different from zero.

Remark 5.A.1. *For the case of homogeneous anisotropic materials (including orthotropic ones) in which the fibers have a constant orientation with respect to the local basis $\{\boldsymbol{a}_\alpha\}$, the terms $\mathbb{C}_{\alpha\beta\gamma\delta,\mu}$ and $\mathbb{C}_{\alpha\beta\gamma\delta,\mu\nu}$ vanish. This is the case, e.g., of multi-layered structures in which stacks of materials with different orientations are used: within each layer (k) the material coefficients $\mathbb{C}^{(k)}_{\alpha\beta\gamma\delta}$ are constant for the chosen basis $\{\boldsymbol{a}_\alpha\}$.*

Finally, the stress derivative terms $\sigma_{\alpha\beta,\mu}$ and $\sigma_{\alpha\beta,\mu\nu}$ required by the recovery integrals (5.23) and (5.24) are computed as:

$$\sigma_{\alpha\beta,\mu} = \left(\boldsymbol{e}_\alpha \otimes \boldsymbol{e}_\beta \right) : \frac{d\mathbb{C}}{dx_\mu} : \boldsymbol{\varepsilon} + \left(\boldsymbol{e}_\alpha \otimes \boldsymbol{e}_\beta \right) : \mathbb{C} : \frac{d\boldsymbol{\varepsilon}}{dx_\mu}, \quad \text{(5.A.8a)}$$

$$\sigma_{\alpha\beta,\mu\nu} = \left(\boldsymbol{e}_\alpha \otimes \boldsymbol{e}_\beta \right) : \frac{d^2\mathbb{C}}{dx_\mu dx_\nu} : \boldsymbol{\varepsilon} + \left(\boldsymbol{e}_\alpha \otimes \boldsymbol{e}_\beta \right) : \frac{d\mathbb{C}}{dx_\mu} : \frac{d\boldsymbol{\varepsilon}}{dx_\nu}$$
$$+ \left(\boldsymbol{e}_\alpha \otimes \boldsymbol{e}_\beta \right) : \frac{d\mathbb{C}}{dx_\nu} : \frac{d\boldsymbol{\varepsilon}}{dx_\mu} + \left(\boldsymbol{e}_\alpha \otimes \boldsymbol{e}_\beta \right) : \mathbb{C} : \frac{d^2\boldsymbol{\varepsilon}}{dx_\mu dx_\nu}.$$
$$\text{(5.A.8b)}$$

Thus, considering Equations (5.A.6), the terms $\sigma_{\alpha\beta,\mu}$ and $\sigma_{\alpha\beta,\mu\nu}$ can be written as:

$$
\begin{aligned}
\sigma_{\alpha\beta,\mu} = & \Big(\mathbb{C}_{\alpha\beta\gamma\delta,\mu} + \mathbb{C}_{\psi\beta\gamma\delta}A_{\psi\alpha\mu} + \mathbb{C}_{\alpha\psi\gamma\delta}A_{\psi\beta\mu} + \mathbb{C}_{\alpha\beta\psi\delta}A_{\psi\gamma\mu} \\
& + \mathbb{C}_{\alpha\beta\gamma\psi}A_{\psi\delta\mu} \Big) \varepsilon_{\gamma\delta} + \mathbb{C}_{\alpha\beta\gamma\delta}\varepsilon_{\gamma\delta,\mu} \, ,
\end{aligned}
\tag{5.A.9a}
$$

$$
\begin{aligned}
\sigma_{\alpha\beta,\mu\nu} = \Big(& \mathbb{C}_{\alpha\beta\gamma\delta,\mu\nu} \\
& + \mathbb{C}_{\psi\beta\gamma\delta,\mu}A_{\psi\alpha\nu} + \mathbb{C}_{\alpha\psi\gamma\delta,\mu}A_{\psi\beta\nu} + \mathbb{C}_{\alpha\beta\psi\delta,\mu}A_{\psi\gamma\nu} + \mathbb{C}_{\alpha\beta\gamma\psi,\mu}A_{\psi\delta\nu} \\
& + \mathbb{C}_{\psi\beta\gamma\delta,\nu}A_{\psi\alpha\mu} + \mathbb{C}_{\alpha\psi\gamma\delta,\nu}A_{\psi\beta\mu} + \mathbb{C}_{\alpha\beta\psi\delta,\nu}A_{\psi\gamma\mu} + \mathbb{C}_{\alpha\beta\gamma\psi,\nu}A_{\psi\delta\mu} \\
& + \mathbb{C}_{\psi\beta\gamma\delta}B_{\psi\alpha\mu\nu} + \mathbb{C}_{\psi\omega\gamma\delta}A_{\psi\alpha\mu}A_{\omega\beta\nu} + \mathbb{C}_{\psi\beta\omega\delta}A_{\psi\alpha\mu}A_{\omega\gamma\nu} + \mathbb{C}_{\psi\beta\gamma\omega}A_{\psi\alpha\mu}A_{\omega\delta\nu} \\
& + \mathbb{C}_{\omega\psi\gamma\delta}A_{\psi\beta\mu}A_{\omega\alpha\nu} + \mathbb{C}_{\alpha\psi\gamma\delta}B_{\psi\beta\mu\nu} + \mathbb{C}_{\delta\mu\psi\omega\delta}A_{\psi\beta\mu}A_{\omega\gamma\nu} + \mathbb{C}_{\delta\mu\psi\gamma\omega}A_{\psi\beta\mu}A_{\omega\delta\nu} \\
& + \mathbb{C}_{\omega\beta\psi\delta}A_{\psi\gamma\mu}A_{\omega\alpha\nu} + \mathbb{C}_{\alpha\omega\psi\delta}A_{\psi\gamma\mu}A_{\omega\beta\nu} + \mathbb{C}_{\alpha\beta\psi\delta}B_{\psi\gamma\mu\nu} + \mathbb{C}_{\alpha\beta\psi\omega}A_{\psi\gamma\mu}A_{\omega\delta\nu} \\
& + \mathbb{C}_{\omega\beta\gamma\psi}A_{\psi\delta\mu}A_{\omega\alpha\nu} + \mathbb{C}_{\alpha\omega\gamma\psi}A_{\psi\delta\mu}A_{\omega\beta\nu} + \mathbb{C}_{\alpha\beta\omega\psi}A_{\psi\delta\mu}A_{\omega\gamma\nu} + \mathbb{C}_{\alpha\beta\gamma\psi}B_{\psi\delta\mu\nu} \Big) \varepsilon_{\gamma\delta} \\
& + \Big(\mathbb{C}_{\alpha\beta\gamma\delta,\mu} + \mathbb{C}_{\psi\beta\gamma\delta}A_{\psi\alpha\mu} + \mathbb{C}_{\alpha\psi\gamma\delta}A_{\psi\beta\mu} + \mathbb{C}_{\alpha\beta\psi\delta}A_{\psi\gamma\mu} + \mathbb{C}_{\alpha\beta\gamma\psi}A_{\psi\delta\mu} \Big) \varepsilon_{\gamma\delta,\nu} \\
& + \Big(\mathbb{C}_{\alpha\beta\gamma\delta,\nu} + \mathbb{C}_{\psi\beta\gamma\delta}A_{\psi\alpha\nu} + \mathbb{C}_{\alpha\psi\gamma\delta}A_{\psi\beta\nu} + \mathbb{C}_{\alpha\beta\psi\delta}A_{\psi\gamma\nu} + \mathbb{C}_{\alpha\beta\gamma\psi}A_{\psi\delta\nu} \Big) \varepsilon_{\gamma\delta,\mu} \\
& + \mathbb{C}_{\alpha\beta\gamma\delta}\varepsilon_{\gamma\delta,\mu\nu} \, ,
\end{aligned}
\tag{5.A.9b}
$$

where $\varepsilon_{\gamma\delta}$, $\varepsilon_{\gamma\delta,\mu}$, and $\varepsilon_{\gamma\delta,\mu\nu}$ are defined in (5.A.4), while $A_{\psi\alpha\mu}$ and $B_{\psi\alpha\mu\nu}$ are:

$$
A_{\psi\alpha\mu} = \frac{\mathrm{d}\boldsymbol{a}_\psi}{\mathrm{d}x_\mu} \cdot \boldsymbol{e}_\alpha \, ,
\tag{5.A.10a}
$$

$$
B_{\psi\alpha\mu\nu} = \frac{\mathrm{d}^2\boldsymbol{a}_\psi}{\mathrm{d}x_\mu \mathrm{d}x_\nu} \cdot \boldsymbol{e}_\alpha \, .
\tag{5.A.10b}
$$

In the case that the basis $\{\boldsymbol{a}_\alpha\}$ depends on the parametric coordinates (ξ^1, ξ^2, ξ^3), its derivatives with respect to the coordinates $\{x_\alpha\}$ can be computed by applying the chain rule. Thus, we first evaluate $\mathrm{d}\boldsymbol{a}_\alpha/\mathrm{d}\xi^\theta$ and $\mathrm{d}^2\boldsymbol{a}_\alpha/\mathrm{d}\xi^\theta \mathrm{d}\xi^\phi$, and from that, the quantities $\mathrm{d}\boldsymbol{a}_\alpha/\mathrm{d}x_\mu$ and $\mathrm{d}^2\boldsymbol{a}_\alpha/\mathrm{d}x_\mu \mathrm{d}x_\nu$ are obtained as

$$
\frac{\mathrm{d}\boldsymbol{a}_\alpha}{\mathrm{d}\xi^\theta} = \frac{\mathrm{d}\boldsymbol{a}_\alpha}{\mathrm{d}x_\mu}\frac{\mathrm{d}x_\mu}{\mathrm{d}X_i}\frac{\mathrm{d}X_i}{\mathrm{d}\xi^\theta} \, ,
\tag{5.A.11a}
$$

$$
\begin{aligned}
\frac{\mathrm{d}^2\boldsymbol{a}_\alpha}{\mathrm{d}\xi^\theta \mathrm{d}\xi^\phi} = & \left(\frac{\mathrm{d}^2\boldsymbol{a}_\alpha}{\mathrm{d}x_\mu \mathrm{d}x_\nu}\frac{\mathrm{d}x_\mu}{\mathrm{d}X_i}\frac{\mathrm{d}x_\nu}{\mathrm{d}X_j} + \frac{\mathrm{d}\boldsymbol{a}_\alpha}{\mathrm{d}x_\mu}\frac{\mathrm{d}^2 x_\mu}{\mathrm{d}X_i \mathrm{d}X_j} \right)\frac{\mathrm{d}X_i}{\mathrm{d}\xi^\theta}\frac{\mathrm{d}X_j}{\mathrm{d}\xi^\phi} \\
& + \frac{\mathrm{d}\boldsymbol{a}_\alpha}{\mathrm{d}x_\rho}\frac{\mathrm{d}x_\rho}{\mathrm{d}X_k}\frac{\mathrm{d}^2 X_k}{\mathrm{d}\xi^\theta \mathrm{d}\xi^\phi} \, .
\end{aligned}
\tag{5.A.11b}
$$

Therefore, the derivatives $\mathrm{d}\boldsymbol{a}_\alpha/\mathrm{d}x_\mu$ and $\mathrm{d}^2\boldsymbol{a}_\alpha/\mathrm{d}x_\mu \mathrm{d}x_\nu$ are computed as:

$$
\frac{\mathrm{d}\boldsymbol{a}_\alpha}{\mathrm{d}x_\mu} = \frac{\mathrm{d}\boldsymbol{a}_\alpha}{\mathrm{d}\xi^\theta}\frac{\mathrm{d}\xi^\theta}{\mathrm{d}X_i}C_{i\mu} \, ,
\tag{5.A.12a}
$$

$$
\frac{\mathrm{d}^2\boldsymbol{a}_\alpha}{\mathrm{d}x_\mu \mathrm{d}x_\nu} = \left(\frac{\mathrm{d}^2\boldsymbol{a}_\alpha}{\mathrm{d}\xi^\theta \mathrm{d}\xi^\phi} - \frac{\mathrm{d}\boldsymbol{a}_\alpha}{\mathrm{d}x_\rho}C_{k\rho}\frac{\mathrm{d}^2 X_k}{\mathrm{d}\xi^\theta \xi^\phi} \right)\frac{\mathrm{d}\xi^\theta}{\mathrm{d}X_i}\frac{\mathrm{d}\xi^\phi}{\mathrm{d}X_j}C_{i\mu}C_{j\nu} \, ,
\tag{5.A.12b}
$$

where the term $\mathrm{d}^2 x_\mu / \mathrm{d} X_i \mathrm{d} X_j$ vanished according to Equations (5.3) and (5.4) and $\mathrm{d}\xi^\theta / \mathrm{d} X_i$ corresponds to the inverse of the derivative of the geometric mapping, i.e.:

$$\frac{\mathrm{d} X_i}{\mathrm{d}\xi^\theta} = \frac{\mathrm{d} \boldsymbol{F}}{\mathrm{d}\xi^\theta} \cdot \boldsymbol{E}_i , \tag{5.A.13}$$

where $\boldsymbol{F}$ is the geometrical mapping that defines the physical domain Ω (previously introduced in Section 5.1.1). Thus, the vectors $\{\mathrm{d}\boldsymbol{F}/\mathrm{d}\xi^1, \mathrm{d}\boldsymbol{F}/\mathrm{d}\xi^2, \mathrm{d}\boldsymbol{F}/\mathrm{d}\xi^3\}$ constitute the covariant basis of $\boldsymbol{F}$. In the same way, $\mathrm{d}^2 X_i / \mathrm{d}\xi^\theta \mathrm{d}\xi^\phi$ are related to the second derivative of F as follows:

$$\frac{\mathrm{d}^2 X_i}{\mathrm{d}\xi^\theta \mathrm{d}\xi^\phi} = \frac{\mathrm{d}^2 \boldsymbol{F}}{\mathrm{d}\xi^\theta \mathrm{d}\xi^\phi} \cdot \boldsymbol{E}_i . \tag{5.A.14}$$

Finally, the derivatives $\mathrm{d}\boldsymbol{a}_\alpha / \mathrm{d}\xi^\theta$ and $\mathrm{d}^2\boldsymbol{a}_\alpha / \mathrm{d}\xi^\theta \mathrm{d}\xi^\phi$, that appear in Equation (5.A.12), are detailed in Section 5.A.3 for a particular choice of the basis $\{\boldsymbol{a}_\alpha\}$.

5.A.2 Divergence of the stress tensor with respect to the global reference system

To fully address the system of Equations (5.14) in the global reference system $\{X_i\}$, we detail the components of the divergence of the stress tensor (5.17) as

$$
\begin{aligned}
\tilde{\sigma}_{ij,j} = \frac{\mathrm{d}\tilde{\sigma}_{ij}}{\mathrm{d} X_j} = \Bigg(& D_{i\alpha} D_{j\beta} D_{k\gamma} D_{l\delta} \frac{\mathrm{d}\mathbb{C}_{\alpha\beta\gamma\delta}}{\mathrm{d} X_j} \\
& + \tilde{A}_{i\alpha j} D_{j\beta} D_{k\gamma} D_{l\delta} \mathbb{C}_{\alpha\beta\gamma\delta} + D_{i\alpha} \tilde{A}_{j\beta j} D_{k\gamma} D_{l\delta} \mathbb{C}_{\alpha\beta\gamma\delta} + D_{i\alpha} D_{j\beta} \tilde{A}_{k\gamma j} D_{l\delta} \mathbb{C}_{\alpha\beta\gamma\delta} \\
& + D_{i\alpha} D_{j\beta} D_{k\gamma} \tilde{A}_{l\delta j} \mathbb{C}_{\alpha\beta\gamma\delta} \Bigg) \tilde{\varepsilon}_{kl} + \tilde{\mathbb{C}}_{ijkl}\, \tilde{\varepsilon}_{kl,j} ,
\end{aligned}
\tag{5.A.15}
$$

where $\tilde{A}_{i\alpha j}$ is defined as:

$$\tilde{A}_{i\alpha j} = \frac{\mathrm{d} D_{i\alpha}}{\mathrm{d} X_j} = \frac{\mathrm{d}\boldsymbol{a}_\alpha}{\mathrm{d} X_j} \cdot \boldsymbol{E}_i = \frac{\mathrm{d}\boldsymbol{a}_\alpha}{\mathrm{d} x_\mu} \cdot \boldsymbol{E}_i\, C_{j\mu} . \tag{5.A.16}$$

The computation of $\mathrm{d}\boldsymbol{a}_\alpha / \mathrm{d} x_\mu$ was already defined in Equation (5.A.12a). Finally, applying the chain rule, the term $\mathrm{d}\mathbb{C}_{\alpha\beta\gamma\delta} / \mathrm{d} X_j$ can be computed from $\mathrm{d}\mathbb{C}_{\alpha\beta\gamma\delta} / \mathrm{d} x_\mu$ as:

$$\frac{\mathrm{d}\mathbb{C}_{\alpha\beta\gamma\delta}}{\mathrm{d} X_j} = \frac{\mathrm{d}\mathbb{C}_{\alpha\beta\gamma\delta}}{\mathrm{d} x_\mu}\, C_{j\mu} . \tag{5.A.17}$$

5.A.3 A pointwise local basis for anisotropic materials

In order to define the orientation of the fibers for anisotropic materials (including orthotropic ones), an appropriate local basis $\{\boldsymbol{a}_\alpha\}$ needs to be set. A particular choice

for this basis is an ortho-normalized version of the covariant basis such that:

$$a_1 = \frac{g_1}{\|g_1\|}, \tag{5.A.18a}$$

$$a_2 = a_3 \times a_1, \tag{5.A.18b}$$

$$a_3 = \frac{g_1 \times g_2}{\|g_1 \times g_2\|}, \tag{5.A.18c}$$

where $\{g_1, g_2, g_3\}$ is the covariant basis, i.e.:

$$g_\theta = \frac{\mathrm{d}F}{\mathrm{d}\zeta^\theta}. \tag{5.A.19}$$

Then, the first derivatives of the basis $\{a_\alpha\}$ with respect to the parametric coordinates are:

$$\frac{\mathrm{d}a_1}{\mathrm{d}\zeta^\theta} = \frac{1}{\|g_1\|}\left(I - a_1 \otimes a_1\right)\frac{\mathrm{d}g_1}{\mathrm{d}\zeta^\theta}, \tag{5.A.20a}$$

$$\frac{\mathrm{d}a_2}{\mathrm{d}\zeta^\theta} = \frac{\mathrm{d}a_3}{\mathrm{d}\zeta^\theta} \times a_1 + a_3 \times \frac{\mathrm{d}a_1}{\mathrm{d}\zeta^\theta}, \tag{5.A.20b}$$

$$\frac{\mathrm{d}a_3}{\mathrm{d}\zeta^\theta} = \frac{1}{\|g_1 \times g_2\|}\left(I - a_3 \otimes a_3\right)\left(\frac{\mathrm{d}g_1}{\mathrm{d}\zeta^\theta} \times g_2 + g_1 \times \frac{\mathrm{d}g_2}{\mathrm{d}\zeta^\theta}\right), \tag{5.A.20c}$$

where I is the identity tensor. Finally, the second derivatives are computed as:

$$\begin{aligned}
\frac{\mathrm{d}^2 a_1}{\mathrm{d}\zeta^\theta \mathrm{d}\zeta^\phi} = \frac{1}{\|g_1\|}\bigg[&-\left(\frac{\mathrm{d}a_1}{\mathrm{d}\zeta^\phi} \otimes a_1 + a_1 \otimes \frac{\mathrm{d}a_1}{\mathrm{d}\zeta^\phi}\right)\frac{\mathrm{d}g_1}{\mathrm{d}\zeta^\theta} \\
&+ \left(I - a_1 \otimes a_1\right)\frac{\mathrm{d}^2 g_1}{\mathrm{d}\zeta^\theta \mathrm{d}\zeta^\phi} - \left(a_1 \cdot \frac{\mathrm{d}g_1}{\mathrm{d}\zeta^\phi}\right)\frac{\mathrm{d}a_1}{\mathrm{d}\zeta^\theta}\bigg],
\end{aligned} \tag{5.A.21a}$$

$$\frac{\mathrm{d}^2 a_2}{\mathrm{d}\zeta^\theta \mathrm{d}\zeta^\phi} = \frac{\mathrm{d}^2 a_3}{\mathrm{d}\zeta^\theta \mathrm{d}\zeta^\phi} \times a_1 + \frac{\mathrm{d}a_3}{\mathrm{d}\zeta^\theta} \times \frac{\mathrm{d}a_1}{\mathrm{d}\zeta^\phi} + \frac{\mathrm{d}a_3}{\mathrm{d}\zeta^\phi} \times \frac{\mathrm{d}a_1}{\mathrm{d}\zeta^\theta} + a_3 \times \frac{\mathrm{d}^2 a_1}{\mathrm{d}\zeta^\theta \mathrm{d}\zeta^\phi}, \tag{5.A.21b}$$

$$\begin{aligned}
\frac{\mathrm{d}^2 a_3}{\mathrm{d}\zeta^\theta \mathrm{d}\zeta^\phi} = \frac{1}{\|g_1 \times g_2\|}\bigg[&-\left(\frac{\mathrm{d}a_3}{\mathrm{d}\zeta^\phi} \otimes a_3 + a_3 \otimes \frac{\mathrm{d}a_3}{\mathrm{d}\zeta^\phi}\right)\left(\frac{\mathrm{d}g_1}{\mathrm{d}\zeta^\theta} \times g_2 + g_1 \times \frac{\mathrm{d}g_2}{\mathrm{d}\zeta^\theta}\right) \\
&+ \left(I - a_3 \otimes a_3\right)\left(\frac{\mathrm{d}^2 g_1}{\mathrm{d}\zeta^\theta \mathrm{d}\zeta^\phi} \times g_2 + \frac{\mathrm{d}g_1}{\mathrm{d}\zeta^\theta} \times \frac{\mathrm{d}g_2}{\mathrm{d}\zeta^\phi} + \frac{\mathrm{d}g_1}{\mathrm{d}\zeta^\phi} \times \frac{\mathrm{d}g_2}{\mathrm{d}\zeta^\theta} + g_1 \times \frac{\mathrm{d}^2 g_2}{\mathrm{d}\zeta^\theta \mathrm{d}\zeta^\phi}\right) \\
&- \left(a_3 \cdot \left(\frac{\mathrm{d}g_1}{\mathrm{d}\zeta^\phi} \times g_2 + g_1 \times \frac{\mathrm{d}g_2}{\mathrm{d}\zeta^\phi}\right)\right)\frac{\mathrm{d}a_3}{\mathrm{d}\zeta^\theta}\bigg].
\end{aligned} \tag{5.A.21c}$$

Appendix 5.B: Fast application of the stress recovery for solid structures

With reference to the equilibrium equation detailed in the local framework (5.21), we express the derivative of the normal out-of-plane stress component with respect to the thickness direction x_3 in terms of the in-plane derivatives of the interlaminar shear stresses and we integrate along the out-of-plane coordinate as

$$\sigma_{33}(x_3) = -\int_{\underline{x}_3}^{x_3} \left(\sigma_{13,1}(\zeta) + \sigma_{23,2}(\zeta) + b_3(\zeta)\right)\mathrm{d}\zeta + \sigma_{33}(\underline{x}_3), \qquad (5.B.1)$$

where $b_3 = \tilde{b}_i\,C_{i3}$ and $\sigma_{13,1}$, $\sigma_{23,2}$ are the local shear stress derivatives, which we described in Section 5.A.1. More specifically, in Equation (5.B.1) we directly substitute the derivatives of the interlaminar shear stresses with respect to the indicated in-plane components obtained *via* Equation (5.A.9a). Recall that in the equilibrium-based stress recovery introduced in Section 5.2, we also need to compute the second-order local derivatives as in Equation (5.A.9b). The lower regularity requirements for the *a posteriori* step described in this Appendix using Equation (5.B.1) lead to a general simplification of the stress recovery technique detailed in Section 5.2. These regularity requirements further simplify because, to compute σ_{33} in Equation (5.B.1), we need to calculate a single integral numerically, instead of the double integral required by the method described in Section 5.2 (see Equations (5.24) and (5.26)).

To further investigate the reduction in regularity requirements for the stress recovery equations, we turn to the simplest possible case in terms of constitutive relations: we consider each layer to be isotropic and elastic. Therefore, we can rewrite the local stress components for every ply in terms of Lamé parameters μ and λ as

$$\sigma_{11} = (2\mu + \lambda)u_{1,1} + \lambda(u_{2,2} + u_{3,3}), \qquad (5.B.2a)$$
$$\sigma_{22} = (2\mu + \lambda)u_{2,2} + \lambda(u_{1,1} + u_{3,3}), \qquad (5.B.2b)$$
$$\sigma_{12} = \mu(u_{1,2} + u_{2,1}), \qquad (5.B.2c)$$
$$\sigma_{\alpha 3} = \mu(u_{\alpha,3} + u_{3,\alpha}) \qquad\qquad \alpha = 1,2, \qquad (5.B.2d)$$
$$\sigma_{33} = (2\mu + \lambda)u_{3,3} + \lambda(u_{1,1} + u_{2,2}). \qquad (5.B.2e)$$

Substituting Equations (5.B.2) into relations (5.23) and (5.B.1), we obtain

$$
\begin{aligned}
\sigma_{13}(x_3) = &-\int_{\underline{x}_3}^{x_3} \big[(2\mu(\zeta) + \lambda(\zeta))u_{1,11}(\zeta) + \lambda(\zeta)(u_{2,21}(\zeta) + u_{3,31}(\zeta)) \\
&+ \mu(\zeta)(u_{1,22}(\zeta) + u_{2,12}(\zeta)) + b_1(\zeta)\big]\mathrm{d}\zeta + \sigma_{13}(\underline{x}_3) \\
= &-\int_{\underline{x}_3}^{x_3} \big[(2\mu(\zeta) + \lambda(\zeta))u_{1,11}(\zeta) + \lambda(\zeta)u_{2,21}(\zeta) \\
&+ \mu(\zeta)(u_{1,22}(\zeta) + u_{2,12}(\zeta)) + b_1(\zeta)\big]\mathrm{d}\zeta + \lambda(\underline{x}_3)u_{3,1}(\underline{x}_3) \\
&+ \sigma_{13}(\underline{x}_3),
\end{aligned}
\qquad (5.B.3a)
$$

$$\sigma_{23}(x_3) = -\int_{\underline{x}_3}^{x_3} \left[(2\mu(\zeta) + \lambda(\zeta))u_{2,22}(\zeta) + \lambda(\zeta)(u_{1,12}(\zeta) + u_{3,32}(\zeta)) \right.$$
$$\left. + \mu(\zeta)(u_{2,11}(\zeta) + u_{1,21}(\zeta)) + b_2(\zeta) \right] \mathrm{d}\zeta + \sigma_{23}(\underline{x}_3)$$
$$= -\int_{\underline{x}_3}^{x_3} \left[(2\mu(\zeta) + \lambda(\zeta))u_{2,22}(\zeta) + \lambda(\zeta)u_{1,12}(\zeta) \right.$$
$$\left. + \mu(\zeta)(u_{2,11}(\zeta) + u_{1,21}(\zeta)) + b_2(\zeta) \right] \mathrm{d}\zeta + \lambda(\underline{x}_3)u_{3,2}(\underline{x}_3)$$
$$+ \sigma_{23}(\underline{x}_3) , \tag{5.B.3b}$$

$$\sigma_{33}(x_3) = -\int_{\underline{x}_3}^{x_3} \left[\mu(\zeta)(u_{1,31}(\zeta) + u_{3,11}(\zeta) \right.$$
$$\left. + u_{2,32}(\zeta) + u_{3,22}(\zeta)) + b_3(\zeta) \right] \mathrm{d}\zeta + \sigma_{33}(\underline{x}_3)$$
$$= -\int_{\underline{x}_3}^{x_3} \left[\mu(\zeta)(u_{3,11}(\zeta) + u_{3,22}(\zeta)) + b_3(\zeta) \right] \mathrm{d}\zeta$$
$$+ \mu(\underline{x}_3)(u_{1,1}(\underline{x}_3) + u_{2,2}(\underline{x}_3)) + \sigma_{33}(\underline{x}_3) . \tag{5.B.3c}$$

We observe that in Equation (5.B.3c) the derivatives with respect to x_3 simplify, while we can still rely on IgA high-order regularity properties of the in-plane shape functions to compute the necessary in-plane derivatives. Moreover, with reference to Equation (5.B.3c), the integrand function can be regarded as the product of a continuous function and discontinuous term through the laminate thickness (i.e., the shear modulus $\mu(\zeta)$). This product turns, once again, into a discontinuous quantity. Then, if the integrand is bounded and piecewise-continuous in the closed interval over which integration is to be performed, we can still approximate the integral as a series of Cauchy-Riemann sums.

Using the new stress recovery strategy described in this Appendix, we investigate the same solid hollow cross-ply cylindrical shell studied in Section 5.4.1, considering an 11-ply and a 33-ply case with $S = 20$ and $S = 50$ and recover the normal out-of-plane stress profile. In Figure 5.B.1, we compare σ_{33} solution profiles derived from a global displacement field obtained with IgG (see Section 5.3.1), before and after the stress recovery application introduced in this Appendix in Equation (5.B.1), with respect to an overkill IgG LW solution, for a sampling point located at $(X_1 = L/3, \theta = \bar{\theta}/3)$. The approximated displacement field results are obtained employing 22x22x4 control points, in-plane degrees of approximation $p = q = 4$, and an out-of plane degree of approximation $r = 3$, while we compute the overkill IgG LW solution using degrees $p = q = 6$, $r = 4$ and 36x36x55 control points.

(a) 11 layers, $S = 20$

(b) 11 layers, $S = 50$

(c) 33 layers, $S = 20$
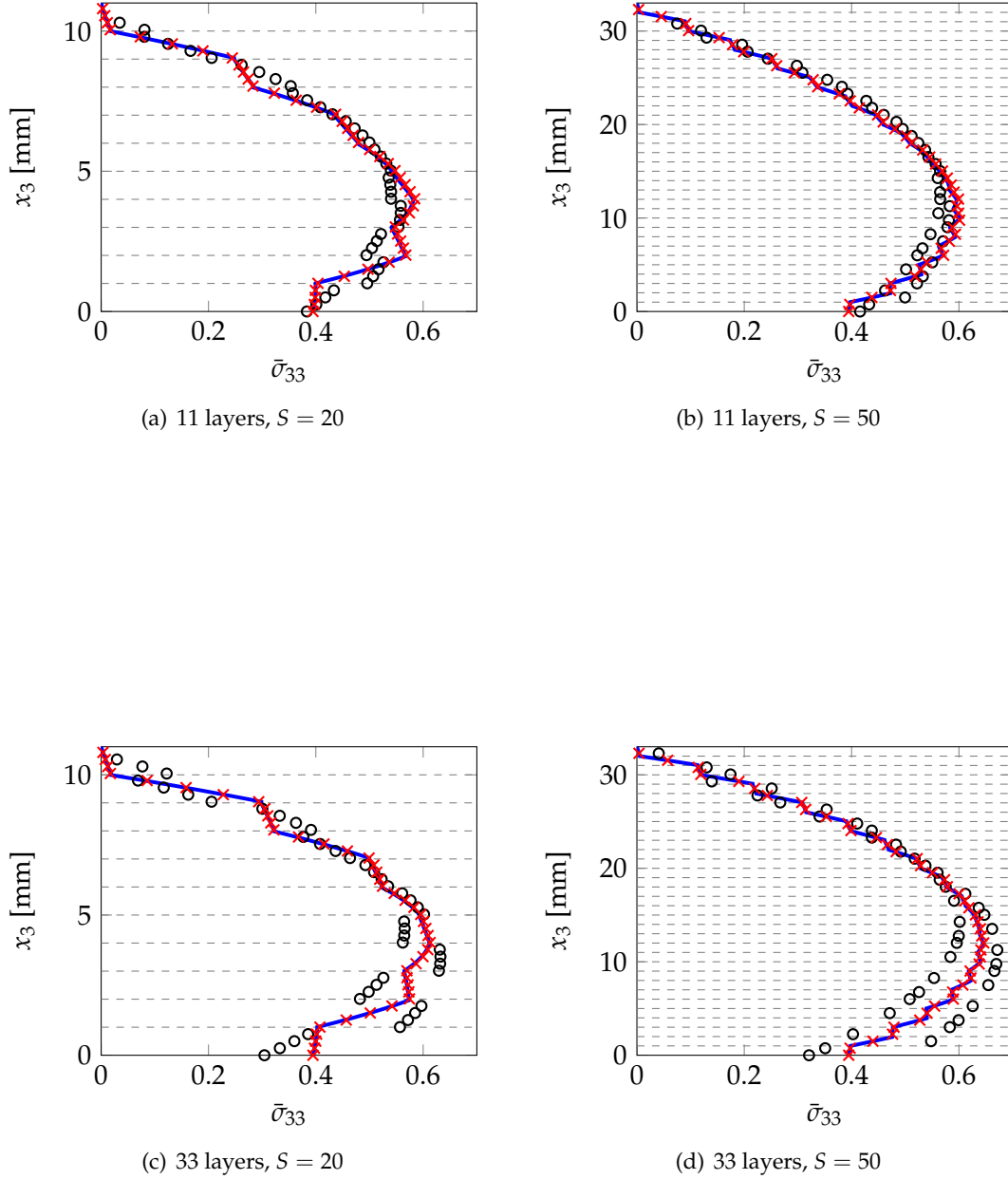
(d) 33 layers, $S = 50$

FIGURE 5.B.1: Through-the-thickness normalized σ_{33} profiles evaluated at $(X_1 = L/3, \theta = \bar{\theta}/3)$ for different IgG approaches (degrees of approximation $p = q = 4$, $r = 3$, and 22x22x4 control points). Case: hollow cross-ply cylindrical shell with 11 and 33 layers, $L = \bar{R}$, and mean radius-to-thickness ratio $S = 20, 50$ (—— overkill IgG LW solution obtained with degrees of approximation $p = q = 6$, $r = 4$ and 36x36x55 control points, ○ single-element approach solution without post-processing, × post-processed solution using Equation (5.B.1)).

Moreover, in Table 5.B.1 we compare the interlaminar normal stress maximum relative error at $(X_1 = L/3, \theta = \bar{\theta}/3)$, obtained either using the post-processing technique already presented in Section 5.2 *via* Equations (5.24) and (5.26) or the new approach based on Equation (5.B.1). We highlight the similar accuracy of the recovery method presented in this Appendix with respect to the approach in Section 5.2. Given that the stress recovery method described in this Appendix provides the same degree of accuracy as the approach in Section 5.2, in the future we plan to explore alternative IgA strategies exploiting the lower regularity of the method in this Appendix, which may prove to be more cost-efficient.

TABLE 5.B.1: Simply-supported hollow cross-ply cylindrical shell under sinusoidal load with a number of layers equal to 11 and 33. Maximum relative error of the out-of-plane normal stress along the thickness with respect to an overkill IgG LW solution (degrees of approximation $p = q = 6$, $r = 4$ and number of control points equal to 36x36x55) at $(X_1 = L/3, \theta = \bar{\theta}/3)$. Assessment of the proposed IgG strategies before and after the application of the two post-processing techniques for approximation degrees $p = q = 4$, $r = 3$ and a fixed mesh comprising 22x22 in-plane control points. One stress recovery technique is based on Equations (5.24), (5.26), while the new one on Equation (5.B.1).

Method		IgG			
Degrees of approximation		$p = q = 4, r = 3$			
11 layers	S [-]	20	30	40	50
$e(\sigma_{33})$	before post-processing	18.7	19.8	22.6	25.2
[%]	after post-processing *via* Eqs. (5.24), (5.26)	1.38	1.18	1.22	1.23
	after post-processing *via* Eq. (5.B.3c)	1.41	1.20	1.24	1.24
33 layers	S [-]	20	30	40	50
$e(\sigma_{33})$	before post-processing	15.56	16.92	18.87	21.14
[%]	after post-processing *via* Eqs. (5.24), (5.26)	0.99	0.73	0.56	0.44
	after post-processing *via* Eq. (5.B.3c)	0.99	0.74	0.56	0.44

Chapter 6

An explicit algorithm for irreversibility enforcement in phase-field modeling of crack propagation

In this chapter, we focus on the phase-field approach for quasi-brittle fracture in elastic solids, considering the displacement and the phase field as primal variables. The phase field can be regarded as a variable that physically models the damage process zone developing in the crack tip region and may be interpreted as a mathematical regularization of a sharp crack in brittle fracture [135] depending on a material characteristic length, which properly accounts for the strain localization occurring in the process zone.

In Section 6.1, we consider a thermodynamically consistent phase-field model, which accounts for a different damaging behavior in tension and compression as in [10, 46]. More specifically, damage is allowed to act only on the positive volumetric and deviatoric part of the elastic energy. The use of a phase field, in this case coinciding with the damage field, allows for the formulation of the crack propagation problem through an elastic medium as a sequence of minimization problems, as detailed in Section 6.2, in which the system energy is minimized separately with respect to displacement and damage increments. Thermodynamic consistency requires the damage increment to monotonically grow during any transformation of the body. This irreversible nature of the phenomenon transforms the energy minimization into a variational inequality, where the stationarity with respect to displacements returns the usual balance of linear momentum, while the minimization with respect to the phase field, under the condition of non-decreasing damage, leads to a *symmetric linear complementarity problem* (SLCP). The spatial discretization of these two subproblems is detailed in Section 6.3. In our case, the coupled displacement-damage problem is solved by means of a staggered iterative scheme, whereby the displacement problem is solved under fixed damage, while the SLCP in the unknown damage increment is solved under fixed displacements.

Different approaches have been proposed in the literature for the solution of the

phase-field problem under fixed displacements. In [134], the constraint is enforced by defining a monotonically growing driving force of the phase field (the so-called history variable), while in [79] a penalty functional is introduced into the formulation to replace the constraint, altering the structure of the original formulation. As a result, the energy minimization problem turns from a variational inequality into a variational equality. Inspired by the work in [45], we use the *Projected Successive Over-Relaxation* (PSOR) algorithm [127] in the present context of phase-field modeling of brittle fracture to formulate a robust and explicit iterative scheme for the solution of the SLCP, as detailed in Section 6.4. This represents a novel approach for a rigorous enforcement of the irreversibility constraint, which yields non-negative damage increments under prescribed displacements.

In Section 6.5, we perform several numerical simulations under the hypotheses of small displacements and quasistatics to assess the performance of the proposed solution algorithm with respect to the penalty formulation introduced in [79]. Finally, we draw our conclusions in Section 6.6.

6.1 Phase-field variational formulation of brittle fracture

6.1.1 State variables and constitutive law

We assume that the reference configuration is an open bounded domain $\Omega \subset \mathbb{R}^3$. Dirichlet boundary conditions $\boldsymbol{g}$ are applied on $\partial\Omega_D$ while Neumann boundary conditions are applied on $\partial\Omega_N$, with $\partial\Omega_D \cup \partial\Omega_N = \partial\Omega$ and $\partial\Omega_D \cap \partial\Omega_N = \emptyset$. Admissible deformations $\boldsymbol{u} : \Omega \to \mathbb{R}^3$ belong to the space

$$\mathcal{U}_{\boldsymbol{u}} := \left\{ \boldsymbol{u} \in H^1(\Omega; \mathbb{R}^3) : \boldsymbol{u} = \boldsymbol{g} \text{ on } \partial\Omega_D \right\}, \tag{6.1}$$

while the phase-field function d belongs to the space

$$\mathcal{U}_d := H^1(\Omega; [0, +\infty)) = \left\{ d \in H^1(\Omega) : d \geq 0 \right\}. \tag{6.2}$$

From the mathematical point of view, here it is convenient to choose a large set for d, even if the phase field d will actually take values in $[0, 1]$.

Given $\boldsymbol{u} \in \mathcal{U}_{\boldsymbol{u}}$, we assume small deformations and strains, thereby denoting the linearized strain by $\boldsymbol{\varepsilon} = \boldsymbol{\varepsilon}(\boldsymbol{u})$ and the volumetric strain by $\varepsilon_v := \operatorname{tr} \boldsymbol{\varepsilon} = \boldsymbol{\varepsilon} : \boldsymbol{I}$, where $\boldsymbol{I}$ denotes the identity matrix. We further introduce the tensile and compressive volumetric strains, respectively, $\varepsilon_v^+ = \langle \varepsilon_v \rangle_+$ and $\varepsilon_v^- = \langle \varepsilon_v \rangle_-$, for which the notation $\langle \cdot \rangle_{\pm}$ denotes the positive and negative parts. Accordingly, the volumetric and deviatoric components of the strain, $\boldsymbol{\varepsilon}_v$ and $\boldsymbol{\varepsilon}_d$, can be written as

$$\boldsymbol{\varepsilon}_v := \tfrac{1}{3}\varepsilon_v \boldsymbol{I} = \tfrac{1}{3}(\varepsilon_v^+ + \varepsilon_v^-)\boldsymbol{I}, \tag{6.3a}$$

$$\boldsymbol{\varepsilon}_d := \boldsymbol{\varepsilon} - \boldsymbol{\varepsilon}_v. \tag{6.3b}$$

We denote by $\lambda > 0$ and $\mu > 0$ the Lamé parameters, from which we compute the bulk modulus $\kappa = \tfrac{2}{3}\mu + \lambda$. Additionally, we consider a degradation function ω given by $\omega(d) = (1 - d)^2 + \eta$, where $0 < \eta \ll 1$ is a small positive parameter that circumvents the full degradation of the energy by leaving the artificial elastic rest

energy density, thereby allowing to prevent numerical difficulties in the late stage of the phase-field evolution when d approaches the limit value 1. Following [10, 46], we assume that damage (or fracture) affects only deviatoric and tensile strains. Therefore, we define the stress tensor in terms of the phase field as

$$\boldsymbol{\sigma} := \omega(d)\left(2\mu\,\boldsymbol{\varepsilon}_d + \kappa\varepsilon_v^+\,\boldsymbol{I}\right) + \kappa\,\varepsilon_v^-\,\boldsymbol{I}. \tag{6.4}$$

6.1.2 Energy functionals

The elastic energy functional is given by

$$\mathcal{E}(\boldsymbol{u}, d) := \int_\Omega \psi(\boldsymbol{\varepsilon}, d)\,\mathrm{d}\Omega\,, \tag{6.5}$$

where the elastic energy density ψ is defined as

$$\psi(\boldsymbol{\varepsilon}, d) := \omega(\psi_D + \psi_V^+) + \psi_V^-\,, \tag{6.6}$$

with $\psi_D = \mu|\boldsymbol{\varepsilon}_d|^2$ and $\psi_V^{\pm} = \frac{1}{2}\kappa\left(\varepsilon_v^{\pm}\right)^2$. The phase-field energy takes the form

$$\mathcal{D}(d) := \int_\Omega \phi(d, \boldsymbol{\nabla}d)\,\mathrm{d}\Omega\,, \tag{6.7}$$

where

$$\phi(d, \boldsymbol{\nabla}d) := \tfrac{1}{2}(l_0^{-1}d^2 + l_0|\boldsymbol{\nabla}d|^2)\,, \tag{6.8}$$

$\boldsymbol{\nabla}$ is the gradient operator, and $0 < l_0 \ll 1$ is the internal (phase-field) length. Finally, denoting the critical fracture energy by G_c, the total energy is given by

$$\Pi(\boldsymbol{u}, d) := \mathcal{E}(\boldsymbol{u}, d) + G_c\mathcal{D}(d) - \mathcal{W}(\boldsymbol{u})\,, \tag{6.9}$$

being $\mathcal{W}(\boldsymbol{u})$ the work of the external forces defined as

$$\mathcal{W}(\boldsymbol{u}) := \int_\Omega \boldsymbol{b} \cdot \boldsymbol{u}\,\mathrm{d}\Omega + \int_{\partial\Omega_N} \boldsymbol{t} \cdot \boldsymbol{u}\,\mathrm{d}\Gamma\,, \tag{6.10}$$

where $\boldsymbol{b}$ are the volume forces, and $\boldsymbol{t}$ are the tractions acting on $\partial\Omega_N$. In Equation (6.9), the term $G_c\mathcal{D}(d)$ accounts for the energy dissipated in the phase field. For this reason, $\mathcal{D}$ will be referred to as *specific dissipation*. It is important to remark that the energy Π is separately convex (and quadratic), i.e., given d the functional $\boldsymbol{u} \mapsto \Pi(\boldsymbol{u}, d)$ is convex (and quadratic) and, *vice versa*, given $\boldsymbol{u}$, the functional $d \mapsto \Pi(\boldsymbol{u}, d)$ is convex (and quadratic). However, Π it is not convex (and not quadratic) as a function of the couple $(\boldsymbol{u}, d)$. We provide an illustrative example of a separately quadratic non-convex function in Appendix 6.C.

In fracture mechanics, the phase-field approach may be interpreted as a regularization of the sharp crack approach: the crack is geometrically represented by the level set $\{d = 1\}$ and the total energy Π is an approximation of the potential energy of a brittle material. This relationship is made rigorous in terms of Γ-convergence [43]. In brief, for $l_0 \to 0$ and $\eta = o(l_0)$ the energy Π converges to a brittle energy in

the form of

$$\mathcal{F}(\boldsymbol{u}, K) := \int_{\Omega \backslash K} \left(\mu |\boldsymbol{\varepsilon}|^2 + \tfrac{1}{2}\lambda |\mathrm{tr}\boldsymbol{\varepsilon}|^2 \right) \, \mathrm{d}\Omega + G_c \mathcal{H}^2(K)$$
$$- \int_{\Omega} \boldsymbol{b} \cdot \boldsymbol{u} \, \mathrm{d}\Omega - \int_{\partial \Omega_N} \boldsymbol{t} \cdot \boldsymbol{u} \, \mathrm{d}\Gamma \,, \tag{6.11}$$

where K denotes the fracture set, $\mathcal{H}^2(K)$ is its surface area, and the displacement $\boldsymbol{u}$ satisfies the (infinitesimal) non-interpenetration condition

$$(\boldsymbol{u}^+ - \boldsymbol{u}^-) \cdot \boldsymbol{n}_K \geq 0 \ \text{ on } K. \tag{6.12}$$

In Equation (6.12), $\boldsymbol{u}^\pm$ denote the displacement in the "upper" and "lower" faces of the crack K and $\boldsymbol{n}_K$ is the unit vector normal to K, pointing from the lower to the upper face of K. The displacement $\boldsymbol{u}$ appearing in the functional $\mathcal{F}$ in Equation (6.11) is discontinuous across the crack and K itself is the set of discontinuity points of $\boldsymbol{u}$. Finally, we remark that the non-interpenetration condition in Equation (6.12) follows right from the volumetric-deviatoric splitting of the constitutive law.

6.1.3   Variations and equilibria

Taking into account the Dirichlet boundary conditions, the space of admissible variations for the displacement field is given by

$$\mathcal{V}_{\boldsymbol{u}} := \left\{ \delta \boldsymbol{u} \in H^1(\Omega; \mathbb{R}^3) : \delta \boldsymbol{u} = \boldsymbol{0} \text{ on } \partial \Omega_D \right\}. \tag{6.13}$$

For $\boldsymbol{u} \in \mathcal{U}_{\boldsymbol{u}}$, the linear balance momentum equation is equivalent to $\partial_{\boldsymbol{u}} \Pi(\boldsymbol{u}, d) = \boldsymbol{0}$, which constitutes the first variation of the total energy Π with respect to $\boldsymbol{u}$, meaning that $\partial_{\boldsymbol{u}} \Pi(\boldsymbol{u}, d)[\delta \boldsymbol{u}] = 0$ for every $\delta \boldsymbol{u} \in \mathcal{V}_{\boldsymbol{u}}$, i.e.,

$$\int_{\Omega} \boldsymbol{\sigma}(\boldsymbol{u}, d) : \boldsymbol{\varepsilon}(\delta \boldsymbol{u}) \, \mathrm{d}\Omega = \int_{\Omega} \boldsymbol{b} \cdot \delta \boldsymbol{u} \, \mathrm{d}\Omega + \int_{\partial \Omega_N} \boldsymbol{t} \cdot \delta \boldsymbol{u} \, \mathrm{d}\Gamma \quad \forall \delta \boldsymbol{u} \in \mathcal{V}_{\boldsymbol{u}}. \tag{6.14}$$

In turn, the variational Equation (6.14) is equivalent to the following strong form problem

$$\begin{cases} -\boldsymbol{\nabla} \cdot \boldsymbol{\sigma}(\boldsymbol{u}, d) = \boldsymbol{b} & \text{in } \Omega, \\ \boldsymbol{\sigma}(\boldsymbol{u}, d) \cdot \boldsymbol{n} = \boldsymbol{t} & \text{on } \partial \Omega_N, \\ \boldsymbol{u} = \boldsymbol{g} & \text{on } \partial \Omega_D, \end{cases} \tag{6.15}$$

where $\boldsymbol{\nabla}\cdot$ is the usual divergence operator and $\boldsymbol{n}$ is the outward unit vector normal to the free boundary $\partial \Omega_N$.

Let us now consider a generic variation δd of the form $\delta d = d' - d$, $\forall d' \in \mathcal{U}_d$. Then, the partial derivative of the energy Π in $(\boldsymbol{u}, d)$ with respect to the variation δd is given by

$$\partial_d \Pi(\boldsymbol{u}, d)[\delta d] = \int_{\Omega} \partial_d \psi(\boldsymbol{\varepsilon}, d) \, \delta d \, \mathrm{d}\Omega + G_c \int_{\Omega} \left(l_0^{-1} d \, \delta d + l_0 \boldsymbol{\nabla} d \cdot \boldsymbol{\nabla}(\delta d) \right) \, \mathrm{d}\Omega. \tag{6.16}$$

In order to define the energy release rate for a given configuration $d \in \mathcal{U}_d$, taking into account the irreversible nature of fracture, admissible variations δd should be of

the form $\delta d = d' - d$ for $d' \geq d$, i.e., δd should belong to the convex set[1]

$$\mathcal{V}_d := \left\{ \delta d \in H^1(\Omega) : \delta d \geq 0 \right\} . \tag{6.17}$$

Then, the unilateral equilibrium condition for the phase-field configuration d is given by the variational inequality $\partial_d \Pi(u, d) \geq 0$, which means $\partial_d \Pi(u, d)[\delta d] \geq 0$, $\forall \delta d \in \mathcal{V}_d$, i.e.,

$$\int_\Omega \partial_d \psi(\varepsilon, d)\, \delta d \, \mathrm{d}\Omega + G_c \int_\Omega \left(l_0^{-1} d\, \delta d + l_0 \nabla d \cdot \nabla(\delta d) \right) \mathrm{d}\Omega \geq 0 \quad \forall \delta d \in \mathcal{V}_d . \tag{6.18}$$

Finally, given $d \in \mathcal{U}_d$ and letting u_d be the (unique) displacement field that solves (6.14), we define the *released energy functional* as

$$\mathcal{G}(d)[\delta d] := -\partial_d \mathcal{E}(u_d, d)[\delta d] \quad \text{for } \delta d \in \mathcal{V}_d . \tag{6.19}$$

With this notation, the unilateral equilibrium condition for the phase field takes the form

$$\begin{aligned} -\partial_d \Pi(u_d, d)[\delta d] &= -\partial_d \mathcal{E}(u_d, d)[\delta d] - G_c \partial_d \mathcal{D}(d)[\delta d] \\ &= \left(\mathcal{G}(d) - G_c \partial_d \mathcal{D}(d) \right)[\delta d] \leq 0 \quad \forall \delta d \in \mathcal{V}_d . \end{aligned} \tag{6.20}$$

6.1.4 Phase-field evolution law

The discussion in the previous subsection concerns the solution of the given *boundary value problem* for a prescribed value of external forces and boundary conditions. However, due to the irreversibility of the fracture phenomena, the problem is path-dependent and its solution requires following the full history of loading, enforcing the irreversibility condition $\dot{d} \geq 0$ at all instants. The equilibrium conditions (6.15) and (6.20) are therefore necessary but not sufficient to define the problem solution for a given history of loading. To completely define the problem, we consider a time interval $[0, T]$ and time dependent external forces and boundary conditions. For the sake of clarity in terms of exposition, we drop the dependence on time of b, t, and g. Given the initial conditions $u_0 \in \mathcal{U}_u$ and $d_0 \in H^1(\Omega, [0, 1])$, we look for an evolution $t \mapsto (u(t), d(t)) \in \mathcal{U}_u \times \mathcal{U}_d$ that solves, for every time t, the following system:

$$\begin{cases} -\nabla \cdot \sigma(u, d) = b & \text{in } \Omega , \\ \sigma(u, d) \cdot n = t & \text{on } \partial\Omega_N , \\ u = g & \text{on } \partial\Omega_D , \end{cases} \tag{6.21}$$

$$\begin{aligned} \left(\mathcal{G}(d) - G_c \partial_d \mathcal{D}(d) \right)[\dot{d}] = 0 , \quad & \left(\mathcal{G}(d) - G_c \partial_d \mathcal{D}(d) \right) \leq 0 , \\ 0 \leq d \leq 1 , \quad \dot{d} \geq 0 , & \end{aligned} \tag{6.22}$$

$$G_c \dot{\mathcal{D}}(d) = G_c \partial_d \mathcal{D}(d)[\dot{d}] \geq 0 . \tag{6.23}$$

Equation (6.21) provides the equilibrium of the displacement field. Equation (6.22) gives a phase-field activation condition, which can be interpreted as a counterpart

---

[1]Note that here, mathematically, it is more convenient to employ the large set $\mathcal{U}_d = H^1(\Omega; [0, +\infty))$ for the phase-field. Using instead $H^1(\Omega; [0, 1])$ the admissible unilateral variations would still depend on d, being of the form $\delta d = d' - d$ for every $d' \in H^1(\Omega; [0, 1])$ with $d' \geq d$.

of Griffith's criterion for brittle fracture, where the monotonicity constraint $\dot{d} \geq 0$ models irreversibility. Finally, Equation (6.23) is a thermodynamic condition, requiring that the amount of energy dissipated by the crack does not decrease in time. We highlight that Equations (6.22) and (6.23) in variational form do not specify any essential boundary conditions for the phase field d. However, natural boundary conditions for d do appear when the conditions implied by (6.22) and (6.23) are written in strong form. Furthermore, we remark that, in general, the irreversibility condition $\dot{d} \geq 0$ is not enough, by itself, to guarantee that $\partial_d \mathcal{D}(d)[\dot{d}] \geq 0$, because

$$\partial_d \mathcal{D}(d)[\dot{d}] = \int_\Omega \left(l_0^{-1} d\dot{d} + l_0 \boldsymbol{\nabla} d \cdot \boldsymbol{\nabla} \dot{d} \right) \, \mathrm{d}\Omega \,, \tag{6.24}$$

where the term $\boldsymbol{\nabla} d \cdot \boldsymbol{\nabla} \dot{d}$ could in principle be negative.

The System (6.21)-(6.23) is satisfied by the solutions $\boldsymbol{u} \in \mathcal{U}_{\boldsymbol{u}}$ and $d \in \mathcal{U}_d$ of the following (rate-independent) system:

$$\begin{cases} \partial_{\boldsymbol{u}} \Pi(\boldsymbol{u}, d) = \boldsymbol{0} \\ \partial_d \Pi(\boldsymbol{u}, d)[\dot{d}] = 0, \ \partial_d \Pi(\boldsymbol{u}, d) \geq 0, \ 0 \leq d \leq 1, \ \dot{d} \geq 0 \,. \end{cases} \tag{6.25}$$

In the System (6.25), the first equation is clearly equivalent to the momentum balance (6.21), as discussed in Section 6.1.3. In particular, if $\boldsymbol{u} = \boldsymbol{u}_d$, then $\partial_d \Pi(\boldsymbol{u}, d) = \partial_d \Pi(\boldsymbol{u}_d, d)$ takes the form of (6.20), i.e.,

$$\partial_d \Pi(\boldsymbol{u}, d) = -\mathcal{G}(d) + G_c \partial_d \mathcal{D}(d) \,. \tag{6.26}$$

As a consequence, the second equation in the System (6.25) gives exactly the phase-field equivalent of Griffith's criterion (6.22).

Then, we verify that (6.25) implies the thermodynamic condition (6.23). Indeed, we can write

$$0 = \partial_d \Pi(\boldsymbol{u}, d)[\dot{d}] = \partial_d \mathcal{E}(\boldsymbol{u}, d)[\dot{d}] + G_c \partial_d \mathcal{D}(d)[\dot{d}] \,, \tag{6.27}$$

where

$$\partial_d \mathcal{E}(\boldsymbol{u}, d)[\dot{d}] = \int_\Omega \partial_d \psi(\boldsymbol{\varepsilon}, d_n) \, \dot{d} \, \mathrm{d}\Omega = \int_\Omega (d-1) \left(2\mu |\boldsymbol{\varepsilon}_d|^2 + \kappa |\varepsilon_v^+|^2 \right) \dot{d} \, \mathrm{d}\Omega \,. \tag{6.28}$$

Since $(d-1) \leq 0$, $\left(2\mu |\boldsymbol{\varepsilon}_d|^2 + \kappa |\varepsilon_v^+|^2 \right) \geq 0$, and $\dot{d} \geq 0$, we get $\partial_d \mathcal{E}(\boldsymbol{u}, d)[\dot{d}] \leq 0$. As a result, (6.27) implies (6.23).

At this point, it is also important to remark that solutions $(\boldsymbol{u}(t), d(t))$ of the System (6.25) may be discontinuous in time [7, 112], due to the occurrence of snap-back instabilities in the structural response, i.e., when the problem stability cannot be guaranteed either under load or displacement control. In fact, this is a common issue in statics in the case of rate-independent systems featuring non-convex energies. From the mathematical point of view, it is still possible [7, 112] to define a notion of solution that solves (6.25) away from time discontinuities and that satisfies a further set of equations in the discontinuity points. The latter, with the aid of a suitable arc-length parametrization, describes the transition of the system between $(\boldsymbol{u}(t^-), d(t^-))$ and $(\boldsymbol{u}(t^+), d(t^+))$ in the discontinuity point t. A rigorous mathematical presentation of these aspects is outside the scope of this work and, for the sake of simplicity,

we will exclude snap-back instabilities and we will refer to problems with solutions obeying the System (6.25).

6.2   Time discretization and staggered evolution

Given a time increment $\tau > 0$ we consider the finite time sequence $t_n = n\tau$ for $n = 0, ..., N$. The evolution is defined by the following incremental problem. Known $\boldsymbol{u}_n$ and d_n at time t_n, we introduce the auxiliary sequences $\boldsymbol{u}^i$ and d^i defined recursively by the following staggered scheme [34]: $\boldsymbol{u}^0 = \boldsymbol{u}_n$, $d^0 = d_n$ and

$$\begin{cases} \boldsymbol{u}^{i+1} \in \operatorname{argmin}\{\Pi_{n+1}(\boldsymbol{u}, d^i) : \boldsymbol{u} \in \mathcal{U}_{\boldsymbol{u}}\} \\ d^{i+1} \in \operatorname{argmin}\{\Pi_{n+1}(\boldsymbol{u}^{i+1}, d) : d \in \mathcal{U}_d \text{ with } d \geq d_n = d^0\}, \end{cases} \tag{6.29}$$

where Π_{n+1} denotes the energy functional with boundary and loading conditions prescribed at time t_{n+1}. Note that, even if the minimization takes place in the whole set $\mathcal{U}_d = H^1(\Omega; [0, +\infty))$, by a simple truncation argument, see e.g. [112], and by the irreversibility constraint $d \geq d^0$, it turns out that the minimizer d^{i+1} takes values in $[0, 1]$. Ideally, the above scheme introduces infinite sequences $\boldsymbol{u}^i$ and d^i for $i \in \mathbb{N}$ and thus we may define $\boldsymbol{u}_{n+1} = \lim_{i \to +\infty} \boldsymbol{u}^i$ and $d_{n+1} = \lim_{i \to +\infty} d^i$ (technically, up to sub-sequences). In practice the scheme ends when a certain stopping criterion on the phase field is met, e.g., at the staggered iteration $i = I$. In this case, we would set $\boldsymbol{u}_{n+1} = \boldsymbol{u}^I$ and $d_{n+1} = d^I$. For ease of presentation, let us stick with the former case, so that the limit configuration $(\boldsymbol{u}_{n+1}, d_{n+1})$ solves the following system (formally passing to the limit in (6.29) as $i \to +\infty$)

$$\begin{cases} \boldsymbol{u}_{n+1} \in \operatorname{argmin}\{\Pi_{n+1}(\boldsymbol{u}, d_{n+1}) : \boldsymbol{u} \in \mathcal{U}_{\boldsymbol{u}}\} \\ d_{n+1} \in \operatorname{argmin}\{\Pi_{n+1}(\boldsymbol{u}_{n+1}, d) : d \in \mathcal{U}_d \text{ with } d \geq d_n\}. \end{cases} \tag{6.30}$$

In other terms the couple $(\boldsymbol{u}_{n+1}, d_{n+1})$ is a separate minimizer of the energy. We remark that, being Π non-convex, $(\boldsymbol{u}_{n+1}, d_{n+1})$ is not necessarily a global minimizer of Π_{n+1}, i.e., it may happen that

$$(\boldsymbol{u}_{n+1}, d_{n+1}) \notin \operatorname{argmin}\{\Pi_{n+1}(\boldsymbol{u}, d) : \boldsymbol{u} \in \mathcal{U}_{\boldsymbol{u}}, d \in \mathcal{U}_d \text{ with } d \geq d_n\}. \tag{6.31}$$

However, computing a global minimizer of the non-convex energy Π_{n+1} is not convenient, from the computational point of view, and not necessary, in view of solving (6.21)-(6.23). Indeed, the system (6.30) is equivalent to the following variational system

$$\begin{cases} \partial_{\boldsymbol{u}}\Pi_{n+1}(\boldsymbol{u}_{n+1}, d_{n+1})[\delta\boldsymbol{u}] = 0 & \forall \delta\boldsymbol{u} \in \mathcal{V}_{\boldsymbol{u}}, \\ \\ \partial_d\Pi_{n+1}(\boldsymbol{u}_{n+1}, d_{n+1})[\delta d] \geq 0 & \forall \delta d \quad \text{of the form} \quad \delta d = d' - d_{n+1} \\ & \qquad\qquad \text{with} \quad d' \in \mathcal{U}_d \quad \text{and} \quad d' \geq d_n. \end{cases} \tag{6.32}$$

Adopting a backward-difference time integration of the phase-field rate, i.e., $\dot{d}_{n+1} := (d_{n+1} - d_n)/\tau = \Delta d_{n+1}/\tau$, and noting that, according to the definition in (6.32), $\delta d = \Delta d' - \Delta d_{n+1}$, with $\Delta d' := d' - d_n$, is not sign-constrained, the above variational

system can be written in complementarity form as [2]

$$
\begin{cases}
\partial_u \Pi_{n+1}(u_{n+1}, d_{n+1}) = \mathbf{0} \\
\partial_d \Pi_{n+1}(u_{n+1}, d_{n+1})[\Delta d_{n+1}] = 0, \quad \partial_d \Pi_{n+1}(u_{n+1}, d_{n+1}) \geq 0, \quad \Delta d_{n+1} \geq 0,
\end{cases}
\tag{6.33}
$$

which represents the time discretization of (6.25). In conclusion, the staggered scheme provides a sequence (u^i, d^i) converging to the configuration (u_{n+1}, d_{n+1}) that solves (6.33). The strong form counterpart of Equation (6.33) is introduced as

$$
\begin{cases}
-\nabla \cdot \sigma(u_{n+1}, d_{n+1}) = b_{n+1} & \text{in } \Omega, \\
\sigma(u_{n+1}, d_{n+1})n = t_{n+1} & \text{on } \partial\Omega_N, \\
u_{n+1} = g_{n+1} & \text{on } \partial\Omega_D,
\end{cases}
\tag{6.34}
$$

$$
\left(\mathcal{G}(d_{n+1}) - G_c \partial_d \mathcal{D}(d_{n+1})\right)[\Delta d_{n+1}] = 0, \quad \left(\mathcal{G}(d_{n+1}) - G_c \partial_d \mathcal{D}(d_{n+1})\right) \leq 0, \quad \Delta d_{n+1} \geq 0,
\tag{6.35}
$$

$$
\partial_d \mathcal{D}(d_{n+1})[\Delta d_{n+1}] \geq 0,
\tag{6.36}
$$

which is a time discretization of (6.21)-(6.23).

If the staggered scheme ends after a finite number I of steps, then (6.32) is replaced by

$$
\begin{cases}
\partial_u \Pi_{n+1}(u^I, d^{I-1})[\delta u] = 0 & \forall \delta u \in \mathcal{V}_u, \\
\partial_d \Pi_{n+1}(u^I, d^I)[\delta d] \geq 0 & \forall \delta d \text{ of the form } \delta d = d' - d^{I-1} \\
& \text{with } d' \in \mathcal{U}_d \text{ and } d' \geq d_n.
\end{cases}
\tag{6.37}
$$

Therefore, taking care of the shifted indices, it is still possible to perform the above calculations leading again to a discretization of the evolution law (6.25) and of the system (6.21)-(6.23).

The choice of the convergence criterion to stop the staggered iteration scheme is not unique [8, 78]. The most common possibilities used in the literature check the variation between two subsequent iterations of either the total energy functional Π_{n+1} or the phase-field variable. The latter option is equivalent to control the dissipated energy $G_c \mathcal{D}_{n+1}$, since it provides a global measure of the damage inside the domain. A third choice would be to employ the first variation of the total energy, either with respect to the displacement variable or with respect to the phase field. The distinction is then made according to how the staggered scheme is structured, i.e., whether the algorithm starts to solve the balance of linear momentum equation first or rather the complementarity problem. In our case, the staggered algorithm is arrested when the out-of-balance work Res_{stag} (see Algorithm 6.1) is smaller than

---

[2] First, note that any $\delta d \geq 0$ is admissible in (6.32), therefore we have

$$
\partial_d \Pi_{n+1}(\mathbf{u}_{n+1}, d_{n+1}) \geq 0.
$$

Choosing $\Delta d' = 0$ and $\Delta d' = 2\Delta d_{n+1}$ we get respectively $\delta d = -\Delta d_{n+1}$ and $\delta d = \Delta d_{n+1}$. Hence, by (6.32) we have both

$$
0 \leq -\partial_d \Pi_{n+1}(\mathbf{u}_{n+1}, d_{n+1})[\Delta d_{n+1}] \text{ and } 0 \leq \partial_d \Pi_{n+1}(\mathbf{u}_{n+1}, d_{n+1})[\Delta d_{n+1}],
$$

which imply $\partial_d \Pi_{n+1}(\mathbf{u}_{n+1}, d_{n+1})[\Delta d_{n+1}] = 0$.

the assigned tolerance $\texttt{TOL}_{stag}$

$$Res_{stag} = \left| \partial_{\mathbf{u}} \Pi_{n+1}(\mathbf{u}^i, d^i)[\Delta \mathbf{u}^i] \right| \leq \texttt{TOL}_{stag}. \tag{6.38}$$

Algorithm 6.1 Staggered iteration algorithm.

---

input : load solution $(\mathbf{u}_n, d_n)$ from step n and boundary conditions $\mathbf{g}_{n+1}$, $\mathbf{t}_{n+1}$ at current step $n + 1$

initialize $i = 0$

set $(\mathbf{u}^0,\ d^0) := (\mathbf{u}_n,\ d_n)$

while $Res_{stag} \geq \texttt{TOL}_{stag}$ **do**

> $i \rightarrow i + 1$
>
> given d^{i-1}, find $\mathbf{u}^i$ solving $\partial_{\mathbf{u}}\Pi(\mathbf{u}^i, d^{i-1}) = \mathbf{0}$
>
> given $\mathbf{u}^i$, find d^i solving $\partial_d\Pi(\mathbf{u}^i, d^i)[\Delta d^i] = 0$ with $\partial_d\Pi_{n+1}(\mathbf{u}^i, d^i) \geq 0$, $\Delta d^i \geq 0$
>
> compute $Res_{stag} = \partial_{\mathbf{u}}\Pi(\mathbf{u}^i, d^i)$

$(\mathbf{u}_{n+1},\ d_{n+1}) \rightarrow (\mathbf{u}^i, d^i)$

output: solution $(\mathbf{u}_{n+1},\ d_{n+1})$

6.3 Space discretization

Adopting an IgG approach, we detail the discretized balance of linear momentum equation and phase-field evolution as a SLCP, focusing on the implementation point of view. To this extent, we will restrict the description of the discretized quantities to model only plain strain problems since in Section 6.5 the tests we implement follow this hypothesis.

6.3.1 IgG approximation at the element level

Adopting an IgG approach and dropping the dependence of the solution upon the time discretization for the sake of clarity, we consider the same spatial discretization for the displacement $\mathbf{u}$, the phase field d, the virtual displacement $\delta \mathbf{u}$, and the virtual phase field δd. Thus, we approximate these variables as a linear combination of NURBS shape functions $R_{\mathbf{i},\mathbf{p}}(\boldsymbol{\xi})$ and the corresponding control variables $\hat{\mathbf{u}}$, $\hat{\mathbf{d}}$, $\delta\hat{\mathbf{u}}$, and $\delta\hat{\mathbf{d}}$, obtaining

$$\mathbf{u}_h = \mathbf{N}_u\hat{\mathbf{u}}\,, \tag{6.39a}$$

$$\delta\mathbf{u}_h = \mathbf{N}_u\delta\hat{\mathbf{u}}\,, \tag{6.39b}$$

$$d_h = \mathbf{N}_d\hat{\mathbf{d}}\,, \tag{6.39c}$$

$$\delta d_h = \mathbf{N}_d\delta\hat{\mathbf{d}}\,. \tag{6.39d}$$

For clarity in the exposition, in Equation (6.39) we also choose to drop the explicit dependence of $R_{\mathbf{i},\mathbf{p}}$ upon $\boldsymbol{\xi}$, the vector of the degrees of approximation $\mathbf{p}$, and the multi-index vector $\mathbf{i}$ (see Section 2.1.2.7). Then, adopting the element point of view, each global vector of the displacement control variables and the shape function matrix $\mathbf{N}_u$ are obtained using the usual assembly operator $\sum_e^{N_e}$, such that

$$\boldsymbol{u}_h = \mathbf{N}_u \hat{\mathbf{u}} = \sum_e^{N_e} \mathbf{N}_u^{(e)} \hat{\mathbf{u}}^{(e)} , \tag{6.40a}$$

$$\delta \boldsymbol{u}_h = \mathbf{N}_u \delta\hat{\mathbf{u}} = \sum_e^{N_e} \mathbf{N}_u^{(e)} \delta\hat{\mathbf{u}}^{(e)} . \tag{6.40b}$$

In Equation (6.40), N_e is the number of elements used in the discretization of the domain, the superscript (e) is the element index (i.e., $e = 1, ..., N_e$), and the $\mathbf{i}$-th block of the element shape functions matrix $\mathbf{N}_u^{(e)} := [\mathbf{N}_{u,\{1,1\}}^{(e)}, ..., \mathbf{N}_{u,\mathbf{i}}^{(e)}, ..., \mathbf{N}_{u,\{p+1,q+1\}}^{(e)}]$ (with degrees of approximation p, q) reads

$$\mathbf{N}_{u,\mathbf{i}}^{(e)} = \begin{bmatrix} R_{\mathbf{i},\mathbf{p}}^{(e)} & 0 \\ 0 & R_{\mathbf{i},\mathbf{p}}^{(e)} \end{bmatrix} . \tag{6.41}$$

Adopting Voigt's notation, the strain vector can also be introduced elementwise as

$$\boldsymbol{\varepsilon}_h = \sum_e^{N_e} \mathbf{B}_u^{(e)} \hat{\mathbf{u}}^{(e)} , \tag{6.42}$$

where the element matrix of the derivatives of the shape functions for the displacement field $\mathbf{B}_u^{(e)} := [\mathbf{B}_{u,\{1,1\}}, ..., \mathbf{B}_{u,\mathbf{i}}, ..., \mathbf{B}_{u,\{p+1,q+1\}}]$ has the $\mathbf{i}$-th block defined by

$$\mathbf{B}_{u,\mathbf{i}} = \begin{bmatrix} \dfrac{\partial R_{\mathbf{i},\mathbf{p}}^{(e)}}{\partial x_1} & 0 \\[2ex] 0 & \dfrac{\partial R_{\mathbf{i},\mathbf{p}}^{(e)}}{\partial x_2} \\[2ex] \dfrac{\partial R_{\mathbf{i},\mathbf{p}}^{(e)}}{\partial x_2} & \dfrac{\partial R_{\mathbf{i},\mathbf{p}}^{(e)}}{\partial x_1} \end{bmatrix} . \tag{6.43}$$

We denote by $\mathbf{N}_d^{(e)} := [R_{\{1,1\},\mathbf{p}}^{(e)}, ..., R_{\mathbf{i},\mathbf{p}}^{(e)}, ..., R_{\{p+1,q+1\},\mathbf{p}}^{(e)}]$ the element shape function row vector of the phase field, thereby rewriting the phase-field variable and virtual phase-field variable discretizations as

$$d_h = \mathbf{N}_d \hat{\mathbf{d}} = \sum_e^{N_e} \mathbf{N}_d^{(e)} \hat{\mathbf{d}}^{(e)} , \tag{6.44a}$$

$$\delta d_h = \mathbf{N}_d \delta\hat{\mathbf{d}} = \sum_e^{N_e} \mathbf{N}_d^{(e)} \delta\hat{\mathbf{d}}^{(e)} , \tag{6.44b}$$

while the approximation of the phase-field and virtual phase-field gradients reads

$$\boldsymbol{\nabla} d_h = \sum_e^{N_e} \mathbf{B}_d^{(e)} \hat{\mathbf{d}}^{(e)} \,, \tag{6.45a}$$

$$\boldsymbol{\nabla} \delta d_h = \sum_e^{N_e} \mathbf{B}_d^{(e)} \delta \hat{\mathbf{d}}^{(e)} \,, \tag{6.45b}$$

where the element matrix of the shape function derivatives for the phase field is defined as $\mathbf{B}_d^{(e)} := [\mathbf{B}_{d,\{1,1\}}^{(e)}, ..., \mathbf{B}_{d,\mathbf{i}}^{(e)}, ..., \mathbf{B}_{d,\{p+1,q+1\}}^{(e)}]$, with the **i**-th block provided by

$$\mathbf{B}_{d,\mathbf{i}}^{(e)} = \begin{bmatrix} \dfrac{\partial R_{\mathbf{i},\mathbf{p}}^{(e)}}{\partial x_1} \\[2ex] \dfrac{\partial R_{\mathbf{i},\mathbf{p}}^{(e)}}{\partial x_2} \end{bmatrix} . \tag{6.46}$$

Hereinafter, all element vectors and matrices are assumed to be assembled into their corresponding global forms.

6.3.2 Discretization of the balance of linear momentum equation

Before presenting the discrete form of the balance of linear momentum equation, we introduce the definition of the element volumetric strain in 2D:

$$\varepsilon_V^{(e)} = \frac{1}{2} \varepsilon_V^{(e)} \mathbf{1} = \frac{1}{2} \left(\boldsymbol{\varepsilon}^{(e)} \cdot \mathbf{1} \right) \mathbf{1} = \frac{1}{2} \left((\mathbf{B}_u^{(e)} \hat{\mathbf{u}}^{(e)}) \cdot \mathbf{1} \right) \mathbf{1} \,, \tag{6.47}$$

where $\mathbf{1} = [1 \;\; 1 \;\; 0]^{\mathrm{T}}$ corresponds to the identity vector in Voigt's notation in plain strain problems. The deviatoric part of the strain vector inside an element reads

$$\boldsymbol{\varepsilon}_D^{(e)} = \boldsymbol{\varepsilon}^{(e)} - \boldsymbol{\varepsilon}_V^{(e)} \,. \tag{6.48}$$

To finalize the discrete split of the considered phase-field model, we introduce the volumetric operator

$$\mathbb{P}_V = \begin{bmatrix} 1 & 1 & 0 \\ 1 & 1 & 0 \\ 0 & 0 & 0 \end{bmatrix} \tag{6.49}$$

and the deviatoric operator

$$\mathbb{P}_D = \frac{1}{2} \begin{bmatrix} 1 & -1 & 0 \\ -1 & 1 & 0 \\ 0 & 0 & 1 \end{bmatrix} . \tag{6.50}$$

Then, we approximate the first variation of the energy functional with respect to the displacement $\partial_u \Pi(\hat{\mathbf{u}}, \hat{\mathbf{d}}^{i-1})$, which is equivalent to the balance of linear momentum equation, as

$$\mathbf{K}(\hat{\mathbf{u}}, \hat{\mathbf{d}}^{i-1}) \, \hat{\mathbf{u}} - \mathbf{F} = \left(\int_\Omega \mathbf{B}_u^{\mathrm{T}} \, \mathbb{D}(\hat{\mathbf{u}}, \hat{\mathbf{d}}^{i-1}) \, \mathbf{B}_u \, \mathrm{d}\Omega \right) \hat{\mathbf{u}} - \mathbf{F} = \mathbf{0} \,, \tag{6.51}$$

where $\mathbf{B}_u$ is the global matrix of the derivatives of the shape functions for the displacement field, $\mathbb{D}(\hat{\mathbf{u}}, \hat{\mathbf{d}}^{i-1})$ the matrix of damaged elastic moduli at iteration $i-1$, which implicitly accounts for the positive-negative split of the volumetric and deviatoric part of the elastic energy density functional ψ (see Equation (6.6)), and $\mathbf{F}$ is the global vector of the external forces, which we do not discretize since it will not be used in the considered examples in Section 6.5. Furthermore, in Equation (6.51) we denote evolving quantities within the Algorithm 6.1 with no superscript $(.)^{i-1}$ for a fixed solution of phase field at the control points $\hat{\mathbf{d}}^{i-1}$. Adopting once again the element point of view, the stiffness matrix $\mathbf{K}$ may be decomposed as

$$\mathbf{K}(\hat{\mathbf{u}}, \hat{\mathbf{d}}^{i-1}) = \sum_e^{N_e} \mathbf{K}^{(e)}(\hat{\mathbf{u}}^{(e)}, (\hat{\mathbf{d}}^{(e)})^{i-1}) = \sum_e^{N_e} \int_{\Omega_e} (\mathbf{B}_u^{(e)})^{\mathrm{T}} \, \mathbb{D}^{(e)}(\hat{\mathbf{u}}^{(e)}, (\hat{\mathbf{d}}^{(e)})^{i-1}) \, \mathbf{B}_u^{(e)} \, \mathrm{d}\Omega_e \,.$$
(6.52)

Finally, in Equation (6.52), the local element material matrix $\mathbb{D}^{(e)}(\hat{\mathbf{u}}^{(e)}, (\hat{\mathbf{d}}^{(e)})^{i-1})^3$ can be defined as

$$\begin{aligned}
\mathbb{D}^{(e)}(\hat{\mathbf{u}}^{(e)}, (\hat{\mathbf{d}}^{(e)})^{i-1}) &= \left((1 - \mathbf{N}_d^{(e)}(\hat{\mathbf{d}}^{(e)})^{i-1})^2 + \eta \right) \left[(\mathbb{D}_V^+)^{(e)}(\varepsilon_V^{(e)}) + \mathbb{D}_D^{(e)} \right] \\
&\quad + (\mathbb{D}_V^-)^{(e)}(\varepsilon_V^{(e)}) \\
&= \left((1 - \mathbf{N}_d^{(e)}(\hat{\mathbf{d}}^{(e)})^{i-1})^2 + \eta \right) \left[\kappa \, f^+(\varepsilon_V^{(e)}) \mathbb{P}_V + 2\mu \, \mathbb{P}_D \right] \\
&\quad + \kappa \, f^-(\varepsilon_V^{(e)}) \mathbb{P}_V \,,
\end{aligned}$$
(6.53)

where $\mathbb{D}_D^{(e)}$ and $(\mathbb{D}_V^{\pm})^{(e)}(\varepsilon_V^{(e)})$ are the local damaged elastic moduli matrices accounting for the fact that we split the strain in deviatoric and volumetric contributions and, additionally, for the latter we further detail positive/negative parts, where $f^{\pm}(x)$ is defined as $f^{\pm}(x) = \dfrac{1 \pm \mathrm{sign}(x)}{2}$. Additionally, we highlight that $\kappa = \lambda + \mu$ for plane strain problems.

With reference to Algorithm 6.1, we remark that both the first variation of the total energy with respect to the displacement variable and the phase-field variable are nonlinear. The non-linearity of $\partial_u \Pi$ is due to the assumption that damage affects only deviatoric and tensile strains, whereas for $\partial_d \Pi$ it is caused by the nature of the constraint minimization problem itself. Therefore, to solve $\partial_u \Pi$ we use a Newton–Raphson procedure (see Section 2.1.4) to iteratively compute u^i for a fixed damage variable d^{i-1}. To control the convergence of this algorithm, we verify that the L^2-norm of the out-of-balance forces at the control-points, defined as

$$Res_{NR,u} := \| \mathbf{K}\hat{\mathbf{u}} - \mathbf{F} \|_{L^2} \,,$$
(6.54)

is smaller than a prescribed tolerance $\mathtt{TOL}_{NR,u} = 10^{-9}$ kJ^4. The strategy to solve the phase-field problem will be instead thoroughly discussed in Section 6.4.

---

[3]We have tested the necessity of setting parameter η in our formulation numerically and we have also found its inclusion to be unnecessary. In fact, all results presented in Section 6.5 set $\eta = 0$.

[4]Note that this tolerance does depend on the adopted units and therefore a special care is needed in fixing its value. We refer interested readers to [79] for more details in terms of a suitable choice of the tolerance value.

6.3.3 Discretized phase-field evolution as a symmetric linear complementarity problem

Since we are using separately quadratic energies, given $\hat{\mathbf{u}}^i$ we can rewrite the energy $\Pi_{n+1}(\hat{\mathbf{u}}^i, \hat{\mathbf{d}})$ in incremental form highlighting the dependence upon the current phase-field increment $\Delta\hat{\mathbf{d}}$ and the phase-field at the previous load step $\hat{\mathbf{d}}_n$ as

$$\Pi_{n+1}(\hat{\mathbf{u}}^i, \hat{\mathbf{d}}) = \frac{1}{2}\Delta\hat{\mathbf{d}}^{\mathsf{T}} \mathbf{Q}^i \Delta\hat{\mathbf{d}} + \Delta\hat{\mathbf{d}}^{\mathsf{T}} \mathbf{q}^i + \Pi_{n+1}(\hat{\mathbf{u}}^i, \hat{\mathbf{d}}_n) , \tag{6.55}$$

with $\Delta\hat{\mathbf{d}} = \hat{\mathbf{d}} - \hat{\mathbf{d}}_n$. In Equation (6.55), $\mathbf{Q}^i$ and $\mathbf{q}^i$ are obtained as

$$\mathbf{Q}^i := \mathbf{\Psi}(\hat{\mathbf{u}}^i) + G_c \mathbf{\Phi} , \quad \mathbf{q}^i := \mathbf{Q}^i \hat{\mathbf{d}}_n - \boldsymbol{\psi}(\hat{\mathbf{u}}^i) , \tag{6.56}$$

where the element dissipation matrix $\mathbf{\Phi}^{(e)}$ comes from the spatial discretization of the phase-field energy in Equation (6.7) and is defined at the element level as

$$\mathbf{\Phi}^{(e)} := \int_{\Omega_e} \left(l_0^{-1} (\mathbf{N}_d^{(e)})^{\mathsf{T}} \mathbf{N}_d^{(e)} + l_0 (\mathbf{B}_d^{(e)})^{\mathsf{T}} \mathbf{B}_d^{(e)} \right) \mathrm{d}\Omega_e . \tag{6.57}$$

Additionally, we highlight that $\mathbf{\Phi}^{(e)}$ does not depend upon the phase-field variable and is therefore constant. On the other hand, the element free energy matrix $\mathbf{\Psi}^{(e)}$ and vector $\boldsymbol{\psi}^{(e)}$, respectively, are obtained from the spatial discretization of the elastic energy (6.5) and are defined as

$$\mathbf{\Psi}^{(e)}((\hat{\mathbf{u}}^{(e)})^i) := \int_{\Omega_e} 2 \left(\psi_V^+((\hat{\mathbf{u}}^{(e)})^i) + \psi_D((\hat{\mathbf{u}}^{(e)})^i) \right) (\mathbf{N}_d^{(e)})^{\mathsf{T}} \mathbf{N}_d^{(e)} \, \mathrm{d}\Omega_e , \tag{6.58}$$

and

$$\boldsymbol{\psi}^{(e)}((\hat{\mathbf{u}}^{(e)})^i) := \int_{\Omega_e} 2 \left(\psi_V^+((\hat{\mathbf{u}}^{(e)})^i) + \psi_D((\hat{\mathbf{u}}^{(e)})^i) \right) (\mathbf{N}_d^{(e)})^{\mathsf{T}} \, \mathrm{d}\Omega_e , \tag{6.59}$$

where

$$\psi_V^+((\hat{\mathbf{u}}^{(e)})^i) = \frac{1}{2}(\mathbf{B}_u^{(e)}(\hat{\mathbf{u}}^{(e)})^i)^{\mathsf{T}} \kappa \, f^+(\varepsilon_V^{(e)}) \mathbb{P}_V \mathbf{B}_u^{(e)}(\hat{\mathbf{u}}^{(e)})^i , \tag{6.60}$$

and

$$\psi_D((\hat{\mathbf{u}}^{(e)})^i) = \frac{1}{2}(\mathbf{B}_u^{(e)}(\hat{\mathbf{u}}^{(e)})^i)^{\mathsf{T}} 2\mu \, \mathbb{P}_D \mathbf{B}_u^{(e)}(\hat{\mathbf{u}}^{(e)})^i . \tag{6.61}$$

Given $\hat{\mathbf{d}}_n$ and $\hat{\mathbf{u}}^i$, the unilateral minimization with respect to the phase-field variable can be written in incremental form as

$$\Delta\hat{\mathbf{d}} \in \mathrm{argmin} \left\{ \frac{1}{2}\Delta\hat{\mathbf{d}}^{\mathsf{T}} \mathbf{Q}^i \Delta\hat{\mathbf{d}} + \Delta\hat{\mathbf{d}}^{\mathsf{T}} \mathbf{q}^i : \Delta\hat{\mathbf{d}} \geq 0 \right\} . \tag{6.62}$$

In turn, this unilateral quadratic minimization problem is equivalent to the following SLCP:

$$(\mathbf{Q}^i \Delta\hat{\mathbf{d}} + \mathbf{q}^i) \cdot \Delta\hat{\mathbf{d}} = 0 , \tag{6.63a}$$

$$-(\mathbf{Q}^i \Delta\hat{\mathbf{d}} + \mathbf{q}^i) \leq 0 , \tag{6.63b}$$

$$\Delta\hat{\mathbf{d}} \geq 0 . \tag{6.63c}$$

The first equality in Equation (6.63) defines the discretized form of the phase-field activation condition. The second equality describes the region of the linear elastic regime, while the last inequality enforces the irreversibility condition. Symmetry of the SLCP (6.63) stems from the constitutive matrix $\mathbf{Q}$ and from the nature of the trial functions. Linearity comes from the linear dependence of the activation function upon $\Delta \hat{\mathbf{d}}$ and is a consequence of the phase-field functional being a quadratic form in the phase field and its gradient.

6.3.4 Further definitions for numerical tests

Herein, we give the definition of some fundamental global quantities at the discrete spatiotemporal level which will be helpful to understand the results displayed in Section 6.5. For each time instant t_n we introduce the imposed displacement u_n, the magnitude of the reaction force R_n, the internal stored energy $\mathcal{E}_n$, and the fracture energy $G_c \mathcal{D}_n$. The reaction force R_n is computed as the integral of the forces at the control points corresponding to the constrained DOFs where the displacement is imposed. The total energy functional for the spatially discretized model is defined as

$$\Pi_n := \mathcal{E}_n + G_c \mathcal{D}_n - \mathcal{W}_n \,, \tag{6.64}$$

with

$$\mathcal{E}_n := \frac{1}{2} \hat{\mathbf{u}}_n^{\mathrm{T}} \mathbf{K}_n \, \hat{\mathbf{u}}_n \,, \tag{6.65a}$$

$$G_c \mathcal{D}_n := G_c \frac{1}{2} \hat{\mathbf{d}}_n^{\mathrm{T}} \boldsymbol{\Phi} \, \hat{\mathbf{d}}_n \,, \tag{6.65b}$$

$$\mathcal{W}_n := \hat{\mathbf{u}}_n^{\mathrm{T}} \mathbf{F}_n \,, \tag{6.65c}$$

where, for completeness, the external energy is also reported in (6.65c), even though the external applied forces are zero in the considered cases of Section 6.5. Additionally, since the alternate minimization algorithm starts solving the balance of linear momentum equation first, in the numerical tests our convergence criterion controls the discretized counterpart of the out-of-balance work (6.38), defined as

$$Res_{stag} = \left| \Delta \hat{\mathbf{u}}_n \cdot (\mathbf{K}_n \, \hat{\mathbf{u}}_n - \mathbf{F}_n) \right| \,. \tag{6.66}$$

Following [79], unless otherwise noted, a tolerance $\mathtt{TOL}_{stag} = 10^{-7}$ kJ is set for the residual Res_{stag} (see Algorithm 6.1).

Finally, we remark that in this work, we consider standard Gauss integration.

6.4 Solution strategy of the phase-field problem

Adopting a staggered algorithm for the finite-step problem (6.29) implies solving the SLCP (6.63) at each iteration. In this work, the SLCP (6.63) is directly handled using the explicit iterative scheme referred to as the PSOR algorithm [127]. Furthermore, we consider the penalty approach proposed in [79], whereby the irreversibility constraint is enforced in an approximate manner, by adding a penalization term to the functional. The results provided by this latter technique will be used as a reference

solution in the numerical tests in Section 6.5, to assess the validity of the proposed PSOR method.

6.4.1 Penalization of the irreversibility constraint

Herein, we briefly describe, in the discrete setting, the penalty approach employed in [79] to solve the unilateral incremental problem for the phase field d.

The idea is to replace the constrained minimization (6.62) with the following unconstrained problem

$$\Delta\hat{\mathbf{d}} \in \operatorname{argmin}\left\{\frac{1}{2}\Delta\hat{\mathbf{d}}^{\mathrm{T}}\mathbf{Q}^i\Delta\hat{\mathbf{d}} + \Delta\hat{\mathbf{d}}^{\mathrm{T}}\mathbf{q}^i + p\left(\mathbf{N}_d\Delta\hat{\mathbf{d}}\right)\right\}. \tag{6.67}$$

In Equation (6.67), the non-linear penalty term $p\left(\mathbf{N}_d\Delta\hat{\mathbf{d}}\right)$ provides the discretization of the functional

$$\tfrac{1}{2}\gamma \int_\Omega \langle d - d_n\rangle_-^2 \,\mathrm{d}\Omega\,, \tag{6.68}$$

where $\langle\cdot\rangle_-$ is the negative Macaulay bracket. The main purpose of the penalization is to introduce an extra energy term in the total energy that diverges when the irreversibility condition is violated, i.e., when $d - d_n < 0$. Clearly, when $\gamma \to +\infty$ we recover the unilateral constraint $d \geq d_n$ and its discretized counterpart $\Delta\hat{\mathbf{d}} \geq 0$. It is worthwhile to notice that the penalization coefficient γ is a dimensional quantity depending on the G_c/l_0 ratio and a wrong choice of its value may lead to ill-conditioning of the system associated to (6.67). A detailed analysis of the computational performance of this approach and a criterion for the choice of the coefficient γ are available in [79].

The minimization of the penalized total energy functional with respect to the phase-field variable provides the following non-linear equation in the phase-field finite increment:

$$\mathbf{Q}^i\Delta\hat{\mathbf{d}} + \mathbf{q}^i + \mathbf{p}(\mathbf{N}_d\Delta\hat{\mathbf{d}}) = \mathbf{0}\,. \tag{6.69}$$

The element penalization vector $\mathbf{p}^{(e)}$ can be computed as follows:

$$\mathbf{p}^{(e)}(\mathbf{N}_d^{(e)}\Delta\hat{\mathbf{d}}^{(e)}) = \int_{\Omega_e}\gamma\,\langle\mathbf{N}_d^{(e)}\Delta\hat{\mathbf{d}}^{(e)}\rangle_-\,(\mathbf{N}_d^{(e)})^{\mathrm{T}}\,\mathrm{d}\Omega_e\,. \tag{6.70}$$

The solution of (6.69) requires a Newton-Raphson iterative scheme in view of the nonlinearity entailed by the presence of the Macaulay bracket. The residual is defined as $\mathbf{r}_d(\Delta\hat{\mathbf{d}}) := \mathbf{Q}^i\Delta\hat{\mathbf{d}} + \mathbf{q}^i + \mathbf{p}(\mathbf{N}_d\Delta\hat{\mathbf{d}})$. The penalty contribution to the element consistent tangent matrix reads:

$$\frac{\partial\mathbf{p}^{(e)}}{\partial\Delta\hat{\mathbf{d}}^{(e)}}(\mathbf{N}_d^{(e)}\Delta\hat{\mathbf{d}}^{(e)}) = \int_{\Omega_e}\gamma\,\mathrm{H}_-\left(\mathbf{N}_d^{(e)}\Delta\hat{\mathbf{d}}^{(e)}\right)\,(\mathbf{N}_d^{(e)})^{\mathrm{T}}\mathbf{N}_d^{(e)}\,\mathrm{d}\Omega_e\,, \tag{6.71}$$

where $\mathrm{H}_-\left(\mathbf{N}_d^{(e)}\Delta\hat{\mathbf{d}}^{(e)}\right)$ is the negative Heaviside function evaluated at the linear combination of the element shape functions and solution of the phase field at the control points. Here, the importance of the penalty coefficient for the numerical stability of the solver is clear. At every Newton-Raphson iteration different entries

of the tangent matrix have an additional contribution of the order of magnitude of γ.

The convergence criterion used in the iterative scheme is a suitable measure, i.e., the L^∞ norm of the difference between two subsequent phase-field increment solutions, namely:

$$Res_{NR,d} := \left\| \Delta \hat{\mathbf{d}}^k - \Delta \hat{\mathbf{d}}^{k-1} \right\|_{L^\infty} , \tag{6.72}$$

where k is the iteration number. Finally, we set the tolerance for the Newton-Raphson scheme to solve the penalty approach as $\text{TOL}_{NR,d} = 10^{-4}$. The choice of relaxing $\text{TOL}_{NR,d}$ with respect to the value proposed in [79] is due to the fact that we control the maximum variation of two subsequent phase-field solutions, which are non-dimensional quantities ranging from 0 to 1.

6.4.2 Projected successive over-relaxation algorithm

In this thesis, we propose to solve the SLCP defined in Equation (6.63) using the PSOR algorithm [127] at each staggered iteration. According to the PSOR algorithm, the matrix $\mathbf{Q}$ is additively decomposed as $\mathbf{Q} = \mathbf{L} + \mathbf{D} + \mathbf{L}^{\mathrm{T}}$, where $\mathbf{L}$ is the strictly lower triangular part, $\mathbf{D}$ is the diagonal, and $\mathbf{L}^{\mathrm{T}}$ its strictly upper triangular part of matrix $\mathbf{Q}$. To simplify the notation, we drop the index i within the staggered scheme in Algorithm 6.1 as well as the $(\hat{\cdot})$ symbol in the solution vector of the phase-field at the control points. The rc-th component of the matrix is denoted as Q_{rc}, where r represents the row-index and c the column-index. The algorithm is iterative and the r-th component of the solution at the k-th PSOR iteration reads:

$$\Delta d_r^k = \left\langle \Delta d_r^{k-1} - D_{rr}^{-1} \left[Q_{rc} \, \Delta d_c^{k-1} + q_r + L_{rc} \left(\Delta d_c^k - \Delta d_c^{k-1} \right) \right] \right\rangle_+ , \tag{6.73}$$

where $r > c$, $L_{rc} := Q_{r>c}$, $D_{rc} := Q_{r=c}$, and $\langle \cdot \rangle_+$ denotes the positive part of the argument. We highlight that irreversibility is enforced componentwise in strong form *via* the Macaulay bracket operator, while the explicit nature of the algorithm is guaranteed by the the strictly lower triangular format of matrix $\mathbf{L}$. This aspect can be noticed looking at the first three components of the solution vector at the k-th PSOR iteration:

$$\Delta d_1^k = \left\langle \Delta d_1^{k-1} - Q_{11}^{-1} \left[Q_{1c} \, \Delta d_c^{k-1} + q_1 \right] \right\rangle_+$$

$$\Delta d_2^k = \left\langle \Delta d_2^{k-1} - Q_{22}^{-1} \left[Q_{2c} \, \Delta d_c^{k-1} + q_1 + Q_{21} \left(\Delta d_1^k - \Delta d_1^{k-1} \right) \right] \right\rangle_+$$

$$\Delta d_3^k = \left\langle \Delta d_3^{k-1} - Q_{33}^{-1} \left[Q_{3c} \, \Delta d_c^{k-1} + q_3 + Q_{31} \left(\Delta d_1^k - \Delta d_1^{k-1} \right) + Q_{32} \left(\Delta d_2^k - \Delta d_2^{k-1} \right) \right] \right\rangle_+$$

$$\dots$$

The symmetric matrix $\mathbf{Q}$ of the SLCP is also a sparse matrix because of the finite support of the shape functions of the spatial discretization. This feature, together with the explicit nature of the algorithm, allows for a particularly compact and effective implementation of the PSOR algorithm, which is illustrated in detail in Appendix 6.A.

By Corollary 2.2 in [127] the sequence $\Delta \mathbf{d}^k$ defined above converges to the unique

minimizer of problem (6.62). The solution of the SLCP involves the fulfillment of the three condtions as in Equation (6.63). Different possibilities to control the solution are described to ensure the convergence of the PSOR algorithm. The irreversibility constraint on the phase-field variable (6.63c) is automatically satisfied by the presence of the Macaulay bracket in (6.73). Therefore, the first possible criterion controls the variation of the phase-field increment between two subsequent iterations only. Specifically, we evaluate the infinity norm of the latter quantity as:

$$Res_{PSOR} := \left\| \Delta \boldsymbol{d}^k - \Delta \boldsymbol{d}^{k-1} \right\|_{L^\infty} . \tag{6.75}$$

Since the phase field is non-dimensional and ranges from 0 to 1, the previous measure is seen as already normalized with respect the reference value $d = 1$. The maximum increment that would be experienced in a single load step cannot be more than the unit. Therefore, a reasonable tolerance seems to be $\texttt{TOL}_{PSOR} = 10^{-4}$, which also allows to compare results with respect to the penalty approach introduced in Section 6.4.1. We highlight that the criterion that controls Res_{PSOR} in Equation (6.75) is the one we actually use in the numerical examples of Section 6.5. In Appendix 6.B, we discuss other two alternative possible criteria involving condition (6.63b), which allows to control the PSOR algorithm.

6.5 Numerical results

In this section, we assess the performance of the proposed PSOR solution strategy in comparison with the penalty approach described in [79]. To this extent, we assume small displacements and quasi-statics and consider two well-known benchmarks in the phase-field literature: the single-edge notched (SEN) specimen under shear and the L-shaped specimen. In both cases, we assume a plane strain regime and a loading-unloading history under displacement control. The material parameters for both tests are reported in Table 6.1, while the geometry, the mesh, and the time history are described in the relevant subsections.

TABLE 6.1: Material properties.

| Material type | E | ν | G_c | l_0 |
	GPa	-	N/mm	mm
1	210.00	0.30	2.700	0.01
2	25.85	0.18	0.095	5.00

Furthermore, with reference to the staggered scheme in Algorithm 6.1, we recall that, unless otherwise noted, we set the corresponding tolerance $\texttt{TOL}_{stag}^{(1)} = 10^{-7}$ kJ following [79], while our convergence criterion controls Equation (6.38) since the alternate minimization algorithm starts first to solve the balance of linear momentum equation. Nevertheless, for the sake of completeness, the evolutions of the discrete total energy functional Π_n and of the fracture energy $G_c \mathcal{D}_n$ are also reported in the results. Additionally, we set the PSOR algorithm and the penalty method tolerances to $\texttt{TOL}_{PSOR}^{(1)} = \texttt{TOL}_{NR,d}^{(1)} = 10^{-4}$ (see Section 6.4). We further tested both algorithms with $\texttt{TOL}_{PSOR}^{(2)} = \texttt{TOL}_{NR,d}^{(2)} = 10^{-6}$ to assess their performance under a more severe
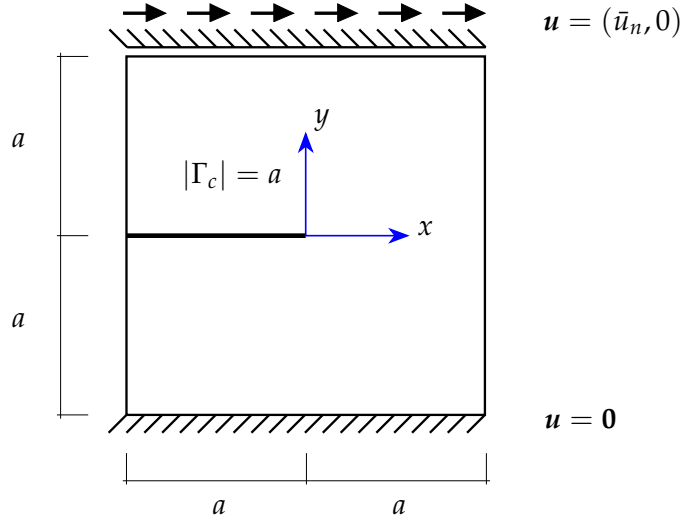
FIGURE 6.1: SEN specimen under shear loading. Geometry and boundary conditions.

convergence criterion. Moreover, we recall that the tolerance for the enforcement of the balance of linear momentum has been set to $\texttt{TOL}_{NR,u} = 10^{-9}$ kJ.

6.5.1   Single edge notched specimen (SEN) under shear

The SEN example, originally considered in Bourdin *et al.* [34], consists of a crack propagation problem in a shear-loaded square plate with a pre-existing crack modeled by a physical geometrical discontinuity (see Figure 6.1). The material parameters are those of material type 1 of Table 6.1. The initial crack length is a, while the square specimen has width $2a = 1$ mm and the specimen thickness is assumed equal to 1 mm. The geometry is spatially discretized adopting a multipatch approach (see Section 2.1.2.9), which allows to account for the initial physical discontinuity. Namely, we consider 2 patches defined by the subdomains: $(-a, a) \times (0, a)$ and $(-a, a) \times (-a, 0)$, such that the notch lies in the patch interface. Each patch is discretized using C^0 linear shape functions and features a uniform mesh of 401x201 control points corresponding to 400x200 elements, such that we consider 4 elements resolving the critical length l_0. The specimen is subject to Dirichlet boundary conditions on the bottom, where it is clamped, and on the top, where it undergoes a horizontal imposed displacement of magnitude u_n with prevented vertical displacement. The load history is subdivided in time steps denoted with n. The reference displacement increment is $\Delta u_n = 3 \cdot 10^{-4}$ mm. Since the first part of the response is linear elastic, a refined time step is not needed and, therefore, the initial displacement is set to $u_1 = 6 \cdot 10^{-3}$ mm. Then, for $n = 2, ..., 21$ the loading branch is characterized by $u_{n+1} = u_n + \Delta u_n$, while in the unloading part of the load history, for $n = 22, ..., 34$, the imposed displacement is $u_{n+1} = u_n - 3\Delta u_n$.

In Figure 6.2, we investigate the global response in terms of reaction force R_n, internal energy $\mathcal{E}_n$, and fracture energy $G_c \mathcal{D}_n$ as a function of the imposed displacement u_n for both the PSOR algorithm and the considered penalty method. The response is nearly linear elastic until the peak corresponding to step 13. Note that the initial part of the elastic energy curve in Figure 6.2(b) should be almost quadratic, even though it does not appear to be so due to the very coarse time step used in

(a) Reaction force.

(b) Internal and fracture energies.
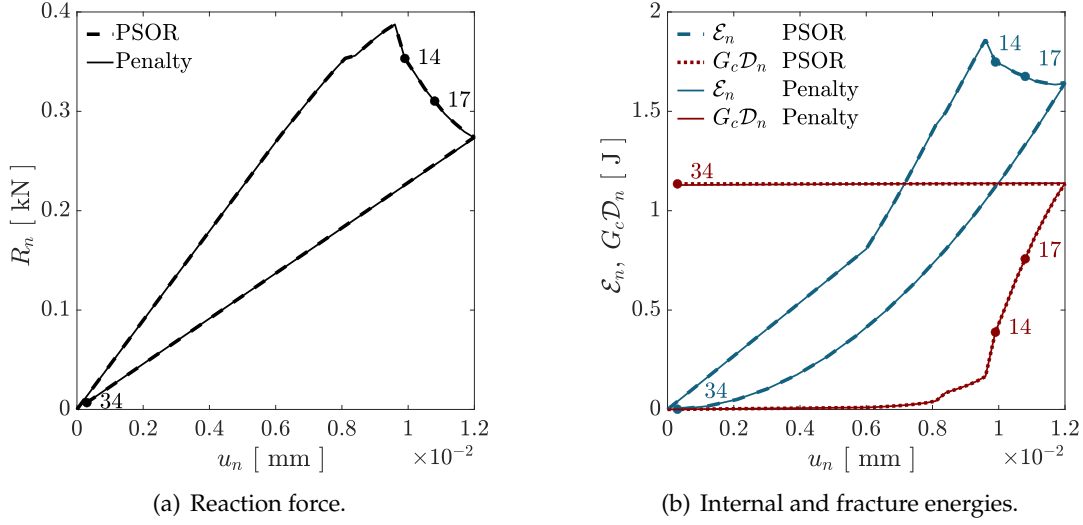
FIGURE 6.2: SEN specimen under shear loading. Global response with PSOR and penalty methods in terms of reaction force R_n, internal energy $\mathcal{E}_n$, and fracture energy $G_c\mathcal{D}_n$ *versus* imposed displacement u_n. Solid marks denote three relevant steps of the time history: step 14, at the start of the softening branch, step 17, intermediate between peak and unloading branch, and step 34 corresponding to the end of the time history.

the initial part of the analysis. At the end of step 13, the stress concentration at the notch tip drives the growth of the phase-field variable until the crack onset, after which the specimen response enters the softening branch. As expected, the unloading path is linear elastic with no further growth of the phase field. Here, the reaction force is linear with reduced (degraded) stiffness, the internal energy is quadratic, and the dissipation remains constant. It is interesting to note that the fracture energy $G_c\mathcal{D}_n$ grows monotonically during the sequence of staggered iterations and, as a consequence, the total energy decreases. During shear loading, the failure pattern deviates from the symmetry axis, as it can be noticed in Figure 6.3. This result stems from the anisotropic degradation of the elastic free energy (i.e., damage only affects the tensile part of the volumetric strain and the deviatoric strain) according to the unilateral contact model [10]. We further highlight that in Figure 6.2 the PSOR algorithm and the penalty method produce virtually the same results.

The convergence of the staggered algorithm is shown in Figure 6.4 for the critical load increment 14, corresponding to the crack onset. We recall that the stopping criterion in our staggered algorithm involves the discretized counterpart of the out-of-balance work, as stated in Equation (6.66). In Figure 6.4, we also plot other two quantities: the total energy Π_n calculated *via* Equation (6.64) and the fracture energy $G_c\mathcal{D}_n$ calculated *via* Equation (6.65b). Both of them could also be used to define alternative convergence criteria. The choice of a suitable stopping criterion is a delicate point of the staggered scheme. This can be appreciated in Figure 6.5, where contour plots of the phase-field variable are shown at different staggered iterations. All of them qualitatively seem reasonable solutions for the crack propagation problem, but they actually correspond to out-of-balance states between internal and external forces. We further remark that while the results of Figures 6.4 and 6.5 correspond to the PSOR algorithm, the same results are observed with the penalty method.

Finally, the computing performances of the PSOR method are compared to those

(a) Step 14.   (b) Step 17.   (c) Step 34.

$$0 \quad 0.2 \quad 0.4 \quad 0.6 \quad 0.8 \quad 1$$
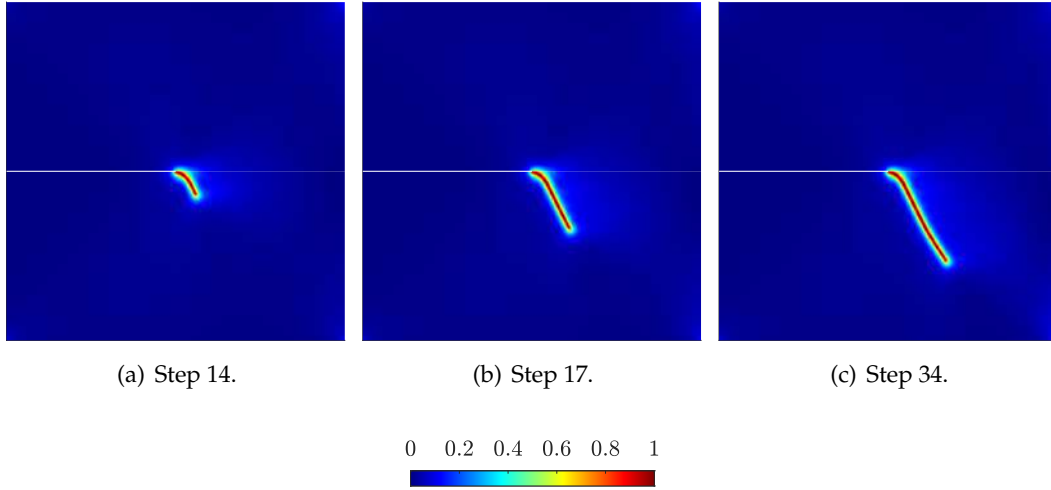
FIGURE 6.3: SEN specimen under shear loading. The phase-field problem is solved *via* the PSOR algorithm and we consider the phase-field evolution at three different steps: steps 14 and 17 correspond to the loading branch, while step 34 is at the end of the unloading branch. During the unloading phase, from step 22 to step 34, the phase field does not evolve.

(a) Staggered residual.   (b) Fracture energy.   (c) Total energy.
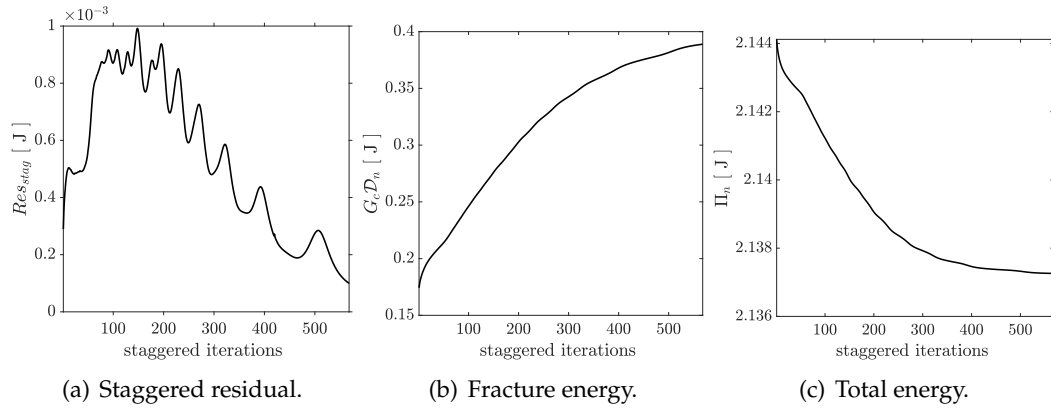
FIGURE 6.4: SEN specimen under shear loading. Convergence of the staggered algorithm using the PSOR method at load step 14 in terms of staggered residual Res_{stag}, fracture energy $G_c \mathcal{D}_n$, and total energy functional Π_n *versus* the number of staggered iterations.

of the penalty method. The overall execution time of both methods (measured *via* MATLAB® command `tic-toc`) in each n-th load step is depicted in Figure 6.6. Due to the explicit nature of the PSOR algorithm, we notice the non-negligible reduction in the analysis time with respect to the penalty approach [79]. Furthermore, we remark that, in the unloading steps $n = 22, ..., 34$, the PSOR method does not iterate, while the penalty method requires at least a couple of Newton-Raphson iterations. For the sake of completeness, the time required for the execution of the phase-field subroutine in the staggered iterations of loading step 14 is reported in Figure 6.7, which shows the stability of the PSOR method in terms of number of iterations and, consequently, of the required computational time to reach convergence. The same stable trend is achieved by the penalty method. It should be mentioned, however, that these results are strictly related to the choice of the tolerance in the two methods. More specifically, for the considered benchmarks we observed that the two approaches have a different behavior close to the solution. The PSOR method needs a significant number of iterations to meet a more

(a) Iteration 10.   (b) Iteration 100.   (c) Iteration 200.

(d) Iteration 300.   (e) Iteration 400.   (f) Iteration 500.
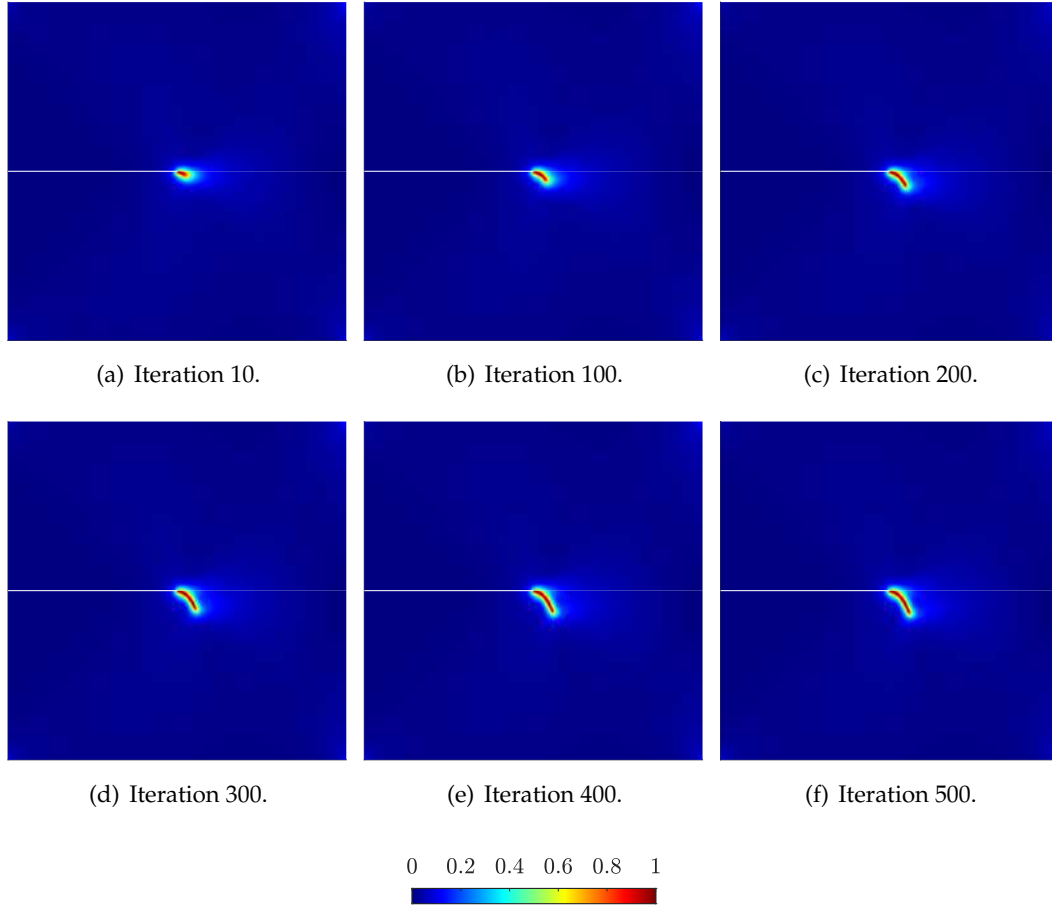
FIGURE 6.5: SEN specimen under shear loading. Phase-field evolution during the staggered iterations (iterations 10, 100, 200, 300, 400, and 500) at load step 14 for the PSOR method.

severe stopping criterion. Conversely, the Newton-Raphson method achieves the usual quadratic convergence rate, both for severe and reduced tolerances. However, for the two tolerances of the PSOR and penalty methods considered in this work (namely $\text{TOL}_{PSOR}^{(1)} = \text{TOL}_{NR,d}^{(1)} = 10^{-4}$ and $\text{TOL}_{PSOR}^{(2)} = \text{TOL}_{NR,d}^{(2)} = 10^{-6}$) we observe that, for the SEN specimen benchmark, the PSOR method provides a significant reduction in terms of elapsed time of the execution of the phase-field subroutine with respect to the penalty approach.

6.5.1.1   Preliminary C^1 quadratic results

The aim of this section is to show that the PSOR algorithm can be efficiently used also with higher-order, higher-continuity methods and is therefore suitable to be adopted in the IgA context. To this end, we further test the PSOR algorithm using a C^1 quadratic B-spline discretization of the SEN specimen and the same multipatch scheme as before. In particular, we investigate meshes with an increasing number of elements to assess whether the high regularity of IgA shape functions can lead to a reduction in terms of mesh size, which translates into faster calculations. To this end, we depart from a mesh with 201x202 C^1 quadratic elements, which we *h*-refine to obtain another two meshes with 271x342 elements and 401x402 elements. We further
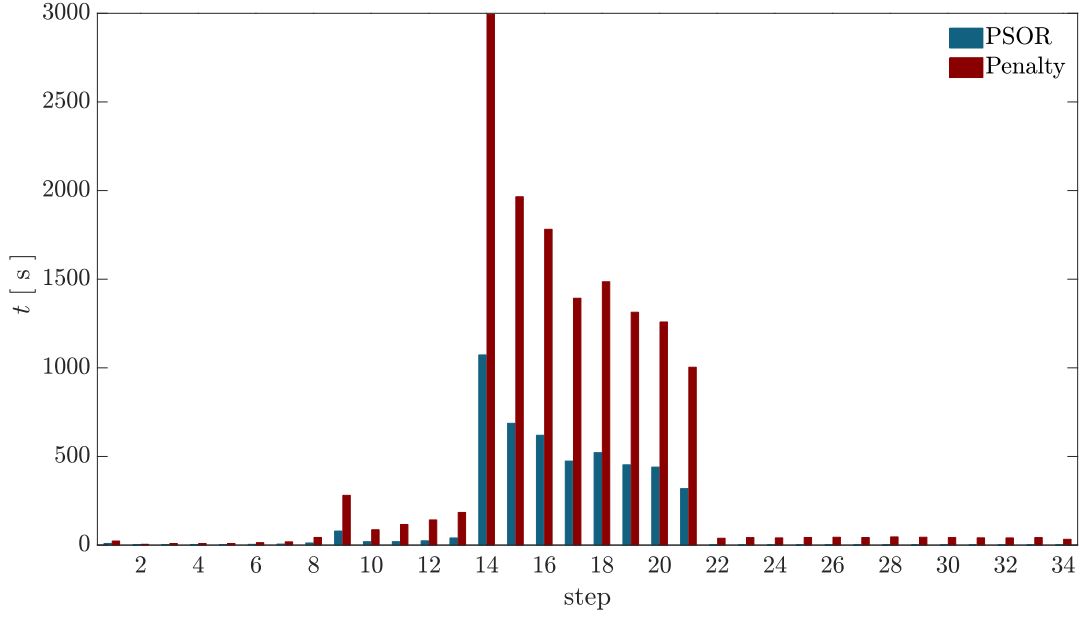
FIGURE 6.6: SEN specimen under shear loading. Total elapsed time to execute the phase-field subroutine at each load step. Comparison between PSOR and penalty methods.
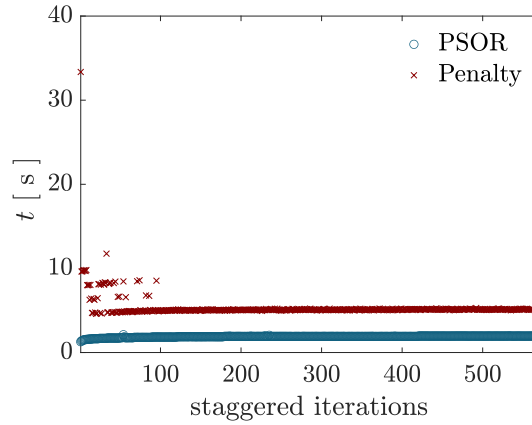
FIGURE 6.7: SEN specimen under shear loading. Total elapsed time to execute the phase-field subroutine at load step 14. Comparison between PSOR and penalty methods.

consider two different tolerances for the staggered method: $\text{TOL}_{stag}^{(1)} = 10^{-7}$ kJ and $\text{TOL}_{stag}^{(2)} = 10^{-10}$ kJ, while for the PSOR method and the Newton-Raphson algorithm we set $\text{TOL}_{PSOR}^{(1)} = \text{TOL}_{NR,d}^{(1)} = 10^{-4}$. Additionally, we use the solution obtained with the penalty method and linear B-spline discretization featuring 400x400 elements as a reference benchmark. However, we use the same number of Gauss points for each method regardless of the polynomial degree of approximation in the spatial discretization.

Figure 6.8 shows the global response of the reaction force R_n during the loading-unloading history of the SEN specimen test obtained with the PSOR method combined with a C^1 quadratic discretization and the benchmark calculated with the penalty method and a linear B-spline element mesh. For the coarsest mesh, with 201x202 C^1 quadratic elements, we observe that increasing TOL_{stag} does not yield a significant improvement in terms of solution accuracy for R_n with respect to the
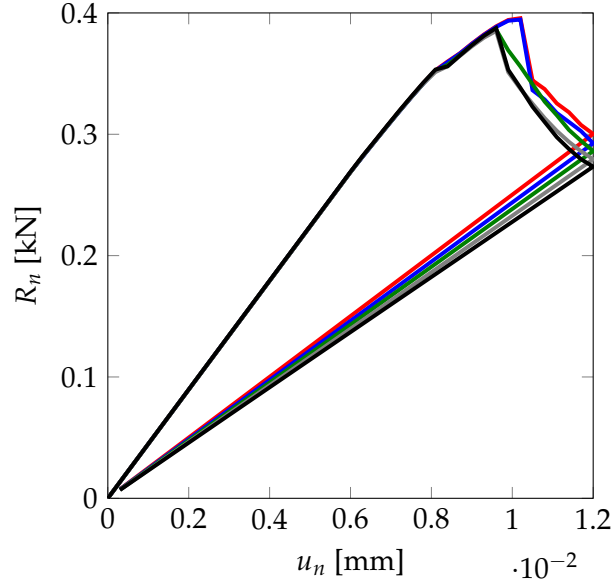
FIGURE 6.8: SEN specimen under shear loading. Comparison of the reaction force obtained with the PSOR method and a C^1 quadratic B-spline discretization *versus* the penalty method and a linear B-spline discretization (— PSOR 201x202 elements $\texttt{TOL}_{stag}^{(1)} = 10^{-7}$ kJ, — PSOR 201x202 elements $\texttt{TOL}_{stag}^{(2)} = 10^{-10}$ kJ, — PSOR 271x342 elements $\texttt{TOL}_{stag}^{(1)} = 10^{-7}$ kJ, — PSOR 401x402 elements $\texttt{TOL}_{stag}^{(1)} = 10^{-7}$, — Penalty 400x400 elements $\texttt{TOL}_{stag}^{(1)} = 10^{-7}$) kJ.

considered benchmark. Additionally, none of the considered tolerances leads to a reaction curve close to the reference solution during the propagation of the crack. This issue results from an insufficient number of elements to resolve the internal length l_0, which is only 2 for the 201x202 mesh. Maintaining $\texttt{TOL}_{stag}^{(1)} = 10^{-7}$ kJ and investigating the PSOR solution over the finer C^1 quadratic meshes, which feature an increased number of elements to represent l_0 (3 for the 271x342 mesh and 4 for the 401x402 mesh), we observe that the resulting reaction force R_n approaches the penalty solution as we progressively refine the mesh. Therefore, in the cases analyzed here we observe that the mesh resolution of the internal length (i.e., the number of elements supporting this length) is more relevant than the regularity of B-spline approximation. Nevertheless, we remark that the results shown in Figure 6.8 are preliminary and we intend to pursue further numerical tests featuring alternative IgA meshes (see Section 8).

6.5.2 L-shaped specimen test

The L-shaped specimen test, as described in [194], does not consider a pre-existing crack and involves fracture nucleation as well as propagation, resulting in a more elaborate test. The problem setup, comprising the geometry and the boundary conditions, is shown in Figure 6.9, where $a = 250$ mm, while the specimen thickness is $t = 100$ mm. The material parameters are assumed to be those of material type 2 in Table 6.1. The zoomed detail in Figure 6.9 shows the trapezoidal reinforcement, glued on the lower wing of the L-shape panel to avoid localized stress singularities inside the specimen. A vertical displacement u_n is applied to the shorter base
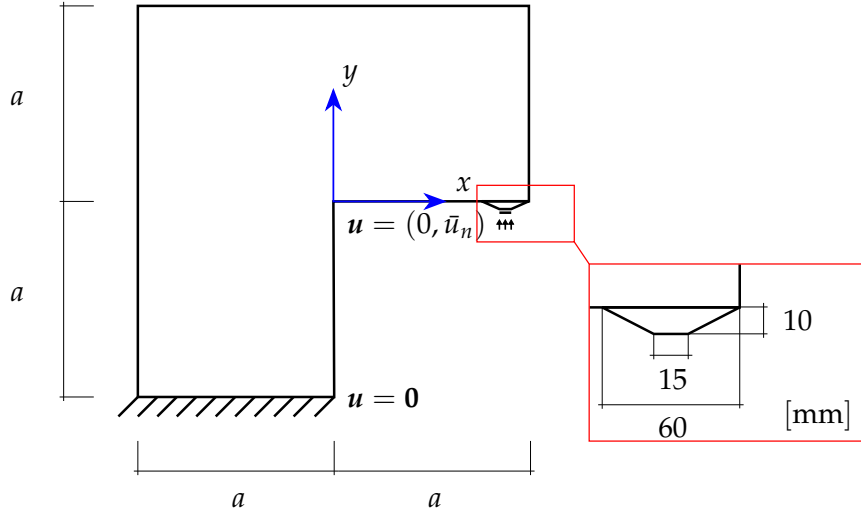
FIGURE 6.9: L-shaped specimen test. Geometry and boundary conditions.

of this ancillary item, while its horizontal degrees of freedom are restrained. The L-shaped structure is also completely clamped at $y = -a$. A loading-unloading displacement history is applied under plane strain conditions: starting from $u_1 = 0.01$ mm and considering $\Delta u_n = 0.01$ mm, 35 loading steps are applied (from 2 to 36), followed by 11 unloading steps (from 37 to 47). The unloading steps are obtained employing a loading decrement $3\Delta u_n$. For the adopted IgA discretization, the domain is subdivided into 4 patches (see Section 2.1.2.9), glued together such that C^0 continuity is granted at the interfaces. These patches are defined by the subdomains: $(-a, 0) \times (-a, 0)$, $(-a, 0) \times (0, a)$, $(0, a) \times (0, a)$, and the trapezoidal reinforcement and are discretized by 200x400, 320x200, 80x200, and 80x10 elements, respectively. We consider C^0 linear shape functions and the minimum mesh size is equal to 0.59 mm, fulfilling the spatial resolution requirements set by the assumed internal length l_0 according to [79], where the minimum element size is considered to be $h_{min} = \frac{1}{4}l_0$.

In Figure 6.10, we show the global response for the L-shaped specimen in terms of reaction force R_n, internal energy $\mathcal{E}_n$, and fracture energy $G_c \mathcal{D}_n$, at each imposed vertical displacement u_n. Three different behaviors of the considered sample can be identified. Until step 23, corresponding to the peak, no propagation occurs and the response is nearly elastic. From step 24 to 36, crack nucleation (see Figure 6.11(a)) and propagation (see, e.g., Figure 6.11(b)) take place, defining the softening part of the curve in Figure 6.10(a) and leading to a significant increase of fracture energy and to a corresponding reduction of elastic energy, noticeable in Figure 6.10(b). Finally, we highlight that during the elastic unloading stage starting after step 36, the level of dissipation remains constant and the crack no longer propagates (see Figure 6.11(c)), satisfying the irreversibility constraint. Furthermore, we remark that for the L-shaped panel test, the penalty method seems to be less accurate, producing a slightly non-constant dissipation in the unloading stage, as one can notice from the slight downward slope for decreasing u_n in the final part of the $G_c \mathcal{D}_n - u_n$ curve. In Figure 6.12, we present the convergence of the staggered algorithm at loading step 24, at the beginning of crack propagation. In particular, we consider the staggered residual (see Figure 6.12(a)), the total energy (see Figure 6.12(c)), and the fracture energy (see Figure 6.12(b)). We notice that for the L-shaped benchmark the discretized counterpart of the out-of-balance work seems to represent a conservative choice, due

(a) Reaction force.

(b) Internal and fracture energies.
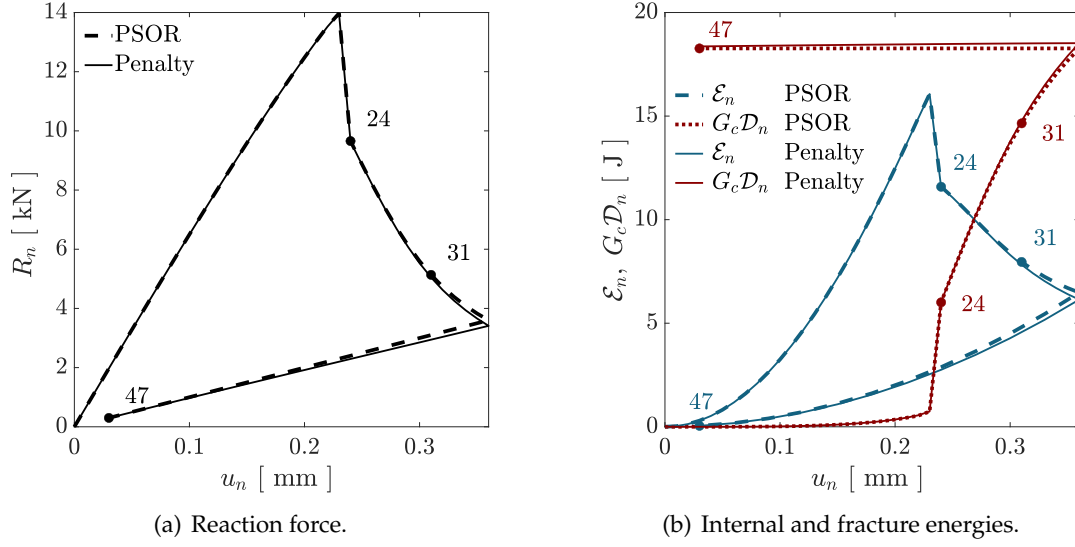
FIGURE 6.10: L-shaped specimen test. Global response with PSOR and penalty methods in terms of reaction force R_n, internal energy $\mathcal{E}_n$, and fracture energy $G_c\mathcal{D}_n$ *versus* imposed displacement u_n. Solid marks denote three relevant steps of the time history: step 24 corresponds to the first step after the beginning of the softening branch, step 31 is an intermediate step between the peak (step 23) and the beginning of the unloading branch, and step 47 is the end of the time history.

(a) Step 24. (b) Step 31. (c) Step 47.
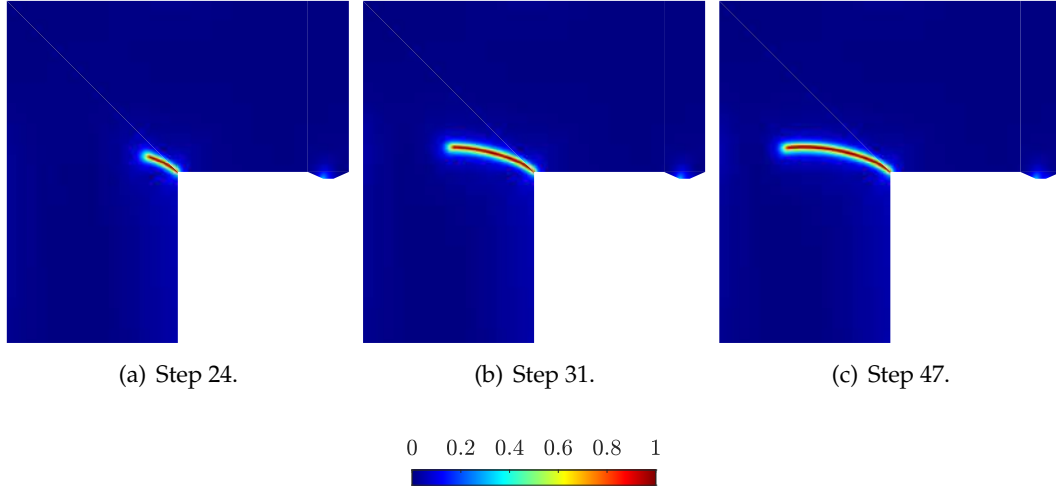
FIGURE 6.11: L-shaped specimen test. The phase-field problem is solved *via* the PSOR algorithm and we consider the phase-field evolution at three different steps: steps 24 and 31 correspond to the loading branch, while step 47 is at the end of the unloading branch. During the unloading phase, from step 37 to step 47, the phase field does not evolve.

to the fact that both the total energy and the fracture energy $G_c\mathcal{D}_n$ at iteration 250 (see Figure 6.12(c) and 6.12(b)) appear to be minimized, while Res_{stag} suggests the need to further iterate. Moreover, Figure 6.13 confirms that there is no remarkable difference in terms of the phase-field solution obtained between iteration 300 and 500 of loading step 24. Furthermore, we remark that results presented in Figures 6.11, 6.12, and 6.13 are obtained using the PSOR method and lead to virtually indistinguishable solutions with respect to the penalty method.

(a) Staggered residual. (b) Fracture energy. (c) Total energy.
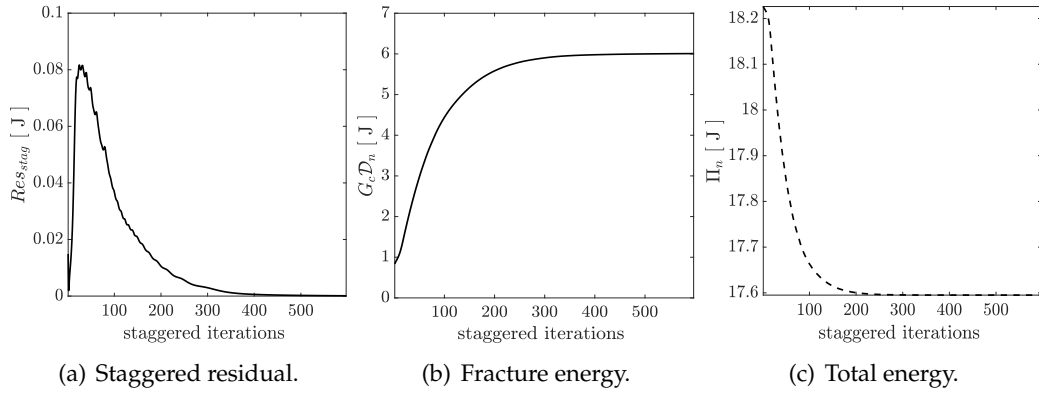
FIGURE 6.12: L-shaped specimen test. Convergence of the staggered algorithm using the PSOR method at load step 24 in terms of staggered residual Res_{stag}, fracture energy $G_c\mathcal{D}_n$, and total energy functional Π_n *versus* the number of staggered iterations.

(a) Iteration 10. (b) Iteration 100. (c) Iteration 200.

(d) Iteration 300. (e) Iteration 400. (f) Iteration 500.
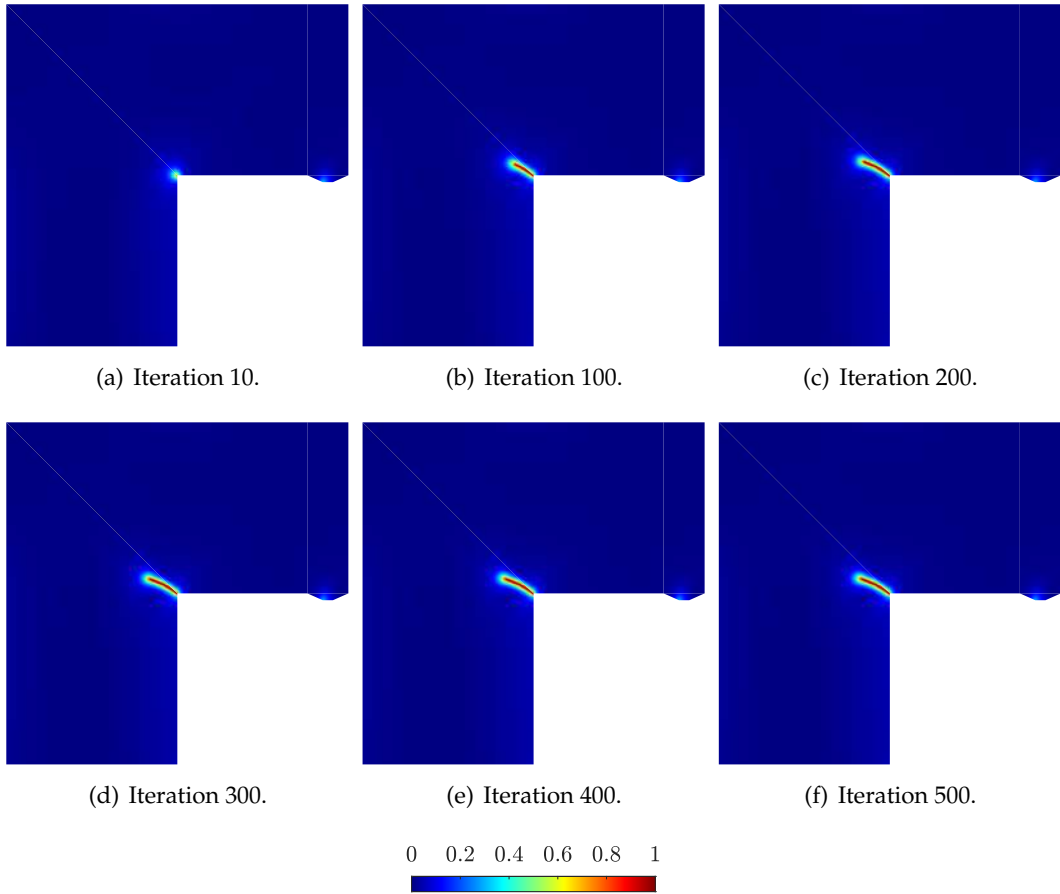
FIGURE 6.13: L-shaped specimen test. Phase-field evolution during the staggered iterations (iterations 10, 100, 200, 300, 400, and 500) at load step 24 for the PSOR method.

A comparison between the total time required for the execution of the phase-field subroutine *via* the PSOR and penalty methods is shown in Figure 6.15, while in Figure 6.14, we assess instead the performance of the PSOR and penalty algorithms in terms of computing time at each staggered iteration of step 24. The explicit nature of the PSOR algorithm leads to a time-saving performance, especially at the computationally more demanding step 24, during which the crack field nucleates.
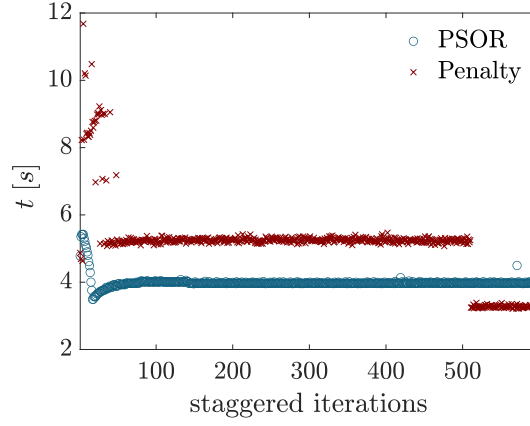
FIGURE 6.14: L-shaped specimen test. Total elapsed time to execute the phase-field subroutine at load step 24. Comparison between PSOR and penalty method.
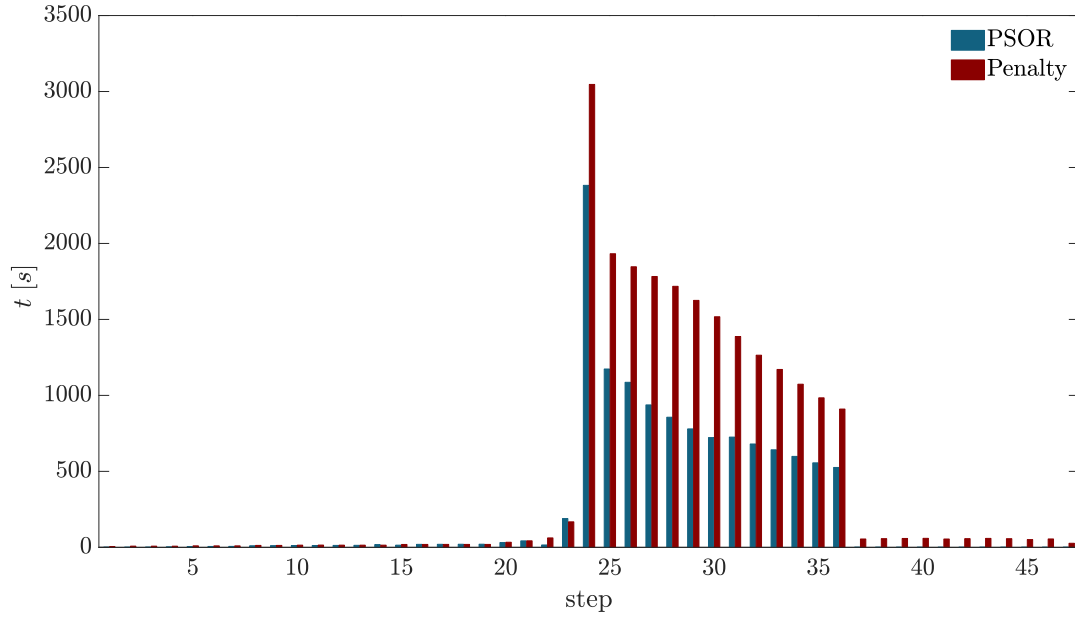
FIGURE 6.15: L-shaped specimen test. Total elapsed time to execute the phase-field subroutine at each load step. Comparison between PSOR and penalty methods.

Figures 6.15 and 6.14 show a similar behavior of the PSOR and penalty method as we reported for the SEN specimen in Section 6.5.1.

Finally, we remark that, to assess the PSOR algorithm we tested two tolerances (i.e., $\text{TOL}_{PSOR}^{(1)} = \text{TOL}_{NR,d}^{(1)} = 10^{-4}$ and $\text{TOL}_{PSOR}^{(2)} = \text{TOL}_{NR,d}^{(2)} = 10^{-6}$) also for the L-shaped specimen test. While for the SEN specimen example, a dramatic reduction of TOL_{PSOR} value leads to the same results in terms of time performance with respect to the penalty method, this is not the case for the L-shaped panel test, which proved to be more computationally demanding for the PSOR method when a tolerance equal to 10^{-6} is considered. Conversely, the performance of the penalty method in terms of required elapsed total subroutine time is less sensitive to the chosen tolerance.

6.6   Conclusions

In this chapter, we present a novel solution technique for the phase-field modeling of brittle fracture in elastic solids using IgA. In particular, we consider a thermodynamically consistent phase-field model, which accounts for a different damaging behavior in tension and compression as in [10]. We alternatively minimize the displacement and damage fields *via* a staggered approach and we propose to use the PSOR algorithm to solve the minimization of the total energy of the system with respect to the phase-field variable. The chosen solution technique directly enforces the irreversibility constraint, cutting negative values of the phase-field increments at the control points. We assess the performance of the PSOR algorithm and we notice a significant reduction of the execution elapsed time of the phase-field subroutine with respect to the penalty approach in [79]. This is related to the explicit nature of the PSOR technique, while the penalty method needs to assemble new matrix and vector terms to minimize the first variation of the penalized total energy function with respect to the phase-field variable for every Newton-Raphson iteration. It will be interesting in the future to compare the PSOR and penalty approaches considering real industrial problems dealing with large systems of equations.

To study the PSOR algorithm we could accurately resolve two standard benchmarks: a SEN specimen and an L-shaped panel both discretized *via* an IgG multipatch approach that features linear shape functions. For both considered cases we test two tolerances (i.e., $\mathtt{TOL}_{PSOR}^{(1)} = \mathtt{TOL}_{NR,d}^{(1)} = 10^{-4}$ and $\mathtt{TOL}_{PSOR}^{(2)} = \mathtt{TOL}_{NR,d}^{(2)} = 10^{-6}$) and we observed that using $\mathtt{TOL}_{PSOR}^{(1)} = \mathtt{TOL}_{NR,d}^{(1)} = 10^{-4}$, the PSOR algorithm allowed for a faster resolution of the problem with respect to the penalty method in both benchmark tests. While for the SEN specimen example, a dramatic reduction of the tolerance leads to the same results in terms of time performance with respect to the penalty method, this is not the case for the L-shaped panel test, which proved to be more computationally demanding for the PSOR method when a tolerance equal to 10^{-6} is considered. Conversely, the performance of the penalty method in terms of required time is less sensitive to the chosen tolerance. We believe that this issue is related to the tuning of the penalty parameter γ, which strongly depends on the toughness-internal length ratio. In fact, the value of γ for the L-shaped panel test is much smaller with respect to its counterpart for the SEN specimen benchmark, thereby representing a more relaxed constraint. On the other hand, it is worth noting that the application of the PSOR method is limited to linear and symmetric formulations of the phase-field problem. In this respect, the penalty approach appears to be of a more general applicability, though conditioned by a proper choice of the penalty parameter. Additionally, we discuss the choice of a suitable stopping criterion for the staggered scheme. Among possible criteria, we identify the control of the variation between two subsequent iterations of either the total energy functional or the phase-field variable. The latter option is equivalent to control the dissipated energy, since it provides a global measure of the damage inside the domain. However, in this study the considered convergence criterion uses the discretized counterpart of the out-of-balance work, which seems to grant the desired control over the staggered scheme.

We also present preliminary results comprising the modeling of the SEN specimen benchmark *via* C^1 quadratic B-splines shape functions, leading to the consideration that the internal length resolution seems to be more relevant than the regularity

of the approximation. It might be the case that using C^1 functions to approximate a physical discontinuity, such as the pre-existing crack in the SEN specimen, does not bring any further benefit. Further immediate studies could explore different approximations for each field in the problem, e.g., the phase field could be described by C^0 linear functions while the displacement could be modeled *via* C^0 quadratic B-splines, such that the both fields share the same number of control points. In any case, we believe that our preliminary results pave the way for future studies on higher-order discretizations [32].

Appendix 6.A: Implementation of the PSOR algorithm for sparse matrices

In Algorithm 6.A.1, we describe the implementation of the PSOR method for a symmetric sparse square matrix of dimension $n_{n_p} \mathrm{x} n_{n_p}$ ($n_{n_p} = m_1 m_2$ is the number of control points) and n_{nz} non-zero entries, according to the compressed column storage (CCS) representation. The input data are the matrix of the values *PA*, the matrix of the row indices *IR*, the array *JC* containing all the pointers to entries of the *IR* array, and the driving vector $\mathbf{q}$ that here is treated as an array q.

In Algorithm 6.A.1, the While loop iterates until the chosen convergence criterion, i.e., the infinite norm of the solution variation between two subsequent iterations, is satisfied.

The outer For loop runs over the sparse matrix columns j_{col} (i.e., over the component of the solution array $\Delta d^k(j_{col})$). Here, the explicit nature of the algorithm is clear, since the solution at every k-th iteration is obtained component-wise and the j_{col}-th component depends on all its previous components (from 1 to $j_{col} - 1$). The scheme exploits the fact that $\mathbf{L}$ is a strict lower triangular matrix. According to the CCS representation, the For loop runs over the columns of the sparse matrix.

The inner For loop runs over the sparse matrix h-th row of the j_{col}-th column. The matrix-to-vector products are performed according to the standard description of sparse matrices. For fixed r-th index, the product $Q_{rc} \Delta d_c^{k-1}$ of Equation (6.73) returns a scalar, which is stored into the quantity $Q\Delta d$.

The first If statement ($i_{row} == j_{col}$) extracts the diagonal term, compute its inverse, and stores it into the scalar variable D^{-1}. The second If statement ($i_{row} < j_{col}$) computes the product $Q_{r>c} (\Delta d_c^k - \Delta d_c^{k-1})$ of Equation (6.73). It is the scalar product between the r-th row of the matrix $\mathbf{L}^T$ and the vector $(\Delta d_c^k - \Delta d_c^{k-1})$. Since $\mathbf{L}^T$ is the strict upper triangular part of the sparse matrix, the If statement reads $i_{row} < j_{col}$. The result of the scalar product $Q_{r<c} (\Delta d_c^k - \Delta d_c^{k-1})$ is stored into the quantity $L\Delta\Delta d$, where $\Delta\Delta d$ refers to the variation of the solution between two subsequent iterations $k - 1$ and k.

Algorithm 6.A.1 PSOR algorithm for sparse matrices.

---

input : $PA(n_{nz}, 1)$, $IR(n_{nz}, 1)$, $JC(n + 1, 1)$, $q(n, 1)$

$\Delta d^0(n, 1) = 0$

while $Res_{PSOR} > \text{TOL}_{PSOR}$ **do**

     $\Delta d^{k-1} = \Delta d^k$

     for $j_{col} \leftarrow 1$ **to** n_{np} **do**

         $Q\Delta d = 0$

         $L\Delta\Delta d = 0$

         for $h \leftarrow JC(j_{col})$ **to** $JC(j_{col} + 1) - 1$ **do**

             $i_{row} = IR(h)$

             $Q\Delta d = Q\Delta d + PA(h)\, \Delta d^{k-1}(i_{row})$

             if $(i_{row} == j_{col})$ **then**

                 $D^{-1} = [PA(k)]^{-1}$

             if $(i_{row} < j_{col})$ **then**

                 $L\Delta\Delta d = L\Delta\Delta d + PA(h)\, \left[\Delta d^k(i_{row}) - \Delta d^{k-1}(i_{row})\right]$

         $\Delta d^k(j_{col}) = \left\langle \Delta d^{k-1}(j_{col}) - D^{-1}\left[Q\Delta d + q(j_{col}) + L\Delta\Delta d \right] \right\rangle_+$

     $Res_{PSOR} = \left\| \Delta d^k - \Delta d^{k-1} \right\|_\infty$

output: $\Delta d^k(n_{np}, 1)$

Appendix 6.B: Alternative stopping criteria of the PSOR algorithm

Other two possible criteria involve the activation condition (6.63b). For every k-th iteration of the PSOR algorithm, let us define the set of control points (i.e., $n_{n_p} = m_1 m_2$ is the maximum number of control points) where the phase-field increment solution Δd_r^k is positive $C_+^{(k)} := \left\{ r \in \left[1, n_{n_p}\right] : \Delta d_r^k > 0 \right\}$ and the set where Δd_r^k is zero $C_0^{(k)} := \left\{ r \in \left[1, n_{n_p}\right] : \Delta d_r^k = 0 \right\}$. Thus, for every $r \in C_+^{(k)}$ the activation condition satisfies $Q_{rc}\Delta d_c^k + q_r = 0$, while for every $r \in C_0^{(k)}$ it should be valid $Q_{rc}\Delta d_c^k + q_r > 0$. In the following, we introduce the other two possible residuals as

$$Res_{d+}^{(k)} := \max_{r \in C_+^{(k)}} \left| Q_{rc}\Delta d_c^k + q_r \right|, \tag{6.B.1a}$$

$$Res_{d0}^{(k)} := - \min_{r \in C_0^{(k)}} \langle Q_{rc}\Delta d_c^k + q_r \rangle_- . \tag{6.B.1b}$$

In the first case (6.B.1a), the criterion checks whether the activation function is different from zero in absolute value. Conversely, in the second case (6.B.1b) the criterion verifies whether the positiveness of the activation function is violated. The residuals in Equation (6.B.1) are problem-dependent since they are dimensional. Therefore, we propose to study very strict tolerances, namely $\text{TOL}_{d+} = 10^{-9}$ and $\text{TOL}_{d0} = 10^{-9}$. It has been observed that $Res_{d0}^{(k)} \leq \text{TOL}_{d0}$ criterion is usually satisfied in all iterations,

while the control of $Res_{d+}^{(k)} \leq \text{TOL}_{d+}$ seems to be the most strict requirement. Thus, the complementarity condition (6.63a) converges faster to zero since it comes from the product of (6.63b) and (6.63c).

Appendix 6.C: A separately quadratic non-convex function

We provide a simple example of a separately quadratic function which is not jointly convex. For $\eta > 0$ let $f : \mathbb{R}^2 \rightarrow \mathbb{R}$ defined by

$$f(x,y) = \tfrac{1}{2}(x^2 + \eta)\, y^2 + \tfrac{1}{2}(1-x)^2. \qquad (6.C.1)$$

Accordingly, its Hessian matrix reads

$$\nabla^2 f(x,y) = \begin{pmatrix} y^2 + 1 & 2xy \\ 2xy & x^2 + \eta \end{pmatrix}. \qquad (6.C.2)$$

In particular, $\nabla^2 f(x,y)$ is not positive definite for $y = x$ when $x, y \gg 1$.

Then, we define $F(x)$ and $G(y)$ as evaluation of Equation (6.C.1) for fixed values of y (i.e., $\bar{y}$) and x (i.e., $\bar{x}$), respectively, as

$$F(x) = \tfrac{1}{2}(x^2 + \eta)\, \bar{y}^2 + \tfrac{1}{2}(1-x)^2, \qquad (6.C.3)$$
$$G(y) = \tfrac{1}{2}(\bar{x}^2 + \eta)\, y^2 + \tfrac{1}{2}(1-\bar{x})^2. \qquad (6.C.4)$$

We compute again the second derivatives of $F(x)$ and $G(y)$:

$$\frac{\partial^2 F(x)}{\partial x^2} = \bar{y}^2 + 1, \qquad (6.C.5)$$

$$\frac{\partial^2 G(y)}{\partial y^2} = \bar{x}^2 + \eta, \qquad (6.C.6)$$

highlighting that function $F(x)$ and $G(y)$ are quadratic and convex.

Chapter 7

Combining boundary-conforming finite elements and isogeometric collocation in the context of fluid-structure interaction

While IgG methods have been integrated into FSI analysis almost from the beginning of IgA [21], IgC so far has been only used for immersed FSI [41] and to the authors best knowledge there has been no application yet to boundary-fitted FSI. Therefore, in this chapter we discuss the spatial coupling between boundary-conforming finite elements (i.e., NEFEM) and IgC, where the coupling conditions only need to be fulfilled at the collocation points (see Figure 7.1). In Section 7.1, we introduce the FSI problem, focusing on the fluid mechanics, the elastodynamics equations of the structure, as well as the FSI conditions. Then, the considered numerical methods are detailed in Section 7.2 that focuses on the boundary-conforming mapping and IgC for nonlinear elastostatics and its extension to elastodynamics. In Section 7.3, several preliminary numerical tests prove the promising potential of the proposed numerical approach. Finally, conclusions are drawn in Section 7.4.
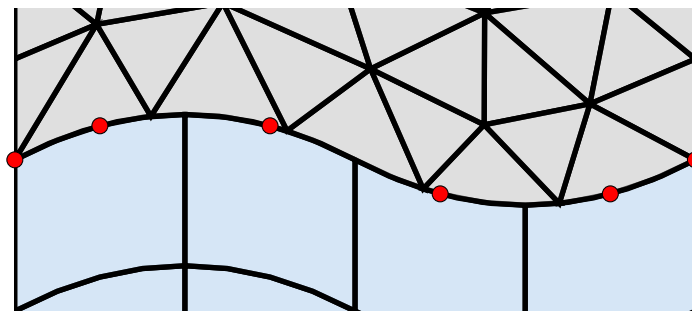
FIGURE 7.1: NEFEM-IgC coupling.

7.1   FSI problem definition

The FSI problem is defined in the following as a surface-coupled problem based on the fundamental laws of continuum mechanics. First, both single-field boundary-value problems are introduced. Even though the two fields only differ in terms of their constitutive relations, they will be detailed in their respective viewpoints, i.e., Eulerian for the fluid and Lagrangian for the structure. Finally, the way the fields interact with each other is defined introducing the coupling conditions on the common interface connecting the fluid and solid domains.

7.1.1   Fluid mechanics

Following an Eulerian viewpoint, the balance laws of the mass and linear momentum for an incompressible material occupying the current domain Ω_x at each instant in time $t \in [0, T]$ can be stated as

$$\nabla \cdot v = 0 \quad \text{in } \Omega_x \ \forall t \in [0, T] \,, \tag{7.1}$$

$$\rho^f \left(\frac{\partial v}{\partial t} + v \cdot \nabla v - \mathbf{f} \right) - \nabla \cdot \mathbf{T} = \mathbf{0} \quad \text{in } \Omega_x \ \forall t \in [0, T] \,, \tag{7.2}$$

where $v(\mathbf{x}, t)$ is the fluid velocity, ρ^f is the fluid density, $\mathbf{T}$ is the total stress tensor, and $\mathbf{f}$ is the vector of external body forces per unit mass of the fluid. Due to the incompressibility constraint, the energy equation is decoupled and not considered here. Thus, the Navier-Stokes equations are closed by leveraging Stokes law, which reflects the main property of a fluid to be unable to sustain shear stress. In the Newtonian case, the total stress tensor $\mathbf{T}$ for incompressible fluids is defined as

$$\mathbf{T}(v, p) = -p\mathbf{I} + 2\mu^f \mathbf{D}(v) \,, \tag{7.3}$$

with

$$\mathbf{D}(v) = \frac{1}{2} \left(\nabla v + (\nabla v)^{\mathrm{T}} \right) \,. \tag{7.4}$$

In Equation (7.3), μ^f denotes the dynamic viscosity, while $p(\mathbf{x}, t)$ represents the pressure.

A well-posed system is obtained by imposing boundary conditions on the external boundary of Ω_x, denoted as Γ_x. Here, we distinguish between Dirichlet and Neumann boundary conditions given by

$$v = h \quad \text{on } (\Gamma_x)_D \,, \tag{7.5}$$

$$\mathbf{T} \cdot n = t \quad \text{on } (\Gamma_x)_N \,, \tag{7.6}$$

where n is the outward normal unit vector, h and t are the velocity and traction values respectively prescribed on $(\Gamma_x)_D$ and $(\Gamma_x)_N$, which denote the Dirichlet and Neumann parts of the boundary such that $(\Gamma_x)_N \cup (\Gamma_x)_D = \Gamma_x$ and $(\Gamma_x)_N \cap (\Gamma_x)_D = \emptyset$.

In the transient case, a divergence-free velocity field for the whole computational domain is needed as an initial condition:

$$v(\mathbf{x}, 0) = v^0(\mathbf{x}) \quad \text{in } \Omega_x \text{ at } t = 0 \,. \tag{7.7}$$

7.1.2 Elastodynamics of the structure

The elastodynamic problem of the structure can be defined adopting the Lagrangian viewpoint. For an isothermal and compressible material occupying the reference domain Ω_X with boundary Γ_X at $t = 0$, the balance law of the linear momentum can be stated as

$$\rho^s \frac{d^2 \boldsymbol{u}}{dt^2} = \boldsymbol{\nabla}_{\mathbf{X}} \cdot (\mathbf{FS}) + \boldsymbol{B} \quad \text{in } \Omega_X \; \forall t \in [0, T] \,. \tag{7.8}$$

In Equation (7.8), the response of a body to an external load is described by the displacement field $\boldsymbol{u}\,(\mathbf{X}, t)$ – the change between the current configuration $\mathbf{x}$ and the initial configuration $\mathbf{X}$ – and the second Piola-Kirchhoff stress tensor $\mathbf{S}$. Furthermore, ρ^s indicates the density of the solid, $\boldsymbol{B}$ the prescribed body forces per unit of volume in the initial configuration, and $\mathbf{F}$ the deformation gradient defined as

$$\mathbf{F} = \frac{\partial \mathbf{x}}{\partial \mathbf{X}} \,. \tag{7.9}$$

A constitutive law has to be introduced to close the system of equations and specify the properties of the considered solid. In this work, we choose a linear stress-strain relation between the second Piola-Kirchhoff stress tensor $\mathbf{S}$ and the Green-Lagrange strain tensor $\mathbf{E}$:

$$\mathbf{E} = \frac{1}{2} \left(\mathbf{F}^{\mathsf{T}} \mathbf{F} - \mathbf{I} \right) , \tag{7.10}$$

$$\mathbf{S} = \mathbb{C} : \mathbf{E} , \tag{7.11}$$

where $\mathbb{C}$ is the constant fourth-order linear elasticity tensor. Due to major and minor symmetry properties of $\mathbb{C}$, it is possible to reduce the full elasticity tensor to two constants in the case of a homogeneous isotropic material, such that Equation (7.11) can be written in the form

$$\mathbf{S} = \lambda^s \mathrm{tr}(\mathbf{E})\mathbf{I} + 2\mu^s \mathbf{E} \,. \tag{7.12}$$

The two constants λ^s and μ^s are termed Lamé parameters. In the literature, the material detailed in Equation (7.12) is known as Saint Venant-Kirchhoff model. It can be used to describe classes of problems where large displacements occur. However, it is restricted to small strains and elastic deformations. Thus, combining Equations (7.8) and (7.12) leads to the balance momentum of geometrically nonlinear and materially linear elastodynamics [77].

As for the fluid, a well-posed system is obtained by imposing boundary conditions on the boundary Γ_X. We again distinguish between Dirichlet and Neumann boundary conditions, defined as in Section 7.1.1 and given by

$$\boldsymbol{u} = \boldsymbol{g} \text{ on } (\Gamma_X)_D \,, \tag{7.13}$$

$$(\mathbf{FS}) \cdot \mathbf{N} = \boldsymbol{t} \text{ on } (\Gamma_X)_N \,, \tag{7.14}$$

where g and t are prescribed displacements and tractions. In Equation (7.14), $\mathbf{N}$ denotes the outward normal unit vector on Γ_X.

Furthermore, we define the initial conditions for the displacement and velocity as

$$u\left(\mathbf{X}, 0\right) = u^0 \quad \text{in } \Omega_X \text{ at } t = 0\,, \tag{7.15}$$

$$\frac{du\left(\mathbf{X}, 0\right)}{dt} = v^0 \quad \text{in } \Omega_X \text{ at } t = 0\,. \tag{7.16}$$

7.1.3   Coupling conditions at the fluid-structure interface

A fluid-structure interaction problem is defined on a fluid domain Ω_x^f and a solid domain Ω_x^s, such that

$$\overline{\Omega_x^f} \cup \overline{\Omega_x^s} = \Omega_x \qquad \text{and} \qquad \Omega_x^f \cap \Omega_x^s = \varnothing\,, \tag{7.17}$$

and both subdomains are separated by a unique interface Γ_x^{fsi}, i.e.,

$$\overline{\Omega_x^f} \cap \overline{\Omega_x^s} = \Gamma_x^{fsi}\,, \tag{7.18}$$

where, in Equations (7.17) and (7.18), $\overline{\Omega_x^f}$ and $\overline{\Omega_x^s}$ denote the closure of Ω_x^f and Ω_x^s, respectively.

The related coupling conditions to be satisfied on Γ_x^{fsi} can be stated as:

$$\mathbf{x}^f = \mathbf{x}^s\,, \tag{7.19}$$

$$v^f = v^s\,, \tag{7.20}$$

$$\mathbf{T} \cdot n^f = \sigma \cdot n^s\,. \tag{7.21}$$

To transfer stresses between the Eulerian and Lagrangian viewpoints in the solid domain, i.e., the current and reference configurations, the following relationship between the total stress tensor $\mathbf{T}$ and second Piola-Kirchhoff stress tensor $\mathbf{S}$ holds on Γ_x^{fsi}

$$\mathbf{S} = \det(\mathbf{F})\mathbf{F}^{-1}\mathbf{T}\,\mathbf{F}^{-T}. \tag{7.22}$$

7.2   Numerical methods

In this section, we propose a partitioned approach to solve the full FSI problem. To this end, we introduce the coupling between NEFEM to solve the fluid problem and IgC to resolve the solid problem. The key feature to couple both methods is the definition of a common spline-based representation of the interface between the solid and fluid subdomains. This is achieved on the fluid side by a boundary-conforming mapping for the elements in the vicinity of the wall involving the spline used on
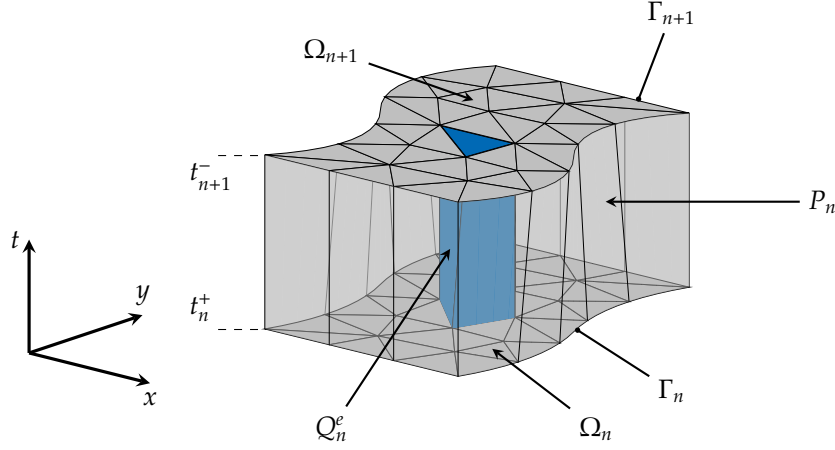
FIGURE 7.2: Example of a discretized space-time slab Q_n^h for the time span $[t_n, t_{n+1}]$.

the solid side. Additionally, we consider a staggered Dirichlet-Neumann coupling, which combines a space-time finite element method and the NEFEM-based boundary mapping on the fluid side with IgC on the solid side. In the following, we first introduce the numerical methods to solve the fluid and the solid problem and, then, we proceed to present the computational strategy for their coupling.

7.2.1 Fluid solver

We use a space-time discretization for the fluid, as shown in Figure 7.2. The key idea is to discretize the space-time continuum Q – assembled by all spatial domains for a given time-span – at once. In this work, we conduct this discretization by applying the most common approach in the literature, which consists of a discontinuous Galerkin formulation in time. However, this discretization can be carried out in alternative ways, e.g., with n-simplices [26, 54, 104]. Initially derived to solve elastodynamic problems [94], the chosen space-time discretization was transferred to incompressible Euler and Navier-Stokes equations on rigid domains [167] and extended as the *deforming-spatial-domain/stabilized space-time method* to deforming domains [174, 175]. A brief introduction of the applied space-time finite element method is given below, followed by a description of the adopted boundary-conforming mapping, which represents the basis for the coupling with the solid solver. We refer readers to [89] for more details.

7.2.1.1 Deforming-spatial-domain/stabilized space-time method

To discretize the space-time domain, we utilize the property of physical time-dependent problems that information flows in the direction of positive time only [94]. The time interval $[0, T]$ is subdivided into subintervals $I_n = (t_n, t_{n+1})$, with t_n and t_{n+1} representing an ordered series of time levels $0 = t_0 < t_1 < t_2 < ... < t_N = T$. We can define the time slab Q_n by defining its bounds $\Omega_n = \Omega_{t_n}$, $\Omega_{n+1} = \Omega_{t_{n+1}}$,

and the surface P_n, which is based on the time varying boundary Γ_t for I_n (see Figure 7.2). The problem is solved sequentially for each space-time slab, starting with:

$$(v_h)_0^+ = v_0. \tag{7.23}$$

Each space-time slab is discretized by extruding a spatial triangulation in the time direction using a single element in time for each element in space (i.e., Q_n^e, see Figure 7.2). Hence, a suitable finite-dimensional interpolation of the space-time domain can be constructed by means of a tensor-product structure, i.e., using shape functions defined as

$$N_a^\alpha = T^\alpha N_a, \tag{7.24}$$

where T^α represents the interpolation function in time and N_a the interpolation function in space. Thus, we introduce the adopted finite-dimensional spaces:

$$(\mathcal{V}_{\delta v}^h)_n = \{\delta v_h \,|\, \delta v_h \in [H^1(Q_n^h)]^{d_s}, \delta v_h = \mathbf{0} \text{ on } (P_n^h)_D\}, \tag{7.25}$$

$$(\mathcal{S}_v^h)_n = \{v_h \,|\, v_h \in [H^1(Q_n^h)]^{d_s}, v_h = h \text{ on } (P_n^h)_D\}, \tag{7.26}$$

$$(\mathcal{S}_p^h)_n = (\mathcal{V}_p^h)_n = \{p_h \,|\, p_h \in H^1(Q_n^h)\}. \tag{7.27}$$

In the following, linear shape functions in time are combined with either linear Lagrangian elements [94, 174, 175] in the interior domain or the boundary-conforming elements introduced in Section 7.2.1.2 in space. Other combinations like spline-based methods in the form of space-time IgG formulations are presented in [173].

Based on the mathematical definitions presented so far, we further introduce the following notation:

$$(v_h)_n^\pm = \lim_{\epsilon \to 0} v(t_n \pm \epsilon), \tag{7.28}$$

$$\int_{Q_n^h} \ldots dQ = \int_{I_n} \int_{\Omega_t^h} \ldots d\Omega \, dt, \tag{7.29}$$

$$\int_{P_n^h} \ldots dP = \int_{I_n} \int_{\Gamma_t^h} \ldots d\Gamma \, dt. \tag{7.30}$$

Then, the stabilized space-time formulation of the incompressible Navier-Stokes equations on deforming domains can be stated as: given $(v_h)_n^-$, find $v_h \in (\mathcal{S}_v^h)_n$

and $p_h \in (\mathcal{S}_p^h)_n$ such that $\forall \delta v_h \in (\mathcal{V}_{\delta v}^h)_n$, $\forall q_h \in (\mathcal{V}_p^h)_n$:

$$
\int_{Q_n^h} \left(\delta v_h \cdot \rho^f \left(\frac{\partial v_h}{\partial t} + v_h \cdot \nabla v_h - \mathbf{f} \right) + \mathbf{D}(\delta v_h) : \mathbf{T}(p_h, v_h) \right) dQ + \int_{Q_n^h} q_h (\nabla \cdot v_h) \, dQ
$$

$$
+ \int_{\Omega_n^h} (\delta v_h)_n^+ \cdot \rho^f \left((v_h)_n^+ - (v_h)_n^- \right) d\Omega
$$

$$
\color{blue}{+ \sum_{e=1}^{N_e} \int_{Q_n^e} \tau_1 \left[\rho^f \left(\frac{\partial \delta v_h}{\partial t} + v_h \cdot \nabla \delta v_h \right) - \nabla \cdot \mathbf{T}(q_h, \delta v_h) \right]}
$$

$$
\color{blue}{\cdot \left[\rho^f \left(\frac{\partial v_h}{\partial t} + v_h \cdot \nabla v_h - \mathbf{f} \right) - \nabla \cdot \mathbf{T}(p_h, v_h) \right] dQ}
$$

$$
\color{blue}{+ \sum_{e=1}^{N_e} \int_{Q_n^e} \tau_2 (\nabla \cdot \delta v_h)(\nabla \cdot v_h) \, dQ}
$$

$$
= \int_{P_n^h} \delta v_h \cdot \mathbf{t} \, dP \,.
$$

$$(7.31)$$

The first two terms in Equation (7.31) are the weak form of Equation (7.1)-(7.2), integrated over the discretized time slab Q_n^h. The third term – called *jump term* – results from applying a discontinuous Galerkin approach in time [94, 100], whereby the continuity of the unknown velocity is enforced in a weak sense between the time slabs. The last two terms on the left-hand side are the stabilization terms for the momentum equation and the velocity field. Following the GLS/SUPG stabilization, these terms (highlighted in blue) enhance the stability of the Galerkin method without degrading accuracy [93] and allow to use equal order interpolation functions for the velocity and pressure, while the Ladyzhenskaya-Babuška-Brezzi condition is circumvented. A detailed analysis for the stabilized Navier-Stokes equations involving viscous stress, velocity, and pressure primary variables is presented in [28]. In the case of linear space-time Lagrangian finite elements, the second order derivative in the viscous term would disappear. To ensure consistency and enhance the convergence, this term is reconstructed following the approach in [98]. Moreover, for the last two terms on the left-hand side in Equation (7.31) the residual form of the momentum equation and the incompressibility condition ensure consistency. The parameters τ_1 and τ_2,

$$
\tau_1 = \tau_{\text{MOM}} \frac{1}{\rho^f} \qquad \text{and} \qquad \tau_2 = \tau_{\text{CONT}} \rho^f \,, \tag{7.32}
$$

are locally defined stabilization parameters, which need to be designed by error estimation, convergence, and dimensional analysis [167]. Further details on the method and its parameters τ_{MOM} and τ_{CONT} can be found in [27, 150].

7.2.1.2 Boundary-conforming mapping

The fluid problem is solved relying on the deforming-spatial-domain/stabilized space-time method with the GLS/SUPG stabilization introduced before. While the solution is approximated with linear Lagrangian shape functions N_a, we consider a standard finite element mesh to only model the interior of the domain. Before discussing how the boundary elements make use of the NURBS boundary, let us first
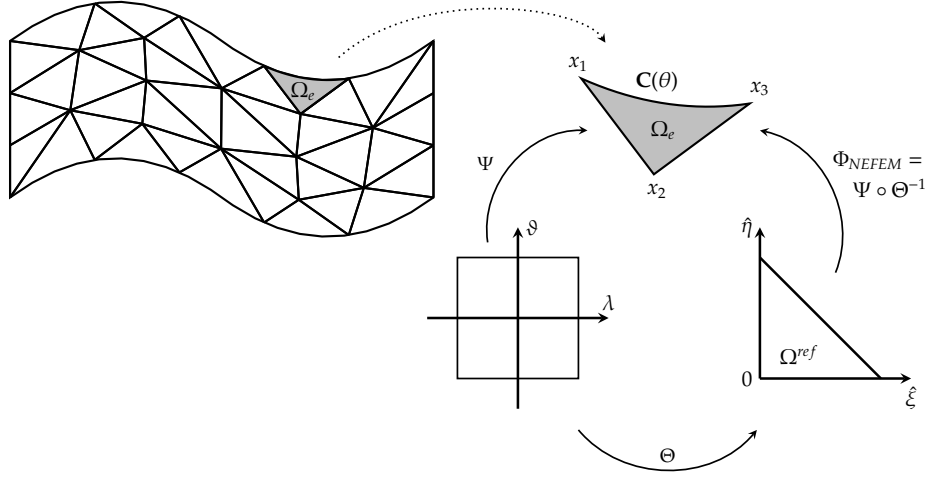
FIGURE 7.3: The Triangle-Rectangle-Triangle (TRT) mapping. The shape function definition is performed on the reference element that is transformed into the global element using a non-linear mapping Φ_{TRT}, which includes the NURBS definition.

define a NURBS curve $\mathbf{C}(\theta) = \sum_{i=1}^{n} R_i^p(\theta)\mathbf{B}_i$ of degree p (with n being the considered number of control points $\mathbf{B}_i$ and $R_i^p(\theta)$ the NURBS shape functions for any θ knot-vector parametric coordinate). Then, the elements on the boundary can be integrated following the idea of NEFEM [165] by means of a Triangle-Rectangle-Triangle (TRT) mapping [89] (see Figure 7.3) for curved triangles in 2D:

$$\Phi_{TRT} = \Theta^{-1} \circ \Psi : \Omega^{ref} \longrightarrow \Omega_e$$

$$\left(\hat{\eta},\hat{\xi}\right) \longmapsto \Phi_{TRT}(\hat{\eta},\hat{\xi}) = (1 - \hat{\eta} - \hat{\xi})x_2 + (\hat{\eta} + \hat{\xi})\mathbf{C}\left(\frac{\theta_1\,\hat{\eta} + \theta_3\,\hat{\xi}}{\hat{\eta} + \hat{\xi}}\right). \tag{7.33}$$

In Equation (7.33), $\hat{\eta}$ and $\hat{\xi}$ denote the parametric coordinates of the triangular reference element, x_2 is the physical coordinate of the interior node, and θ_1, θ_3 are the parametric coordinates of the NURBS curve at which the element boundary nodes are located.

7.2.2 Isogeometric collocation

In this section, we derive the spatial discretization of the nonlinear elastostatics problem considering a 2D solid domain and employing an IgC scheme following [116]. To this extent, we restrict the description to model 2D problems since in Section 7.3 the tests we implement are bi-dimensional benchmarks. Afterwards, the application of IgC is extended to the nonlinear elastodynamics model.

7.2.2.1 Isogeometric collocation for nonlinear elastostatics

Considering the balance equations of elastodynamics (7.8) with boundary conditions (7.13) and (7.14), a 2D nonlinear elastostatics problem, neglecting body forces, reads: find $u : \Omega_X \to \mathbb{R}^2$ such that

$$
\begin{cases}
\boldsymbol{\nabla}_X \cdot (\mathbf{FS}) = \mathbf{0} & \text{in } \Omega_X, & \text{(7.34a)} \\[2mm]
u = g & \text{on } (\Gamma_X)_D, & \text{(7.34b)} \\[2mm]
(\mathbf{FS}) \cdot \mathbf{N} = t & \text{on } (\Gamma_X)_N. & \text{(7.34c)}
\end{cases}
$$

Following the work of Kruse *et al.* [115], the discretized collocated strong form of (7.34) is derived based on its weak form, which can be expressed by

$$
\int_{\Omega_X} [\boldsymbol{\nabla}_X \cdot (\mathbf{FS})] \cdot \delta u \ \mathrm{d}\Omega_X - \int_{\Gamma_X} [(\mathbf{FS}) \cdot \mathbf{N} - t] \cdot \delta u \ \mathrm{d}\Gamma = 0, \tag{7.35}
$$

for every test function $\delta u \in [H^1(\Omega_X)]^{d_s}$ satisfying homogeneous Dirichlet boundary conditions, i.e.,

$$
\delta u = \mathbf{0} \quad \text{on } (\Gamma_X)_D. \tag{7.36}
$$

Following IgC (see Section 2.1.3.2), the geometry $\mathbf{X}$, the unknown displacements u, and the virtual displacements δu are approximated by Equations (2.29) and (2.30), obtaining

$$
\int_{\Omega_X} [\boldsymbol{\nabla}_\mathbf{X} \cdot (\mathbf{F}_h \mathbf{S}_h)] \cdot \delta u_h \ \mathrm{d}\Omega_X - \int_{\Gamma_X} [(\mathbf{F}_h \mathbf{S}_h) \cdot \mathbf{N} - t] \cdot \delta u_h \ \mathrm{d}\Gamma = 0, \tag{7.37}
$$

where the deformation gradient $\mathbf{F}_h$ and the stress tensor $\mathbf{S}_h$ are approximated due to their dependence on the displacements u_h. As in Equation (2.46), we compute a set of collocation points $\tau_i^d = \dfrac{\sum_{l=1}^{p_d} \xi_{i+l}}{p_d}$, with $d = 1, 2$ and $i = 1, ..., m_d$. Thus, it is necessary to distinguish between collocation points located in the interior of the domain, on the Dirichlet boundary, and on Neumann boundary. To this end, we define different sets of indices

$$
\eta_{interior} := \{ i \in \{1, ..., m_d\} : \tau_i^d \in \Omega_X \}, \tag{7.38}
$$
$$
\eta_D := \{ i \in \{1, ..., m_d\} : \tau_i^d \in (\Gamma_X)_D \}, \tag{7.39}
$$
$$
\eta_N := \{ i \in \{1, ..., m_d\} : \tau_i^d \in (\Gamma_X)_N \}. \tag{7.40}
$$

Thus, approximating relations in (7.34), the collocated strong form of the equation in the interior Ω_X reads as

$$
[\boldsymbol{\nabla}_\mathbf{X} \cdot (\mathbf{F}_h \mathbf{S}_h)] (\tau_i^d) = \mathbf{0} \quad \forall i \in \eta_{interior}. \tag{7.41}
$$

It becomes apparent that an alternative interpretation of IgC is the strict enforcement of the respective balance law (7.34a) at fixed discrete points, i.e., at the collocation points. For the enforcement of the Neumann boundary conditions in Equation

(7.34c) (see Section 2.1.3.2), we distinguish between collocation points that are located at the edges or corners of $(\Gamma_X)_N$, yielding:

$$[(\mathbf{F}_h\mathbf{S}_h) \cdot \mathbf{N} - \mathbf{t}](\tau_i^d) = \mathbf{0} \quad \forall i \in \eta_N \text{ on edges}, \tag{7.42}$$

$$[(\mathbf{F}_h\mathbf{S}_h) \cdot (\mathbf{N}' + \mathbf{N}'') - (\mathbf{t}' + \mathbf{t}'')](\tau_i^d) = \mathbf{0} \quad \forall i \in \eta_N \text{ on corners}. \tag{7.43}$$

In Equation (7.43), $\mathbf{N}'$ and $\mathbf{N}''$ are the outward normals of the two Neumann boundaries meeting at the considered corner and $\mathbf{t}'$ and $\mathbf{t}''$ are the corresponding imposed tractions. To avoid any issue related to inaccurate imposition of the Neumann boundary conditions, we alternatively consider an EC technique, imposing Neumann boundary conditions on edges as

$$[\boldsymbol{\nabla}_\mathbf{X} \cdot (\mathbf{F}_h\mathbf{S}_h)](\tau_i^d) - \frac{C^*}{h}[(\mathbf{F}_h\mathbf{S}_h) \cdot \mathbf{N} - \mathbf{t}](\tau_i^d) = \mathbf{0} \quad \forall i \in \eta_N \text{ on edges}, \tag{7.44}$$

where we refer to Section 2.1.3.3 for the meaning of h and the chosen value of C^*. At the corners we still apply the same approach as denoted in Equation (7.43) [67]. Instead, on the Dirichlet boundary $(\Gamma_X)_D$ we can directly impose

$$\mathbf{u}_h(\tau_i^d) = \mathbf{g}(\tau_i^d) \quad \forall i \in \eta_D. \tag{7.45}$$

Thus, we obtain a system of nonlinear equations, which we want to solve for the unknown displacement control variables $\hat{\mathbf{u}}_\mathbf{i}$. To this end, we utilize the Newton-Raphson method, which is an common approach based on the linearization of the residual of the governing system of equations [77]. In the following, we proceed to describe the linearization of the collocated Equations (7.41)-(7.44) according to the approach described by Kruse *et al.* in [115]. For convenience, the subscript h and the evaluation at the collocation points τ_i^d are omitted in the equations.

Thus, we start with Equation (7.41), which can be written in residual form as

$$\mathbf{R} = \boldsymbol{\nabla}_\mathbf{X} \cdot (\mathbf{FS}) = \mathbf{0}. \tag{7.46}$$

Using the tensor relations $\boldsymbol{\nabla}_\mathbf{X} \cdot (\mathbf{FS}) = \mathbf{F}(\boldsymbol{\nabla}_\mathbf{X} \cdot \mathbf{S}) + \boldsymbol{\nabla}_\mathbf{X}\mathbf{F} : \mathbf{S}$ and $\boldsymbol{\nabla}_\mathbf{X} \cdot \mathbf{S} = \text{tr}(\mathbb{C} : \boldsymbol{\nabla}_\mathbf{X}\mathbf{E})$, Equation (7.46) can be transformed into

$$\mathbf{R} = \mathbf{F}\,\text{tr}(\mathbb{C} : \boldsymbol{\nabla}_\mathbf{X}\mathbf{E}) + \boldsymbol{\nabla}_\mathbf{X}\mathbf{F} : \mathbf{S} = \mathbf{0}, \tag{7.47}$$

$$R_i = F_{ik}\mathbb{C}_{kjlm}E_{lm,j} + F_{ik,j}S_{kj} \quad i,j,k,l,m = 1,2. \tag{7.48}$$

In Equations (7.47) and (7.48), the stress tensor $\mathbf{S}$ and the elasticity tensor $\mathbb{C}$ are kept general and depend on the chosen constitutive law. Linearization of Equation (7.47) leads to the definition of the consistent tangent stiffness matrix $\mathbf{K}(\mathbf{u}_k)$ needed for the Newton-Raphson method (see Section 2.1.4). Here, with the symbol Δ we indicate the results of the tensor Gateaux derivative and therefore

$$\Delta\mathbf{R} = \Delta\mathbf{F}\,\text{tr}(\mathbb{C} : \boldsymbol{\nabla}_\mathbf{X}\mathbf{E}) + \mathbf{F}\,\text{tr}[(\mathbb{D} : \Delta\mathbf{E}) : \boldsymbol{\nabla}_\mathbf{X}\mathbf{E} + \mathbb{C} : \boldsymbol{\nabla}_\mathbf{X}\Delta\mathbf{E}] \tag{7.49}$$
$$+ \boldsymbol{\nabla}_\mathbf{X}\Delta\mathbf{F} : \mathbf{S} + \boldsymbol{\nabla}_\mathbf{X}\mathbf{F} : (\mathbb{C} : \Delta\mathbf{E}),$$

with

$$\mathbb{D} = \partial\mathbb{C}/\partial\mathbf{E}. \tag{7.50}$$

As we are using a Saint Venant-Kirchhoff material (see Section 7.1.2), the elasticity tensor $\mathbb{C}$ is constant and thus $\mathbb{D} = \mathbf{0}$. Therefore, equation (7.49) reduces to

$$\Delta \mathbf{R} = \Delta \mathbf{F} \, \text{tr}(\mathbb{C} : \boldsymbol{\nabla}_{\mathbf{X}} \mathbf{E}) + \mathbf{F} \, \text{tr}(\mathbb{C} : \boldsymbol{\nabla}_{\mathbf{X}} \Delta \mathbf{E}) + \boldsymbol{\nabla}_{\mathbf{X}} \Delta \mathbf{F} : \mathbf{S} + \boldsymbol{\nabla}_{\mathbf{X}} \mathbf{F} : (\mathbb{C} : \Delta \mathbf{E}) \,,$$
$$\Delta \mathrm{R}_i = \Delta \mathrm{F}_{ik} \mathbb{C}_{kjlm} \mathrm{E}_{lm,j} + \mathrm{F}_{ik} \mathbb{C}_{kjlm} \Delta \mathrm{E}_{lm,j} + \Delta \mathrm{F}_{ik,j} \mathrm{S}_{kj} + \mathrm{F}_{ik,j} \mathbb{C}_{kjlm} \Delta \mathrm{E}_{lm} \,. \tag{7.51}$$

Linearization has to be applied also for the resulting equations on the Neumann boundary, as they are also nonlinear. Considering the basic version of IgC and a collocation point located on an edge, Equation (7.42) can be written in residual form as

$$\mathbf{R_N} = (\mathbf{FS}) \cdot \mathbf{N} - \boldsymbol{t} \,, \tag{7.52}$$
$$\mathrm{R_{N}}_i = \mathrm{F}_{ij} \mathrm{S}_{jk} \mathrm{N}_k - t_i \,. \tag{7.53}$$

Linearization of the Equations (7.52) and (7.53) leads to

$$\Delta \mathbf{R_N} = (\Delta \mathbf{FS}) \cdot \mathbf{N} + (\mathbf{F} \Delta \mathbf{S}) \cdot \mathbf{N} - \Delta \boldsymbol{t} \,. \tag{7.54}$$

Assuming a deformation-independent applied pressure (i.e., $\Delta \boldsymbol{t} = \mathbf{0}$) and considering that $\Delta \mathbf{S} = \mathbb{C} : \Delta \mathbf{E}$, Equation (7.54) reduces to

$$\Delta \mathbf{R_N} = (\Delta \mathbf{FS}) \cdot \mathbf{N} + \left[\mathbf{F}(\mathbb{C} : \Delta \mathbf{E}) \right] \cdot \mathbf{N} \,, \tag{7.55}$$
$$\Delta \mathrm{R_{N}}_i = \Delta \mathrm{F}_{ij} \mathrm{S}_{jk} \mathrm{N}_k + \mathrm{F}_{ij} \mathbb{C}_{jklm} \Delta \mathrm{E}_{lm} \mathrm{N}_k \,. \tag{7.56}$$

In an analogous way, the residual form and its linearization can be derived for Neumann collocation points located in corners as well as for EC. Notice that, within the partitioned solution proposed herein, the structural solver obtains the total stress tensor $\mathbf{T}$ from the flow solver, which has to be incorporated into the structural boundary conditions by means of Equation (7.22). Combining the residuals (7.46) and (7.52) and stiffness matrices (7.51) and (7.55) for the interior and Neumann boundary together with Equation (7.45) for the Dirichlet boundary, a solvable linear system for the increment $\Delta \mathbf{u}$ is obtained (see Section 2.1.4 for more details on the solving algorithm). The definition of all tensors occurring in the above equations is provided in Appendix 7.B (see [87, 115] for further references).

7.2.2.2   Extension to nonlinear Elastodynamics

In the transient case, we consider the balance equations of geometrically nonlinear and materially linear elastodynamics stated in Equation (7.8) (neglecting body forces) with corresponding boundary and initial conditions (see Section 7.1.2). Applying the EC method, as indicated in Section 7.2.2.1, the resulting semi-discrete problem reads [67]: find $\boldsymbol{u}_h$ such that

$$
\begin{cases}
\rho \dfrac{d^2 \boldsymbol{u}_h(\tau_i^d, t)}{dt^2} = [\boldsymbol{\nabla}_{\mathbf{x}} \cdot (\mathbf{F}_h \mathbf{S}_h)](\tau_i^d, t) & \forall i \in \eta_{interior}, \forall t \in [0, T], & (7.57a) \\[3mm]
\boldsymbol{u}^h(\tau_i^d, t) = \boldsymbol{g}(\tau_i^d, t) & \forall i \in \eta_D, \forall t \in [0, T], & (7.57b) \\[3mm]
\rho \dfrac{d^2 \boldsymbol{u}_h(\tau_i^d, t)}{dt^2} = [\boldsymbol{\nabla}_{\mathbf{x}} \cdot (\mathbf{F}_h \mathbf{S}_h)](\tau_i^d, t) & & \\[3mm]
\qquad - \dfrac{C^*}{h}[(\mathbf{F}_h \mathbf{S}_h) \cdot \mathbf{N}) - \boldsymbol{t}](\tau_i^d, t) & \forall i \in \eta_N, \forall t \in [0, T], & (7.57c) \\[3mm]
\boldsymbol{u}_h(\tau_i^d, 0) = \boldsymbol{u}_0(\tau_i^d) & \forall i \in \{1, ..., m_d\}, & (7.57d) \\[3mm]
\dfrac{d\boldsymbol{u}_h(\tau_i^d, 0)}{dt} = \boldsymbol{v}_0(\tau_i^d) & \forall i \in \{1, ..., m_d\}. & (7.57e)
\end{cases}
$$

It is now possible to rewrite the isogeometric semi-discrete problem (7.57) in the form

$$
\mathbf{M} \frac{d^2 \boldsymbol{u}_h(t)}{dt^2} + \mathbf{f}^{int}(\boldsymbol{u}_h(t)) = \mathbf{f}^{ext}(t), \tag{7.58}
$$

with initial conditions (7.57d) and (7.57e). In Equation (7.58), $\mathbf{M}$ is the mass matrix, $\mathbf{f}^{int}(\boldsymbol{u}_h(t))$ is the vector of nonlinear internal forces, and $\mathbf{f}^{ext}(t)$ represents the vector containing external forces. To solve the resulting nonlinear system of ordinary differential equations, we have to apply a time integration algorithm to (7.58). In this work, the so-called *generalized-α method* is implemented, which is commonly used in computational mechanics [97].

For convenience, the acceleration $\dfrac{d^2 \boldsymbol{u}_h(t)}{dt^2}$ and the velocity $\dfrac{d\boldsymbol{u}_h(t)}{dt}$ are abbreviated by $\boldsymbol{a}$ and $\boldsymbol{v}$ and the subscript h is omitted. Let n denote the current time step. Then, applying the generalized-α method to Equation (7.58) leads to the residual form of the nonlinear elastodynamics problem defined by

$$
\mathbf{R}(\boldsymbol{u}_{n+1}^k) = \frac{(1 - \alpha_m)}{\beta \Delta t^2} \mathbf{M} \boldsymbol{u}_{n+1}^k + \mathbf{f}_{n+1-\alpha_f}^{int} - \mathbf{f}_{n+1-\alpha_f}^{ext} - \mathbf{M} \boldsymbol{\phi}_n, \tag{7.59}
$$

with

$$
\boldsymbol{\phi}_n = \big(\frac{1 - \alpha_m}{\beta \Delta t^2} (\boldsymbol{u}_n + \Delta t \boldsymbol{v}_n) + \frac{1 - \alpha_m - 2\beta}{2\beta} \boldsymbol{a}_n \big). \tag{7.60}
$$

The parameters α_f, α_m, β, and γ have an influence on the overall stability of the algorithm. Appropriate values can be taken from the literature [97]. Regarding the nonlinear internal and external forces, we assume that they are approximated following the same approach as in [66], i.e.,

$$
\mathbf{f}_{n+1-\alpha_f}^{int} = \mathbf{f}^{int}(\boldsymbol{u}_{n+1-\alpha_f}) = (1 - \alpha_f) \mathbf{f}^{int}(\boldsymbol{u}_{n+1}) + \alpha_f \mathbf{f}^{int}(\boldsymbol{u}_n), \tag{7.61}
$$

$$
\mathbf{f}_{n+1-\alpha_f}^{ext} = \mathbf{f}^{ext}(t_{n+1-\alpha_f}) = (1 - \alpha_f) \mathbf{f}^{ext}(t_{n+1}) + \alpha_f \mathbf{f}^{ext}(t_n). \tag{7.62}
$$

The consistent tangent stiffness matrix is then defined by

$$
\Delta \mathbf{R}(\boldsymbol{u}_{n+1}^k) = \frac{(1 - \alpha_m)}{\beta \Delta t^2} \mathbf{M} + (1 - \alpha_f) \frac{\partial \mathbf{f}^{int}(\boldsymbol{u}_{n+1}^k)}{\partial \boldsymbol{u}_{n+1}^k}. \tag{7.63}
$$

The expressions of $\mathbf{f}^{int}_{n+1-\alpha_f}$, $\dfrac{\partial \mathbf{f}^{int}(\boldsymbol{u}^k_{n+1})}{\partial \boldsymbol{u}^k_{n+1}}$, and $\mathbf{f}^{ext}_{n+1-\alpha_f}$ can be inferred from the semidiscrete elastodynamics problem (see Equations (7.57) and (7.58)). Finally, the resulting linear system can be solved by means of standard iterative methods to obtain the update of the displacement field $\Delta \boldsymbol{u}$ and, hence, the displacement field in the next time step.

7.2.3 Coupling

If the NURBS representing the geometry in IgC for the solid problem is taken into account by the curved-boundary mapping (7.33) on the fluid side, a matching interface representation is obtained, even though the discretization is still non-matching (see Figure 7.1). The coupling conditions to be satisfied along the common spline representing Γ^{fsi}_x are given by Equations (7.19)-(7.21), where due to the shared spline representation of the fluid-solid interface $\boldsymbol{n}^f = \boldsymbol{n}^s$. To solve the full FSI problem, we propose a partitioned approach that relies on a Dirichlet-Neumann coupling. Due to the fact that the same spline geometry is used to define the fluid-solid interface, the fluid grid can be deformed according to the discretized solution at each control point $\hat{\mathbf{u}}^s_i$ of the solid solver, i.e.,

$$\boldsymbol{u}^f_j = \sum_{i=1}^{n_{fsi}} R_i(\xi_j)\hat{\mathbf{u}}^s_i \qquad \text{on} \qquad \Gamma^{fsi}_x, \tag{7.64}$$

where n_{fsi} are the control points belonging to the fluid-solid interface Γ^{fsi}_x, $R_i(\xi_j)$ denotes the NURBS shape functions evaluated at a certain parametric coordinate $\xi_j \in \Gamma^{fsi}_x$, and $\boldsymbol{u}^f_j$ is the resulting interpolated deformation of the fluid. Therefore, the Dirichlet step simplifies to applying the interface velocity – determined by the varying deformation of the solid domain in time – on the FSI interface as Dirichlet boundary conditions for the fluid problem.

For the Neumann step, the non-matching discretizations need to be incorporated. The related boundary condition can be derived with the weak form of the dynamic coupling condition in Equation (7.21), i.e.,

$$\int_{\Gamma^{fsi}_x} \delta\boldsymbol{u} \cdot [(\boldsymbol{\sigma} - \mathbf{T}) \cdot \boldsymbol{n}]\, d\Gamma = 0. \tag{7.65}$$

Using the sifting property (2.49), a collocation form of the dynamic coupling condition can be stated as

$$\int_{\Gamma^{fsi}} \delta(\mathbf{x} - \tau^d_i)[(\boldsymbol{\sigma}(\mathbf{x}) - \mathbf{T}(\mathbf{x})) \cdot \boldsymbol{n}(\mathbf{x})]\, d\Gamma = \boldsymbol{\sigma}(\tau^d_i) - \mathbf{T}(\tau^d_i) = 0, \tag{7.66}$$

which only has to be fulfilled at the collocation points τ^d_i on Γ^{fsi}_x, i.e.,

$$\boldsymbol{\sigma}(\tau^d_i) = \mathbf{T}(\tau^d_i) \qquad \text{on} \quad \Gamma^{fsi}_x. \tag{7.67}$$

Evaluating the stresses at the collocation points along the spline boundary of the
finite element grid on the fluid side, we obtain

$$\mathbf{T}_i = \mathbf{T}(\tau_i^d) = \sum_{j=1}^{n_f} R_j(\tau_i^d)\mathbf{T}_j \qquad \text{on } \Gamma_x^{fsi}, \tag{7.68}$$

where n_f is the number of fluid nodes on the interface and τ_i^d is a certain colloca-
tion point on Γ_x^{fsi}. Taking into account the relationship between the Eulerian and
Lagrangian viewpoints in Equation (7.22), the Neumann step can be introduced in
terms of the fluid-induced tractions on the solid given by

$$\boldsymbol{t}^s = (\mathbf{FS})\cdot\mathbf{N} = \det(\mathbf{F})(\mathbf{TF}^{-\text{T}})\cdot\mathbf{N} \qquad \text{on } \Gamma^{fsi}. \tag{7.69}$$

Then, within IgC, the Neumann step is introduced in the solid problem either by
(7.42)–(7.43) or (7.44).

Based on the Dirichlet and Neumann steps that we have just introduced in this
section, the iterative procedure applied in the present work to solve the FSI problem
in a partitioned manner for t^{n+1} can be summarized for $k = 1,\dots$ until convergence
as

1. *Prediction step:* Prescribe $(\boldsymbol{u}_1^s)^{n+1}$ based on the total stress tensor $\mathbf{T}_n$ at the pre-
   vious time step t^n.

2. *Dirichlet step:* Deform the fluid grid according to $(\boldsymbol{u}_k^s)^{n+1}$, solve the fluid prob-
   lem for $(\boldsymbol{v}_k)^{n+1}, (p_k)^{n+1}$ and compute the total stress $(\mathbf{T}_k)^{n+1}$.

3. *Neumann step*: Solve the solid problem for $(\boldsymbol{u}_{k+1}^s)^{n+1}$ by imposing the tractions
   coming from the fluid problem *via* Equation (7.69).

4. *Check convergence*: if $\left|\left|(\boldsymbol{u}_{k+1}^s)^{n+1} - (\boldsymbol{u}_k^s)^{n+1}\right|\right| < \epsilon$ proceed to the next time step,
   otherwise continue iterating with $k = k + 1$ and go to step 2.

7.3   Numerical results

In this section we present a series of numerical results, which allow to have a prelim-
inary validation of the proposed computational approach described in Section 7.2,
combining a boundary-conforming finite element method (i.e., NEFEM) on the fluid
side with the IgC nonlinear elastodynamics solver [116] on the structural side and
leveraging a common spline representation of the fluid-structure interface. We con-
sider the Turek-Hron benchmark [182]. This FSI test problem describes the laminar
flow of an incompressible Newtonian fluid around a fixed cylinder with an elastic
beam attached to its right side (see Figure 7.4) and allows to investigate both the
steady and unsteady regime according to the inlet velocity. The setting of the prob-
lem along with the interaction of the flow and the elastic beam causes self-induced
oscillations of the latter, which undergoes a quasi-steady periodic wave-like defor-
mation. If we consider an unsteady regime, over time, this flow-structure interaction
effect induces large amplitude oscillations in the elastic beam.
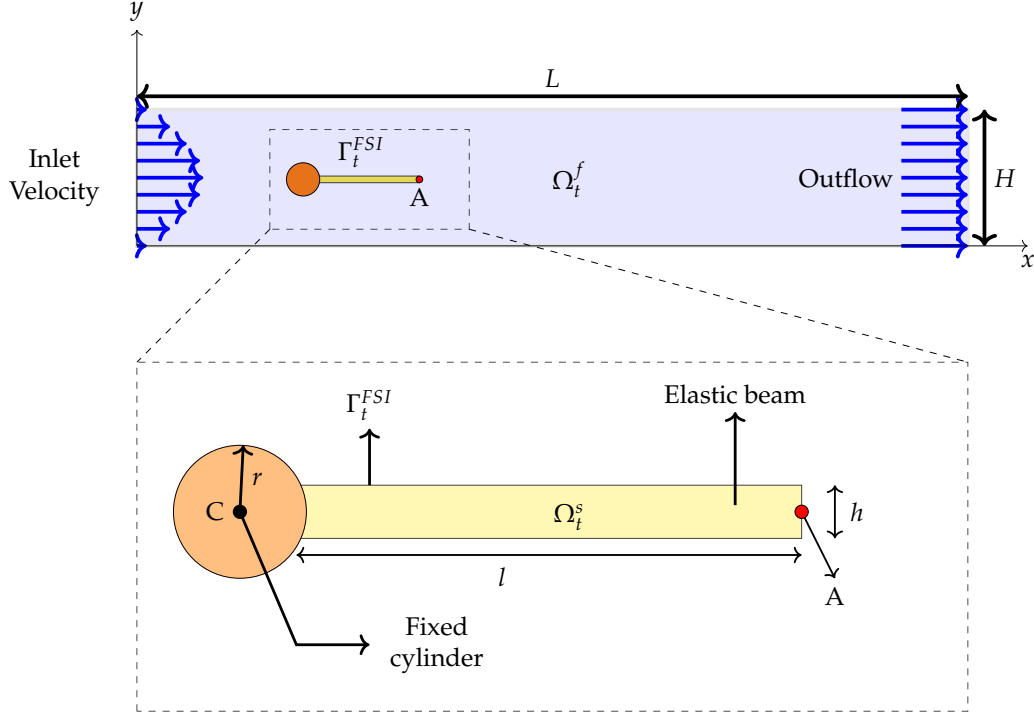
FIGURE 7.4: Sketch of the Turek-Hron moving flag benchmark [116].

In order to assess our spatiotemporal coupling, we first validate only the structural solver by means of a simple stand-alone test, for which a constant load is applied on the bottom edge of the deformable beam. We present a refinement study in Figure 7.5, investigating both a linear and a nonlinear case. In these plots, we show the relative error computed at the lower right corner of the beam using an increasing number of control points: 17x5, 33x9, 65x17, and 129x33 (i.e., $|u - u^{ref}|/|u^{ref}|$, where u^{ref} is the IgG solution obtained for the finest mesh). As expected, we note that IgG converges faster with respect to IgC for a fixed number of DOFs. In fact, if we consider each subplot of Figure 7.5, IgC needs 3 further levels of mesh refinement to reach the same level of accuracy of the IgG solution with 17x5 control points.

Then, we analyze the steady regime in the Turek-Hron benchmark [182] considering the values for the geometric and physical parameters specified in Tables 7.A.1 and 7.A.2. A parabolic velocity profile is set at the inlet and no-slip conditions are applied to the upper and lower walls, as well as to the cylinder and the flag, while a free-flow boundary condition is applied to the outlet (see [117] for additional details). In order to further validate our partitioned approach for FSI problems, we compare the results obtained with NEFEM on the fluid side coupled with the IgC method described in Section 7.2.2 on the structural side (NEFEM-IgC) with the results computed leveraging an IgG method on the structural side (NEFEM-IgG) (see [88]), which showed very good agreement with the reference value in the literature [182]. Thus, we run a full FSI steady simulation for the nonlinear beam and in Figure 7.6, we display a new proof of convergence to validate the steady FSI solver and the NEFEM-IgC coupling. In the literature, a typical reference value quantity for the comparison of numerical approaches is the amplitude of the vertical displacement of point A, located at the tail of the flag (see Figure 7.4). Figure 7.6 compares the relative error of the vertical displacement computed at point A of the beam for the NEFEM-IgC and the NEFEM-IgG methods. The relative error is evaluated using the

(a) linear elasticity

(b) linear elasticity

(c) nonlinear elasticity

(d) nonlinear elasticity
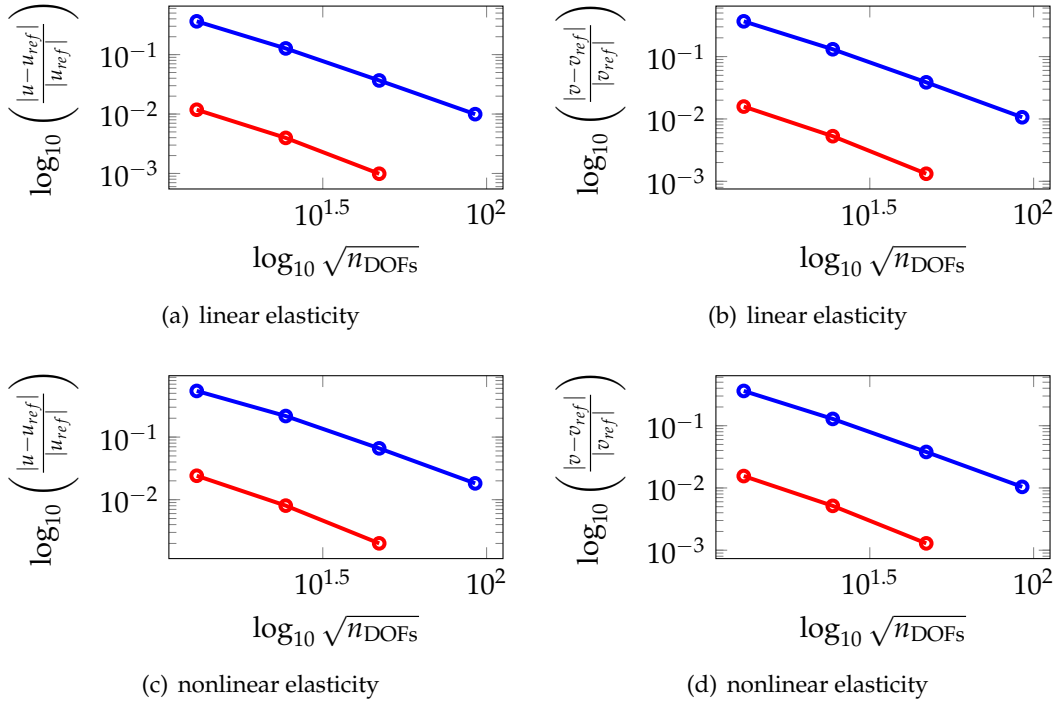
FIGURE 7.5: Convergence study for linear and nonlinear implementation during the structural stand-alone test. Relative error of the horizontal (u) and vertical (v) displacements computed at the lower right corner of the beam for 17x5, 33x9, 65x17, and 129x33 control points *versus* the square root of the total number of DOFs for each considered mesh: IgC ⊸⊶, IgG ⊸⊶.
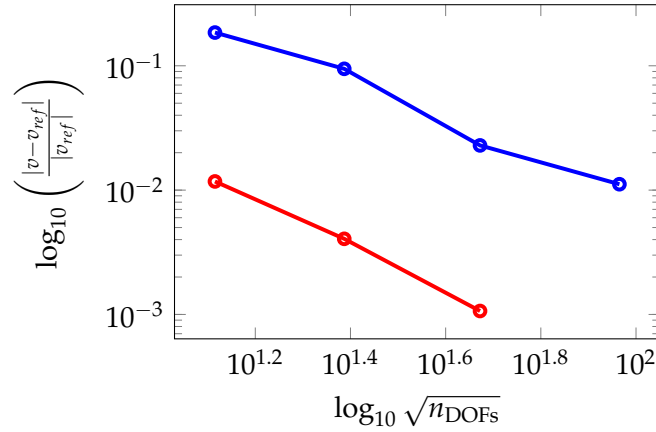
FIGURE 7.6: Convergence study for the steady FSI Turek benchmark. Relative error of the vertical displacement computed at point A of the beam (v; see Figure 7.4) for 17x5, 33x9, 65x17, and 129x33 control points *versus* the square root of the total number of DOFs for each considered mesh: IgC ⊸⊶, IgG ⊸⊶.

same definition and meshes (i.e., 17x5, 33x9, 65x17, and 129x33 control points) as in Figure 7.5, for which the reference value v^{ref} once again is the IgG solution obtained for the finest mesh of 129x33 control points. We highlight that also in the case of an FSI steady test IgG converges faster with respect to IgC for a fixed number of DOFs and to reach the same level of accuracy of the IgG solution with 17x5 control points, IgC needs 129x33 collocation points.
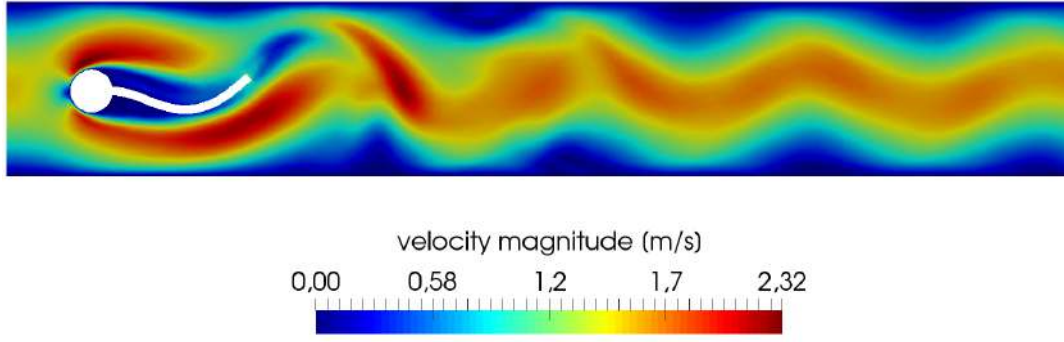
FIGURE 7.7: Turek-Hron benchmark: snapshot of the velocity of the flow field and flag movement taken at $t = 7.4$ s.

Finally, we run an unsteady analysis of the Turek-Hron benchmark considering the physical parameters described in Table 7.A.3. We discretize the geometry of the elastic beam with 25x25 control points using C^1 quadratic B-splines, while for the fluid grid we consider 14288 linear triangular finite elements. In particular, the NEFEM interface modeling the boundary of the beam features 147 elements: 71 at the top and bottom of the beam and 5 at the right edge, while the time step size is $\Delta t = 0.002$ s. Figure 7.7 shows a snapshot of the simulated flow field and beam deformation at $t = 7.4$ s using our partitioned algorithm. It is clearly visible that the beam has deformed due to external forces exerted by the fluid flow. After an initial response phase, the beam oscillates with a constant frequency and amplitude. Our simulations qualitatively agreed with the previous results for this benchmark [88], thereby showing a preliminary good performance of the partioned approach to solve FSI problems presented in Section 7.2.

Additionally, Figure 7.8 shows the displacement in y-direction of point A (see Figure 7.4) over time for the two computational approaches (i.e., NEFEM-IgC and NEFEM-IgG). For the simulation using NEFEM-IgC and NEFEM-IgG, we consider the same discretization as before as well as the same time step. In Figure 7.8, both plots qualitatively agree, but they exhibit relevant quantitative differences. In fact, in the case of the NEFEM-IgC approach, the beam oscillates with a larger amplitude than for the simulation with the NEFEM-IgG method. Moreover, there is a non-negligible temporal offset between the oscillations obtained with each method.
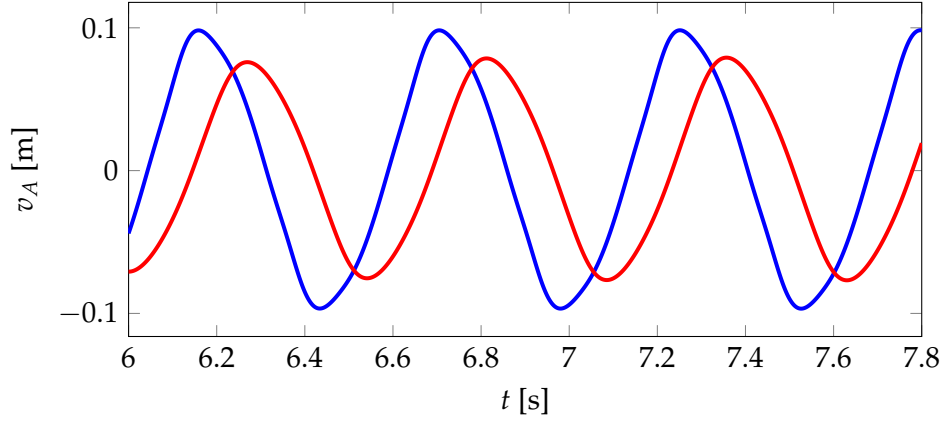
FIGURE 7.8: Response of the vertical displacement for point A (v_A; see Figure 7.4) for a sampled time interval $t \in [6\,\text{s}, 7.8\,\text{s}]$: comparison between the coupled structural solver based on IgG ——— and IgC ———.

7.4 Conclusions

This chapter presents a novel coupling scheme for FSI problems, which is based on the use of boundary-conforming finite elements (NEFEM) on the fluid side, IgC on the structural side, and a common spline representation of the fluid-solid interface. The coupling of the structural and the fluid solution, greatly facilitated by the common spline interface, is granted by means of a partitioned approach. In particular the necessary information is exchanged between the structure and the fluid using a Neumann/Dirichlet load transfer approach. Our simulations consider the Turek-Hron benchmark and preliminary convergence tests prove that the coupling is working in the case of steady FSI simulations. Nevertheless, further investigations need to be carried out in terms of transient FSI configurations, although very promising preliminary results for unsteady flow confirm that the spatiotemporal coupling is achieved. In any case, the results in terms of convergence are promising and we expect to improve them, for example, by refining the discretization of the beam in y-direction, as new tests highlighted that the discretization of the beam in y-direction had a significant influence on the stability and quality of the computations. In fact, if the number of collocation points was scarce, the solution diverged. Additionally, we could investigate whether increasing the degrees of approximation on the solid side might be beneficial to improve the performance of IgC. Furthermore, the required computational time for a complete simulation should be reduced, since, especially for the unsteady nonlinear case, computations take several days depending on the discretization. Therefore, parallelization should be explored for the nonlinear solver.

Appendix 7.A: Geometric and physical parameters of Turek-Hron FSI benchmark

TABLE 7.A.1: Definition of the geometric parameters for the Turek-Hron FSI benchmark [117].

Geometry parameters	Abbreviations	Value [m]
Channel length	L	2.5
Channel width	H	0.41
Structure length	l	0.35
Structure thickness	h	0.02
Cylinder radius	r	0.05
Cylinder center position	C	(0.2,0.2)
Reference point (at $t = 0$)	A	(0.6,0.2)

TABLE 7.A.2: Definition of the physical parameters for the Turek-Hron FSI benchmark for the steady regime [117].

Physical parameters (fluid)	Abbreviations	Value	Unit
Density	ρ^f	10^3	kg/m^3
Viscosity	ν^f	10^{-3}	m^2/s
Mean inflow velocity	$\bar{U}$	0.2	m/s
Reynolds number	Re	20	-
Physical parameters (solid)	**Abbreviations**	**Value**	
Density	ρ^s	10^3	kg/m^3
Poisson Ratio	ν^s	0.4	-
Young's modulus	E	$1.4 \cdot 10^6$	kg/ms^2

TABLE 7.A.3: Definition of the physical parameters for the Turek-Hron FSI benchmark for the unsteady regime [117].

Physical parameters (fluid)	Abbreviations	Value	Unit
Density	ρ^f	10^3	kg/m^3
Viscosity	ν^f	10^{-3}	m^2/s
Mean inflow velocity	$\bar{U}$	1	m/s
Reynolds number	Re	100	-
Physical parameters (solid)	**Abbreviations**	**Value**	
Density	ρ^s	10^4	kg/m^3
Poisson Ratio	ν^s	0.4	-
Young's modulus	E	$1.4 \cdot 10^6$	kg/ms^2

Appendix 7.B: Tensor definitions

TABLE 7.B.1: Tensor and index notation for tensors occurring in the linearized nonlinear elastostatic equations (see Section 7.2.2.1).

Tensors	Tensor notation	Index notation
Deformation gradient	$\mathbf{F} = \mathbf{I} + \nabla_{\mathbf{X}} u$	$F_{ij} = \delta_{ij} + u_{i,j}$
Gradient of deformation gradient	$\nabla_{\mathbf{X}} \mathbf{F}$	$F_{ij,k} = u_{i,jk}$
Right Cauchy-Green tensor	$\mathbf{C} = \mathbf{F}^{\mathrm{T}} \mathbf{F}$	$C_{ij} = \delta_{ki} \delta_{kj} + u_{i,j} + u_{j,i} + u_{k,i} u_{k,j}$
Green-Lagrange strain	$\mathbf{E} = \dfrac{1}{2}(\mathbf{F}^{\mathrm{T}} \mathbf{F} - \mathbf{I})$	$E_{ij} = \dfrac{1}{2}(u_{i,j} + u_{j,i} + u_{k,i} u_{k,j})$
Gradient of Green-Lagrange strain	$\nabla_{\mathbf{X}} \mathbf{E}$	$E_{ij,k} = \dfrac{1}{2}(u_{i,jk} + u_{j,ik} + u_{n,ik} u_{n,j} + u_{n,i} u_{n,jk})$
Second Piola-Kirchhoff stress tensor	$\mathbf{S} = \lambda \mathrm{tr}(\mathbf{E}) \mathbf{I} + 2\mu \mathbf{E}$	$S_{ij} = \lambda E_{kk} \delta_{ij} + 2\mu E_{ij}$
fourth-order elasticity tensor	$\mathbb{C} = \partial \mathbf{S} / \partial \mathbf{E}$	$\mathbb{C}_{ijkl} = \lambda \delta_{ij} \delta_{kl} + \mu(\delta_{ik} \delta_{jl} + \delta_{il} \delta_{jk})$

Linearized Tensors	Tensor notation	Index notation
Deformation gradient	$\Delta \mathbf{F} = \nabla_{\mathbf{X}} \Delta u$	$\Delta F_{ij} = \Delta u_{i,j}$
Gradient of Deformation gradient	$\nabla_{\mathbf{X}} \Delta \mathbf{F}$	$\Delta F_{ij,k} = \Delta u_{i,jk}$
Green-Lagrange strain	$\Delta \mathbf{E} = \mathrm{sym}(\mathbf{F}^{\mathrm{T}} \nabla_{\mathbf{X}} \Delta u)$	$\Delta E_{ij} = \dfrac{1}{2}(\Delta u_{i,j} + \Delta u_{j,i} + u_{k,j} \Delta u_{k,i} + u_{k,i} \Delta u_{k,j})$
Gradient of Green-Lagrange strain	$\nabla_{\mathbf{X}} \Delta \mathbf{E}$	$\Delta E_{ij,k} = \dfrac{1}{2}(\Delta u_{i,jk} + \Delta u_{j,ik} + u_{n,jk} \Delta u_{n,i} + u_{n,j} \Delta u_{n,ik} + u_{n,ik} \Delta u_{n,j} + u_{n,i} \Delta u_{n,jk})$

Chapter 8

Conclusions and Future perspectives

In this work, we have developed advanced computational methods in the context of IgA with the aim of providing a reliable support for the design and optimization of engineering products. These computational technologies have the potential to allow for a better understanding of the complex underlying physical phenomena in engineering applications and ultimately reduce the necessity of experimental tests, which are often expensive and time-consuming. In particular, our main focus has been on IgC methods and we have explored formulations allowing for cost-efficient simulations that render highly accurate results in comparison to renown validation benchmarks or fine IgG solutions.

Accordingly, in **Chapter 3** we propose a novel approach to simulate solid laminated plates characterized by a symmetric distribution of plies. This technique combines a 3D displacement-based method solved *via* IgC with an equilibrium-based procedure to appropriately reconstruct the interlaminar stresses. First, we discretize the plate using a single element through the thickness of the laminate and solve mechanical equilibrium with an IgC formulation. To account for the variation of the material properties through the thickness of the plate, we average the constitutive behavior of each layer considering a homogenized response. We examine a validation benchmark, which is well known in the composites literature and provides an analytical solution. Our simulations show that our IgC approach can render comparable results in terms of displacements and in-plane stresses. However, the resulting out-of-plane through-the-thickness stress contravenes mechanical equilibrium. To recover accurate interlaminar stresses, we propose to perform an *a posteriori* step consisting of a direct integration of the equilibrium equations along the laminate out-of-plane coordinate. This post-processing step requires the integration of higher-order derivatives of the previously computed displacement field. Therefore, the shape functions used in their approximation must be highly continuous, but this demand is fully granted by the usual functional spaces employed in IgA. Our results prove that this stress recovery approach is effective even for very coarse in-plane meshes and, regardless of the number of layers, gives better results the more slender the composites are. Additionally, the approximation improves for stacking sequences made of a significant number of plies, since a stack with a large number of thin layers is indeed closer to a plate with averaged properties. Furthermore, we

remark that simulations with a single high-order in-plane element (in-plane degrees of approximation $p = q = 6$ and out-of-plane degree of approximation $r = 4$) exhibit maximum percentage errors of 1% or lower in plates with 11 and 33 layers and length-to-thickness ratio $S \geq 30$. Nevertheless, a homogenized approach with a single-element through the thickness is directly effective only for symmetric layer distributions along the thickness of the plate, as for non-symmetric ply stacking sequences the middle plane of the plate is not balanced. In the case of non-symmetric layer distributions, the stacking sequence can typically be split into two symmetric piles, using one element per homogenized stack with a C^0 interface.

In **Chapter 4**, we extend our modeling strategy for laminated composites from 3D plates to bivariate Kirchhoff plates, considering both IgG and IgC formulations. To this end, we leverage CLPT to model laminated Kirchhoff plates beacuse this paradigm provides the lowest computational cost among known literature strategies for laminates. The CLPT features high-order PDEs. Additionally, in the case of laminated composite Kirchhoff plates, the in-plane continuity requirements to apply the equilibrium-based stress recovery are higher with respect to the solid plate case (i.e., C^3-continuity due to Kirchhoff's hypothesis *versus* C^2-continuity in the solid plates in Chapter 3). However, these challenges can be fully addressed thanks to the highly continuous functional spaces usually employed in IgA. This highlights once again the flexibility of IgA to easily pave the way to new modeling techniques with respect to standard FEA. Furthermore, according to CLPT, interlaminar stresses are identically zero when computed using the constitutive equations. Therefore, our stress recovery technique produces a unique, primal approximation of the out-of-plane stress within the CLPT framework. Our simulations show that the coupling of homogenized single-element IgC and IgG formulations with our equilibrium-based stress recovery technique produces highly accurate results when compared to the same analytical benchmark as in Chapter 3. In particular, CLPT enables to analyze laminated plates with both an even and an odd number of layers with a single element through the thickness (i.e., featuring both symmetric and non-symmetric ply distributions). Our simulations show that the proposed methodology successfully recovers the out-of-plane stress state in both cases. Moreover, we remark that the proposed IgG and IgC modeling techniques provide excellent results in simply supported rectangular plates even using a coarse mesh composed of a single sixth-order element. In fact, for the considered plate cases, a single in-plane element with 7x7 DOFs is able to provide maximum differences of 4% or lower on the boundary and of 2.5% or lower inside the plate domain for the IgG method coupled with the proposed stress recovery technique, while the IgC approach combined with the equilibrium-based stress recovery strategy allows to obtain maximum differences of 8% or lower on the border and of 3% or lower inside the plate. For more complex geometries, like simply-supported circular plates, our preliminary numerical tests show that the high continuity across elements granted by IgA shape functions is a pivotal asset to obtain highly accurate cost-efficient results.

The extension of our modeling strategy from solid plates to solid shells is also successfully investigated in **Chapter 5** for both IgG and IgC methods. For these 3D curved structures, we cannot longer refer to in-plane and out-of-plane stresses with respect a global reference system, as we previously did in Chapters 3 and 4. Thus, we adopt a pointwise local geometrical description of the solid shell, which allows to identify in-plane and out-of-plane stress components. Hence, this convenient description of the problem grants a direct and inexpensive stress recovery, which can

be performed only at locations of interest. Conversely, the use of curvilinear coordinates to express equilibrium would couple together the in-plane and out-of-plane components, which would require the numerical resolution of a system of equations to appropriately recover the interlaminar stresses. We consider again the homogenized single-element IgC and IgG formulation, but, for the latter, we further propose a layer-by-layer integration rule comprising $r - 1$ quadrature points per ply. This numerical scheme allows to correctly capture the behavior of laminated composites for any stacking sequence (e.g., with an even or and odd number of variously oriented layers) and to consider more general constitutive models (e.g., plasticity). Our simulations show that considering $r - 1$ quadrature points per layer leads to the same accuracy as using $r + 1$ integration points, which is a more common choice in standard IgG approaches. For the considered solid curved geometries, the stress recovery approach leads to errors that are typically in the 10% range or lower at convergence despite the chosen displacement-based approach. More specifically, the IgG method provides errors in the order of 2% in average for the analyzed cases, while IgC allows to obtain errors in the range of 5%-10% or lower for slender structures (i.e., $S \geq 30$). Additionally, in this Chapter we draft a new equilibrium-based post-processing approach that grants lower continuity requirements for the recovery of the out-of-plane stresses. This technique only uses first-order derivatives of the shear interlaminar stresses with respect to in-plane coordinates to obtain the out-of-plane normal stress component, whereas the general stress recovery technique requires second-order derivatives of the in-plane stresses. We present a preliminary study showcasing that, for the same number of DOFs, the alternative low-continuity formulation to reconstruct interlaminar stresses exhibits remarkable accuracy compared to the general stress recovery strategy proposed in this thesis, so we plan to further investigate this low-continuity approach in forthcoming studies.

We believe that the methodologies to model laminated composite plates presented in this thesis constitute a promising step towards the construction of cost-effective, highly accurate computational tools to calculate the mechanical behavior of complex engineering designs featuring these materials (e.g., aircrafts). Therefore, among the future research topics, we highlight the extension of our modeling approach to more complex structures, such as bivariate shells. Additionally, more efficient through-the-thickness integration strategies as well as the inclusion of large deformations and material nonlinearities will be considered in future studies. In particular, the extension of the out-of-plane stress recovery to include material nonlinearities could consider J^2-flow theory as a starting point. We have recently started exploring this strategy by leveraging an IgG method built for an elasto-plastic framework. In brief, we update the state variables in time by means of the Newton-Raphson method, requiring a consistent tangent derivation. At every Newton-Raphson iteration, the out-of-plane stress state needs to be post-processed for every Gauss point starting from the in-plane components to retrieve the constraint imposed by the equilibrium equations (i.e., as we did in Chapters 3-5). This adjustment represents an additional computational cost, which can be reasonably estimated to be small due to the stated accuracy-cost ratio of the stress recovery for the linear cases explored in this thesis. While this research is still ongoing, we plan to ultimately assess and compare the accuracy and computational efficiency of this procedure to those granted by other methods (see [62]). So far, we have identified two delicate issues, concerning the type of yield surface as well as the choice of projection algorithm (see [168]). We have investigated alternative methods for integrating general classes of inelastic constitutive equations and we have ultimately focused on

the so-called cutting-plane algorithm [143] for small-deformation rate-independent inelastic materials. Regarding the limit function to be adopted, we believe that two possible strategies could be considered: one based on the Ottosen type yield function [144] and the other on the Tsai-Wu yield surface [181].

In the future, we also plan to explore the extension of our modeling approaches for laminated composites to include delamination, which is a common mode of failure for these materials and is driven by an excessive interlaminar stress. To this end, in this thesis we take a first step and explore a novel IgA solution technique for the phase-field modeling of brittle fracture in elastic solids, considering a thermodynamically consistent phase-field model, which accounts for a different damaging behavior in tension and compression as in [10, 46], i.e., damage is allowed to act only on the positive volumetric and deviatoric part of the elastic energy. In **Chapter 6**, we consider a staggered scheme to alternatively minimize the displacement and damage fields and we propose to use the PSOR algorithm to solve the minimization of the total energy of the system with respect to the phase-field variable, thereby allowing for a direct and rigorous enforcement of the irreversibility constraint by cutting negative values of the phase-field increments at the control points and, hence, yielding either zero or positive increments of the phase-field variable. The explicit nature of the chosen solution technique allows to significantly reduce the elapsed time of the execution of the phase-field subroutine with respect to state-of-the art methods, such as the penalty approach in [79]. Furthermore, as our method directly enforces the irreversibility constraint, it does not require to iteratively resolve a system when an unloading stage is eventually considered (in contrast to the penalty method from [79]).

To study the PSOR algorithm we test a SEN specimen and an L-shaped panel both discretized *via* an IgG multipatch approach leveraging linear shape functions and using two tolerances (i.e., $\text{TOL}_{PSOR}^{(1)} = 10^{-4}$ and $\text{TOL}_{PSOR}^{(2)} = 10^{-6}$). We further compare the performance of our computational approach with respect to a renown penalty method [79]. While for the SEN specimen, a dramatic reduction of the tolerance leads to the same results in terms of time performance with respect to the penalty method, this is not the case for the L-shaped panel test, which proved to be more computationally demanding for the PSOR method when a tolerance equal to 10^{-6} is considered. Conversely, the performance of the penalty method in terms of required time is less sensitive to the chosen tolerance. We believe that this issue is related to the tuning of the penalty parameter γ, which strongly depends on the toughness-internal length ratio. In fact, the value of γ for the L-shaped panel test is much smaller with respect to its counterpart for the SEN specimen benchmark, thereby representing a more relaxed constraint in the former benchmark test.

Additionally, we discuss the choice of a suitable stopping criterion for the staggered scheme. In this study, the considered convergence criterion uses the discretized counterpart of the out-of-balance work, which seems to grant the desired control over the alternated minimization algorithm. Other possible criteria control the variation between two subsequent iterations of either the total energy functional or the phase-field variable. The latter option is equivalent to control the dissipated energy, since it provides a global measure of the damage inside the domain. Finally, we present preliminary results of the modeling of the SEN specimen benchmark *via* quadratic C^1 B-spline shape functions, which show that the resolution of the internal length seems to be more relevant than the regularity of the IgA approximation.

We hypothesize that the use of C^1 functions to approximate a physical discontinuity, such as the pre-existing crack in the SEN specimen, might not bring any further benefit. Thus, future immediate studies could address the modeling of the displacement and the phase fields using different approximations, e.g., respectively using C^0 quadratic and linear B-spline basis functions and such that the two fields share the same number of control points. Alternatively, the preliminary results shown in Chapter 6 also pave the way to explore high-order models of fracture [32]. In an attempt to develop a more sophisticated software to simulate delamination in composite structures, future research studies should address the inclusion of plasticity as well as delamination within our phase-field model of brittle fracture. For instance, we could consider the elasto-plasticity model in [6] to directly exploit the PSOR algorithm. The authors also use a staggered approach, with which they first minimize the system energy with respect to the displacements and plastic strains and, then, with respect to the damage field. More specifically, the minimization step with respect to the displacement is equivalent to solve a linear elasticity problem, while the minimization step with respect to the plastic strain is equivalent to a linear local projection, because of the perfect-plasticity framework. The minimization step with respect to the phase field is to be performed for a fixed value of displacement and plastic strain, thereby allowing for a direct application of the PSOR algorithm. With regard to the inclusion of delamination effects, we plan to investigate more sophisticated phase-field damage models for orthotropic materials. For example, the fracture energy in [58] is assumed to depend on a structure tensor and the model is capable of capturing cracks growing within and between the laminae, which is of key importance in modeling transitions between intra- and interlaminar failure.

Finally, we have also explored new IgA formulations in the context of FSI problems, which are usually present in advanced engineering applications and tend to be very demanding computationally. In **Chapter 7**, we propose a novel coupling scheme that combines a boundary-conforming finite-element formulation (i.e., NE-FEM) on the fluid side with IgC on the structural side using a spline description of the fluid-structure interface. More specifically, the necessary information is exchanged between the structure and the fluid using a Neumann/Dirichlet load transfer approach, namely forces resulting from the fluid boundary stresses are projected onto the structure as a Neumann boundary condition, while the structural deformations are transferred to the fluid as a Dirichlet boundary condition. This projection is greatly facilitated by the common spline description of the interface. In order to test this strategy, we leverage a partitioned algorithm to solve the FSI problem, relying on a space-time discretization strategy previously proposed in [89] and extending our structural solver to address nonlinear elastodynamic cases. The preliminary results presented in Chapter 7 show a promising potential for our computational strategy, also confirming the spatiotemporal coupling in terms of the solution of the problem. Additionally, further convergence tests prove that the proposed coupling between the fluid and structural formulations is working in the case of steady FSI tests. Future investigations should explore more sophisticated transient FSI problems that are closer to demanding engineering applications. To this end, we think it is essential to reduce the computational time for a complete simulation, as the unsteady nonlinear case considered in Chapter 7 can take several days to complete. Therefore, we could investigate whether increasing the degrees of approximation on the solid side might be beneficial to improve the performance of IgC. Additionally, parallelization should be explored for the nonlinear solver, which would also enable an insightful assessment of the computational cost and accuracy of the IgC method

for the structural part of the FSI problem. In the future, we believe that our hybrid method to address FSI problems could be seamlessly integrated with our post-processing stress recovery technique for 3D curved laminated composite structures, thereby facilitating an accurate and cost-efficient design of complex geometries to serve fluid dynamics requirements in engineering applications.

Bibliography

[1] https://www.airbus.com/.

[2] http://kevinrhart.com/research/.

[3] C. Adams, M. Fagerström, and J.J.C. Remmers. "Efficient modelling of delamination growth using adaptive isogeometric continuum shell elements". *Computational Mechanics* 65 (2020), 99–117.

[4] I. Akkerman, Y. Bazilevs, V.M. Calo, T.J.R. Hughes, and S. Hulshoff. "The role of continuity in residual-based variational multiscale modeling of turbulence". *Computational Mechanics* 41 (2008), 371–378.

[5] A. Alesadi, M. Galehdari, and S. Shojaee. "Free vibration and buckling analysis of composite laminated plates using layerwise models based on isogeometric approach and Carrera unified formulation". *Mechanics of Advanced Materials and Structures* 25 (2018), 1018–1032.

[6] R. Alessi, J.-J. Marigo, C. Maurini, and S. Vidoli. "Coupling damage and plasticity for a phase-field regularisation of brittle, cohesive and ductile fracture: One-dimensional examples". *International Journal of Mechanical Sciences* 149 (2018), 559 –576.

[7] S. Almi and M. Negri. "Analysis of Staggered Evolutions for Nonlinear Energies in Phase Field Fracture". *Archive for Rational Mechanics and Analysis* 236 (2020), 189–252.

[8] M. Ambati, T. Gerasimov, and L. De Lorenzis. "A review on phase-field models of brittle fracture and a new fast hybrid formulation". *Computational Mechanics* 55 (2015), 383–405.

[9] M. Ambati, J. Kiendl, and L. De Lorenzis. "Isogeometric Kirchhoff–Love shell formulation for elasto-plasticity". *Computer Methods in Applied Mechanics and Engineering* 340 (2018), 320–339.

[10] H. Amor, J.-J. Marigo, and C. Maurini. "Regularized formulation of the variational brittle fracture with unilateral contact: Numerical experiments". *Journal of the Mechanics and Physics of Solids* 57 (2009), 1209–1229.

[11] C. Anitescu, Y. Jia, Y.J. Zhang, and T. Rabczuk. "An isogeometric collocation method using superconvergent points". *Computer Methods in Applied Mechanics and Engineering* 284 (2015), 1073–1097.

[12] P. Antolín. "Fast assembly of Galerkin matrices for 3D solid laminated composites using finite element and isogeometric discretizations". *Computational Mechanics* 65 (2020), 135–148.

[13]   P. Antolín, J. Kiendl, M. Pingaro, and A. Reali. "A simple and effective method based on strain projections to alleviate locking in isogeometric solid shells". *Computational Mechanics* 65 (2020), 1621–1631.

[14]   F. Auricchio, F. Calabrò, T.J.R. Hughes, A. Reali, and G. Sangalli. "A simple algorithm for obtaining nearly optimal quadrature rules for NURBS-based isogeometric analysis". *Computer Methods in Applied Mechanics and Engineering* 249-252 (2012), 15–27.

[15]   F. Auricchio, L. Beirão da Veiga, T.J.R. Hughes, A. Reali, and G. Sangalli. "Isogeometric collocation for elastostatics and explicit dynamics". *Computer Methods in Applied Mechanics and Engineering* 249-252 (2012), 2–14.

[16]   F. Auricchio, L. Beirão da Veiga, T.J.R. Hughes, A. Reali, and G. Sangalli. "Isogeometric collocation methods". *Mathematical Models & Methods in Applied Sciences* 20 (2010), 2075–2107.

[17]   F. Auricchio, L. Beirão da Veiga, J. Kiendl, C. Lovadina, and A. Reali. "Locking-free isogeometric collocation methods for spatial Timoshenko rods". *Computer Methods in Applied Mechanics and Engineering* 263 (2013), 113 –126.

[18]   F. Auricchio, L. Beirão da Veiga, C. Lovadina, and A. Reali. "The importance of the exact satisfaction of the incompressibility constraint in nonlinear elasticity: mixed FEMs versus NURBS-based approximations". *Computer Methods in Applied Mechanics and Engineering* 199 (2010), 314–323.

[19]   F. Auricchio *et al.* "A fully "locking-free" isogeometric approach for plane linear elasticity problems: A stream function formulation". *Computer Methods in Applied Mechanics and Engineering* 197 (2007), 160–172.

[20]   G. Balduzzi, S. Morganti, F. Auricchio, and A. Reali. "Non-prismatic Timoshenko-like beam model: Numerical solution via isogeometric collocation". *Computers & Mathematics with Applications* 74 (2017), 1531–1541.

[21]   Y. Bazilevs, V.M. Calo, T.J.R. Hughes, and Y. Zhang. "Isogeometric fluid-structure interaction: theory, algorithms, and computations". *Computational Mechanics* 43 (2008), 3–37.

[22]   Y. Bazilevs, M.-C. Hsu, J. Kiendl, R. Wüchner, and K.-U. Bletzinger. "3D simulation of wind turbine rotors at full scale. Part II: Fluid–structure interaction modeling with composite blades". *International Journal for Numerical Methods in Fluids* 65 (2011), 236–253.

[23]   Y. Bazilevs and T.J.R. Hughes. "NURBS-based isogeometric analysis for the computation of flows about rotating components". *Computational Mechanics* 43 (2008), 143–150.

[24]   Y. Bazilevs *et al.* "Variational multiscale residual-based turbulence modeling for large eddy simulation of incompressible flows". *Computer Methods in Applied Mechanics and Engineering* 197 (2007), 173–201.

[25]   A. Beckert. "Coupling fluid (CFD) and structural (FE) models using finite interpolation elements". *Aerospace Science and Technology* 4 (2000), 13–22.

[26]   M. Behr. "Simplex space-time meshes in finite element simulations". *International Journal for Numerical Methods in Fluids* 57 (2008), 1421–1434.

[27]   M. Behr and T.E. Tezduyar. "Finite element solution strategies for large-scale flow simulations". *Computer Methods in Applied Mechanics and Engineering* 112.1-4 (1994), 3–24.

[28] M.A. Behr, L.P. Franca, and T.E. Tezduyar. "Stabilized finite element methods for the velocity-pressure-stress formulation of incompressible flows". *Computer Methods in Applied Mechanics and Engineering* 104 (1993), 31–48.

[29] D.J. Benson, Y. Bazilevs, M.C. Hsu, and T.J.R. Hughes. "Isogeometric shell analysis: The Reissner–Mindlin shell". *Computer Methods in Applied Mechanics and Engineering* 199 (2010). Computational Geometry and Analysis, 276–289.

[30] C. de Boor. *A Practical Guide to Splines*. Springer, 1978.

[31] C. De Boor. "On calculation with B-splines". *Journal of Approximation Theory* 6 (1972), 50–62.

[32] M.J. Borden, T.J.R. Hughes, C.M. Landis, and C.V. Verhoosel. "A higher-order phase-field model for brittle fracture: Formulation and analysis within the isogeometric analysis framework". *Computer Methods in Applied Mechanics and Engineering* 273 (2014), 100 –118.

[33] M.J. Borden *et al.* "A phase-field description of dynamic brittle fracture". *Computer Methods in Applied Mechanics and Engineering* 217-220 (2012), 77–95.

[34] B. Bourdin, G. A. Francfort, and J.-J. Marigo. "Numerical experiments in revisited brittle fracture". *Journal of the Mechanics and Physics of Solids* 48 (2000), 797–826.

[35] A. Buffa, C. de Falco, and G. Sangalli. "IsoGeometric Analysis: Stable elements for the 2D Stokes equation". *International Journal for Numerical Methods in Fluids* 65 (2011), 1407–1422.

[36] R. Sevilla Cárdenas. "NURBS-enhanced finite element method (NEFEM)". PhD thesis. Universitat Politècnica de Catalunya, 2009.

[37] E. Carrera, S. Brischetto, and P. Nali. *Plates and Shells for Smart Structures: Classical and Advanced Theories for Modeling and Analysis*. John Wiley & Sons, 2011.

[38] E. Carrera, M. Cinefra, M. Petrolo, and E. Zappino. *Finite Element Analysis of Structures through Unified Formulation*. John Wiley & Sons, 2014.

[39] C.F. Casanova and A. Gallego. "NURBS-based analysis of higher-order composite shells". *Composite Structures* 104 (2013), 125–133.

[40] J.F. Caseiro *et al.* "On the Assumed Natural Strain method to alleviate locking in solid-shell NURBS-based finite elements". *Computational Mechanics* 53 (2014), 1341–1353.

[41] H. Casquero, C. Bona-Casas, and H. Gomez. "A NURBS-based immersed methodology for fluid–structure interaction". *Computer Methods in Applied Mechanics and Engineering* 284 (2015), 943–970.

[42] J.R. Cebral and R. Lohner. "Conservative load projection and tracking for fluid-structure problems". *AIAA Journal* 35 (1997), 687–692.

[43] A. Chambolle, S. Conti, and G.A. Francfort. "Approximation of a brittle fracture energy with a constraint of non-interpenetration". *Archive for Rational Mechanics and Analysis* 228 (2018), 867–889.

[44] A. Chiappa, C. Groth, A. Reali, and M.E. Biancolini. "A stress recovery procedure for laminated composite plates based on strong-form equilibrium enforced via the RBF Kansa method". *Composite Structures* 244 (2020), 112292.

[45]   C. Comi and U. Perego. "A generalized variable formulation for gradient dependent softening plasticity". *International Journal for Numerical Methods in Engineering* 39 (1996), 3731–3755.

[46]   C. Comi and U. Perego. "Fracture energy based bi-dissipative damage model for concrete". *International Journal of Solids and Structures* 38 (2001), 6427–6454.

[47]   *Committee on Durability and National Research Council Life Prediction of Polymer Matrix Composites in Extreme Environments, Going to Extremes: Meeting the Emerging Demand for Durable Polymer Matrix Composites.* Washington, D.C.: National Academies Press, 2005.

[48]   *Composites Market by Fiber Type (Glass Fiber Composites, Carbon Fiber Composites, Natural Fiber Composites), Resin Type (Thermoset Composites, Thermoplastic Composites), Manufacturing Process, End-use Industry and Region - Global Forecast to 2025.* `https : / / www . marketsandmarkets . com / Market - Reports / composite-market-200051282.html`.

[49]   L. Coradello *et al.* "Hierarchically refined isogeometric analysis of trimmed shells". *Computational Mechanics* 66 (2020), 431–447.

[50]   J.A. Cottrell, T.J.R. Hughes, and Y. Bazilevs. *Isogeometric analysis: toward integration of CAD and FEA.* John Wiley & Sons, 2009.

[51]   J.A. Cottrell, T.J.R. Hughes, and A. Reali. "Studies of refinement and continuity in isogeometric structural analysis". *Computer Methods in Applied Mechanics and Engineering* 196 (2007), 4160–4183.

[52]   J.A. Cottrell, A. Reali, Y. Bazilevs, and T.J.R. Hughes. "Isogeometric analysis of structural vibrations". *Computer Methods in Applied Mechanics and Engineering* 195 (2006), 5257–5296.

[53]   F. Daghia, S. de Miranda, F. Ubertini, and E. Viola. "A hybrid stress approach for laminated composite plates within the First-order Shear Deformation Theory". *International Journal of Solids and Structures* 45 (2008), 1766–1787.

[54]   M. von Danwitz, V. Karyofylli, N. Hosters, and M. Behr. "Simplex space-time meshes in compressible flow simulations". *International Journal for Numerical Methods in Fluids* 91 (2019), 29–48.

[55]   L. De Lorenzis, J.A. Evans, T.J.R. Hughes, and A. Reali. "Isogeometric collocation: Neumann boundary conditions and contact". *Computer Methods in Applied Mechanics and Engineering* 284 (2015), 21–54.

[56]   S. de Miranda and F. Ubertini. "Recovery of consistent stresses for compatible finite elements". *Computer Methods in Applied Mechanics and Engineering* 191 (2002), 1595–1609.

[57]   S. Demko. "On the Existence of Interpolating Projections onto Spline Spaces". *Journal of Approximation Theory* 43 (1985), 151–156.

[58]   B. Dhas, M. Masiur Rahaman, K. Akella, D. Roy, and J.N. Reddy. "A Phase-Field Damage Model for Orthotropic Materials and Delamination in Composites". *Journal of Applied Mechanics* 85 (2017), 011010.

[59]   R.P. Dhote, H. Gomez, R.N.V. Melnik, and J. Zu. "Isogeometric analysis of a dynamic thermomechanical phase-field model applied to shape memory alloys". *Computational Mechanics* 53 (2014), 1235–1250.

[60] V.N. Van Do and C.-H. Lee. "Static bending and free vibration analysis of multilayered composite cylindrical and spherical panels reinforced with graphene platelets by using isogeometric analysis method". *Engineering Structures* 215 (2020), 110682.

[61] W. Dornisch, S. Klinkel, and B. Simeon. "Isogeometric Reissner-Mindlin shell analysis with exactly calculated director vectors". *Computer Methods in Applied Mechanics and Engineering* 253 (2013), 491–504.

[62] J.-E. Dufour, P. Antolín, G. Sangalli, F. Auricchio, and A. Reali. "A cost-effective isogeometric approach for composite plates based on a stress recovery procedure". *Composites Part B: Engineering* 138 (2018), 12–18.

[63] C.L. Dym and I.H. Shames. *Solid Mechanics: A Variational Approach, Augmented Edition*. Springer Science & Business Media, 2013.

[64] T. Elguedj, Y. Bazilevs, V.M. Calo, and T.J.R. Hughes. "$\overline{B}$ and $\overline{F}$ projection methods for nearly incompressible linear and non-linear elasticity and plasticity using higher-order NURBS elements". *Computer Methods in Applied Mechanics and Engineering* 197 (2008), 2732–2762.

[65] J.J. Engblom and O.O. Ochoa. "Through-the-thickness stress predictions for laminated plates of advanced composite materials". *International Journal for Numerical Methods in Engineering* 21 (1985), 1759–1776.

[66] S. Erlicher, L. Bonaventura, and O. Bursi. "The analysis of the Generalized -α method for non-linear dynamic problems". *Computational Mechanics* 28 (2002), 83–104.

[67] J.A. Evans, R. Hiemstra, T.J.R. Hughes, and A. Reali. "Explicit higher-order accurate isogeometric collocation methods for structural dynamics". *Computer Methods in Applied Mechanics and Engineering* 338 (2018), 208–240.

[68] C. Fagiano, M.M. Abdalla, C. Kassapoglou, and Z. Gürdal. "Interlaminar stress recovery for three-dimensional finite elements". *Composites Science and Technology* 70 (2010), 530–538.

[69] F. Fahrendorf, L. De Lorenzis, and H. Gomez. "Reduced integration at superconvergent points in isogeometric analysis". *Computer Methods in Applied Mechanics and Engineering* 328 (2018), 390–410.

[70] F. Fahrendorf, S. Morganti, A. Reali, T.J.R. Hughes, and L. De Lorenzis. "Mixed stress-displacement isogeometric collocation for nearly incompressible elasticity and elastoplasticity". *Computer Methods in Applied Mechanics and Engineering* 369 (2020), 113112.

[71] C. de Falco, A. Reali, and R. Vázquez. "GeoPDEs: A research tool for Isogeometric Analysis of PDEs". *Advances in Engineering Software* 42 (2011), 1020–1034.

[72] S. Faroughi, E. Shafei, and T. Rabczuk. "Anisotropic solid-like shells modeled with NURBS-based isogeometric approach: vibration, buckling, and divergence analyses". *Composite Structures* 241 (2020), 111964.

[73] A. Farzam and B. Hassani. "A new efficient shear deformation theory for FG plates with in-plane and through-thickness stiffness variations using isogeometric approach". *Mechanics of Advanced Materials and Structures* 26 (2019), 512–525.

[74]   P. Fedeli, A. Frangi, F. Auricchio, and A. Reali. "Phase-field modeling for polarization evolution in ferroelectric materials via an isogeometric collocation method". *Computer Methods in Applied Mechanics and Engineering* 351 (2019), 789–807.

[75]   C. Felippa. *Advanced Finite Element Analysis (ASEN 6367)*. Available at `http://www.colorado.edu/engineering/CAS/courses.d/AFEM.d/`. University of Colorado at Boulder: CRC Press, 2017.

[76]   C. A. Felippa, K.C. Park, and C. Farhat. "Partitioned analysis of coupled mechanical systems". *Computer methods in applied mechanics and engineering* 190 (2001), 3247–3270.

[77]   M. Franke. "Discretisation techniques for large deformation computational contact elastodynamics". PhD thesis. Karlsruher Institut für Technologie, 2014.

[78]   T. Gerasimov and L. De Lorenzis. "A line search assisted monolithic approach for phase-field computing of brittle fracture". *Computer Methods in Applied Mechanics and Engineering* 312 (2016), 276 –303.

[79]   T. Gerasimov and L. De Lorenzis. "On penalization in variational phase-field models of brittle fracture". *Computer Methods in Applied Mechanics and Engineering* 354 (2019), 990–1026.

[80]   R.F. Gibson. *Principles of Composite Material Mechanics*. McGraw-Hill, 1994.

[81]   H. Gomez, V.M. Calo, Y. Bazilevs, and T.J.R. Hughes. "Isogeometric analysis of the Cahn–Hilliard phase-field model". *Computer Methods in Applied Mechanics and Engineering* 197 (2008), 4333–4352.

[82]   H. Gomez, T.J.R. Hughes, X. Nogueira, and V.M. Calo. "Isogeometric analysis of the isothermal Navier–Stokes–Korteweg equations". *Computer Methods in Applied Mechanics and Engineering* 199.25 (2010), 1828–1840.

[83]   H. Gomez, A. Reali, and G. Sangalli. "Accurate, efficient, and (iso)geometrically flexible collocation methods for phase-field models". *Journal of Computational Physics* 262 (2014), 153–171.

[84]   Y. Guo, A.P. Nagy, and Z. Gürdal. "A layerwise theory for laminated composites in the framework of isogeometric analysis". *Composite Structures* 107 (2014), 447–457.

[85]   Y. Guo and M. Ruess. "A layerwise isogeometric approach for NURBS-derived laminate composite shells". *Composite Structures* 124 (2015), 300–309.

[86]   Z. Hashin. *Theory of fiber reinforced materials*. Tech. rep. NASA-CR-1974. NASA, 1972.

[87]   G.A. Holzapfel. *Nonlinear Solid Mechanics: A Continuum Approach for Engineering Science*. John Wiley & Sons, 2000.

[88]   N. Hosters. "Spline-based methods for fluid-structure interaction". PhD thesis. RWTH Aachen University, 2018.

[89]   N. Hosters, J. Helmig, A. Stavrev, M. Behr, and S. Elgeti. "Fluid–structure interaction with NURBS-based coupling". *Computer Methods in Applied Mechanics and Engineering* 332 (2018), 520–539.

[90]   M.-C. Hsu *et al.* "Dynamic and fluid-structure interaction simulations of bioprosthetic heart valves using parametric design with T-splines and Fung-type material models". *Computational Mechanics* 55 (2015), 1211–1225.

[91] T.J.R. Hughes, J.A. Cottrell, and Y. Bazilevs. "Isogeometric analysis: CAD, finite elements, NURBS, exact geometry and mesh refinement". *Computer Methods in Applied Mechanics and Engineering* 194 (2005), 4135–4195.

[92] T.J.R. Hughes, J.A. Evans, and A. Reali. "Finite element and NURBS approximations of eigenvalue, boundary-value, and initial-value problems". *Computer Methods in Applied Mechanics and Engineering* 272 (2014), 290–320.

[93] T.J.R. Hughes, L.P. Franca, and G.M. Hulbert. "A new finite element formulation for computational fluid dynamics: VIII. The Galerkin/least-squares method for advective-diffusive equations". *Computer Methods in Applied Mechanics and Engineering* 73 (1989), 173–189.

[94] T.J.R. Hughes and G.M. Hulbert. "Space-time finite element methods for elastodynamics: formulations and error estimates". *Computer Methods in Applied Mechanics and Engineering* 66 (1988), 339–363.

[95] T.J.R. Hughes, A. Reali, and G. Sangalli. "Duality and unified analysis of discrete approximations in structural dynamics and wave propagation: Comparison of p-method finite elements with k-method NURBS". *Computer Methods in Applied Mechanics and Engineering* 197 (2008), 4104–4124.

[96] T.J.R. Hughes, A. Reali, and G. Sangalli. "Efficient quadrature for NURBS-based isogeometric analysis". *Computer Methods in Applied Mechanics and Engineering* 199 (2010), 301–313.

[97] J. J. Chung and G.M. Hulbert. "A Time Integration Algorithm for Structural Dynamics With Improved Numerical Dissipation: The Generalized-α Method". *Journal of Applied Mechanics* 60 (1993), 371–375.

[98] K.E. Jansen, S.S. Collis, C. Whiting, and F. Shaki. "A better consistency for low-order stabilized finite element methods". *Computer Methods in Applied Mechanics and Engineering* 174 (1999), 153–170. (Visited on 06/30/2017).

[99] C. Jareteg *et al.* "Geometry Assurance Integrating Process Variation With Simulation of Spring-In for Composite Parts and Assemblies". *Journal of Computing and Information Science in Engineering* 16 (2016), 031003.

[100] C. Johnson, U. Nävert, and J. Pitkäranta. "Finite element methods for linear hyperbolic problems". *Computer Methods in Applied Mechanics and Engineering* 45 (1984), 285–312.

[101] R.W. Johnson. "A B-spline collocation method for solving the incompressible Navier-Stokes equations using an ad hoc method: The Boundary Residual method". *Computers & Fluids* 34 (2005), 121–149.

[102] R. Jones. *Mechanics of Composite Materials*. Taylor & Francis, 1998.

[103] H. Kapoor, R.K. Kapania, and S.R. Soni. "Interlaminar stress calculation in composite and sandwich plates in NURBS Isogeometric finite element analysis". *Composite Structures* 106 (2013), 537–548.

[104] V. Karyofylli, M. Frings, S. Elgeti, and M. Behr. "Simplex space-time meshes in two-phase flow simulations". *International Journal for Numerical Methods in Fluids* 86 (2018), 218–230.

[105] R. Khandan, S. Noroozi, P. Sewell, and J. Vinney. "The development of laminated composite plate theories: a review". *Journal of Materials Science* 47 (2012), 5901–5910.

[106] J. Kiendl, F. Auricchio, T.J.R. Hughes, and A. Reali. "Single-variable formulations and isogeometric discretizations for shear deformable beams". *Computer Methods in Applied Mechanics and Engineering* 284 (2015), 988–1004.

[107] J. Kiendl, F. Auricchio, and A. Reali. "A displacement-free formulation for the Timoshenko beam problem and a corresponding isogeometric collocation approach". *Meccanica* 53 (2018), 1403–1413.

[108] J. Kiendl, F. Auricchio, L. Beirão da Veiga, C. Lovadina, and A. Reali. "Isogeometric collocation methods for the Reissner–Mindlin plate problem". *Computer Methods in Applied Mechanics and Engineering* 284 (2015), 489 –507.

[109] J. Kiendl, K.U. Bletzinger, J. Linhard, and R. Wüchner. "Isogeometric shell analysis with Kirchhoff-Love elements". *Computer Methods in Applied Mechanics and Engineering* 198 (2009), 3902–3914.

[110] J. Kiendl, E. Marino, and L. De Lorenzis. "Isogeometric collocation for the Reissner–Mindlin shell problem". *Computer Methods in Applied Mechanics and Engineering* 325 (2017), 645–665.

[111] T. Klöppel, A. Popp, U. Küttler, and W.A. Wall. "Fluid-structure interaction for non-conforming interfaces based on a dual mortar formulation". *Computer Methods in Applied Mechanics and Engineering* 200 (2011), 3111–3126.

[112] D. Knees and M. Negri. "Convergence of alternate minimization schemes for phase field fracture and damage". *Mathematical Models and Methods in Applied Sciences* 27 (2017), 1743–1794.

[113] S. Kollmannsberger, A. Düster, and E. Rank. "Force Transfer for high order finite element methods using intersected meshes". In: *ASME 2007 Pressure Vessels and Piping Conference*. American Society of Mechanical Engineers, 2007, 111–116.

[114] I. Kreja. "A literature review on computational models for laminated composite and sandwich panels". *Central European Journal of Engineering* 1 (2011), 59–80.

[115] R. Kruse, N. Nguyen-Thanh, L. De Lorenzis, and T.J.R. Hughes. "Isogeometric collocation for large deformation elasticity and frictional contact problems". *Computer Methods in Applied Mechanics and Engineering* 296 (2015), 73–112.

[116] N. Kubicki. "Ein Beitrag zur Kombination von NURBS-erweiterten Finiten Elementen und Isogeometrischer Kollokation im Rahmen der Fluid-Struktur-Interaktion". MA thesis. RWTH Aachen University, 2020.

[117] Angewandte Mathematik und Numerik Lehrstuhl III. *Numerical Benchmarking of fluid-structure Interaction between an elastic Object and laminar incompressible Flow*. http://www.featflow.de/en/benchmarks/cfdbenchmarking/fsi_benchmark.html.

[118] L. Leonetti *et al.* "A simplified Kirchhoff-Love large deformation model for elastic shells and its effective isogeometric formulation". *Computer Methods in Applied Mechanics and Engineering* 354 (2019), 369–396.

[119] D. Li. "Layerwise Theories of Laminated Composite Structures and Their Applications: A Review". *Archives of Computational Methods in Engineering* 28 (2021), 577–600.

[120] K.M. Liew, Z.Z. Pan, and L.W. Zhang. "An overview of layerwise theories for composite laminates and structures: Development, numerical implementation and application". *Composite Structures* 216 (2019), 240–259.

[121] S. Lipton, J.A. Evans, Y. Bazilevs, T. Elguedj, and T.J.R. Hughes. "Robustness of isogeometric structural discretizations under severe mesh distortion". *Computer Methods in Applied Mechanics and Engineering* 199 (2010), 357–373.

[122] D. Liu and X. Li. "An Overall View of Laminate Theories Based on Displacement Hypothesis". *Journal of Composite Materials* 30 (1996), 1539–1561.

[123] J. Liu, H. Gomez, J.A. Evans, T.J.R. Hughes, and C.M. Landis. "Functional entropy variables: A new methodology for deriving thermodynamically consistent algorithms for complex fluids, with particular reference to the isothermal Navier–Stokes–Korteweg equations". *Journal of Computational Physics* 248 (2013), 47–86.

[124] K.H. Lo, R.M. Christensen, and E.M. Wu. "A High-Order Theory of Plate Deformation—Part 2: Laminated Plates". *Journal of Applied Mechanics* 44 (1977), 669–676.

[125] G. Lorenzo, T.J.R. Hughes, P. Dominguez-Frojan, A. Reali, and H. Gomez. "Computer simulations suggest that prostate enlargement due to benign prostatic hyperplasia mechanically impedes prostate cancer growth". *Proceedings of the National Academy of Sciences of the United States of America* 116 (2009), 1152–1161.

[126] Y. Lu, T. Helfer, B. Bary, and O. Fandeur. "An efficient and robust staggered algorithm applied to the quasi-static description of brittle fracture by a phase-field approach". *Computer Methods in Applied Mechanics and Engineering* 370 (2020), 113218.

[127] O.L. Mangasarian. "Solution of Symmetric Linear Complementarity Problems by Iterative Methods". *Journal of Optimization Theory and Applications* 22 (1977), 465–485.

[128] C. Manni, A. Reali, and H. Speleers. "Isogeometric collocation methods with generalized B-splines". *Computers & Mathematics with Applications* 70 (2015), 1659 –1675.

[129] E. Marino, J. Kiendl, and L. De Lorenzis. "Explicit isogeometric collocation for the dynamics of three-dimensional beams undergoing finite motions". *Computer Methods in Applied Mechanics and Engineering* 343 (2019), 530–549.

[130] Enzo Marino. "Isogeometric collocation for three-dimensional geometrically exact shear-deformable beams". *Computer Methods in Applied Mechanics and Engineering* 307 (2016), 383–410.

[131] Enzo Marino. "Locking-free isogeometric collocation formulation for three-dimensional geometrically exact shear-deformable beams with arbitrary initial curvature". *Computer Methods in Applied Mechanics and Engineering* 324 (2017), 546–72.

[132] F. Massarwi, P. Antolín, and G. Elber. "Volumetric untrimming: Precise decomposition of trimmed trivariates into tensor products". *Computer Aided Geometric Design* 71 (2019), 1–15.

[133] F. Maurin, F. Greco, L. Coox, D. Vandepitte, and W. Desmet. "Isogeometric collocation for Kirchhoff–Love plates and shells". *Computer Methods in Applied Mechanics and Engineering* 329 (2018), 396–420.

[134] C. Miehe, M. Hofacker, and F. Welschinger. "A phase field model for rate-independent crack propagation: robust algorithmic implementation based on operator splits". *Computer Methods in Applied Mechanics and Engineering* 199 (2010), 2765–2778.

[135] C. Miehe, F. Welschinger, and M. Hofacker. "Thermodynamically consistent phase-field models of fracture: Variational principles and multi-field FE implementations". *International Journal for Numerical Methods in Engineering* 83 (2010), 1273–1311.

[136] C. Mittelstedt and W. Becker. "Free-Edge Effects in Composite Laminates". *Applied Mechanics Reviews* 60 (2007), 217–245.

[137] G. Molnár and A. Gravouil. "2D and 3D Abaqus implementation of a robust staggered phase-field solution for modeling brittle fracture". *Finite Elements in Analysis and Design* 130 (2017), 27 –38.

[138] M. Montardini, G. Sangalli, and L. Tamellini. "Optimal-order isogeometric collocation at Galerkin superconvergent points". *Computer Methods in Applied Mechanics and Engineering* 316 (2017), 741–757.

[139] S. Morganti, C. Callari, F. Auricchio, and A. Reali. "Mixed isogeometric collocation methods for the simulation of poromechanics problems in 1D". *Meccanica* 53 (2018), 1441–1454.

[140] S. Morganti *et al.* "Patient-specific isogeometric structural analysis of aortic valve closure". *Computer Methods in Applied Mechanics and Engineering* 284 (2015), 508–520.

[141] T.N. Nguyen, C.H. Thai, H. Nguyen-Xuan, and J. Lee. "NURBS-based analyses of functionally graded carbon nanotube-reinforced composite shells". *Composite Structures* 203 (2018), 349–360.

[142] H. Nguyen-Xuan, Chien H. Thai, and T. Nguyen-Thoi. "Isogeometric finite element analysis of composite sandwich plates using a higher order shear deformation theory". *Composites Part B: Engineering* 55 (2013), 558–574.

[143] M. Ortiz and J.C. Simo. "An analysis of a new class of integration algorithms for elastoplastic constitutive relations". *International Journal for Numerical Methods in Engineering* 23 (1996), 353–366.

[144] N.S. Ottosen and M. Ristinmaa. *The Mechanics of Constituive modeling*. Elsevier Science, 2005.

[145] N.J. Pagano. "Exact Solutions for Rectangular Bidirectional Composites and Sandwich Plates". *Journal of Composite Materials* 4 (1970), 20–34.

[146] N.J. Pagano and R.B. Pipes. "Some observations on the interlaminar strength of composite laminates". *International Journal of Mechanical Sciences* 15 (1973), 679–688.

[147] N.J. Pagano and R.B. Pipes. "The Influence of Stacking Sequence on Laminate Strength". *Journal of Composite Materials* 5 (1971), 50–57.

[148] A. Patton, P. Antolín, J.-E. Dufour, J. Kiendl, and A. Reali. "Accurate equilibrium-based interlaminar stress recovery for isogeometric laminated composite Kirchhoff plates". *Composite Structures* 256 (2021), 112976.

[149] A. Patton, J.-E. Dufour, P. Antolín, and A. Reali. "Fast and accurate elastic analysis of laminated composite plates via isogeometric collocation and an equilibrium-based stress recovery approach". *Composite Structures* 225 (2019), 111026.

[150] L. Pauli. "Stabilized finite element methods for computational design of blood-handling devices". PhD thesis. RWTH Aachen University, 2016.

[151] G.S. Pavan and K.S. Nanjunda Rao. "Bending analysis of laminated composite plates using isogeometric collocation method". *Composite Structures* 176 (2017), 715–728.

[152] P. Phung-Van, T.V. Loc, A.J.M. Ferreira, H. Nguyen-Xuan, and M. Abdel-Wahab. "Nonlinear transient isogeometric analysis of smart piezoelectric functionally graded material plates based on generalized shear deformation theory under thermo-electro-mechanical loads". *Nonlinear Dynamics* 87 (2017), 879–894.

[153] L. Piegl and W. Tiller. *The NURBS Book*. Berlin, Heidelberg: Springer-Verlag, 1997.

[154] C.W. Pryor and R.M. Barker. "A finite-element analysis including transverse shear effects for applications to laminated plates". *AIAA Journal* 9 (1971), 912–917.

[155] P. Qiao and J. Wang. "Transverse Shear Stiffness of Composite Honeycomb Cores and Efficiency of Material". *Mechanics of Advanced Materials and Structures* 12 (2005), 159–172.

[156] A. Reali. "An isogeometric analysis approach for the study of structural vibrations". *Journal of Earthquake Engineering* 10 (2006), 1–30.

[157] A. Reali and H. Gomez. "An isogeometric collocation approach for Bernoulli-Euler beams and Kirchhoff plates". *Computer Methods in Applied Mechanics and Engineering* 284 (2015), 623–636.

[158] J.N. Reddy. "A Simple Higher-Order Theory for Laminated Composite Plates". *Journal of Applied Mechanics* 51 (1984), 745–752.

[159] J.N. Reddy. *Mechanics of Laminated Composite Plates and Shells: Theory and Analysis*. CRC Press, 2003.

[160] J.J.C. Remmers, C.V. Verhoosel, and R. de Borst. "Isogeometric analysis for modelling of failure in advanced composite materials". In: *Numerical Modelling of Failure in Advanced Composite Materials*. Ed. by P.P. Camanho and S.R. Hallett. Woodhead Publishing Series in Composites Science and Engineering. Woodhead Publishing, 2015, 309–329.

[161] G. Sangalli and M. Tani. "Matrix-free weighted quadrature for a computationally efficient isogeometric k-method". *Computer Methods in Applied Mechanics and Engineering* 338 (2018), 117–133.

[162] D. Schillinger, J.A. Evans, A. Reali, M.A. Scott, and T.J.R. Hughes. "Isogeometric collocation: Cost comparison with Galerkin methods and extension to adaptive hierarchical NURBS discretizations". *Computer Methods in Applied Mechanics and Engineering* 267 (2013), 170–232.

[163] R. Sevilla. "HDG-NEFEM for two dimensional linear elasticity". *Computers & Structures* 220 (2019), 69–80.

[164] R. Sevilla, S. Fernández-Méndez, and A. Huerta. "NURBS-enhanced finite element method (NEFEM)". *International Journal for Numerical Methods in Engineering* 76 (2008), 56–83.

[165] R. Sevilla, S. Fernández-Méndez, and A. Huerta. "NURBS-Enhanced Finite Element Method (NEFEM): A seamless bridge between CAD and FEM". *Archives of Computational Methods in Engineering* 18 (2011), 441–484.

[166] E. Shafei, S. Faroughi, and A. Reali. "Geometrically nonlinear vibration of anisotropic composite beams using isogeometric third-order shear deformation theory". *Composite Structures* 252 (2020), 112627.

[167] F. Shakib. "Finite element analysis of the compressible Euler and Navier-Stokes equations". PhD thesis. Stanford University, 1989.

[168] J.C. Simo and T.J.R. Hughes. *Computational Inelasticity*. New York: Springer, 1998.

[169] S. Sridharan. *Delamination Behaviour of Composites*. Woodhead Publishing, 2008.

[170] A. Stavrev, P. Knechtges, S. Elgeti, and A. Huerta. "Space-time NURBS-enhanced finite elements for free-surface flows in 2D". *International Journal for Numerical Methods in Fluids* 81 (2016), 426–450.

[171] C.T. Sun and S. Li. "Three-Dimensional Effective Elastic Constants for Thick Laminates". *Journal of Composite Materials* 22 (1988), 629–639.

[172] B. Szabó, A. Düster, and E. Rank. "The p-Version of the Finite Element Method". In: *Encyclopedia of Computational Mechanics*. American Cancer Society, 2004. Chap. 5.

[173] K. Takizawa and T.E. Tezduyar. "Multiscale space-time fluid-structure interaction techniques". *Computational Mechanics* 48 (2011), 247–267.

[174] T.E. Tezduyar, M. Behr, and J. Liou. "A new strategy for finite element computations involving moving boundaries and interfaces—The deforming-spatial-domain/space-time procedure: I. The concept and the preliminary numerical tests". *Computer Methods in Applied Mechanics and Engineering* 94 (1992), 339–351.

[175] T.E. Tezduyar, M. Behr, S. Mittal, and J. Liou. "A new strategy for finite element computations involving moving boundaries and interfaces—The deforming-spatial-domain/space-time procedure: II. Computation of free-surface flows, two-liquid flows, and flows with drifting cylinders". *Computer Methods in Applied Mechanics and Engineering* 94 (1992), 353–371.

[176] C.H. Thai, A.J.M. Ferreira, M. Abdel-Wahab, and H. Nguyen-Xuan. "A generalized layerwise higher-order shear deformation theory for laminated composite and sandwich plates based on isogeometric analysis". *Acta Mechanica* 227 (2016), 1225–1250.

[177] C.H. Thai, H. Nguyen-Xuan, S.P.A. Bordas, N. Nguyen-Thanh, and T. Rabczuk. "Isogeometric Analysis of Laminated Composite Plates Using the Higher-Order Shear Deformation Theory". *Mechanics of Advanced Materials and Structures* 22 (2015), 451–469.

[178] C.-L. Thanh, A.J.M. Ferreira, and M. Abdel-Wahab. "A refined size-dependent couple stress theory for laminated composite micro-plates using isogeometric analysis". *Thin-Walled Structures* 145 (2019), 106427.

[179] C.-L. Thanh, L.V. Tran, T.Q. Bui, H.X. Nguyen, and M. Abdel-Wahab. "Isogeometric analysis for size-dependent nonlinear thermal stability of porous FG microplates". *Composite Structures* 221 (2019), 110838.

[180] F. Tornabene, N. Fantuzzi, and M. Bacciocchi. "A new doubly-curved shell element for the free vibrations of arbitrarily shaped laminated structures based on Weak Formulation IsoGeometric Analysis". *Composite Structures* 171 (2017), 429–461.

[181]   S.W. Tsai and E.M. Wu. "A General Theory of Strength for Anisotropic Materials". *Journal of Composite Materials* 5 (1971), 58–80.

[182]   S. Turek and J. Hron. "Proposal for numerical benchmarking of fluid-structure interaction between an elastic object and laminar incompressible flow". In: *Fluid-Structure Interaction*. Ed. by H.-J. Bungartz and M. Schäfer. Vol. 53. Lecture Notes in Computational Science and Engineering. Springer, Berlin, Heidelberg, 2006, 371–385.

[183]   F. Ubertini. "Patch recovery based on complementary energy". *International Journal for Numerical Methods in Engineering* 59 (2004), 1501–1538.

[184]   T.K. Varadan and K. Bhaskar. "Bending of laminated orthotropic cylindrical shells—An elasticity approach". *Composite Structures* 17 (1991), 141 –156.

[185]   L. Beirão da Veiga, A. Buffa, C. Lovadina, M. Martinelli, and G. Sangalli. "An isogeometric method for the Reissner–Mindlin plate bending problem". *Computer Methods in Applied Mechanics and Engineering* 209-212 (2012), 45–53.

[186]   L. Beirão da Veiga, C. Lovadina, and A. Reali. "Avoiding shear locking for the Timoshenko beam problem via isogeometric collocation methods". *Computer Methods in Applied Mechanics and Engineering* 241-244 (2012), 38–51.

[187]   J.R. Vinson and R.L. Sierakowski. *The Behavior of Structures Composed of Composite Materials*. Springer, 1986.

[188]   C.M. Wang, J.N. Reddy, and K.H. Lee. *Shear Deformable Beams and Plates. Relationships with Classical Solutions*. Elsevier Science Ltd, 2000.

[189]   O. Weeger, B. Narayanan, L. De Lorenzis, J. Kiendl, and M.L. Dunn. "An isogeometric collocation method for frictionless contact of Cosserat rods". *Computer Methods in Applied Mechanics and Engineering* 321 (2017), 361–382.

[190]   O. Weeger, S.-K. Yeung, and M.L. Dunn. "Fully isogeometric modeling and analysis of nonlinear 3D beams with spatially varying geometric and material parameters". *Computer Methods in Applied Mechanics and Engineering* 342 (2018), 95–115.

[191]   O. Weeger, S.-K. Yeung, and M.L. Dunn. "Isogeometric collocation methods for Cosserat rods and rod structures". *Computer Methods in Applied Mechanics and Engineering* 316 (2017), 100–122.

[192]   J.M. Whitney and A.W. Leissa. "Analysis of Heterogeneous Anisotropic Plates". *Journal of Applied Mechanics* 36 (1969), 261–266.

[193]   T. Wick. "Modified Newton methods for solving fully monolithic phase-field quasi-static brittle fracture propagation". *Computer Methods in Applied Mechanics and Engineering* 325 (2017), 577 –611.

[194]   B.J. Winkler. "Traglastuntersuchungen von unbewehrten und bewehrten Betonstrukturen auf der Grundlage eines objektiven Werkstoffgesetzes für Beton". PhD thesis. Innsbruck University Press, 2001.